Metamorphic and melt-migration history of midcrustal migmatitic gneisses from Nupskåpa, the Maud Belt, Antarctica

Sukey Thomas

a thesis submitted for the degree of
Master of Science
at the University of Cape Town, Cape Town,
South Africa.

2014

Plagiarism Declaration:
I know the meaning of plagiarism and declare that all the work in the document, save for that which is properly acknowledged, is my own.

Sukey Anna Jay Thomas

15 August 2014

Abstract

Melt migration is an important process in the crust that causes significant mass transport, as well as differentiation and stabilisation of continental crust. Melt migration near the source occurs pervasively, through interconnected networks of melt-bearing structures. This style is restricted to the suprasolidus mid- to lower crust, while focused migration and ascent of magma occurs in isolated dyke-like structures under subsolidus conditions, generally in the upper crust where brittle fracturing of rocks can occur. The details of how and when melt migration changes from a pervasive to focused style are poorly understood, particularly the temperature, pressure and deformation conditions which allow the transition to occur. The Nupskåpa nunatak, in Dronning Maud Land of East Antarctica, exposes large cliffs that record evidence of multiple episodes of melt movement, in the form of pervasive leucogranite vein networks cross-cut by larger leucogranite dykes.

Mineral equilibria modelling with THERMOCALC and comparison of results with previous work indicates that the Nupskåpa nunatak records both Grenvillian and Pan-African metamorphism. Coarse-grained peak assemblages in samples from the Nupskåpa area record conditions of 820–880 °C at 9.5–11.6 kbar, while post-tectonic retrograde assemblages record late Pan-African conditions of 555–595 °C at 3.2–4.8 kbar. These later conditions lie between the wet solidus and the brittle-viscous transition and are inferred to represent the conditions of intrusion for post-tectonic composite dykes.

Small-scale leucosomes predominantly lie parallel to the gneissic host rock fabric and define a pervasive network across the Nupskåpa cliff. These leucosomes exhibit diffuse feathery boundaries and are inferred to represent *in situ* melting and melt segregation during M_1 granulite facies peak metamorphism. Composite leucogranitic dykes cross-cut both the early leucosome phase and Pan-African shear zones in the field area. These north-trending, subvertical dykes are near-

orthogonal to the gneissic fabric. They are 0.5–2 m wide and spaced ∼10–20 m apart but not interconnected except where two dykes coalesce. The dykes show almost no shear displacement, indicating that they formed via tensile fracture. This indicates that their intrusion occurred during extensional or strike-slip deformation, under conditions of low differential stress, probably coupled to high melt pressure. The composite dykes resulted from the far-field transport of melt from a source 5 to 15 km below the Nupskåpa outcrop. Although individually they are discrete and focused structures, they are numerous across the field area and closely spaced, so together they do not represent a wholly focused melt transfer system.

The style of melt migration displayed by the composite dykes is an example of the transition from pervasive to focused migration, occurring in the mid-crust at subsolidus conditions. This transition involved a network of smaller melt-filled fractures gradually coalescing into larger ones with decreasing depth. If pervasive migration becomes focused via this gradual transition, melt accumulation and mixing need not occur solely in the source or final emplacement structure, but rather occurs throughout transport of the magma.

Acknowledgements

I would like to thank SANAP for funding my field work in Antarctica and the National Research Foundation for my Innovation Scholarship. Thank you to my supervisors Johann Diener and Åke Fagereng for their guidance and assistance and for the amazing opportunities they have provided me with. Thank you to friends and family for their proof-reading skills and confidence in me.

Contents

List of Tables

List of Figures

Chapter 1

Introduction

Granitic melt migration is an important process in the Earth's continental crust. It causes significant mass transport, as well as differentiation and stabilisation of continental crust (Sawyer, 1994; Brown & Solar, 1998a; Bons *et al.*, 2004; Brown, 2004, 2010; Sawyer *et al.*, 2011). The presence of even a low melt fraction can significantly weaken the continental crust, and therefore has important consequences for how deformation and orogenic events occur (Brown, 1994; Brown & Solar, 1998a; Vigneresse, 2006; Schulmann *et al.*, 2008; Beaumont *et al.*, 2009; Brown, 2010; Sawyer *et al.*, 2011; Jamieson & Beaumont, 2011)

Granitic melt forms in the lower crust through partial melting of extensive volumes of rock (Stevens *et al.*, 1997; Vielzeuf & Schmidt, 2001). How much melt forms depends on the rock type, the temperature and pressure at which melting occurs, and the hydrous fluid content of the source rocks (Clemens & Vielzeuf, 1987; Stevens *et al.*, 1997; Vigneresse, 2006). Melt forms in the lower crust at depths anywhere between 20 and 70 km (but on average at ∼30 km; Brown *et al.*, 2011; Sawyer *et al.*, 2011), with large volumes of rock producing melt dispersed along grain boundaries (i.e. millimetre to submillimetre scale) (Vigneresse, 2006). Melt emplaces in the upper crust as discrete plutonic bodies (up to tens of kilometres in size) in the upper crust, at ∼10 km depth, or may erupt as lava (Brown *et al.*, 2011; Sawyer *et al.*, 2011). Thus melt must accumulate into larger volumes and migrate through the crust, before being emplaced in the upper crust. On its way through the crust melt must move through country rocks at suprasolidus conditions, into shallower country rock at subsolidus conditions and, in some instances, cross the brittle-viscous transition(Sawyer *et al.*, 2011); all without crystallising. The solidus represents the transition from melt-bearing to melt-absent rocks, and the brittle-viscous transition represents the change from distributed to localised

deformation of the country rock. Thus, both form major rheological boundaries and rocks on either side will respond very differently to deformation (Brown & Solar, 1999; Vigneresse, 2006; Brown, 2010; Sawyer *et al.*, 2011). It is therefore unlikely that melt can move from the lower to upper crust via one mechanism that is capable of overcoming all of these rheological changes (Clemens & Mawer, 1992; Paterson & Fowler, 1993; Brown, 1994; Weinberg, 1996).

Melt migration is generally thought to occur via one (or a combination) of two end-member mechanisms, which operate in different parts of the crust: pervasive flow in the lower, hotter parts of the crust (see Collins & Sawyer, 1996; Weinberg, 1999; Bons *et al.*, 2004; Hall & Kisters, 2012), and focused flow in the upper, cooler parts of the crust (see Clemens & Mawer, 1992; Brown, 1994; Weinberg, 1996; Clemens *et al.*, 1997; Petford *et al.*, 1994). The conditions and processes by which one mechanism transforms to the other have not been resolved (e.g. Brown & Solar, 1998a). This project aims to address some of these issues, in particular: by what mechanisms, and under what pressure, temperature and deformation conditions melt moves through the mid-crust, as well as how and when the style of movement changes from pervasive to focused.

1.1 Mechanisms of melt ascent

There are three main end-member models of how melt ascent can take place:

1. Diapirism involves the gradual rising of buoyant magma as large single volumes. Ductile deformation in the hot surrounding rock controls the rate of ascent (Bons *et al.* (2004) and others therein). Up until the early 1990s, this was the preferred mechanism of ascent for granitic melt (Sweeney, 1975; Marsh, 1982; Bateman, 1984). Many researchers (e.g. Clemens & Mawer, 1992; Brown, 1994; Weinberg, 1996; Clemens *et al.*, 1997; Bons *et al.*, 2004) now agree that evidence for frequent diapirism in the crust is lacking, and consider it to be an unfeasible explanation for the ascent of melt and emplacement of most plutons and magma chambers in the upper crust. Others (e.g Weinberg & Podladchikov, 1994) regard it as a suitable explanation for the ascent and emplacement of plutons in the lower crust. In particular, the emplacement of the well-studied Sierra Nevada batholith is thought to have involved diapirism, as well as other mechanisms such as fracturing (Paterson & Vernon, 1995; McNulty *et al.*, 2000). Extensive computer modelling by Mahon *et al.* (1988), based on calculating an ascent velocity relationship for granitoid diapirs and applying this to a heat flow model within

the crust, has shown that despite varying the magma volume, temperature, starting depth and density contrast between diapir and country rock, and irrespective of likely changes in geothermal gradient, diapiric granitic magma bodies eventually crystallize and do not emplace higher than the mid-crust. Because diapirism is thought to occur only under very specific circumstances, it will not be considered further in this study.

2. Focused flow involves the ascent of magma via a limited number of conduits, such as conventional dykes, self-propagating fractures and crustal-scale shear zones (Weertman, 1971; Sleep, 1988; Lister & Kerr, 1991; Clemens & Mawer, 1992; Petford *et al.*, 1993; Brown, 1994; Petford *et al.*, 1994; Weinberg, 1996; Clemens *et al.*, 1997; Bons *et al.*, 2004; Hall & Kisters, 2012). It was known as a mechanism for the transport of mafic magmas (e.g Weertman, 1971), and researchers were doubtful as to its application to granitic magmas, owing to the much lower viscosity contrast between granitic magma and country rocks. However, it has since been shown that granitic magmas can also ascend via dyke structures and that this is an efficient mechanism of transporting large volumes of melt through subsolidus crust (Clemens & Mawer, 1992; Petford *et al.*, 1993; Brown & Solar, 1999; Hall & Kisters, 2012).

   Focused flow may occur via brittle mechanisms, where fracturing occurs as a result of melt pressure building up sufficiently to overcome the tensile strength of the rock at the fracture tip, creating a path along which melt can then move (Sleep, 1988; Petford, 1996; Brown, 2004; Weinberg, 1999; Kisters *et al.*, 2009). This results in dykes and/or self-propagating fractures.

   The aspect ratio (i.e. width verses length) of a dyke or self-propagating fracture is a function of effective normal stress and tensile strength (Clemens & Mawer, 1992; Vermilye & Scholz, 1995). This aspect ratio is thus limited by gradients in effective normal stress as a result of the differing rates of increase between lithostatic pressure and melt pressure with depth, and is also limited by the tensile stress caused by melt pressure and therefore by melt-supply (Weertman, 1971). If a melt-filled fracture exceeds its maximum length (on the order of several tens to hundreds of metres), or if melt supply is insufficient to keep the dyke open, it may start to close on one end while simultaneously opening on the other (Clemens & Mawer, 1992; Weinberg, 1999; Bons *et al.*, 2001, 2004; Kisters *et al.*, 2009). Melt is then envisaged as moving through these 'mobile' fractures as individual pulses, controlled by the supply of magma in the source region.

In subduction zones, these pulses are thought to be frequent and of small volume, as less-frequent, larger volumes would require more storage time in larger crustal reservoirs (Brown, 2004). Because the fracture closes up after the individual batch of melt has passed through, this mechanism may leave little evidence behind in exposed outcrops, with dykes appearing much thinner after having been almost totally drained of melt (Clemens & Mawer, 1992; Petford *et al.*, 1994; Weinberg, 1999; Bons *et al.*, 2008; Brown, 2004).

It is thought that smaller melt-filled fractures gradually coalesce into larger fractures, creating a self-similar system, which eventually drains into crustal-scale features ((Figure 1.1; Weinberg, 1999; Bons *et al.*, 2004; Sawyer *et al.*, 2011). These large features are then able to drain the source and transport a large volume of magma through a small number of individual structures (Weinberg, 1996; Bons *et al.*, 2004; Brown, 2004).

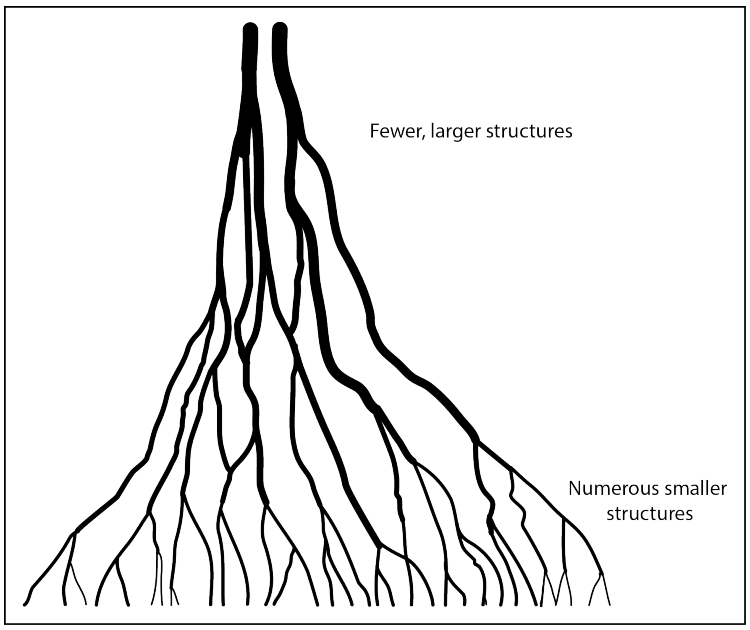

Figure 1.1: Schematic illustration of the way in which melt-filled fractures are thought to gradually coalesce into larger fractures, creating a self-similar system. The larger fractures drain into crustal-scale features such as large dykes and shear zones. (After Faber, 2012)

Focused flow may also occur via ductile or strain-controlled mechanisms. Owing to the anisotropic nature of the lower crust, the anatectic region is unlikely to be a simple tabular horizontal section of the crust. Similarly, it is likely that sections of the anatectic zone will be inclined to one of the principal stresses and thus shear stresses will operate

across that section. Melt-filled fractures experiencing shear stresses will deform more easily than the surrounding melt-free rock. This leads to the development of melt-lubricated shear zones (Hollister & Crawford, 1986; Brown & Solar, 1998a,b, 1999; Handy *et al.*, 2001). Dykes may initiate in suprasolidus crust through ductile fracture but, during ascent through increasingly viscous subsolidus crust, this ductile fracture process may change to a brittle-elastic fracture process (Weinberg & Regenauer-Lieb, 2010; Brown *et al.*, 2011; Brown, 2013).

It has been shown that melt migration via this method, in discrete structures that are on the order of a few metres wide, is an efficient process that allows for the transport of large volumes of magma through the subsolidus crust, at rapid rates, to the emplacement level in the upper crust (Clemens & Mawer, 1992; Petford *et al.*, 1993, 1994; Rubin, 1995; Petford, 1996).

The regional stress regime operating in the crust during magma ascent will greatly influence the style of focused flow, particularly the deformation mechanism but also the shape and orientations of the fractures or melt-ascent-features (Petford, 1996; Weinberg, 1996). Conventional (vertical) dyking as an ascent mechanism may be inhibited in convergent orogenies, for instance, as fractures generally form parallel to maximum (and normal to minimum) compressive stress (Anderson, 1951; Brown, 1994; Vanderhaeghe, 2001; Vigneresse, 2006). Assuming Andersonian mechanics, this means that dykes in convergent orogenies will be horizontal, normal to a vertical σ_3. Thus melt will migrate laterally in fractures and dykes but upward movement of melt will be inhibited. In such a case it is more likely that melt will ascend via crustal-scale shear zone structures (Clemens & Mawer, 1992; Brown, 1994; Brown & Solar, 1998b).

In order for dyking to initiate and operate, the surrounding rock must be brittle, at least momentarily and locally at the fracture tip, as rock behaving viscously will flow instead of fracturing, thus dissipating the fracture propagation energy (Clemens & Mawer, 1992). Brittle failure by tensile fracture is possible in rocks in the anatectic zone if the melt pressure is larger than the combination of the tensile strength of the rocks and the least compressive stress. This required melt pressure will increase with depth because of increases in confining stress, resulting in larger melt pressures being required to initiate fractures. Under the high temperature conditions of the lower crust, rocks will be more likely to flow viscously before this large required melt pressure is

reached. If enough melt pressure does build up to cause hydraulic fracturing, that melt pressure is soon dissipated and will take a while to build up again. This may lead to melt being transported via discrete pulses or batches (e.g. Bons *et al.*, 2004), but will not result in continuous melt flow from the source to the upper crust (Brown, 1994).

Thus, the formation of dykes that transport large volumes of magma vertically upwards is most likely limited to the higher subsolidus parts of the crust as their formation and propagation is inhibited in the lower, high-pressure crust (Clemens & Mawer, 1992; Petford *et al.*, 1994; Bons *et al.*, 2004).

3. Pervasive melt migration envisages melt moving through interconnected permeability or fracture systems (Collins & Sawyer, 1996; Weinberg, 1999; Vanderhaeghe, 2001; Leitch & Weinberg, 2002; Bons *et al.*, 2004; Weinberg & Regenauer-Lieb, 2010; Hall & Kisters, 2012). The movement of magma in these pervasive networks is thought to be driven by local pressure gradients caused by tectonic deformation (and in some instances buoyancy), and operates efficiently in rocks at suprasolidus conditions (Brown, 1994; Weinberg, 1999). Deformation of anisotropic crust leads to the development of pressure gradients and structural heterogeneities on all scales. These pressure gradients cause melt to move towards sites of low pressure (Brown, 1994; Sawyer, 1994; Collins & Sawyer, 1996; Brown & Solar, 1999). Thus melt exploits existing anisotropies and dilatancy sites such as layering, foliation planes, fold hinges, mineral lineation and boudin necks (Brown, 1994; Collins & Sawyer, 1996; Weinberg, 1999).

   The orientation of dilational sites depends on the orientation of the principal stresses and on the orientation of pre-existing anisotropies, which may vary depending on when they formed, as they may have formed in a separate deformation phase (Sawyer *et al.*, 2011; Hall & Kisters, 2012; Reichardt & Weinberg, 2012). Thus, the dilational sites and existing anisotropies that melt exploits may commonly be subhorizontal, and so melt may experience extensive lateral migration before any vertical ascent occurs (Brown, 1994). In the absence of a pressure gradient, if melt volume is locally very high, or if the strain rate caused by deformation is greater than the rate at which melt can move to low-pressure sites, melt pressure can increase, reducing effective normal stress and causing hydraulic fracturing of the country rock (Clemens & Mawer, 1992; Brown, 1994; Weinberg, 1999; Hall & Kisters, 2012).

   Because the small melt bodies making up the pervasive network are susceptible to solidi-

fication as a result of heat loss, melt migration may cease if the thermal contrast between melt and country rock becomes too large. Pervasive flow is therefore generally limited to hotter parts of the crust, usually to the level of the crustal isotherm corresponding to the solidus of the melt (Brown & Solar, 1998a; Weinberg, 1999). Thus, pervasive flow generally occurs within, or close to, the anatectic region (Weinberg, 1999; Brown, 2004; Hall & Kisters, 2012). However, the limits of pervasive flow may be extended to shallower levels in the crust through feedback relationships between melt migration and thermal structure (Weinberg, 1996; Brown & Solar, 1998a; Weinberg, 1999). Once melt has been removed from its source, the remaining volume of rock will be less fertile and so will have an elevated solidus (White & Powell, 2002). Thus, segregated melt tends to have a lower solidus temperature than the rocks it formed from (sometimes by as much as 100°C; Weinberg, 1999), and so can migrate away from its source before freezing. The movement of melt up through the crust allows heat to be transferred to shallower crustal levels, moving isotherms higher and allowing melt to migrate further before it freezes, thus extending the limits of pervasive migration (Brown & Solar, 1999). With favourable conditions, the zone of pervasive melt migration may be extended above the anatectic zone, by about 3–5 km (Weinberg, 1999; Faber, 2012). Controls such as rate of melt production and extraction, as well as the rate of heat advection, will cause pervasive flow to eventually cease operating and thus, pervasive flow cannot account for large volumes of magma intruded into colder and/or shallower levels of the crust (Weinberg, 1999; Leitch & Weinberg, 2002).

Pervasive flow occurs via a dispersed network of many small centimetre- to metre-scale structures, whereas focused flow operates via fewer, separated structures, on the order of a few metres in width, and up to several hundreds of metres high. Pervasive migration occurs in the lower crust, where melt is formed, whereas focused flow operates in the upper crust where melt is emplaced (Weinberg, 1999; Sawyer *et al.*, 2011). Both of these melt migration mechanisms are greatly inhibited under the conditions at which the other operates. However, melt is able to ascend through the crust and so there must be some depth in the crust at which the mechanism of melt ascent changes from a pervasive network and instead occurs in fewer, discrete, focused structures.

The details of how and when pervasive flow changes to focused flow are poorly constrained. Specifically, little is known about the mechanisms that might result in the linking

of distributed melt-bearing networks, close to the anatectic region, to larger discrete bodies that allow melt ascent through subsolidus crust. (Brown & Solar, 1998a,b; Weinberg, 1999; Connolly & Podladchikov, 2007; Hall & Kisters, 2012; Brown, 2013).

Bons *et al.* (2004) produced a numerical model to investigate stepwise segregation and accumulation of melt batches during progressive melting of a source region. Instead of a discrete point at which one migration style changes to another, their model explained melt movement as occurring, from initial segregation into centimetre-scale leucosomes to far-field melt transfer and emplacement, via one holistic system of mobile hydrofractures. This self-similar fracture system, as illustrated in Figure 1.1, is thought to link the pervasive network with the larger dykes or shear zones that eventually feed plutons. Ito & Martel (2002) performed laboratory experiments and numerical calculations in order to investigate how dykes may coalesce owing to interactions with the local stress field. They found that neighbouring dykes create distortions in the local stress field that can be attractive or repulsive according to vertical and horizontal spacing. Two adjacent dykes will tend to merge as they interact, if they are spaced closely enough to each other. However, their study was more applicable to the low-viscosity asthenosphere below mid-ocean ridges, and the possibility of a similar situation operating in the continental crust was not evaluated. Weinberg & Regenauer-Lieb (2010) suggested dyking by ductile fracturing as a mechanism for melt extraction from rocks with a low melt fraction. These ductile fractures would have blunt tips and irregular margins. If they were to grow large enough, they might have sufficient buoyancy to overcome the fracture toughness at their tips, or could transport melt to cooler and more competent parts of the crust where brittle-elastic dyking could take over. In this way, brittle-elastic dykes may have their origins as ductile fracture dykes in the hotter regions of the crust. While this model was only valid for pure-shear systems, it does appear to corroborate, to some extent, the 'one holistic system' of Bons *et al.* (2004).

Diener *et al.* (2014) described an example of melt segregation and substantial melt accumulation occurring in the near-source region, allowing larger volumes of melt to accumulate. This substantial melt accumulation implies that the change from a pervasive to focused melt migration mechanism can happen in the source rather than higher in the crust (Rubin, 1995; Diener *et al.*, 2014).

Morfin *et al.* (2013) described an example where melt migrated into a near-solidus region, with injection occurring along thin dykes parallel to the existing bedding or foliation planes. The melt was never channelled into larger structures capable of transporting melt through

the crust, and so the near-source region instead forms an injection complex.

Faber (2012) described an example where pervasive melt migration occurred in rocks above the solidus, and operated as an effective mechanism of melt migration beyond the source region and through the suprasolidus mid-crust. Faber (2012) also acknowledged the limitations of pervasive migration, to about 3-5 km above the source region, as well as the need for the pervasive network to become amalgamated into the larger structures that feed plutons. Faber (2012) suggested that melt migration was a pervasive process, and involved networks of dykes throughout the crust that become less interconnected and less numerous towards shallower levels, much like the model suggested by Bons *et al.* (2004).

The various models of how pervasive flow changes to focused flow lack consensus, and more descriptions of exhumed field examples are needed. Furthermore, the temperature, pressure and deformation conditions, which allow pervasive flow to become more focused, are poorly understood. This project will attempt to address these questions, through the investigation of well-exposed mid-crustal rocks that exhibit a style of melt-migration that contains aspects of both pervasive and focused mechanisms. These rocks are exposed at Nupskåpa in Dronning Maud Land, Antarctica, and form part of the polymetamorphic Maud Belt that joins the Grunehogna craton with the central cratonic block (or 'Mawson Continent') of Antarctica (Fitzsimons, 2000a).

This study examines the petrography of several samples taken from the Nupskåpa area in order to identify the different mineral assemblages preserved in the samples. The textures of minerals in each sample are examined to better identify equilibrium mineral assemblages. Mineral chemistry of individual samples, determined using an electron microprobe, are analysed in terms of compositional variations both across the sample and within individual mineral grains. This provides insight into how minerals re-equilibrated as a response to changes in pressure and temperature experienced by the rocks. Both the petrographic and mineral chemistry studies are combined with the results of mineral equilibria modelling, through the program THERMOCALC, to determine the P-T history recorded by the rocks in the Nupskåpa area, specifically, the metamorphic conditions under which the composite dykes intruded. The geometry and orientations of the leucogranitic dykes and host-rock fabric are also described. This provides insight into the deformational conditions under which the dykes intruded, and allows description of the physical conditions of this style of melt migration.

Chapter 2

Geological Setting

The East Antarctic Shield is made up of several Archaean cratonic nuclei, separated by polydeformed mobile belts that preserve evidence of complex metamorphic and deformation histories (Figure 2.1; Fitzsimons, 2000a; Board, 2001). Two major tectonothermal episodes are recorded in the high-grade gneisses of the polymetamorphic Maud Belt. The first, at ∼1300 to 900 Ma, corresponds to the Grenvillian event and the amalgamation of the Rodinia supercontinent, and involved high-grade metamorphism accompanied by major tectonism (Groenewald & Hunter, 1991; Grantham *et al.*, 1995). The second, at ∼600 Ma to ∼450 Ma, corresponds to the Pan-African event and the amalgamation of Gondwana and was originally thought to have involved heating with little associated deformation (e.g Groenewald *et al.*, 1991; Grantham *et al.*, 1995) but is now interpreted to have also involved significant tectonism (Fitzsimons, 2000a; Board *et al.*, 2005; Bisnath & Frimmel, 2005).

The high-grade Maud Belt lies along the southern edge of the Grunehogna Province, an Antarctic fragment of the Kaapvaal-Zimbabwe craton (Fitzsimons, 2000a). The belt stretches for over 700 km northeast-southwest (Figure 2.1). It is composed of upper amphibolite- to granulite-facies supracrustal rocks of the Sverdrupfjella Group that experienced multiple phases of deformation from the Mesoproterozoic to early Cambrian, as well as several pre-, syn- and post-tectonic intrusions, mostly granitic or mafic in composition (Groenewald *et al.*, 1995; Paulsson & Austrheim, 2003; Bisnath *et al.*, 2006). The belt is made up of several different geographic sections which have been studied to varying degrees. From southwest to northeast they are: Heimefrontfjella, Kirwanveggen and H.U. Sverdrupfjella. Further east of H.U. Sverdrupfjella are the Gjelsvikfjella, Mühlig-Hofmannfjella and Central Dronning Maud Land sections. Correlation between the different sections can be problematic owing

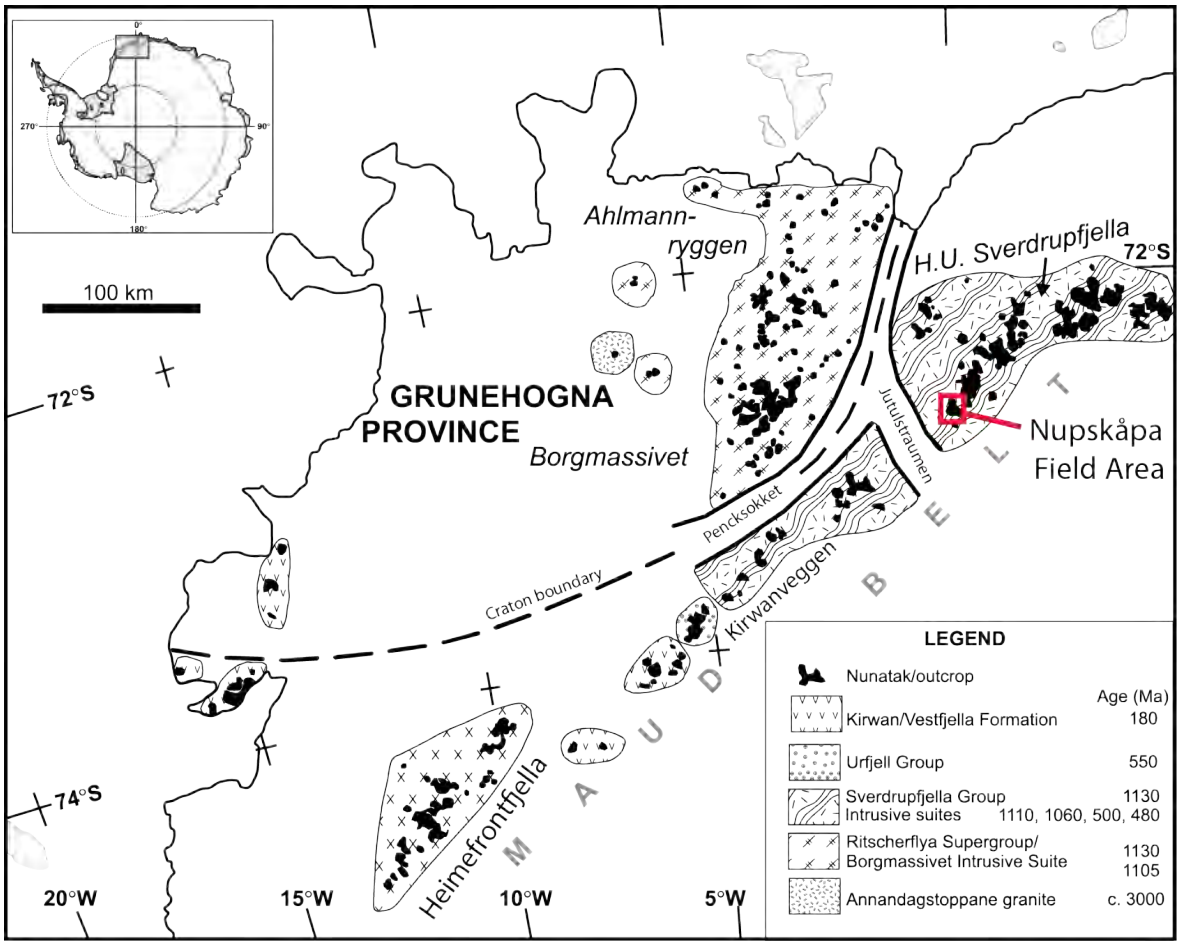

Figure 2.1: Geological map of western Antarctica, with field area indicated. After Board *et al.* (2005)

to the lack of outcrop in between. H.U. Sverdrupfjella, lying between the Kirwanveggen and Gjelsvikfjella ranges in the central part of the Maud Belt, represents one of the more thoroughly-studied sections (Grantham *et al.*, 1995; Groenewald *et al.*, 1995; Board *et al.*, 2005) and forms the focus of this study.

2.1 Stratigraphy

Several different stratigraphic subdivisions have been proposed for the rocks of the H.U. Sverdrupfjella area (e.g. Grantham & Hunter, 1988). The subdivisions used here are those of Hjelle (1974) as modified by Groenewald *et al.* (1995) and Board *et al.* (2005).

The gneisses of the Sverdrupfjella Group are made up of both amphibolite-facies assemblages and partially retrogressed granulites (Hjelle, 1974; Groenewald *et al.*, 1995; Grantham

et al., 1995; Board *et al.*, 2005). The relative proportions of these different rock types varies from area to area.

2.1.1 Jutulrøra Formation

The gneisses of the Jutulrøra Formation form most of the outcrop in the western section of H.U. Sverdrupfjella, and show U–Pb zircon ages of 1160–1140 Ma (Arndt *et al.*, 1991; Groenewald *et al.*, 1995; Paulsson & Austrheim, 2003; Board *et al.*, 2005; Bisnath *et al.*, 2006). This formation is made up of tonalitic gneisses intercalated with banded mafic to felsic ortho- and paragneisses. These, together with the oldest intrusive rocks that preserve ages of 1140–1130 Ma, are thought to represent part of a larger Mesoproterozoic volcanic arc system (Groenewald *et al.*, 1995; Bisnath *et al.*, 2006).

2.1.2 Fuglefjellet and Rootshorga Formations

The eastern and southeastern sections of H.U. Sverdrupfjella comprise the Fuglefjellet and Rootshorga Formations. The former (and structurally lower) is a sequence of predominantly carbonates intercalated with quartzofeldspathic, calc-silicate, magnesian and mafic rocks (Groenewald *et al.*, 1995; Board *et al.*, 2005). The Rootshorga Formation makes up most of the eastern H.U. Sverdrupfjella and shows more diversity in composition, containing pelitic to quartzofeldspathic paragneiss and intermediate to felsic orthogneiss, with minor zones of mafic and calc-silicate composition (Board, 2001). A sedimentary origin is indicated for this formation by the gradational compositional variations, banding on a metre scale and interlayering of gneisses derived from pelites, greywackes, conglomerates, diamictites and arenites (Groenewald *et al.*, 1995; Board *et al.*, 2005). The Fuglefjellet and Rootshorga Formations together are inferred to represent a retro-arc marginal basin succession (Groenewald *et al.*, 1995)

2.1.3 Mafic intrusive rocks

Intrusive mafic rocks occur throughout the Sverdrupfjella Group, usually as lenses, boudins and isolated layers within gneisses. They vary in composition, including gabbro, pyroxenite, olivine gabbronorite and dunite. They are mostly pretectonic, with the interior of the lenses or boudins protected from the gneissic foliation which anastomoses around the mafic lenses (Groenewald *et al.*, 1995; Board, 2001). Several Jurassic dolerite dykes are found in the H.U.

Sverdrupfjella area, and are related to the breakup of Gondwana (Harris & Grantham, 1993; Groenewald *et al.*, 1995; Board, 2001).

2.1.4 Granitic intrusive phases

Multiple phases of early (relating to the Grenvillian orogeny) leucogranitic intrusions are found in H.U. Sverdrupfjella. Harris *et al.* (1995) identified early tabular granite bodies (1103 ± 17 Ma; Harris *et al.*, 1995) as well as garnet-biotite granites (1131 ± 25 Ma; Harris *et al.*, 1995). Various generations of smaller leucogranitic bodies are also found across the area (Board *et al.*, 2005). The various age relations can be difficult to correlate between localised areas but there appears to be a progressive change in the melt compositions over time. They show a progressive change from early near minimum melt compositions to decompression melts, and finally to volcanic arc types which may represent second-stage melting of subducted rocks.This is characteristic of an extended period of collisional tectonics, possibly followed by second-stage melting of subducted rocks leading to the formation of a volcanic arc (Groenewald *et al.*, 1995).

The Sveabreen gneissic granites described by Groenewald *et al.* (1995) extend throughout the eastern and south-eastern H.U. Sverdrupfjella, where they are intercalated with the Rootshorga Formation through a series of thrusts (Board *et al.*, 2005). These gneissic granites are megacrystic and show S-type characteristics, with garnet and sillimanite present in isolated areas. Groenewald *et al.* (1995) interpreted the Sveabreen granites as having an early syn-tectonic origin. They have been dated at 1061 ±14 Ma by Harris *et al.* (1995).

Younger, post-tectonic intrusions found in the H.U. Sverdrupfjella area include the Brattskarvet Intrusive Suite, which comprises alkaline to peralkaline A-type granites, thought to have resulted from a major heating event between ∼550 and 450 Ma(Grantham *et al.*, 1995; Groenewald *et al.*, 1995; Board *et al.*, 2005) as well as abundant monzogranitic dykes and veins, which show ages of 469 ± 5 Ma (Board (2001); after Grantham (1992)).

2.2 Deformational History

The two orogenic events recorded in the H.U. Sverdrupfjella area have near-identical kinematic expressions. They both appear to have resulted in the formation of shallowly-dipping fabrics and top-to-the-NW shear-sense indicators. Discriminating between the structures and fabrics of the two orogenic periods is therefore challenging and somewhat controversial

(Grantham *et al.*, 1995; Groenewald *et al.*, 1995; Board *et al.*, 2005).

Throughout H.U. Sverdrupfjella rootless intrafolial folds, defined by compositional banding and quartzofeldspathic leucosome domains, are associated with an axial-planar fabric (S_1) which parallels compositional layering. This fabric is the oldest recognisable structure and corresponds to the D_1 deformational event which is thought to have involved folding and transposition as well as tectonic interleaving via a series of top-to-the-NW thrusts (Grantham *et al.*, 1995; Board, 2001). Grantham *et al.* (1995) identified an age of ∼1100 Ma for this event and attributed the majority of deformation in the H.U. Sverdrupfjella area to it.

The D_2 event involved the development of a regionally penetrative fabric (L_2-S_2) through serial transposition and ductile thrusting. This fabric has a consistent dip of ∼20–50 ° to the southeast (Board, 2001). Coplanar with S_2 are zones of high shear strain that are characterised by mylonitic rocks and intensely sheared gneiss (McGibbon, 2014). These zones occur throughout H.U. Sverdrupfjella and are a few metres to several hundreds of metres wide, with the larger zones showing continuity across the field area (see Figure 2.3). Abundant kinematic indicators such as δ- and σ-clasts consistently indicate a top-to-the-northwest shear sense (Board *et al.*, 2005). Grantham *et al.* (1995) suggested that the Pan-African event involved a mainly-thermal overprint with some slight reshaping on a regional scale. However, Board *et al.* (2005) used U-Pb SHRIMP dating on monazite inclusions in S_2-fabric-forming minerals from H.U. Sverdrupfjella, and found an age of ∼540 Ma for this fabric. Bisnath *et al.* (2006) found identical peak metamorphic assemblages and fabric-forming minerals in the Gjelsvikfjella area and inferred the same age for the main tectonic fabric. According to McGibbon (2014), the deformation related to the Pan-African orogenic event did not form a penetrative fabric across the Nupskåpa area, but was instead partitioned the localised shear zones seen across the field area. The cumulative evidence indicates a major tectono-thermal overprint by the Pan-African orogeny, at least in these particular geographic sections of the Maud Belt, between 540 and 530 Ma (Board *et al.*, 2005; Bisnath *et al.*, 2006).

A minor deformational event involving warping of the existing D_1 and D_2 features on a regional scale is thought to be related to the intrusion of dykes and plutons belonging to the Brattskarvet Suite at ∼475 Ma (Grantham *et al.*, 1995; Board, 2001).

The final deformational event resulted in the formation of vertical north-south trending fractures and joints. These structures correspond with the intrusion of Jurassic dolerite dykes and the breakup of Gondwana (Grantham *et al.*, 1995; Groenewald *et al.*, 1995; Board, 2001).

2.3 Metamorphic History

Researchers such as Grantham *et al.* (1995), Groenewald *et al.* (1995) and Board *et al.* (2005) have proposed that there are two high-grade metamorphic events recorded in the Maud Belt. The first (M_1), between 1040 Ma and 1030 Ma, corresponds with Grenvillian orogenic events whereas the second (M_2), between ∼565 and 499 Ma, corresponds with Pan-African tectonism (Groenewald & Hunter, 1991; Grantham *et al.*, 1995; Groenewald *et al.*, 1995; Bisnath & Frimmel, 2005; Board *et al.*, 2005). The metamorphic conditions and timing of the two events, identified by the different researchers, show some variation and are summarised in Figure 2.2.

Groenewald & Hunter (1991) studied the northern end of H.U. Sverdrupfjella, and by using thermobarometry on core, rim and corona assemblages of garnet, pyroxene, plagioclase and quartz, found an early M1 stage with initial peak conditions in the high-pressure granulite facies (9–11 kbar at ∼850 °C) followed by rehydration and retrogression to a later stage with conditions of 6–7 kbar at ∼650 °C . Groenewald & Hunter (1991) suggested that both these events occurred before the Pan-African orogeny (Figure 2.2).

Grantham *et al.* (1995) indentified three main metamorphic episodes in H.U. Sverdrupfjella. The first, recorded in an assemblage of garnet, clinopyroxene, plagioclase and quartz, is thought to have occurred around 1000 Ma, at conditions of ∼12 kbar and 675–750 °C . The second episode is recorded in retrogressive textures and records temperatures of 600–700 °C at 7–9.5 kbar. The timing of this event is not well constrained but grain-boundary annealing and closure temperature ages indicate this period involved prolonged residence time at mid-crustal levels. Grantham *et al.* (1995) recognised a third metamorphic episode recorded in the west part of H.U. Sverdrupfjella. This event occurred around 500 Ma at conditions of 620–700 °C and 3–9 kbar (Figure 2.2). However, the regional extent of this episode is unclear.

Groenewald *et al.* (1995) attributes high-pressure assemblages in the eastern H.U. Sverdrupfjella, recording more than 12 kbar at 750–790 °C , to an early stage of the Grenvillian event. This was then followed by a later (M1) stage of medium-pressure granulite-facies conditions (8–10 kbar at ∼850 °C) which led to decompression melting and the generation of the Sveabreen granites. Groenewald *et al.* (1995) identified a second major event at ∼500 Ma, which involved conditions of ∼600 °C at 5–6 kbar and thrusting leading to emplacement of tectonostratigraphically-lower rocks above higher ones and rapid exhumation and uplift,

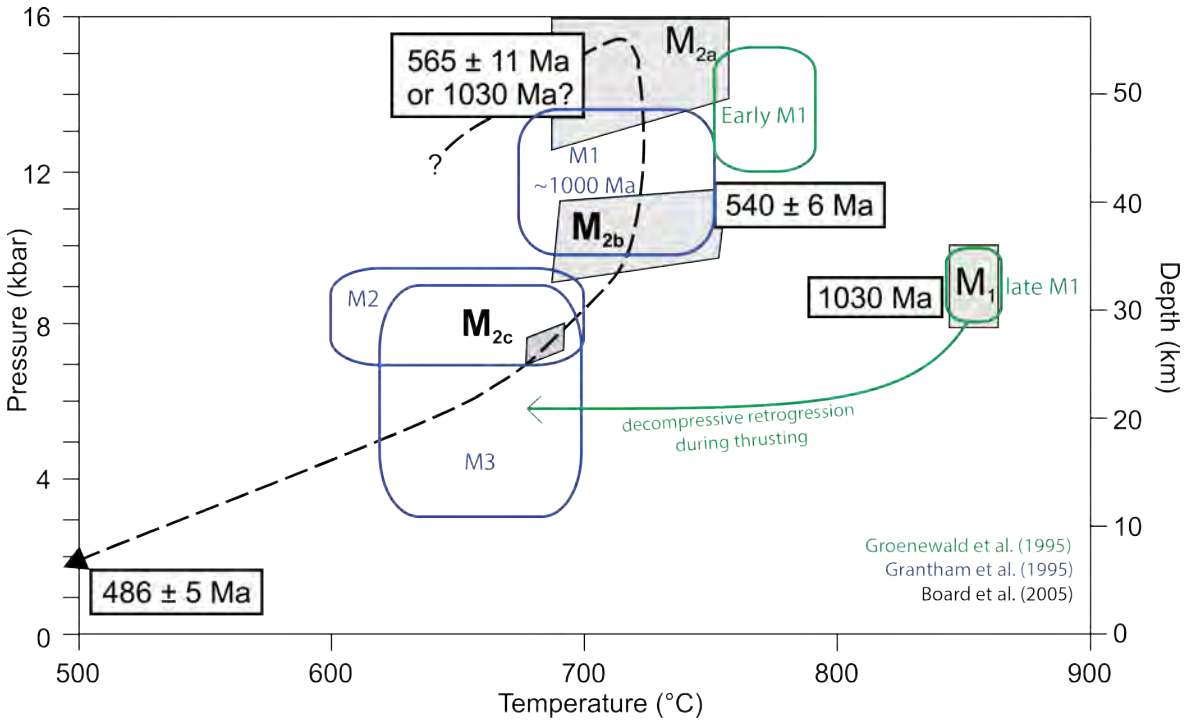

Figure 2.2: Summary of metamorphic conditions and timing of the orogenic events recorded in the H.U. Sverdrupfjella area, as identified by different researchers. Depth scale based on an average crustal density of 2.8 g/cm^3, after Board *et al.* (2005).

which then resulted in decompressive retrogression (Figure 2.2).

Whereas early workers interpreted the peak of metamorphism to be associated with the Grenvillian tectonic event, more recent workers have suggested the Pan-African also involved high-pressure conditions. Board *et al.* (2005) found several stages of metamorphism in the southern H.U. Sverdrupfjella. The oldest metamorphic stage is only preserved in strain-protected mafic boudins which record eclogite-facies conditions with pressures greater than 12.9 kbar. No reliable temperature constraint could be made, but Board *et al.* (2005) assumed similar temperatures to those of the overprinting amphibolite-facies stage that occurred after decompression. The second stage records amphibolite-facies conditions of ~690–760 °C at 9.4–11.3 kbar which were responsible for the majority of the mineral assemblages. The metapelitic samples record a third metamorphic stage with lower grade than the second, most likely owing to their lower competency when compared with the mafic rocks. Lower competency means that they would be weaker and so the chances of dilation and fluid infiltration occurring would be higher, resulting in more extensive retrogression. This stage occurred under conditions of ~690 °C at 7–7.5 kbar, and is not associated with any preferred

orientation of minerals (see chapter 5), indicating that it occurred after the fabric-forming deformation.

The eclogite-facies stage remains to be reliably dated, and may correspond to either the Grenvillian or Pan-African metamorphic event. Board *et al.* (2005) view it as an early stage of the Pan-African event (M2a), mainly because the widespread and well-preserved symplectitic decompression textures (making up M2b) appear to indicate a smooth transition from eclogite to amphibolite-facies conditions, and show no evidence of reheating along a second prograde path. Furthermore, the Grenvillian event preserves evidence of granulite-, rather than eclogite-, -facies peak conditions (Figure 2.2 Groenewald & Hunter, 1991; Grantham *et al.*, 1995; Fitzsimons, 2000b).

Ar^{40}–Ar^{39} dating of hornblende from various amphibolites provided insight into the final cooling history as the peak temperatures exceeded the closure temperature to argon diffusion in hornblende (∼500 °C , Harrison & Fitzgerald, 1986). Board *et al.* (2005) found an Ar^{40}–Ar^{39} cooling age of 486 ±5 Ma. Thus the rocks are thought to have cooled through 500 °C for the last time at ∼486 Ma (Figure 2.2).

2.4 The Nupskåpa nunatak and surrounds

The field area for this study forms the southernmost end of H.U. Sverdrupfjella range, at the Nupskåpa nunatak (red square in Figure 2.1). This area is underlain by quartzofeldspathic paragneisses and metapelites of the Rootshorga Formation, intercalated with the Sveabreen orthogneisses by a series of shearzone thrusts (see Figure 2.3; Grantham *et al.*, 1995; McGibbon, 2014; Ohta, 1996). The thrusted slabs of ortho- and paragneiss are generally 100–200 m thick and dip consistently at ∼20 ° to the southwest. They are laterally continuous, and can be traced across the field area and beyond, over a distance of 10 km (Grantham *et al.*, 1995; Bisnath *et al.*, 2006). The area also records evidence of multiple generations of leucogranitic and mafic intrusions that occurred throughout the duration of both deformation events (Groenewald *et al.*, 1995; Board, 2001).

2.4.1 Sveabreen Orthogneisses

The Sveabreen orthogneisses vary in grain size from outcrop to outcrop. They are generally megacrystic but can be much finer grained, particularly where they have experienced high strain and mylonitization in shear zones. They are generally interpreted as having an early

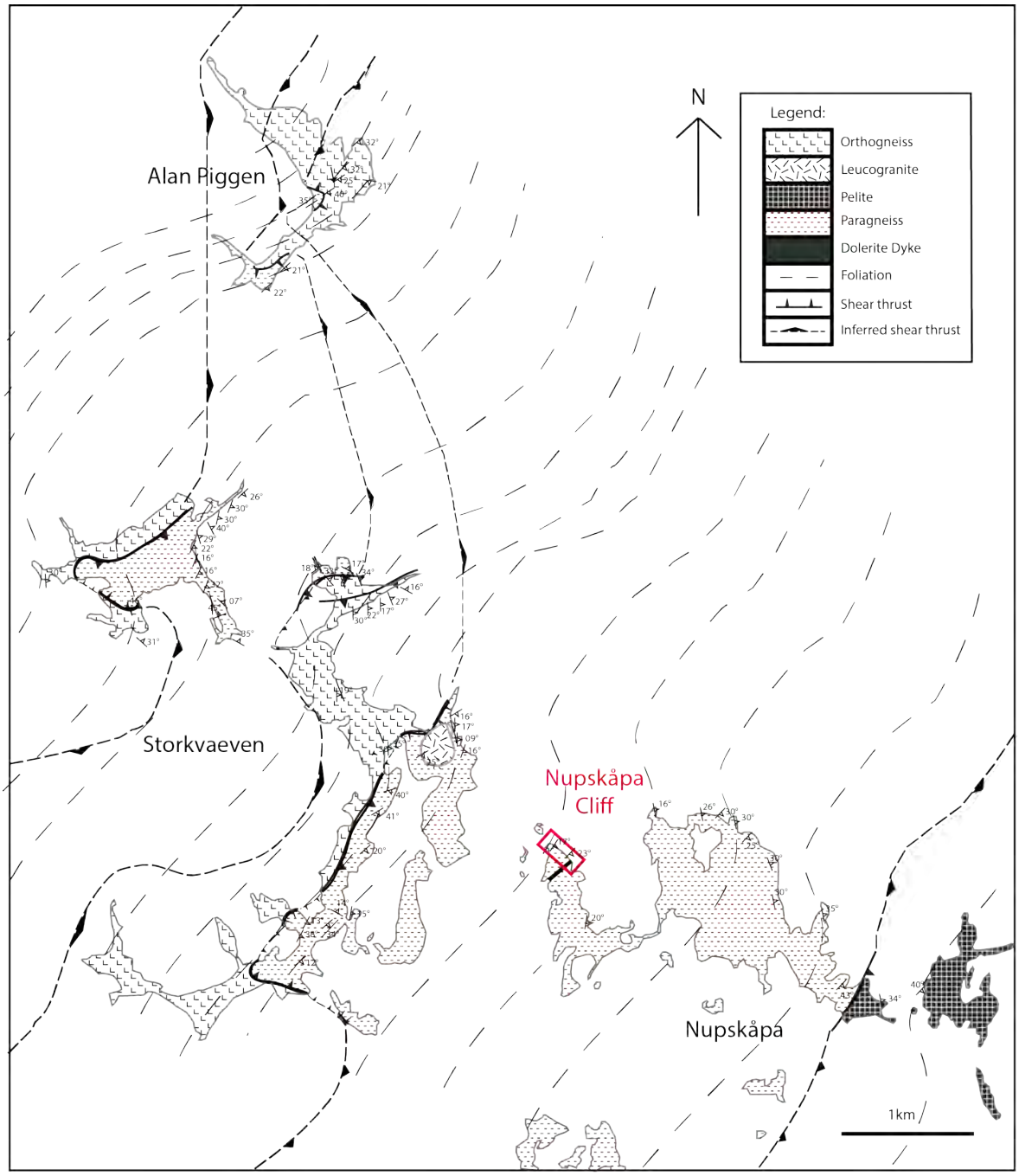

Figure 2.3: Geological map of the field area, with the location of the Nupskåpa Cliff indicated in red (From McGibbon, 2014)

intrusive origin as they share gradational as well as thrust contacts with the paragneiss in more northern sections of H.U. Sverdrupfjella (Board, 2001; Groenewald *et al.*, 1995). The orthogneisses contain K-feldspar, plagioclase, quartz and biotite, with minor garnet and sphene. K-feldspar is commonly present as large (2–5 cm) porphyroclasts, giving the gneiss an augen appearance. The sub-horizontal fabric in the orthogneiss is defined by fine layers of leucosome as well as the tectonic alignment of biotite, which wraps around porphyroclasts of K-feldspar and quartz (Figure 2.4).

Figure 2.4: An example of the orthogneiss found in the Nupskåpa area, with a leucogranitic dyke cutting through layers showing different grainsizes. The inset shows a close-up of the K-feldspar porphyroclasts in the coarser orthogneiss.

The presence of large amounts of stromatic leucosome implies that this rock may have experienced melting. Evidence of retrogression is present in the form of biotite and quartz pseudomorphing garnet, and microcline having been replaced by muscovite.

2.4.2 Paragneisses of the Rootshorga Formation

The paragneiss is more compositionally variable than the orthogneiss, with some layers (on the order of ∼10 m in thickness) showing more quartzofeldspathic and others more mafic compositions. According to Groenewald *et al.* (1995), these different paragneisses formed from pelites, arenites and greywackes. This compositional heterogeneity may have also been enhanced by the selective retrogression and fluid infiltration of the different lithologies (Groenewald *et al.*, 1995).

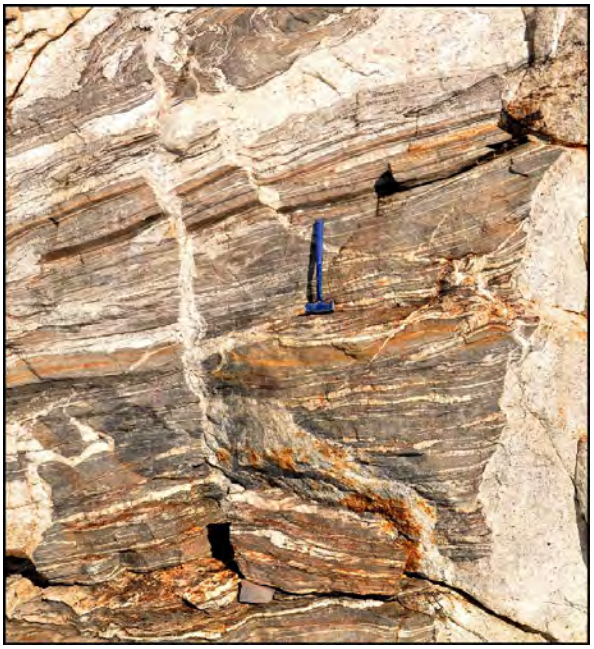

Figure 2.5: An example of the paragneiss found in the Nupskåpa area.

The major proportion of outcrop volume is made up of metapsammitic paragneiss, with garnet-bearing semi-pelitic paragneiss and sillimanite-bearing aluminous metapelite forming smaller layers in some outcrops (Figure 2.5). The metapelitic paragneiss dominates the south-eastern end of the field area (see Figure 2.3). All lithologies contain quartz, k-feldspar, plagioclase, biotite and sphene in varying proportions, with some layers containing garnet, hornblende, epidote and rutile. Mafic rocks occur either as several-metres-wide layers or isolated metabasic pods and lenses within the paragneiss (Figure 2.6). The mafic rocks in the lenses record the entire deformational history of the area and have been interpreted as having a pre-tectonic origin (Board, 2001). They are generally 0.5–2 m in diameter, tens of metres long, and are contained within the gneisses throughout the area. They are generally medium to coarse-grained and massive, showing only weakly-developed internal fabrics and

are wrapped by the fabric of the gneissic host-rocks. Some mafic lenses were sampled (e.g. S01, see Appendix) and seen to vary in composition; the majority are made up of hornblende and plagioclase but some show unusual textures and mineralogies (e.g well-developed corona textures, with symplectites of garnet and hornblende surrounding ilmenite grains; very similar to those described by Whitney & McLelland (1983)). They do not cross-cut the pre-tectonic orthogneisses (of the Sveabreen suite) which are thought to be the next oldest.

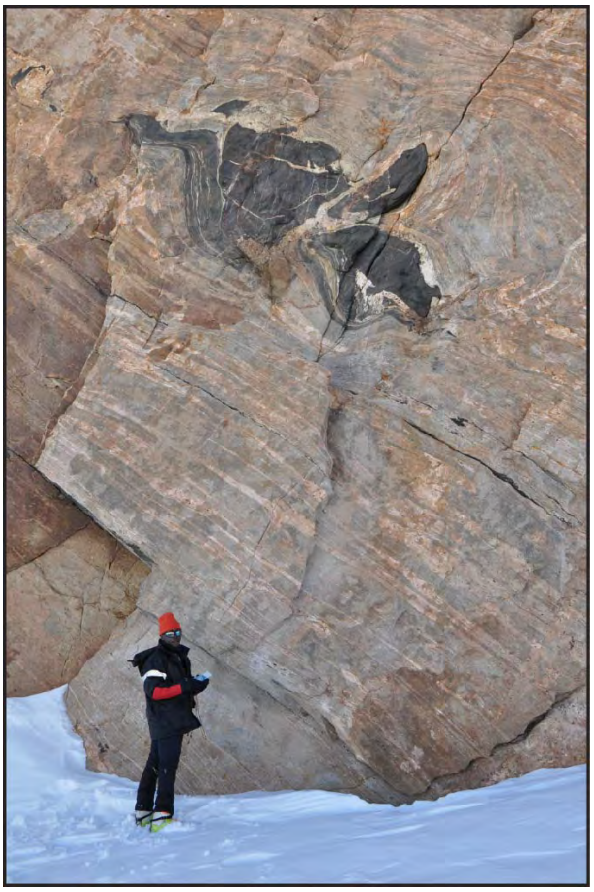

Figure 2.6: An example of a mafic lense contained within paragneiss.

The paragneiss preserves evidence of melting in the large amount of leucosome contained within the rock. Evidence of retrogression is provided by sillimanite and K-feldspar being replaced by muscovite, as well as by garnet-breakdown textures. The fabric is also mostly sub-horizontal, although it anastomoses and can be seen to steepen to around 40 ° in localised areas. Like the orthogneiss, the fabric is defined by leucosome-melanosome layering as well as by the alignment of biotite and sillimanite.

2.4.3 Intrusive Phases

Syn-tectonic leucogranites are represented by intensely deformed, pervasive stromatic leucosome, which ranges from <5 mm to >10 m in thickness and is contained within hundred-metre-scale sections of the ortho- and paragneiss in the area. The leucosomes are intensely deformed and, in places, wrapped by the foliation and form pinch-and-swell structures. Locally, smaller leucosome structures join up to larger ones which cross-cut the gneissic host-rock fabric. This stromatic leucosome is thought to have been formed by early syn-tectonic (with respect to the Grenvillian orogeny) partial melting of the host rock (Board, 2001).

Several generations of felsic intrusions that post-date both major deformational events can be found throughout H.U. Sverdrupfjella, with Board (2001) having identified at least three separate generations of leucogranites. These monzogranitic bodies occur either as subvertical dykes, between 20 cm and 60 m wide, or as sub-horizontal sheet-like bodies, between 10 cm and 2 m thick, that are generally discordant to the local fabric but in places have exploited the gneissic foliation of the host rock. The sharp and coarse-grained edges of the dykes and lack of any contact metamorphic aureole in the paragneisses may indicate a low degree of thermal contrast between the host rock and the melt at the time of intrusion (Board, 2001). However it may also be a result of the country rock having reached suprasolidus metamorphic conditions prior to the intrusion of the dykes (White & Powell, 2002).

Finally, numerous undeformed dolerite dykes are present in H.U. Sverdrupfjella. These near-vertical dykes are oriented north-south, parallel to late fractures and joints, and vary in thickness from 3 cm to ∼50 m, commonly displaying chilled margins. They cross-cut all the other lithologies, as well as the late felsic intrusions and are thought to be related to the break-up of Gondwana (Grantham *et al.*, 1995; Groenewald *et al.*, 1995; Board, 2001).

The following chapter will describe the geometry and mineralogy of the various leucogranites that are pervasive through this area by examining a 100 metre long cliff section that is representative of the typical intrusive phases and the characteristics they display across the greater Nupskåpa area. The location of this cliff is indicated in Figure 2.3.

Chapter 3

The Nupskåpa Outcrop

The various generations of leucogranites present in the Nupskåpa area are particularly well exposed in a vertical northeast-facing cliff face at the base of the Nupskåpa nunatak. This outcrop is approximately 100 metres wide by 80 metres high and composed of metapsammitic paragneiss, with a variable but mostly sub-horizontal foliation. Field work was conducted over 10 days, during the 2012-2013 field season. Structural and lithological mapping of the area was conducted by McGibbon (2014). Approximately 60 samples were collected, and from these the most representative and useful samples (for determining P and T conditions) were seleced. The Nupskåpa cliff was mapped according to lithology and cross-cutting relationships of the various intrusive phases. The first ∼5 metres from the base of the cliff was accessible through scrambling, and the rest was mapped from the edge of a windscoop (some way up the cliff but about 10 metres away from it) and later digitised with the aid of photo interpretation. The upper 15 metres of the cliff was not digitised as it could not be accurately mapped. The outcrop records evidence of a primary, concordant segregation leucosome phase as well as several episodes of discordant melt intrusion and transport. Several of these intrusive phases, particularly composite dykes (the post-tectonic 'monzogranitic' dykes of Board, 2001) and pegmatitic intrusions, show similar characteristics (size, spacing, lack of interconnectivity) across much of the field area (see Figure 3.1).

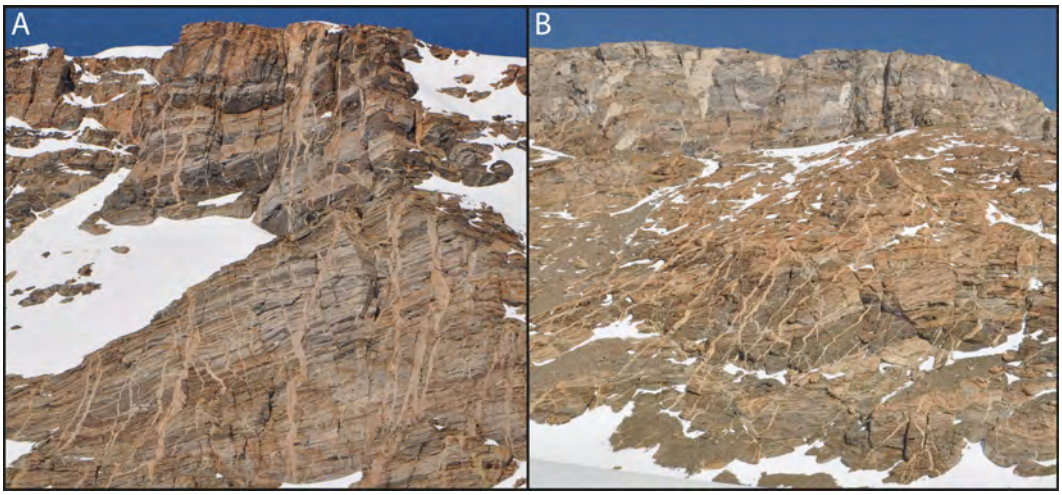

Figure 3.1: Other outcrops in the field area showing similar intrusive phases. A) shows the outcrops several hundred metres above the Nupskåpa Cliff (note the darker, more mafic gniess layers). B) is an outcrop to the east of Nupskåpa. Both photos are taken facing southwest.

3.1 Lithologies and fabrics

The Nupskåpa cliff shows two main rock types. The majority of the cliff is composed of a regular metapsammitic paragneiss containing plagioclase, k-feldspar, biotite, hornblende and quartz, with minor garnet and sphene. The gneiss contains a strong layering defined by alternating layers of stromatic leucosome (used here to describe coarse-grained quartzofeldspathic veins or layers, formed as a result of high-grade metamorphism and in-situ melting) and melanosome. This layering defines a migmatitic banding that is oriented parallel to the tectonic fabric in the rocks.

Contained within the metapsammitic gneiss are isolated lenses, 8-15 metres in length, of a more mafic paragneiss. This rock type occurs throughout the area and at some locations forms extensive layers, such as in the cliff above the Nupskåpa outcrop (Figure 3.1). These lenses commonly contain hornblende, biotite and plagioclase, with some containing clinopyroxene, and are commonly retrogressed.

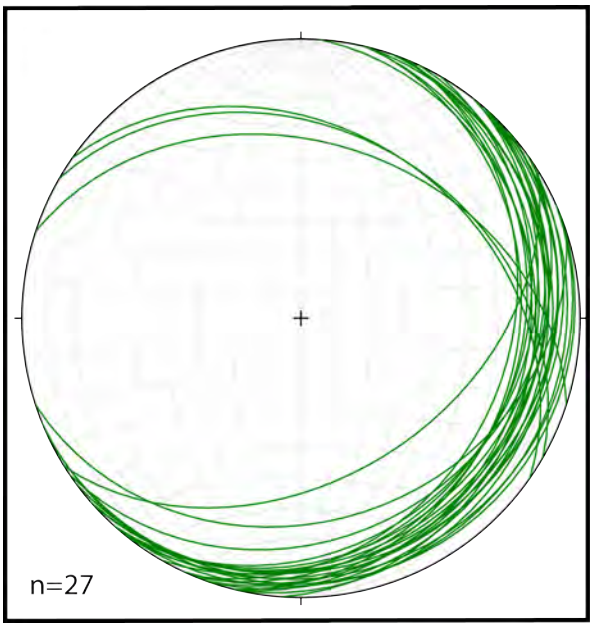

Figure 3.2: Equal area, lower hemisphere stereonet showing the orientation of the foliation in the Nupskåpa cliff, defined by the layering of leucosome and melanosome.

The gneissic fabric was measured in several places along the cliff and found to be striking NNE-SSW and dipping gently (07–26 °) east to south east (Figure 3.2). The fabric shows more folding in the upper left side of the cliff, and appears to steepen towards the northwest side of the cliff. The traces of this foliation have been approximated by dashed lines in Figure 3.3.

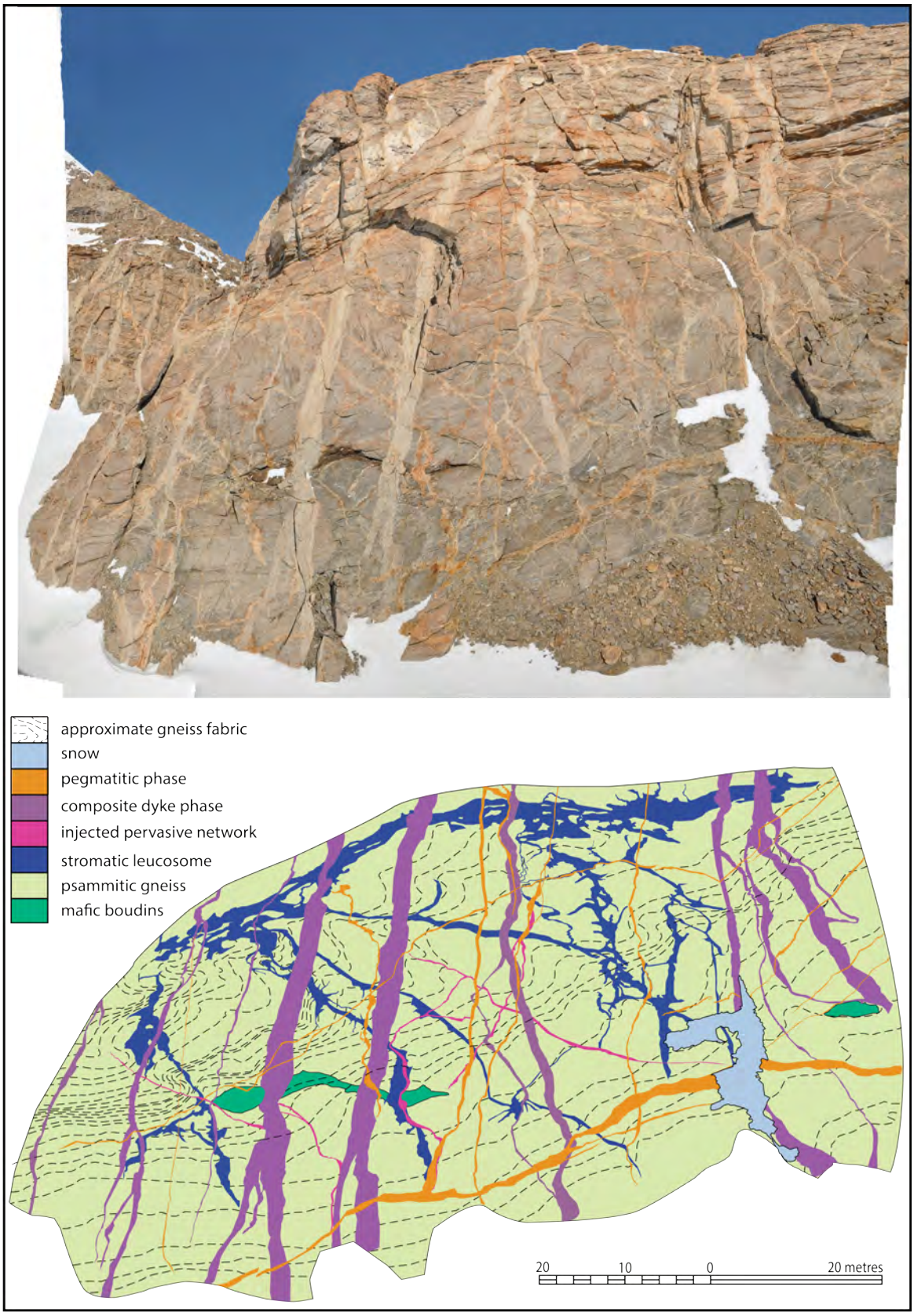

Figure 3.3: The Nupskåpa cliff, with the various intrusive phases mapped from the photo above. The photo was taken towards the southwest.

3.2 Leucogranite Phases

Four separate leucogranite phases are identified, based on cross-cutting relations. The phases differ in orientation, width and mineralogy and are mapped in Figure 3.3.

3.2.1 Stromatic leucosome

The oldest leucogranitic phase is made up of medium-grained k-feldspar and quartz, with some plagioclase and very rare garnets. It occurs exclusively in fine structures, such that it forms a small to mesoscale pervasive leucosome network. This network consists of predominantly centimetre-scale subhorizontal leucosomes that have diffuse boundaries (Figure 3.4), exhibit pinch-and-swell and boudinage structures, and define the gneissic host rock fabric (see Figure 3.5A). The fine leucosomes appear to feed into larger, discordant structures that have very diffuse boundaries and appear to connect the fold hinges of the host-rock fabric (note the dotted lines approximating the fabric in Figure 3.3) and in turn connect to a subhorizontal, ~2 metre thick melt layer towards the top of the cliff. The larger melt structures have been mapped in blue in Figure 3.3. The fine, distributed nature of the leucosome as well as the diffuse boundaries indicate that this melt likely formed from melting of the host rock.

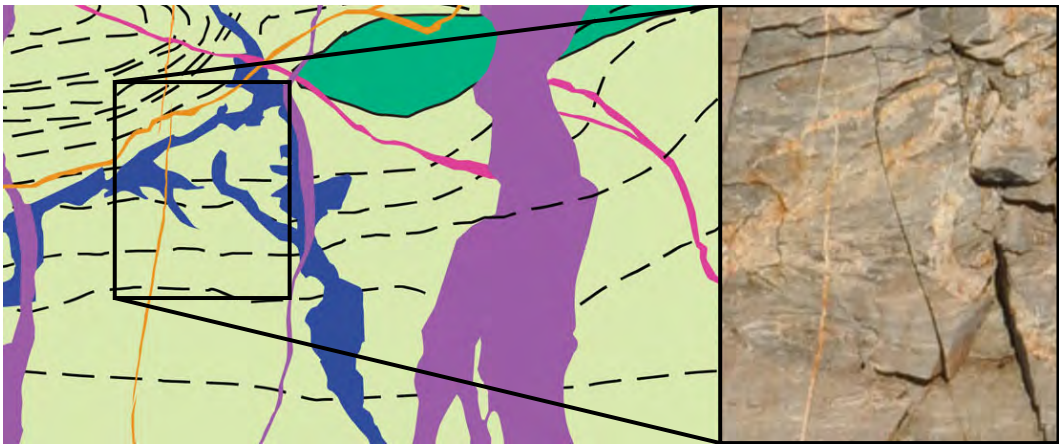

Figure 3.4: Close-up of the Nupskåpa cliff, showing the diffuse nature of the stromatic leucosome phase (mapped in blue). For scale and lithologies, refer to previous figure.

3.2.2 Injected pervasive network

Cross-cutting and overprinting this pervasive network is a less extensive but still interconnected series of narrow (5–20 cm) but long (10–15 m) leucogranite-bearing structures. The

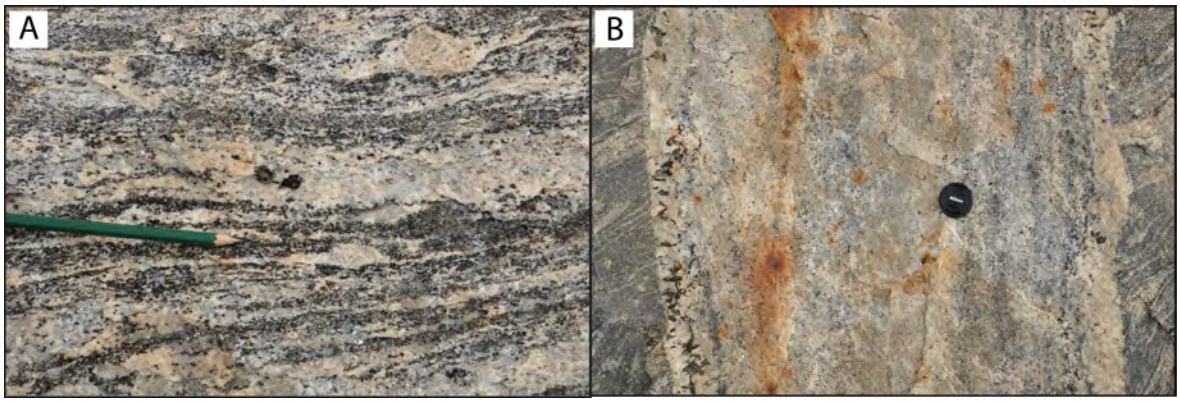

Figure 3.5: A) Close up of the primary pervasive melt phase. Note the diffuse boundaries. B) Close-up of a composite dyke. Note the sharp boundaries with the host rock, and the different melt phases within the dyke.

individual features have sharp edges and their orientations vary, but are generally discordant and approximately perpendicular to each other. These structures are not very extensive across the outcrop, and are mapped in pink in Figure 3.3. The mineralogy of this phase is very similar to the stromatic leucosome phase.

3.2.3 Composite dykes

The two early leucosome networks are cross-cut by a younger generation of injected composite leucogranitic dykes. The dykes show slightly different orientations but generally strike north-south and are subvertical, with the exception of two that dip at ∼25 ° to the east (Figure 3.6). These highly discordant dykes are 0.5–2 m wide, and are closely and regularly spaced (∼10–20 m apart) but show little interconnectivity except towards the base of the cliff where smaller dykes coalesce into larger ones (Figure 3.7). The dykes are the most obvious feature in the cliff, and can be identified throughout the field area. They correspond to the 'monzogranitic dykes' of Board (2001).

These younger composite dykes show sharp edges, and show only minor (maximum ∼30 cm) shear displacement of the host rock fabric. They can be seen to cross-cut the Pan-African shear zones in other outcrops in the field area (Figure 3.8). They comprise at least four different leucogranite phases (Figure 3.5B). These phases are distinguishable in the field and define banded layers or flow structures which are parallel to the edges of the dykes. However, there are no consistent cross-cutting age relations amongst the different phases. These dykes are mapped in purple in Figure 3.3.

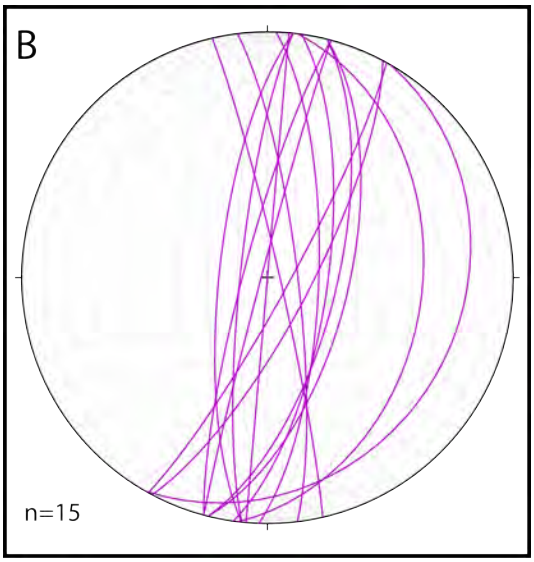

Figure 3.6: Equal area, lower hemisphere stereonet showing the orientations of the various composite-phase dykes, mapped in purple in Figure 3.3.

Figure 3.7: Close-up photograph of two narrower composite dykes joining up to make a single wider dyke, with edge of dykes outlined in black. Image is approximately 5 m across. A late-stage pegmatitic-phase dyke can be seen cross-cutting the composite dyke towards the base of the cliff.

Figure 3.8: Example of an outcrop where composite dykes can be seen to cross-cut a shallowly dipping thrust shear zone (the brown lower half of the outcrop) These shear zones were dated by Board *et al.* (2005) to have a Pan-African age. Field of view is roughly 15 m across.

Leucogranite phases of composite dykes

Equigranular leucogranitic phase A medium to coarse-grained (2–5 mm) equigranular leucogranite, consisting of quartz and k-feldspar in equal proportions, and minor biotite. This phase is not pegmatitic, and makes up ∼60 % of the dykes by volume (Figure 3.9A).

Biotite-rich pegmatitic phase A medium to coarse-grained pegmatitic (4–20 mm) biotite-rich phase makes up 10–20 % of the dyke volume and contains occasional k-feldspar phenocrysts. The biotite grains show a wide range of grain sizes, up to 10 mm, and have no preferred orientation (Figure 3.9B).

Biotite-poor pegmatitic phase Very coarse-grained, contains predominantly k-feldspar with minor quartz and very little biotite, making up 10–20 % of the dykes by volume. The 0.5–1 mm biotite blades are randomly oriented and the quartz and feldspar are intergrown, giving the phase a graphic appearance (Figure 3.9C).

Fine-grained equigranular phase A fine-grained (1–2 mm) equigranular phase, rich in biotite and quartz, with minor k-feldspar. This phase makes up ∼10 % of the dykes by volume and gives them a schlierened appearance (Figure 3.9D).

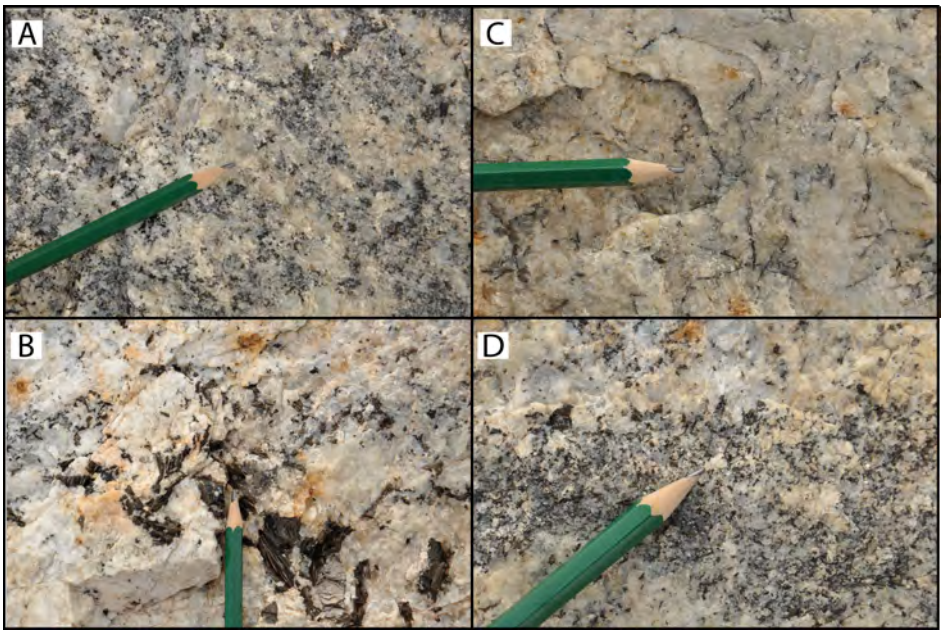

Figure 3.9: Photos of the different phases making up the composite dykes, as seen in the field. A) Equigranular leucogranitic phase B) Biotite-rich pegmatitic phase C) Biotite-poor pegmatitic phase D) Fine-grained equigranular phase.

3.2.4 Pegmatitic phase

The youngest intrusion in the Nupskåpa cliff is made up of a very coarse grained (pegmatitic) phase. Some of these pegmatitic intrusions are subhorizontal and appear to have exploited the weakness of the host rock fabric (Figure 3.11), while others are subvertical and strike north-to-northwest. Two of these features strike east-west and dip ∼75 ° to the northnorthwest (Figure 3.10). The pegmatitic dykes also have sharp boundaries and are generally much narrower than the composite phase dykes, ranging from several 10's of cm to 1 m wide (measured perpendicular to fracture plane). The sub-horizontal dyke at the base of the cliff shows more variation, from less than 0.5 m to more than 2 m in width, measured perpendicular to fracture plane. There is at most only ∼30 cm of shear offset across the pegmatitic dyke structures. While the differently oriented dykes may represent slightly different generations (with the subhorizontal structures being slightly older as some of the concordant structures are cut by discordant ones), their mineralogy is very similar. This phase is mapped in orange in Figure 3.3.

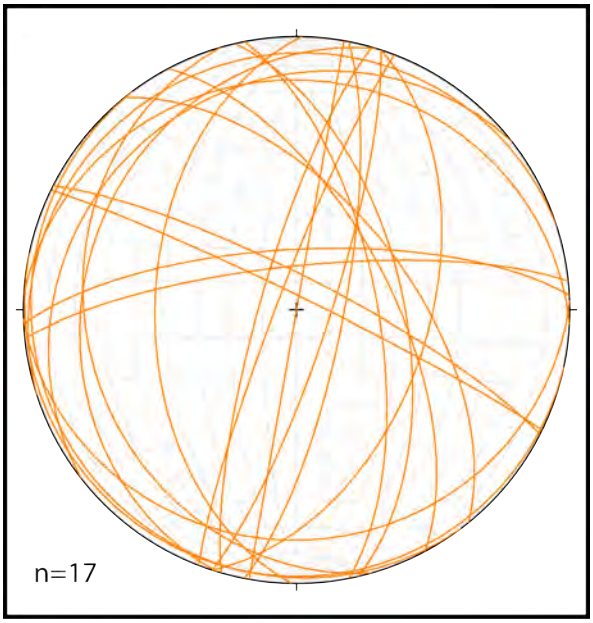

Figure 3.10: Equal area, lower hemisphere stereonet showing the orientations of the various single-phase pegmatitic intrusive features, mapped in orange in Figure 3.3.

Figure 3.11: A close-up image of the concordant pegmatitic dyke at the base of the Nupskåpa cliff. Note how the intrusion has exploited the weakness of the gneissic foliation. This phase is mapped in orange in Figure 3.3.

Chapter 4

Petrography and Mineral Chemistry

More than 24 samples were collected in the field area, from rocks that were representative of the textures and mineralogy of the area. Of those collected, four mafic and two pelitic samples proved useful for mineral equilibria modelling and constraining the pressure and temperature conditions experienced by the Nupskåpa section of the Maud Belt during the Rodinian and Pan-African metamorphic events. The locations of samples in the field area are indicated by red stars in Figure 4.1. The petrography and mineral chemistry of the samples is outlined below. For the sake of consistancy, mineral abbreviations used are the same as those used in the THERMOCALC program. These are listed in Table 4.1.

Table 4.1: Mineral names and abbreviations used in this study, as used in THERMOCALC.

albite	ab	garnet	g	orthopyroxene	opx
andalusite	and	hornblende	hb	paragonite	pa
biotite	bi	ilmenite	ilm	plagioclase	pl
chlorite	chl	jadeite	jd	quartz	q
clinopyroxene	cpx	K-feldspar	ksp	rutile	ru
cordierite	cd	kyanite	ky	sillimanite	sil
cummingtonite	cu	melt	liq	sphene	sph
diopside	di	muscovite	mu		

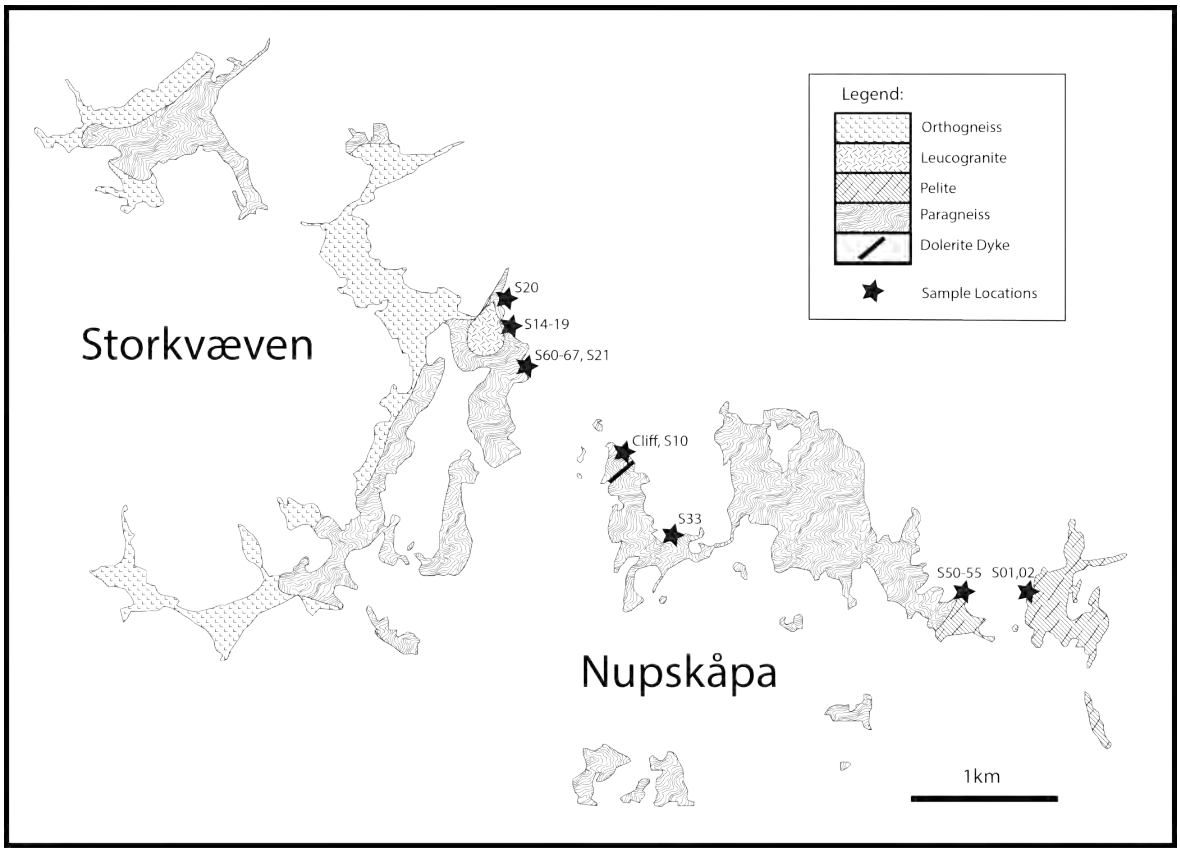

Figure 4.1: The field area, as mapped by McGibbon (2014), with sample locations indicated with red stars.

4.1 Petrography

4.1.1 Mafic Samples

All mafic samples contain hornblende, plagioclase and biotite, with clinopyroxene occurring in S33 and resorbed garnets occurring in S65 and S67. With the exception of S53, the samples all show a coarse assemblage locally replaced by a finer symplectitic assemblage. Generally, garnet or clinopyroxene has been partially resorbed by finer grains of plagioclase, biotite and amphiboles. Some samples show clear compositional differences between these coarser and finer symplectite minerals, while other samples show clear zoning of feldspars or alteration of the rims of coarse-grained amphiboles. Samples S65 and S67 show a medium to strong foliation defined by the alignment of biotite and hornblende, which anastomoses around the resorbed garnet grains.

S33 shows a coarse-grained assemblage of diopside-hornblende-plagioclase-sphene-quartz-biotite. The diopside occurs as large (6–8 mm) anhedral grains which show a high degree of alteration. The rims of these grains have been altered to actinolite (see Figure 4.2 C&D). The hornblende grains are 2–4 mm and form stubby prismatic grain shapes, with weakly coloured rims in plane polarised light. Biotite is present as 1–2 mm laths and shows a weak allignment in the more feldspar-rich bands, whereas biotite amongst the hornblende-rich bands shows very little alignment. The plagioclase grains are coarse grained and subhedral, with triple-junction grain boundaries (see Figure 4.2 A&B).

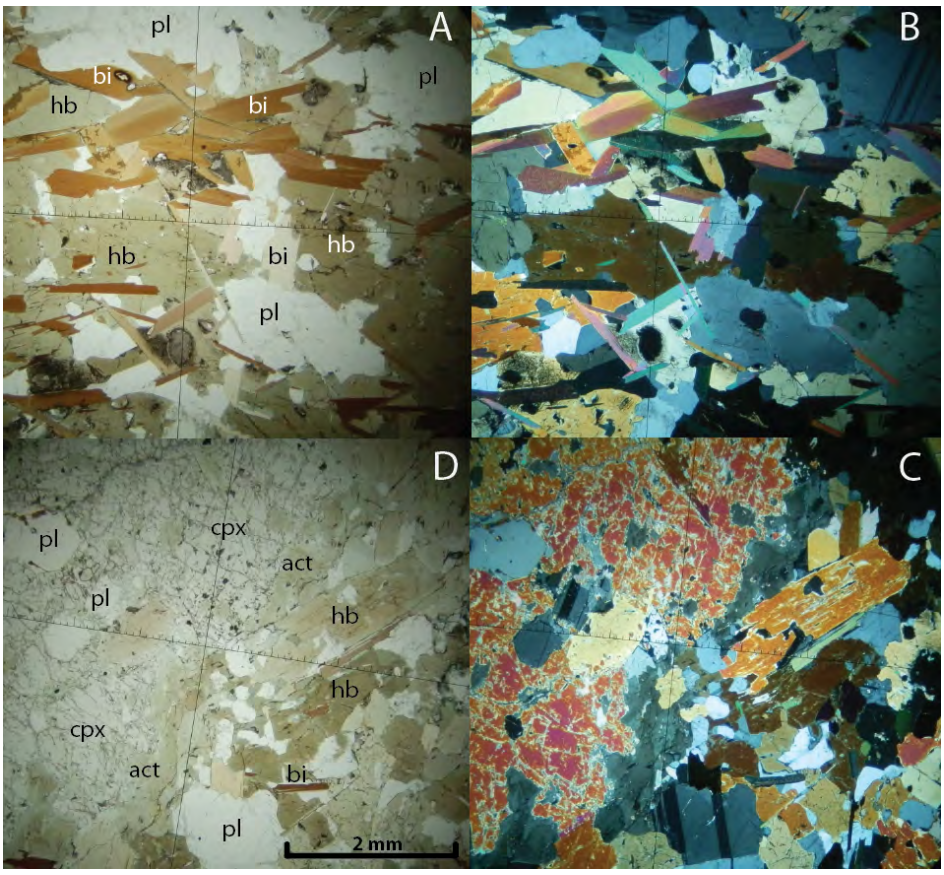

Figure 4.2: Thin section textures of S33 in plane-polarised (ppl) and crossed-polarised (xpl) light. A) and B) show the general texture of the sample, with medium- to coarse-grained biotite, hornblende and plagioclase. C) and D) show a portion of a large clinopyroxene grain (top left) with the rim having been altered to actinolite, as well as the pale weakly coloured rims of hornblende grains surrounding the clinopyroxene grain. The scale is the same for all 4 images.

S53 contains an assemblage of hornblende-biotite-plagioclase-sphene-quartz. Biotite and hornblende grains show a slight preferred orientation. Hornblende and biotite are sub- to euhedral and form weakly elongated stubby prisms (1–2 mm), while plagioclase is finer grained (0.1–0.5 mm) and appears to be interstitial to the more euhedral hornblende and biotite (Figure 4.3). No garnet or clinopyroxene is present, and the sample contains less plagioclase than S33.

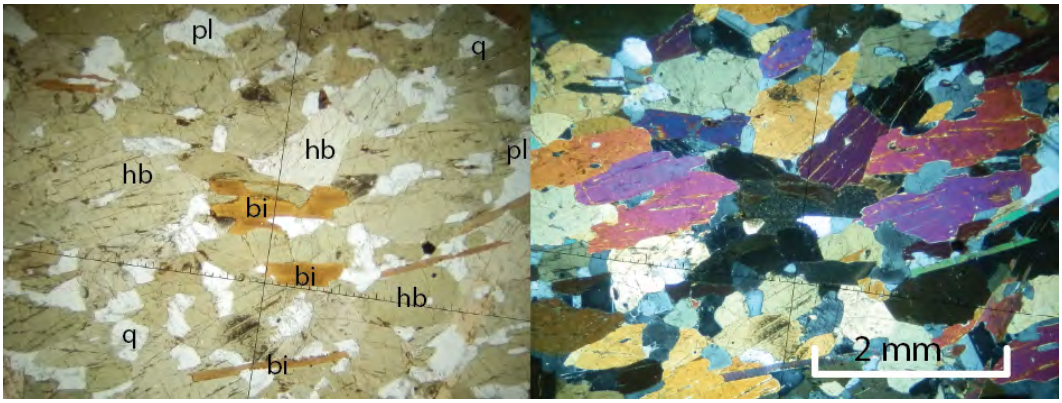

Figure 4.3: Representative thin section texture of S53 in ppl (left) and xpl (right), showing sub- to euhedral hornblende and biotite with finer interstitial plagioclase and quartz.

S65 is dominated by slightly elongate 1–3 mm hornblende grains which make up ∼75% of the sample. Together with very elongate 1–3 mm biotite grains, they show a moderately preferred orientation. The hornblende grains in particular have sub- to euhedral grain shapes, including triple-junction grain boundaries. Plagioclase and quartz occur as fine grains (<1 mm) interstitial to the hornblende and biotite (Figure 4.4). Garnet occurs as rare, isolated subrounded 0.5–1 mm grains, with individual grains often exhibiting embayed grain boundaries. These small grains are surrounded by a 1–1.5 mm symplectite of fine-grained anhedral plagioclase, cummingtonite, hornblende and rutile. The sample does not show any clear banding.

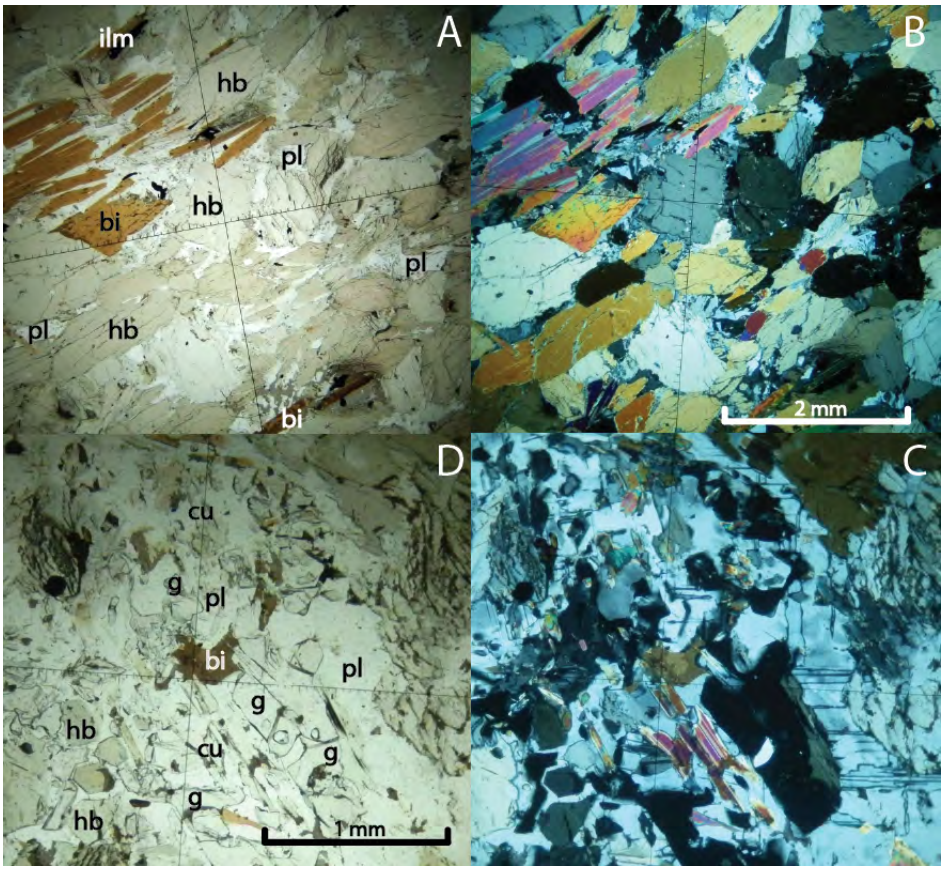

Figure 4.4: Thin section textures of S65 in plane-polarised and cross-polarised light. A) and B) show the more predominant coarse-grained, euhedral assemblage. C) and D) show the symplectite of plagioclase, biotite, hornblende and cummingtonite that occurs around small resorbed garnet grains.

S67 is dominated by hornblende, biotite and plagioclase which make up ∼80% of the sample, with the rest being comprised of isolated garnet grains and minor ilmenite. There appears to be two texturally distinct generations of hornblende, biotite and plagioclase. One generation is coarse-grained (1–3 mm), euhedral and defines a strong foliation (Figure 4.5A). The other is much finer-grained (<1 mm), anhedral, shows no alignment and occurs as symplectic intergrowths pseudomorphing garnet grains. These garnet grains exhibit embayed and resorbed grain boundaries. The fabric defined by the coarse, euhedral hornblende and biotite anastomoses around the symplectites (Figure 4.5B). Ilmenite and quartz are present as fine grains distributed throughout the sample.

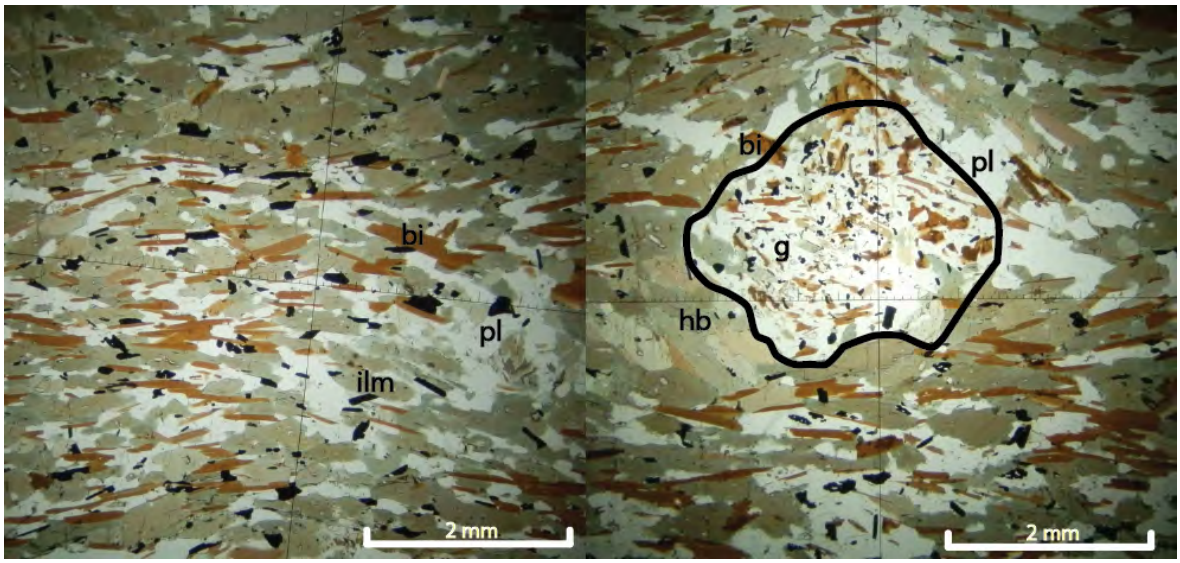

Figure 4.5: Thin section textures of S67 in plane-polarised light. A) shows the assemblage of coarser, euhedral, aligned biotite and hornblende. B) shows the remains of a garnet grain (outlined in black), surrounded by finer-grained, anhedral biotite and hornblende. The fabric defined by the minerals in A) anastomoses around the pseudomorphed garnet seen in B).

4.1.2 Metapelitic Samples

Both samples are metapelitic gneisses, showing an inferred peak assemblage of biotite, plagioclase, K-feldspar, quartz, garnet and possible sillimanite. Both show evidence of replacement of the sillimanite and feldspar by muscovite, as well as the breakdown of garnet. The samples show a strong foliation defined by biotite and compositional layering of biotite- and muscovite-rich layers alternating with feldspar- and quartz-rich layers.

S62 shows an assemblage of biotite–muscovite–plagioclase–K-feldspar–garnet–quartz with biotite- and muscovite-rich layers alternating with recrystallised feldspar- and quartz-rich layers. Biotite laths show a strong preferred orientation and are clustered together with clots of muscovite. Garnet is present as small grains (0.5–1 mm) or clusters thereof, often showing embayed grain boundaries and usually surrounded by plagioclase (1–2 mm), and sometimes biotite (0.1–2 mm) or muscovite. Feldspar (1–2 mm) and quartz (0.5–1 mm) grains are highly recrystallized, showing sutured grain boundaries. Two texturally distinct generations of muscovite are present. One generation exists as clumps of very fine ($\sim$0.1 mm) needles, in amongst the slightly larger biotite needles. It is possible that they are pseudomorphing sillimanite as they resemble the fibrous clots

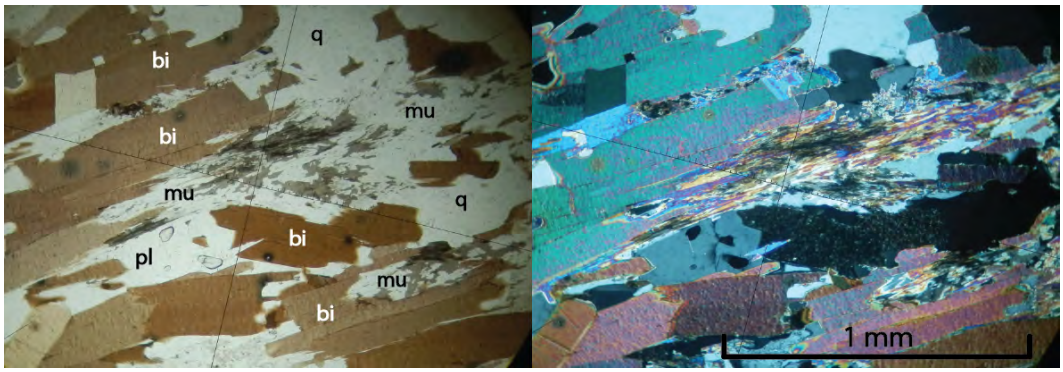

Figure 4.6: Thin-section texture in S62 showing a clot of fine-grained muscovite surrounded by coarser biotite and plagioclase grains. Together the mica grains show a strong allignment.

sillimanite needles tend to form(however, electron microprobe data shows them to be muscovite; Figure 4.6). Together the biotite and muscovite show a strong alignment. The second muscovite generation takes the form of coarser (2–4 mm) grains which are often associated with K-feldspar or surround small (<1 mm) garnets (Figure 4.7). These coarser grains show very little alignment to each other or to the fabric defined by biotite and the fine muscovite, and are situated in the more quartzo-feldspathic layers.

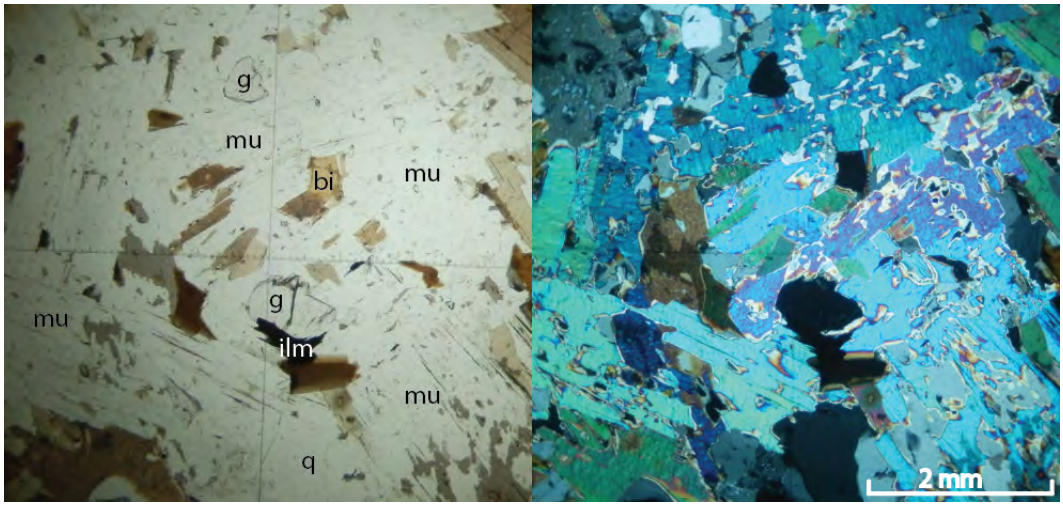

Figure 4.7: Thin-section textures in S62 showing coarse grained muscovite with embayed grain boundaries surrounding smaller garnet grains.

S64 shows the assemblage biotite–muscovite–plagioclase–sillimanite–K-feldspar–garnet–quartz, with mica-rich layers alternating with feldspar- and quartz-rich layers (Figure 4.9). Garnet is present as 0.5–1 mm rare, isolated rounded grains, usually surrounded by plagioclase (2–4 mm). The quartz (0.5–2 mm) and feldspar (2–4 mm) are recrystallised,

exhibiting sutured grain boundaries. The biotite laths (0.1–0.2 mm) show a strong alignment, and surround clots of very fine-grained sillimanite. Muscovite is present as ∼0.2 mm wide beards on the rims of these sillimanite clots (Figure 4.8). SOme sillimanite clots are not completely surrounded by these beards.

Figure 4.8: Thin-section textures in S64 showing a clot of sillimanite with a beard of muscovite, amongst coarser biotite.

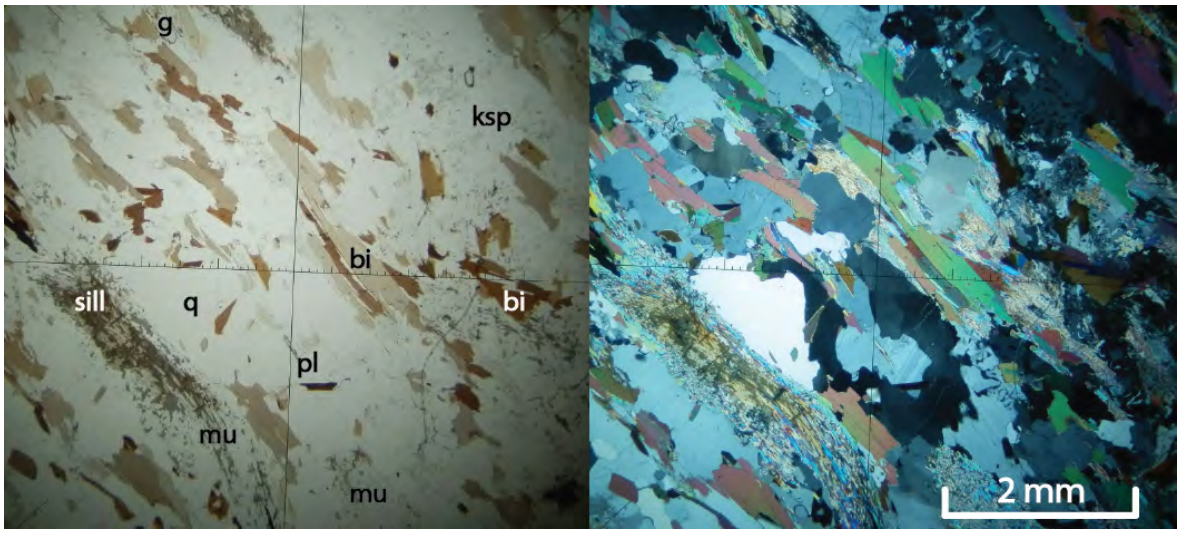

Figure 4.9: Thin-section textures in S64 showing layering of mica-rich zones with more feldspar- and quartz-rich zones.

4.2 Mineral Chemistry

Mineral compositions were determined using a JEOL JXA-8100 electron microprobe housed at the University of Cape Town. Analyses were carried out using a 15 kV acceleration voltage, 20 nA probe current and 2–3 μm spot size. Counting times were 5 seconds for backgrounds and 10 seconds for peaks on all elements. Typical compositions for minerals in each of the samples are presented in Tables 4.2 to 4.7 and all analyses are in the appendix tables.

4.2.1 Mafic Samples

s33 Amphiboles show significant compositional variation within grains (Figure 4.10). The strongly coloured cores show Na content of 0.25–0.43, and Al(VI) content of 0.35–0.64 cations per formula unit (based on 23 oxygens) whereas the lighter-coloured rims are more actinolitic, with Na=0.11–0.42 and Al(VI)=0.21–0.63. Actinolite with Na=0.02–0.15 and Al(VI)=0.06–0.19 cations per formula unit (based on 23 oxygens) also occurs as rims on clinopyroxene (Figures 4.2 and 4.10). Plagioclase shows minor variation across grains, with cores showing An/(An+Ab+Or) ratios (X_{An}) of 0.27–0.35 and rims X_{An}=0.23–0.34 (Figure 4.11). The clinopyroxene shows negligible core-to-rim compositional variation and contains very little Al or Na, with X_{Di}~0.71, X_{Hed}~0.28 and X_{Jd}~0.01. Biotite shows little compositional variability, with Ti=0.14–0.18, Al(VI)=0.16–0.23 cations per formula unit, based on 11 oxygens, and Fe/Mg ratio (X_{Fe}) of 0.48–0.50.

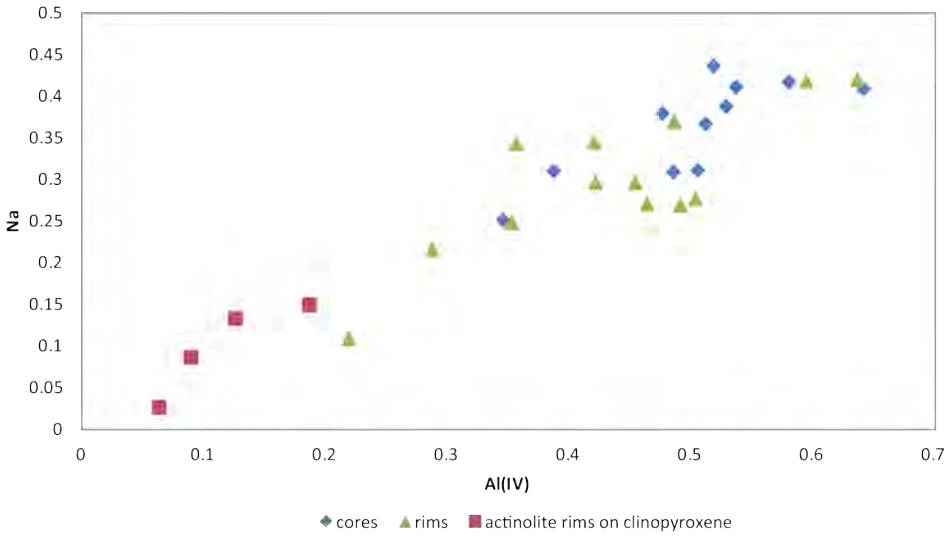

Figure 4.10: Graph to show distribution of Al and Na in hornblende grains in S33. Cores (blue diamonds) of hornblende grains are generally richer in both elements than the rims (green triangles). Clinopyroxene grains are rimmed by actinolite (red squares).

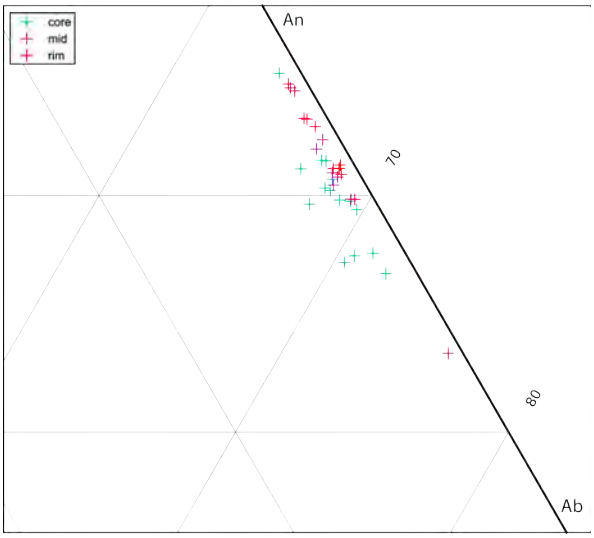

Figure 4.11: Graph to show distribution of feldspar compositions in S33. Cores (blue crosses) appear to be slightly more albitic than rims (red crosses).

Table 4.2: Representative mineral compositions for sample S33

	pl	hb core	hb rim	act	bi
SiO_2	60.20	42.44	43.65	50.14	36.66
TiO_2	0.13	1.61	1.43	0.10	3.35
Al_2O_3	25.24	12.11	11.26	2.77	16.29
Cr_2O_3	0.00	0.09	0.11	0.10	0.11
FeO	0.03	16.64	16.49	13.41	19.93
MnO	0.03	0.39	0.34	0.35	0.25
MgO	0.00	9.98	10.35	13.35	11.41
CaO	6.30	12.05	12.17	13.57	0.00
Na_2O	7.71	1.50	1.35	0.30	0.11
K_2O	0.12	1.30	1.17	0.25	9.66
Total	99.76	98.10	98.32	99.51	97.77
Oxygens	8	23	23	23	11
Si	2.68	6.37	6.52	7.59	2.74
Ti	0.00	0.18	0.16	0.01	0.19
Al	1.33	2.14	1.98	0.49	1.43
Cr	0.00	0.01	0.01	0.01	0.01
Fe	0.00	2.09	2.06	1.70	1.24
Mn	0.00	0.05	0.04	0.05	0.02
Mg	0.00	2.23	2.30	3.01	1.27
Ca	0.30	1.94	1.95	2.20	0.00
Na	0.67	0.44	0.39	0.09	0.02
K	0.01	0.25	0.22	0.05	0.92
Total	4.99	15.71	15.63	15.21	7.83

S53 The amphibole present is hornblende, with no discernible core-rim compositional zoning. Cores show Na=0.34–0.47 and Al(VI)=0.51–0.67 while rims show Na=0.38–0.45 and Al(VI)=0.56–0.64. Plagioclase grains vary in composition across the sample, as well as across individual grains. Cores show X_{An}=0.32—0.45 and rims show X_{An}=0.30–0.48. When plotted on a triangular graph it is clear that the cores are generally slightly more albitic than the rims (Figure 4.12). Biotite shows little variation, with X_{Fe}=0.40–0.44, Ti=0.07–0.17 and Al(VI)=0.11–0.19 cations per formula unit based on 11 oxygens.

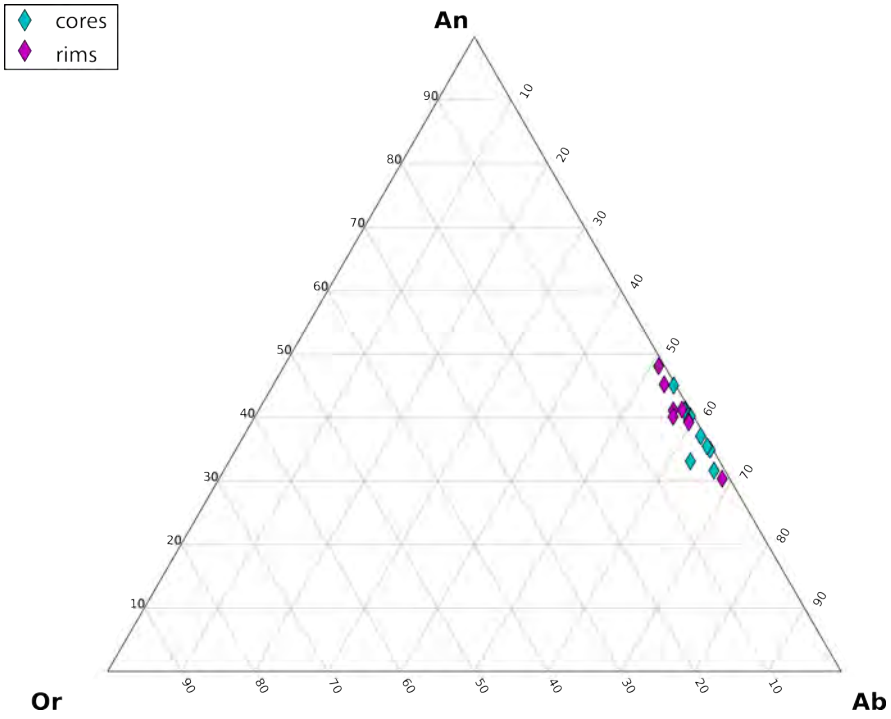

Figure 4.12: Feldspar compositions in S53. Cores (blue) appear slightly more albitic than rims (purple).

S65 Coarser hornblende grains show little compositional difference between cores (Na=0.33–0.38, Al(VI)=0.75–0.84 cations per formula unit based on 23 oxygens) and rims (Na=0.34–0.36, Al(VI)=0.75-0.81 cations per formula unit based on 23 oxygens). These values are slightly higher than those of the finer hornblende grains in the symplectite surrounding garnet, which again show little distinction between cores (Na=0.34–0.39, Al(VI)=0.81-0.91 cations per formula unit based on 23 oxygens) and rims (Na=0.36–0.39 and, Al(VI)=0.82-0.95 cations per formula unit based on 23 oxygens) (Figure 4.13). Hornblende shows the opposite variation in terms of X_{Fe}, with the finer grains in the

Table 4.3: Representative mineral compositions for sample S53

	pl core	pl rim	hb core	hb rim	bi
SiO_2	57.73	57.51	42.80	42.67	36.88
TiO_2	0.00	0.00	1.41	1.39	2.28
Al_2O_3	27.07	27.12	13.18	12.95	17.02
Cr_2O_3	0.00	0.00	0.06	0.08	0.09
FeO	0.03	0.09	14.58	15.08	17.85
MnO	0.07	0.04	0.21	0.23	0.20
MgO	0.00	0.01	11.29	11.36	14.17
CaO	8.27	8.46	12.32	12.29	0.06
Na_2O	6.74	6.54	1.52	1.40	0.30
K_2O	0.08	0.18	1.25	1.33	9.19
Total	99.99	99.96	98.62	98.79	98.04
Oxygens	8	8	23	23	11
Si	2.58	2.58	6.32	6.31	2.71
Ti	0.00	0.00	0.16	0.15	0.13
Al	1.43	1.43	2.29	2.26	1.47
Cr	0.00	0.00	0.01	0.01	0.01
Fe	0.00	0.00	1.80	1.86	1.10
Mn	0.00	0.00	0.03	0.03	0.01
Mg	0.00	0.00	2.49	2.50	1.55
Ca	0.40	0.41	1.95	1.95	0.00
Na	0.58	0.57	0.44	0.40	0.04
K	0.00	0.01	0.24	0.25	0.86
Total	5.00	5.00	15.71	15.73	7.88

symplectite showing X_{Fe} of ~0.35, while matrix hornblende grains show lower values of ~0.31. In the symplectites surrounding the garnets, cummingtonite shows Na=0.01-0.05 and Al(VI)=0.02-0.14 cations per formula unit (based on 23 oxygens). Plagioclase compositions vary greatly across the sample, from X_{An}=0.37 to X_{An}=0.70. There is no clear distinction in composition between cores and rims, or between the coarser matrix grains and the finer symplectite grains, except that the matrix grains do show particularly albite-rich compositions (X_{An}=0.28–0.32) that the symplectite grains do not (Figure 4.14). Garnets show zoning, with Fe/Mg ratios (X_{Fe}) ranging from 0.62 in the cores to 0.72 on the rims of grains. End-member compositions also vary slightly, with cores showing X_{Py}=0.31, X_{Alm}=0.54, X_{Gr}=0.13, X_{Spss}=0.02 and rims showing X_{Py}=0.24, X_{Alm}=0.58, X_{Gr}=0.14, X_{Spss}=0.04. Biotite composition is variable, with finer grains in the symplectites around garnet showing Ti=0.04–0.11 and Al(VI)=0.14–0.33 cations per formula unit based on 11 oxygens, while coarser grains in the rest of the sample show less variability, with Ti=0.08–0.11 and Al(VI)=0.21–0.27 cations per formula unit based on 23 oxygens. Neither show clear distinction between rim and core compositions (Figure 4.15).

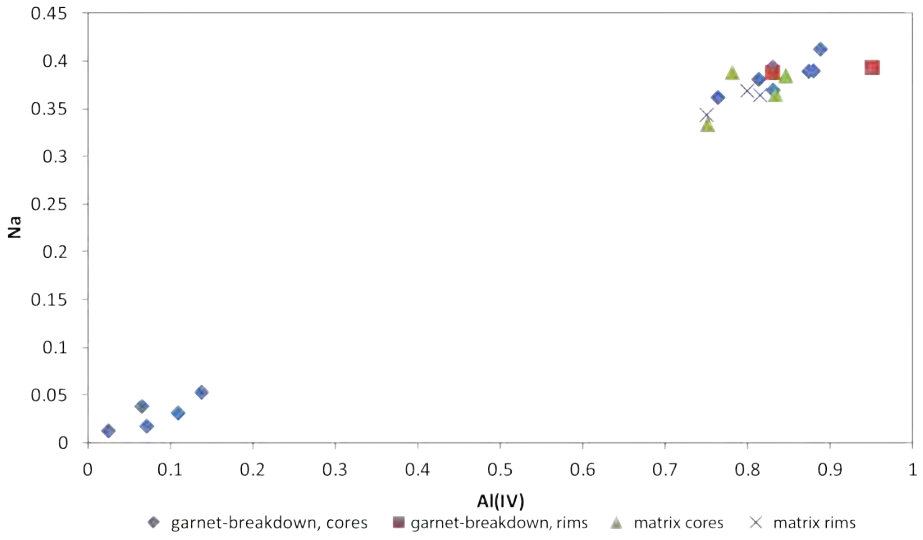

Figure 4.13: Al(VI) and Na in amphibole grains in S65. Cummingtonite (very low Al(VI) and Na values) is only found surrounding garnets. Besides this, there is no clear distinction in terms of composition between amphiboles surrounding garnets ('garnet-breakdown') and those in the rest of the rock ('matrix'). Likewise there is no clear difference between rims and cores of individual grains.

Table 4.4: Representative mineral compositions for sample S65. Abbreviation indicate position in mineral texture. M indicates a mineral in the coarse-grained 'matrix', while GB indicates a mineral in garnet-breakdown textures. C indicates the core of a mineral and R the rim.

	pl MC	pl MR	pl GBC	pl GBR	g	hb MC	hb MR	hb GBC	hb GBR	cu	bi
SiO_2	60.66	61.83	48.62	56.28	38.30	45.23	45.64	45.42	45.07	53.73	37.69
TiO_2	0.02	0.03	0.00	0.01	0.06	1.11	1.00	0.84	1.01	0.09	1.59
Al_2O_3	25.43	24.89	33.57	27.99	22.77	13.66	13.46	13.88	14.08	1.89	17.40
Cr_2O_3	0.00	0.00	0.00	0.00	0.12	0.21	0.06	0.16	0.11	0.05	0.14
FeO	0.05	0.23	0.05	0.25	25.87	11.14	11.43	11.79	10.91	19.75	16.08
MnO	0.08	0.05	0.08	0.06	1.07	0.16	0.16	0.27	0.20	0.58	0.07
MgO	0.00	0.00	0.01	0.09	7.17	13.50	13.61	13.40	13.40	20.37	15.09
CaO	6.33	5.70	15.08	8.83	5.71	12.04	11.77	11.68	12.16	1.00	0.06
Na_2O	7.33	7.98	2.49	5.26	0.02	1.40	1.33	1.34	1.40	0.14	0.22
K_2O	0.03	0.02	0.00	0.19	0.00	0.46	0.38	0.35	0.46	0.01	8.09
Total	99.93	100.73	99.90	98.96	101.09	98.91	98.85	99.12	98.81	97.61	96.43
Oxygens	8	8	8	8	24	23	23	23	23	23	11
Si	2.69	2.72	2.22	2.54	5.88	6.48	6.53	6.49	6.45	7.74	2.76
Ti	0.00	0.00	0.00	0.00	0.01	0.12	0.11	0.09	0.11	0.01	0.09
Al	1.33	1.29	1.81	1.49	4.12	2.30	2.27	2.34	2.38	0.32	1.50
Cr	0.00	0.00	0.00	0.00	0.01	0.02	0.01	0.02	0.01	0.01	0.01
Fe	0.00	0.01	0.00	0.01	3.32	1.33	1.37	1.41	1.31	2.38	0.99
Mn	0.00	0.00	0.00	0.00	0.14	0.02	0.02	0.03	0.02	0.07	0.00
Mg	0.00	0.00	0.00	0.01	1.64	2.88	2.90	2.86	2.86	4.38	1.65
Ca	0.30	0.27	0.74	0.43	0.94	1.85	1.80	1.79	1.87	0.15	0.00
Na	0.63	0.68	0.22	0.46	0.01	0.39	0.37	0.37	0.39	0.04	0.03
K	0.00	0.00	0.00	0.01	0.00	0.08	0.07	0.06	0.08	0.00	0.76
Total	4.96	4.97	4.99	4.95	16.05	15.48	15.44	15.46	15.48	15.10	7.79

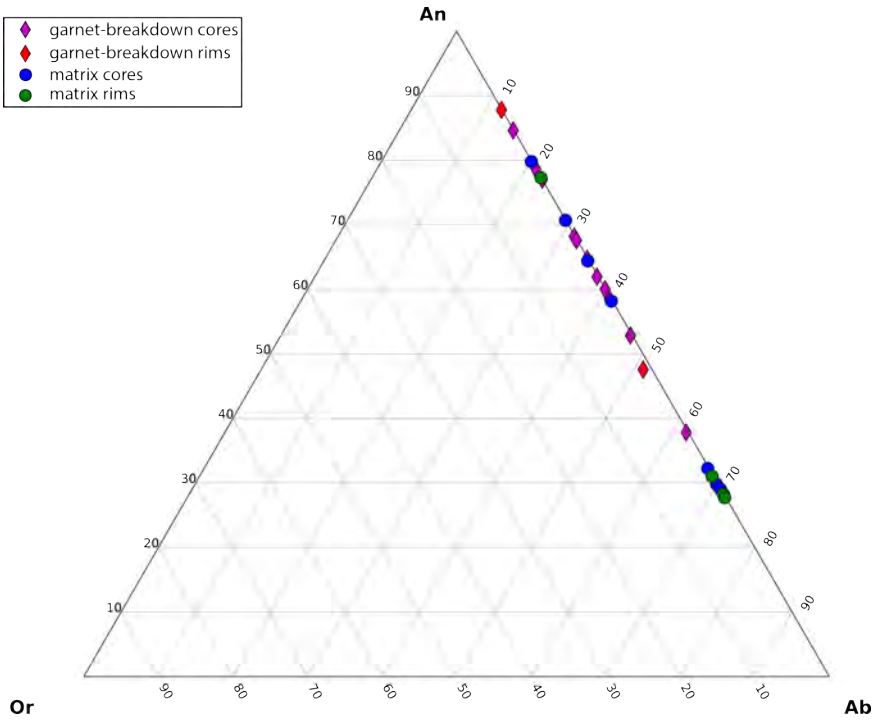

Figure 4.14: Plagioclase compositions in S65. While there is not a clear difference between rims and cores of individual minerals, the grains around garnets ('garnet-breakdown') do not show the strongly albitic compositions shown by grains in the rest of the rock ('matrix').

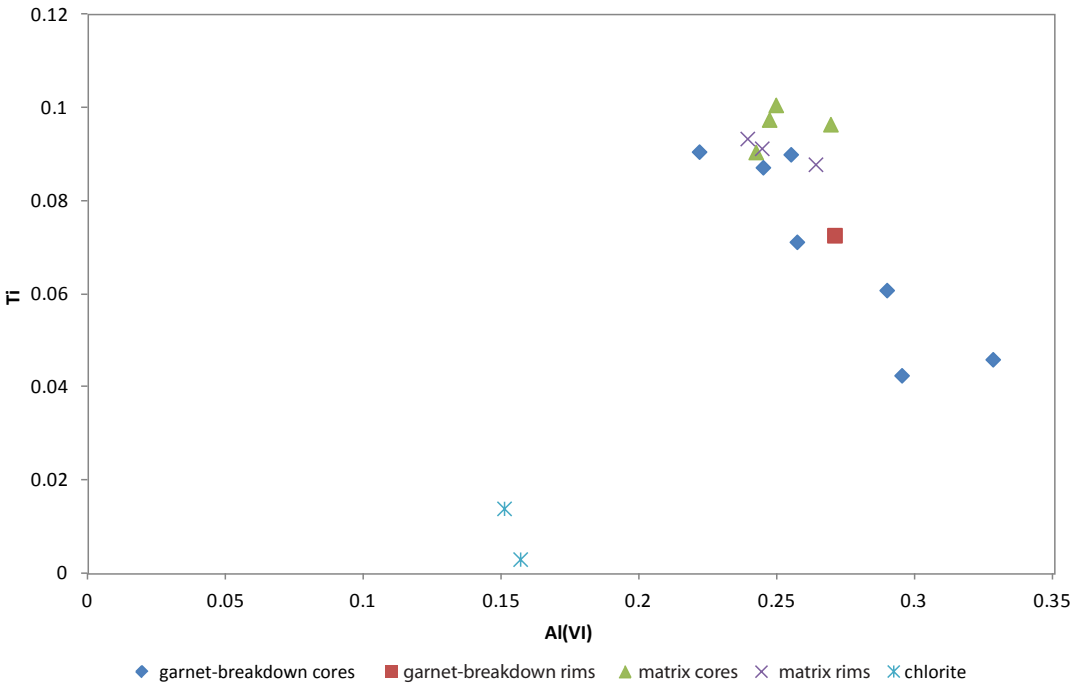

Figure 4.15: Graph showing Al and Ti in biotite grains in S65

S67 Cores of hornblende grains in the symplectites show Na=0.24–0.30 and Al(VI)=0.65–0.76 cations per formula unit based on 23 oxygens, while the rims show Na=0.25–0.28 and Al(VI)=0.68–0.76 cations per formula unit based on 23 oxygens. Coarse hornblende grains in the matrix are generally richer in both elements, with cores showing Na=0.30–0.35 and Al(VI)=0.74–0.88 and rims showing Na=0.26–0.33 and Al(VI)=0.72–0.81 (Figure 4.16). Plagioclase in the symplectites surrounding garnet shows cores of X_{An}=0.88–0.92 while the rims show X_{An}=0.88–0.91. Plagioclase in the rest of the sample shows very similar compositions with cores showing X_{An}=0.83–0.89 and rims showing X_{An}=0.87–0.89. In both types of plagioclase grains, rims are less likely to show more albitic compositions shown by cores (Figure 4.17). Garnet cores show X_{Fe}=0.77–0.83, X_{Py}=0.16, X_{Alm}=0.60, X_{Gr}=0.23, X_{Spss}=0.01 whereas rims show X_{Fe}=0.80–0.85, X_{Py}=0.12, X_{Alm}=0.60, X_{Gr}=0.23, X_{Spss}=0.05. Biotite grains in the symplectites show Ti=0.09–0.14, Al(VI)=0.13–0.25 and in the rest of the rock show Ti=0.1–0.13, Al(VI)=0.21–0.25 cations per formula unit based on 11 oxygens.

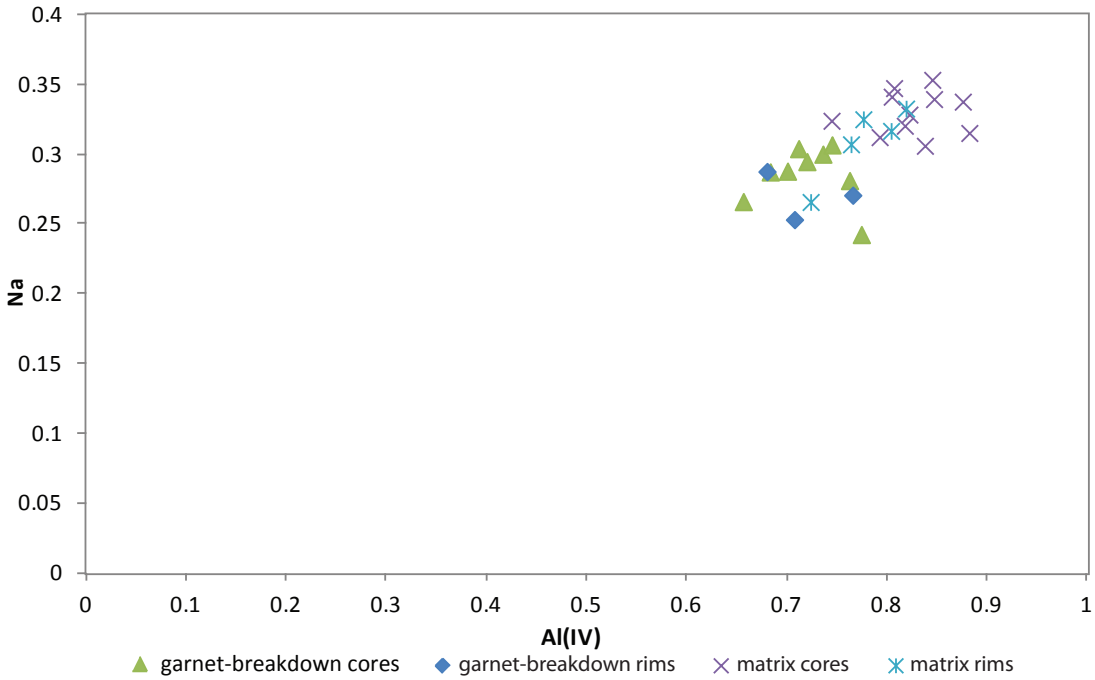

Figure 4.16: Al and Na in amphibole grains in S67. While individual grains do not show clear zoning, grains in the symplectites surrounding garnet ('garnet-breakdown') are generally lower in Al(VI) and Na than grains in the rest of the rock ('matrix').

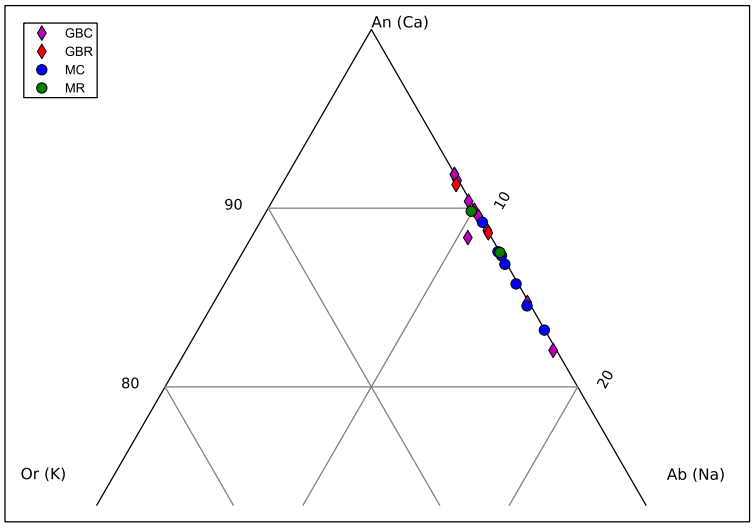

Figure 4.17: Feldspar compositions in S67. Rims are less likely to show more albitic compositions.

4.2.2 Metapelitic Samples

S62 The feldspars are orthoclase (X_{Or}=0.87–0.9, X_{Ab}=0.13–0.88) and oligoclase, which varies slightly across the sample and within grains, with X_{An}=0.21–0.26, X_{Or}=0.009–0.01 and X_{Ab}=0.73–0.77 (Figure 4.18). Garnet also has very little variation within grains and across the sample, with X_{Fe} of ∼0.89, X_{Py}=0.08, X_{Alm}=0.73, X_{Gr}=0.31, X_{Spss}=0.15. Biotite grains show Ti=0.13–0.22, Al(VI)=0.39–0.46 cations per formula unit based on 11 oxygens, and X_{Fe}=0.58–0.61.

Table 4.5: Representative mineral compositions for sample S67. Abbreviation indicates position in mineral texture. M indicates a mineral in the coarse-grained 'matrix', while GB indicates a mineral in garnet-breakdown textures. C indicates the core of a mineral and R the rim

	pl MC	pl MR	pl GBC	pl GBR	g core	g rim	hb MC	hb MR	hb GBC	hb GBR	bi
SiO_2	46.04	45.61	45.33	44.86	37.75	37.73	43.20	44.40	45.27	45.44	36.69
TiO_2	0.00	0.01	0.00	0.04	0.03	0.04	1.28	0.77	0.75	0.55	2.01
Al_2O_3	35.15	35.44	34.46	36.14	21.91	22.11	13.91	12.74	12.32	12.01	16.51
Cr_2O_3	0.00	0.00	0.00	0.00	0.02	0.06	0.11	0.10	0.07	0.08	0.07
FeO	0.10	0.11	0.81	0.32	27.87	26.00	15.54	15.64	15.52	15.32	19.41
MnO	0.10	0.00	0.01	0.00	1.54	0.74	0.17	0.25	0.18	0.17	0.14
MgO	0.02	0.00	0.34	0.03	3.67	5.00	10.34	11.03	11.24	11.53	13.32
CaO	16.75	16.50	15.95	17.40	7.83	8.50	11.40	11.42	11.49	11.22	0.07
Na_2O	1.39	1.30	1.05	0.89	0.03	0.06	1.14	1.07	0.99	0.95	0.21
K_2O	0.02	0.00	0.17	0.04	0.00	0.00	0.69	0.50	0.40	0.38	8.21
Total	99.57	98.97	98.12	99.72	100.64	100.24	97.78	97.92	98.22	97.65	96.63
Oxygens	8	8	8	8	24	24	23	23	23	23	11
Si	2.12	2.11	2.12	2.07	5.93	5.89	6.40	6.55	6.63	6.68	2.74
Ti	0.00	0.00	0.00	0.00	0.00	0.01	0.14	0.09	0.08	0.06	0.11
Al	1.91	1.93	1.90	1.96	4.06	4.07	2.43	2.21	2.13	2.08	1.45
Cr	0.00	0.00	0.00	0.00	0.00	0.01	0.01	0.01	0.01	0.01	0.00
Fe	0.00	0.00	0.03	0.01	3.66	3.40	1.92	1.93	1.90	1.88	1.21
Mn	0.00	0.00	0.00	0.00	0.20	0.10	0.02	0.03	0.02	0.02	0.01
Mg	0.00	0.00	0.02	0.00	0.86	1.16	2.28	2.43	2.46	2.53	1.48
Ca	0.83	0.82	0.80	0.86	1.32	1.42	1.81	1.80	1.80	1.77	0.01
Na	0.12	0.12	0.10	0.08	0.01	0.02	0.33	0.31	0.28	0.27	0.03
K	0.00	0.00	0.01	0.00	0.00	0.00	0.13	0.09	0.07	0.07	0.78
Total	4.99	4.98	4.98	4.99	16.04	16.07	15.47	15.45	15.39	15.38	7.83

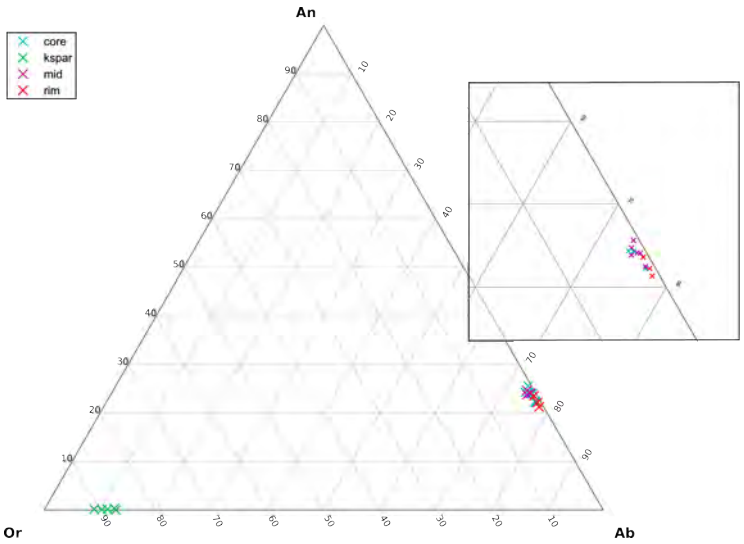

Figure 4.18: Graph to show distribution of feldspar compositions in S62.

S64 The feldspars are orthoclase (X_{Or}~0.90, X_{Ab}~0.10) and oligoclase, which shows X_{An}=0.19–0.25, X_{Or}=0–0.2 and X_{Ab}=0.71–0.80 (Figure 4.19). Garnet compositions are quite uniform across the sample, with X_{Fe} of ~0.86, X_{Py}=0.11, X_{Alm}=0.75, X_{Gr}=0.04, X_{Spss}=0.10. Biotite cores show Ti=0.31–0.39, Al(VI)=0.58–0.59 cations per formula unit based on 11 oxygens, and rims show Ti=0.36–0.53, Al(VI)=0.58–0.60.

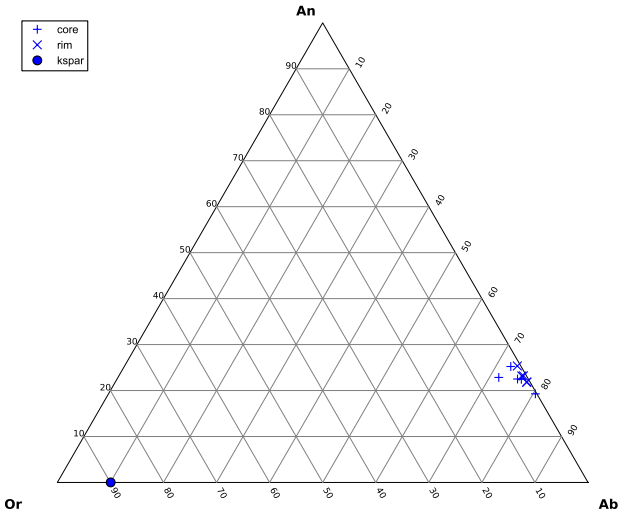

Figure 4.19: Graph to show distribution of feldspar compositions in S64.

Table 4.6: Representative mineral compositions for sample S62

	pl core	pl rim	ksp	g	bi	mu
SiO_2	63.76	63.53	66.53	39.36	35.94	46.18
TiO_2	0.03	0.01	0.00	0.00	2.98	0.61
Al_2O_3	23.53	23.47	18.39	21.42	20.25	37.52
Cr_2O_3	0.00	0.00	0.00	0.01	0.01	0.02
FeO	0.00	0.18	0.02	32.87	21.66	1.08
MnO	0.00	0.05	0.00	6.53	0.28	0.06
MgO	0.00	0.01	0.00	2.32	8.03	0.49
CaO	4.83	4.58	0.03	1.12	0.00	0.00
Na_2O	8.18	8.80	1.24	0.05	0.11	0.57
K_2O	0.21	0.11	14.88	0.00	9.62	10.39
Total	100.54	100.74	101.09	103.67	98.89	96.92
Oxygens	8	8	8	24	11	11
Si	2.80	2.79	3.02	6.12	2.66	3.01
Ti	0.00	0.00	0.00	0.00	0.17	0.03
Al	1.22	1.21	0.98	3.93	1.76	2.89
Cr	0.00	0.00	0.00	0.00	0.00	0.00
Fe	0.00	0.01	0.00	4.27	1.34	0.06
Mn	0.00	0.00	0.00	0.86	0.02	0.00
Mg	0.00	0.00	0.00	0.54	0.89	0.05
Ca	0.23	0.22	0.00	0.19	0.00	0.00
Na	0.70	0.75	0.11	0.01	0.02	0.07
K	0.01	0.01	0.86	0.00	0.91	0.87
Total	4.95	4.98	4.97	15.92	7.76	6.98

Table 4.7: Representative mineral compositions for sample S64

	pl core	pl rim	ksp	g	bi	mu	sill
SiO_2	58.59	59.48	43.01	36.92	32.69	42.61	33.66
TiO_2	0.02	0.00	0.06	0.04	2.73	0.69	0.04
Al_2O_3	23.60	24.31	37.37	22.05	20.51	38.41	66.41
Cr_2O_3	0.00	0.00	0.00	0.04	0.03	0.00	0.04
FeO	0.00	0.16	0.79	34.58	21.16	1.05	0.16
MnO	0.03	0.02	0.02	4.21	0.19	0.01	0.06
MgO	0.02	0.00	0.37	2.90	8.54	0.56	0.01
CaO	4.55	4.78	0.00	1.85	0.01	0.00	0.02
Na_2O	8.43	8.68	0.71	0.01	0.20	0.60	0.04
K_2O	0.35	0.10	9.63	0.00	9.35	10.32	0.05
Total	95.59	97.53	91.96	102.59	95.42	94.25	100.47
Oxygens	8	8	8	24	11	11	11
Si	2.72	2.71	2.15	5.84	2.52	2.87	2.00
Ti	0.00	0.00	0.00	0.00	0.16	0.04	0.00
Al	1.29	1.30	2.20	4.11	1.87	3.05	4.65
Cr	0.00	0.00	0.00	0.00	0.00	0.00	0.00
Fe	0.00	0.01	0.03	4.57	1.37	0.06	0.01
Mn	0.00	0.00	0.00	0.56	0.01	0.00	0.00
Mg	0.00	0.00	0.03	0.68	0.98	0.06	0.00
Ca	0.23	0.23	0.00	0.31	0.00	0.00	0.00
Na	0.76	0.77	0.07	0.00	0.03	0.08	0.00
K	0.02	0.01	0.61	0.00	0.92	0.89	0.00
Total	5.02	5.03	5.09	16.10	7.86	7.05	6.68

4.3 Inferred equilibrium assemblages

4.3.1 Mafic Samples

All mafic samples are amphibolites. Some exhibit traces of a higher-grade history in the form of garnet-breakdown textures, and some show extensive retrogression and replacement of peak minerals, (such as muscovite replacing sillimanite and K-feldspar) commonly in texturally isolated areas.

S33 shows one textural assemblage comprising diopside, hornblende, plagioclase, sphene and quartz. The edges of hornblende grains show lower Na and Al(VI) values than the rims, particularly where these grains are in contact with clinopyroxene grains, where Al(VI) is generally less than 0.2 cations per formula unit (based on 23 oxygens). This indicates that hornblende was partially re-equilibrated towards an actinolitic composition, with grains in contact with clinopyroxene showing more extensive retrogression. Thus it is assumed that apart from the altered rims of hornblende grains and the actinolite on the rims of clinopyroxene, the minerals and mineral compositions represent an equilibrium assemblage. Therefore the inferred peak assemblage is diopside, hornblende, plagioclase, sphene and quartz, with inferred retrograde alteration to form actinolite on the rims of clinopyroxene grains.

In S53, there is no significant zoning of the amphibole grains and there are no separate textural domains in the thin section. Grain compositions are fairly consistent across the sample and the majority of grains show annealed boundaries, indicating all minerals are in equilibrium, resulting in an inferred peak assemblage of hornblende, biotite, plagioclase, sphene and quartz.

S65 and S67 both show two distinct textural assemblages. In S65, the first assemblage is made up of coarse euhedral grains of biotite, hornblende, plagioclase and inferred garnet. The second assemblage is confined to symplectites that pseudomorph garnets. It consists of biotite, hornblende, plagioclase and cummingtonite, intergrown around resorbed garnets. The first assemblage (with the addition of garnet) is interpreted as representing an equilibrated matrix of minerals, in which the second assemblage formed owing to the breakdown of coarse garnet grains. While there is little compositional difference between the hornblende in the different assemblages, the plagioclase in the peak assemblage shows compositions of X_{An}~0.3 that are not seen in the grains of the garnet-breakdown assemblage. Biotite grains in the this assemblage show a wider range of Ti and Al(VI) content than grains in the peak assemblage.

In S67, the inferred peak assemblage is characterised by coarse euhedral grains of horn-

blende and biotite that show a strong alignment, inferred coarse garnets, and interstitial grains of plagioclase. The secondary assemblage is characterised by finer anhedral grains of hornblende and biotite, that do not show alignment and are intergrown with plagioclase around resorbed garnet grains. While there does not seem to be any significant compositional difference between the plagioclase or biotite grains in the two assemblages, hornblende in the first assemblage shows higher Na and Al(VI) values than in the second assemblage.The second assemblage is inferred to have formed as a result of the breakdown of coarse garnet grains in the first assemblage and is therefore considered to be retrograde and, due to a lack of mineral alignment, to have formed after the fabric-forming deformation.

4.3.2 Metapelitic Samples

Both S62 and S64 show evidence of having been granulites, containing in-situ leucosome in outcrop. Thus, the muscovite in the sample cannot have been in equilibrium with the peak assemblage as it would have been consumed to make melt (White & Powell, 2002). In S62, muscovite is present as either a fine mass of needle-like grains, resembling the fibrous clots that sillimanite needles tend to form, or as medium-coarse grains with which appear to have formed at the expense of K-feldspar. (Figures 4.6 and 4.7). In S64 the muscovite is present as a beard on the rim of sillimanite clots (Figure 4.8). It therefore appears that all muscovite in these samples formed through the retrograde breakdown of peak granulite facies minerals, and so must have formed as a result of rehydration and retrogression of the samples.

S62 shows an inferred peak assemblage of biotite, garnet, K-feldspar, plagioclase quartz and ilmenite, with the inferred presence of melt. Sillimanite may have been present, but has been completely replaced by muscovite during retrogression and rehydration. S64 shows the same assemblage but with sillimanite definitely present. It is inferred that melt was present at peak conditions, but then froze following the start of retrograde metamorphism. With the addition of fluid, muscovite then formed to completely replace sillimanite and partially replace K-feldspar. (In S64 the replacement of sillimanite was less extensive, perhaps because less fluid was added.) Garnet also appears to have undergone breakdown, and is only present as small remnants, surrounded by plagioclase. The other peak minerals are still stable, making the inferred retrograde assemblage for S62 muscovite, biotite, plagioclase, K-feldspar, quartz and ilmenite, and for S64 the same but with sillimanite still stable.

Chapter 5

Mineral Equilibria Modelling

The metamorphic evolution of the Nupskåpa samples was investigated through the use of calculated pseudosections to determine the P–T conditions preserved by the mineral assemblages present in the samples.

5.1 Methodology

Pseudosections were calculated in the model system Na_2O–CaO–K_2O–FeO–MgO–Al_2O_3–SiO_2–H_2O–TiO_2–Fe_2O_3 (NCKFMASHTO) using THERMOCALC 3.33 (Powell and Holland, 1988, updated June 2009) with an updated version of the internally consistent dataset of Holland and Powell (1998, dataset file tc-ds55.txt, created 22/11/2003).

The phases considered in the modelling and references to the activity-composition models used are biotite (White *et al.*, 2007) , epidote (Holland & Powell, 1998), orthopyroxene and spinel–magnetite (White *et al.*, 2002), muscovite–paragonite (Coggon & Holland, 2002), amphibole (Diener *et al.*, 2007, updated by Diener & Powell, 2012), clinopyroxene (Green *et al.*, 2007), updated by (Diener & Powell, 2012), chlorite (Holland *et al.*, 1998), plagioclase–K-feldspar (Holland & Powell, 2003) and ilmenite–hematite (White *et al.*, 2000). The sphene, quartz and aqueous fluid (H_2O) are pure end-member phases.

Bulk rock compositions for the samples were determined by X-ray fluorescence (XRF) analysis using a Philips X'Unique II wavelength-dispersive spectrometer housed at the University of Cape Town. The XRF results are presented in Table 5.1. Selected analyses were converted to the NCKFMASHTO system by disregarding the small amounts of MnO, Cr_2O_3 and P_2O_5 and converting selected amounts of total Fe to Fe^{3+}. For the pelitic samples ~10%,

and for the mafic samples ∼15%, of total Fe was converted to Fe^{3+} (Diener and Powell, 2010). These re-calculated values are presented in Table 5.2.

Table 5.1: XRF whole-rock analyses of selected samples

	S33	**S53**	**S62**	**S64**	**S65**	**S67**
SiO_2	49.31	44.79	54.12	59.31	45.49	48.78
TiO_2	1.05	1.32	1.27	0.88	0.91	2.76
Al_2O_3	14.38	14.69	19.94	18.18	14.45	14.91
Fe_2O_3	11.60	14.21	10.04	7.96	12.20	13.84
MnO	0.19	0.20	0.10	0.11	0.16	0.19
MgO	7.19	9.27	3.20	2.67	12.33	6.68
CaO	9.60	10.13	1.35	1.98	10.19	8.90
Na_2O	3.07	2.29	2.56	2.90	1.51	0.86
K_2O	1.66	1.82	5.29	4.00	0.53	1.42
P_2O_5	0.16	0.10	0.08	0.12	0.10	0.41
SO_2	0.01	0.02	0.01	0.01	0.04	0.03
Cr_2O_3	0.06	0.07	0.05	0.04	0.12	0.06
NiO	0.03	0.02	0.01	0.01	0.05	0.01
H_2O-	0.55	0.07	0.09	0.04	0.06	0.05
LOI	0.65	0.58	1.33	1.02	1.38	0.91
Total	99.52	99.57	99.45	99.23	99.53	99.82

The abundant leucosome present in the metapelitic samples is consistent with the rocks having produced a significant amount of melt. However, the peak granulite facies assemblage is well preserved, indicating that a significant amount of melt was lost from these rocks before substantial cooling occurred (White & Powell, 2002). The petrography of the pelitic samples suggests muscovite formed at the expense of sillimanite and K-feldspar, which is consistent with rehydration (Spear, 1995). The current composition of these rocks therefore represents that of a residuum that has been modified first by melt loss, and then by the addition of fluid. For the residuum pseudosections, H_2O content for each sample was estimated such that the inferred peak assemblage was stable at conditions immediately above the residuum solidus, to reflect conditions where the assemblage would have been in equilibrium with the

Table 5.2: Bulk compositions (in mol %) used to construct pseudosections

	S33	**S53**	**S62**	**S64**	**S65**	**S67**
Si	53.31	47.98	62.53	67.21	47.83	53.34
Ti	0.86	1.07	1.11	0.75	0.72	2.27
Al	9.17	9.27	13.58	12.14	8.96	9.61
FeT	9.44	11.46	8.73	6.79	9.66	11.39
Mn	0.17	0.18	0.10	0.11	0.15	0.17
Mg	11.58	14.79	5.50	4.51	19.32	10.89
Ca	11.12	11.62	1.68	2.40	11.48	10.43
Na	3.21	2.38	2.87	3.18	1.54	0.91
K	1.15	1.24	3.90	2.89	0.36	0.99
O	0.70	0.85	0.45	0.30	0.75	0.85

remaining melt (White *et al.*, 2004; Diener *et al.*, 2008). For the rehydrated pseudosections, the minimum H_2O content needed to stabilise the retrograde assemblage was selected. Fluid was assumed to be in excess for the mafic amphibolites, and no mafic granulites were selected for pseudosection calculations because the current silicate melt model is not appropriate for mafic compositions and their suprasolidus evolution cannot be quantitatively investigated yet (White & Powell, 2002). Where necessary, contours were calculated for mineral compositions and in some cases, mineral modes. These were used to further constrain pressure and temperature ranges of stable assemblages. The calculated pseudosections are presented in Figures 5.1 to 5.8.

5.2 Results

5.2.1 Mafic Samples

S65

The inferred peak assemblage of hornblende, rutile, quartz, plagioclase and garnet (with biotite and H_2O in excess) is stable over a large P-T range, above 9 kbar and at more than 725 °C (Figure 5.1). The field is bounded by the breakdown of garnet below ∼9 kbar, and of plagioclase to lower temperatures. At higher temperatures and lower pressures, quartz

breaks down. The peak assemblage field was contoured for Fe/Mg ratio in garnet. These contours are sensitive to changes in pressure and temperature, and show that the Fe/Mg ratio increases with decreasing temperature and pressure. The contours range from X_{Fe}=0.60 at the high end of the field, to X_{Fe}=0.72 at the lower end.

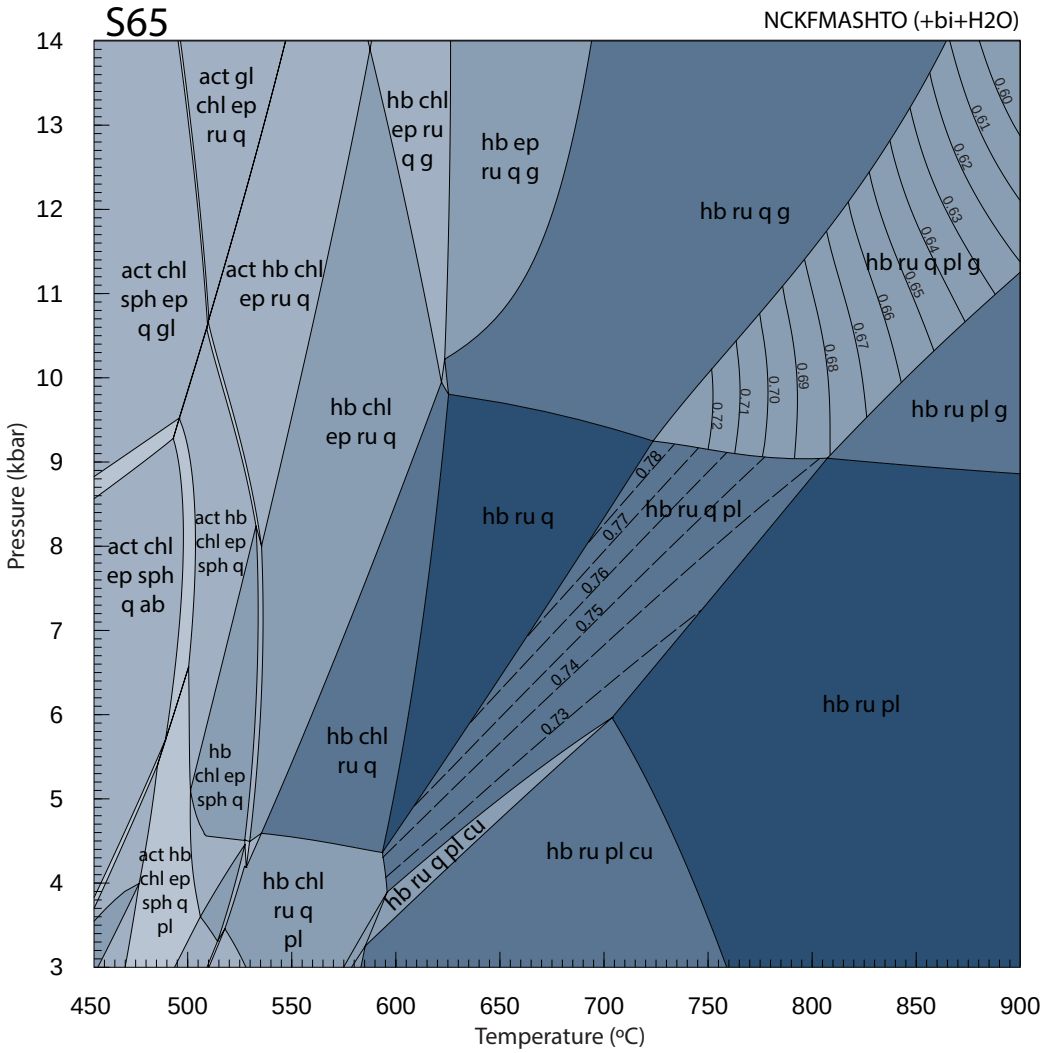

Figure 5.1: Calculated pseudosection for S65. The inferred peak assemblage stability field (hb–ru–q–pl–g) has been contoured for X_{Fe} ratio in garnet. These range from 0.60 at high T and P, to 0.72 at lower T and P. The inferred retrograde assemblage stability field (hb–ru–q–pl–cu) was too small to warrant contouring, but the field between the inferred peak and retrograde fields (hb–ru–q–pl) has been contoured for anorthite content in plagioclase (dotted lines). These show decreasing values from higher to lower pressures.

Between ∼600 and 700 °, at 4-6 kbar below garnet stability, cummingtonite becomes

stable and quartz breaks down almost immediately thereafter. The inferred retrograde assemblage, present in the garnet-replacement textures, is then hornblende, rutile, quartz, plagioclase and cummingtonite and is stable in a narrow field between 585 and 705 °C, and 3.3 and 6.0 kbar. However, the position of the quartz-breakdown line is highly dependent on Si content in the rock, and so the lower pressure estimate is far less reliable than the upper (Figure 5.1).

S67

The inferred peak assemblage of hornblende, quartz, rutile, plagioclase and garnet (with biotite and H_2O in excess) is stable above 7 kbar, and from 650 to above 850 °C . The assemblage is bounded by the breakdown of garnet to lower pressures, and by the stabilisation of epidote to lower temperatures (Figure 5.2).

Contours showing Fe/Mg ratio in garnet and anorthite content in plagioclase vary from X_{Fe}=0.74, X_{An}=0.76 at 10 kbar and 800 °C , to X_{Fe}=0.88, X_{An}=0.90 at 7 kbar and 650 °C , in the stability field of the peak assemblage. The retrograde assemblage of hornblende, quartz, rutile, plagioclase, biotite and excess H_2O is stable at 550-650 °C and 3–7 kbar (Figure 5.2). The field is bounded by the garnet-breakdown line to higher pressures, and the stabilisation of epidote to lower temperatures and cummingtonite to lower pressures. Towards higher temperatures, orthopyroxene becomes stable.

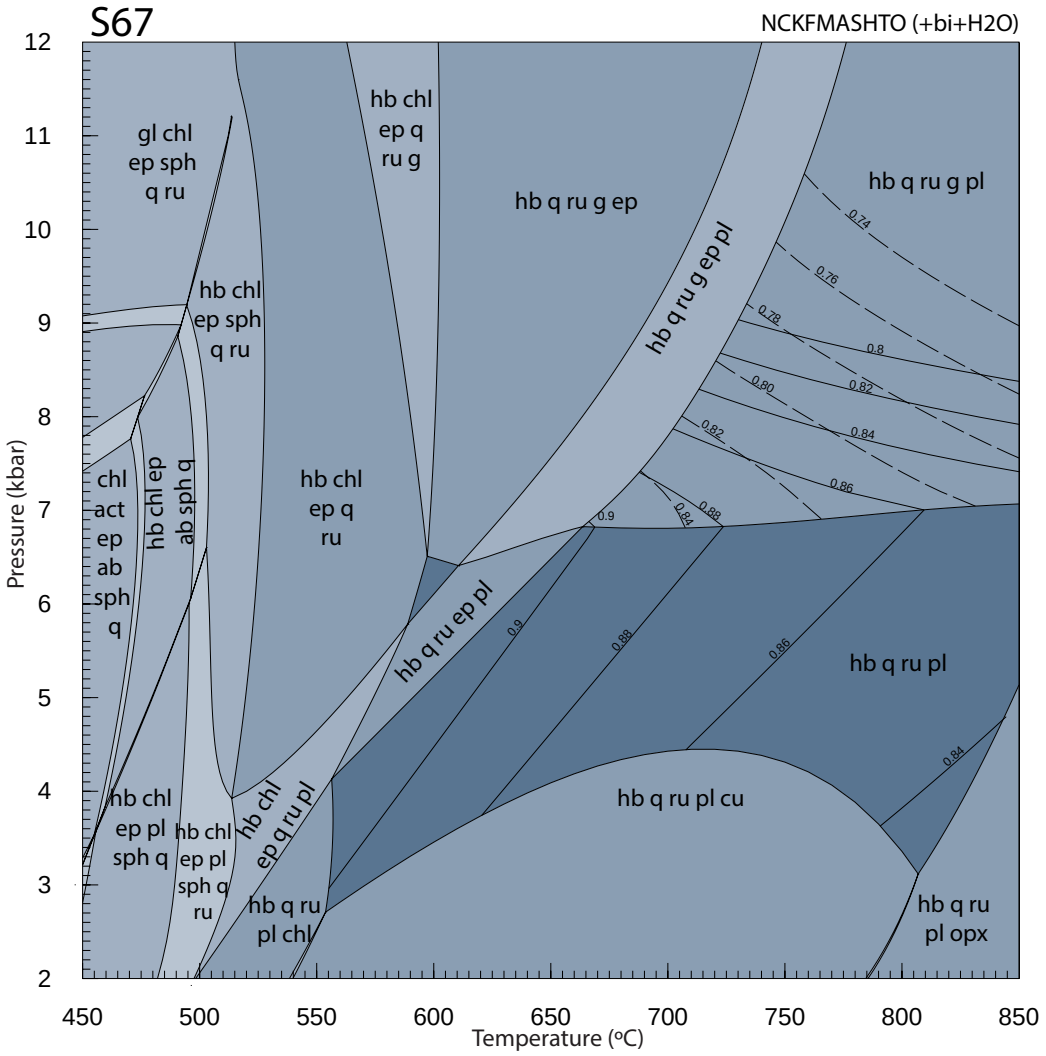

Figure 5.2: Calculated pseudosection for S67. The inferred peak assemblage stability field (hb–q–ru–g–pl) has been contoured for X_{Fe} ratio in garnet (dashed lines) and anorthite content in plagioclase (solid lines). Both sets of contours have fairly shallow negative slope and increase towards lower P and T. The inferred retrograde assemblage stability field (hb–q–ru–pl) has also been contoured for anorthite content in plagioclase. These steeper contours have a positive slope and increase with decreasing T.

S33

The inferred peak assemblage of diopside, hornblende, plagioclase, sphene and quartz (with biotite and H_2O in excess) is stable over a wide range of pressures, from 4 to 11 kbar, and a narrower range of temperatures, from 525 to 700 °C. The field is bounded by the stabilisation of epidote to lower temperatures and higher pressures, actinolite to lower temperatures at low

pressures, and of rutile to higher temperatures. To lower pressures quartz breaks down and at higher pressures (greater than ∼11 kbar) garnet becomes stable. This field was contoured for Na content in hornblende. The contours are sensitive to pressure, and range from X_{Na}=0.29 at ∼4 kbar to X_{Na}=0.55 at ∼9 kbar. The presence of actinolitic rims on hornblende grains, and of actinolite alteration rims on clinopyroxene grains implies a retrograde assemblage of diopside, hornblende, plagioclase, sphene, quartz and actinolite (with biotite and H_2O in excess) which is stable over a small area, from 510–520 °C and 3–3.4 kbar. The field is bounded by the breakdown of quartz to lower pressures, and by the stabilisation of epidote to higher pressures.

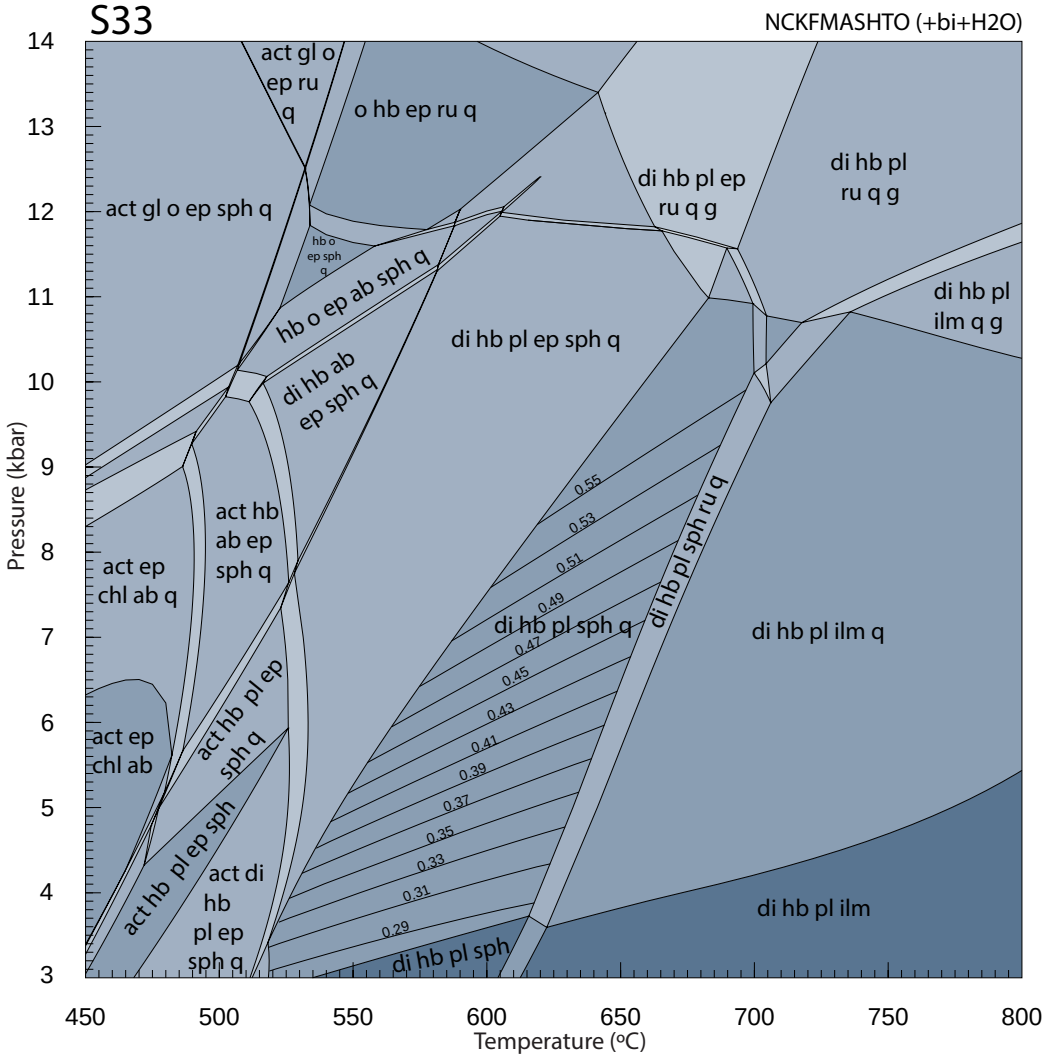

Figure 5.3: Calculated pseudosection for S33. The inferred peak assemblage stability field has been contoured for A-site Na in hornblende, and these range from 0.55 at ∼9 kbar and ∼650 °C , to 0.29 at ∼3 kbar and ∼550 °C

S53

The inferred diopside-free peak metamorphic assemblage of hornblende, plagioclase, sphene, biotite and excess fluid seen in S53 is not stable anywhere in the S53 pseudosection. However, this assemblage with additional diopside is stable over a wide range of pressures and temperatures. The field is bounded by the presence of orthopyroxene to higher temperatures, and by garnet to higher pressures. Calculations show that the modal proportions of diopside in this field is uniformly low, between 1 and 6 volume %. The sample does not contain any epidote or quartz (stabilised to lower temperatures) or garnet such that the best representation of the peak assemblage on the pseudosection is taken to be hornblende, plagioclase, sphene, biotite and diopside with possible fluid. The discrepancy between the sample and the model could be the result of the bulk composition not accurately representing the thin section or the presence of diopside being easily overlooked owing to its low abundance. This field is stable over a wide range of temperatures, above 475 °C and below 10 kbar (Figure 5.4). The diopside-bearing peak field has also been contoured for anorthite content in plagioclase (solid lines). These contours have a positive slope and increase towards higher temperature and lower pressure conditions.

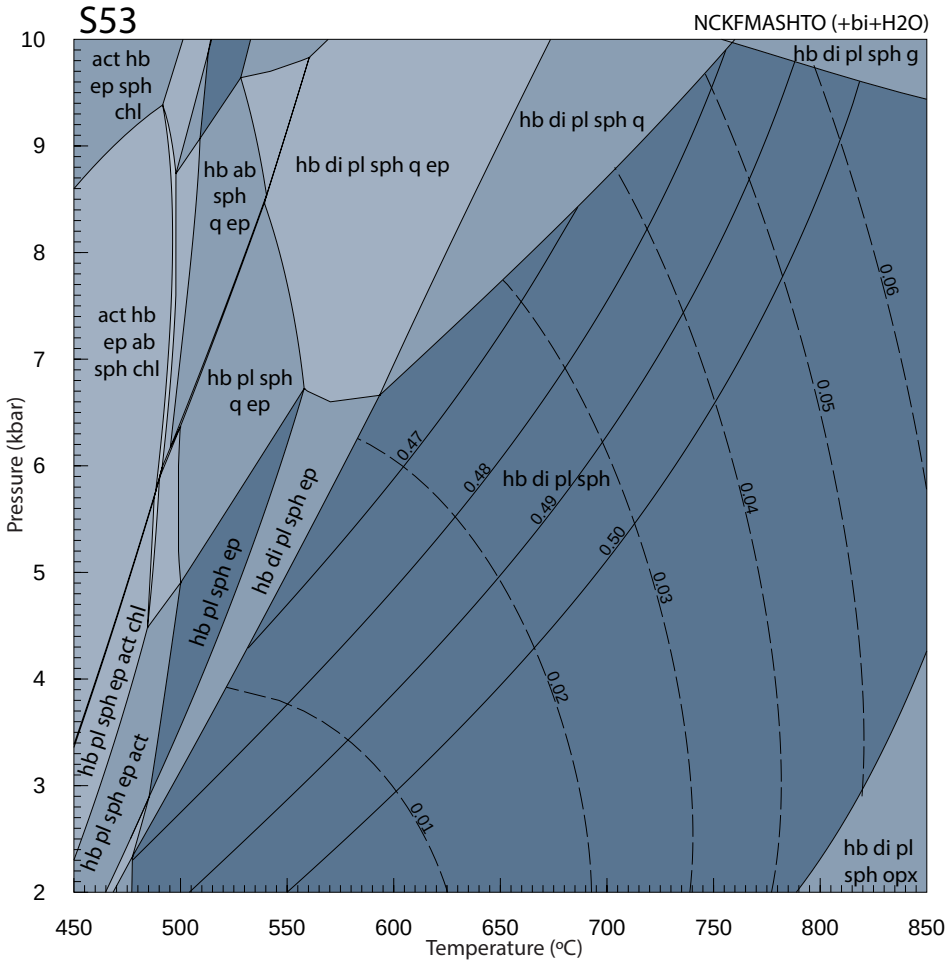

Figure 5.4: Calculated pseudosection for S53. The inferred peak assemblage stability field has been contoured for the mode of diopside in the sample (dotted lines), which range from 1 vol. % at lower pressures and temperatures, to 6 vol. % at higher temperatures and pressures. The field has also been contoured for anorthite content in plagioclase (solid lines). These contours have a positive slope and increase towards higher temperature and lower pressure conditions.

5.2.2 Metapelitic Samples

S62

The inferred granulite facies peak assemblage of biotite, garnet, K-feldspar, plagioclase, quartz, sillimanite, ilmenite and melt is stable on the residual pseudosection between 820 and 880 °C , and 6.4–11.6 kbar (Figure 5.5). The field is bounded by the solidus to lower temperatures and by biotite breakdown to higher temperatures. To higher pressures, kyanite

is stable instead of sillimanite, and cordierite becomes stable at pressures below ∼6 kbar. The inferred retrograde assemblage of muscovite, biotite, plagioclase, K-feldspar, quartz and ilmenite is not stable anywhere on the pseudosection for the residual composition, as muscovite is missing. Petrographic analysis suggests that muscovite formed at the expense of sillimanite and K-feldspar, which is consistent with rehydration (Spear, 1995). Rehydrated pseudosections were calculated with varying fluid contents. The inferred retrograde assemblage becomes stable with a minimum water content of 7.5 wt% H_2O, between 430 and 600 °C and below 5 kbar (Figure 5.6). The field is bounded by k-feldspar breakdown and the solidus to higher temperature, and aluminosilicate stabilisation to lower temperatures and higher pressures.

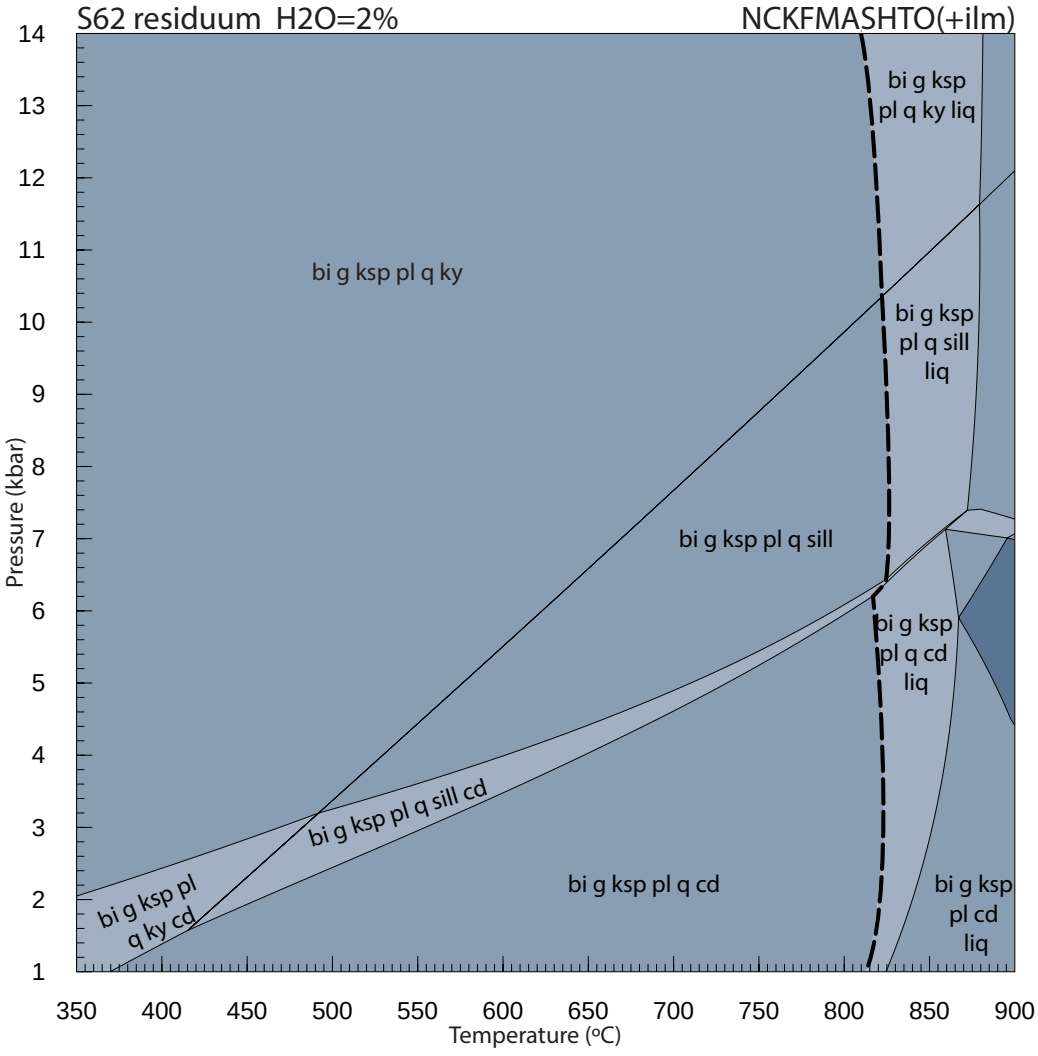

Figure 5.5: Calculated pseudosection for the residuum composition of sample S62. The solidus is indicated with a dashed line.

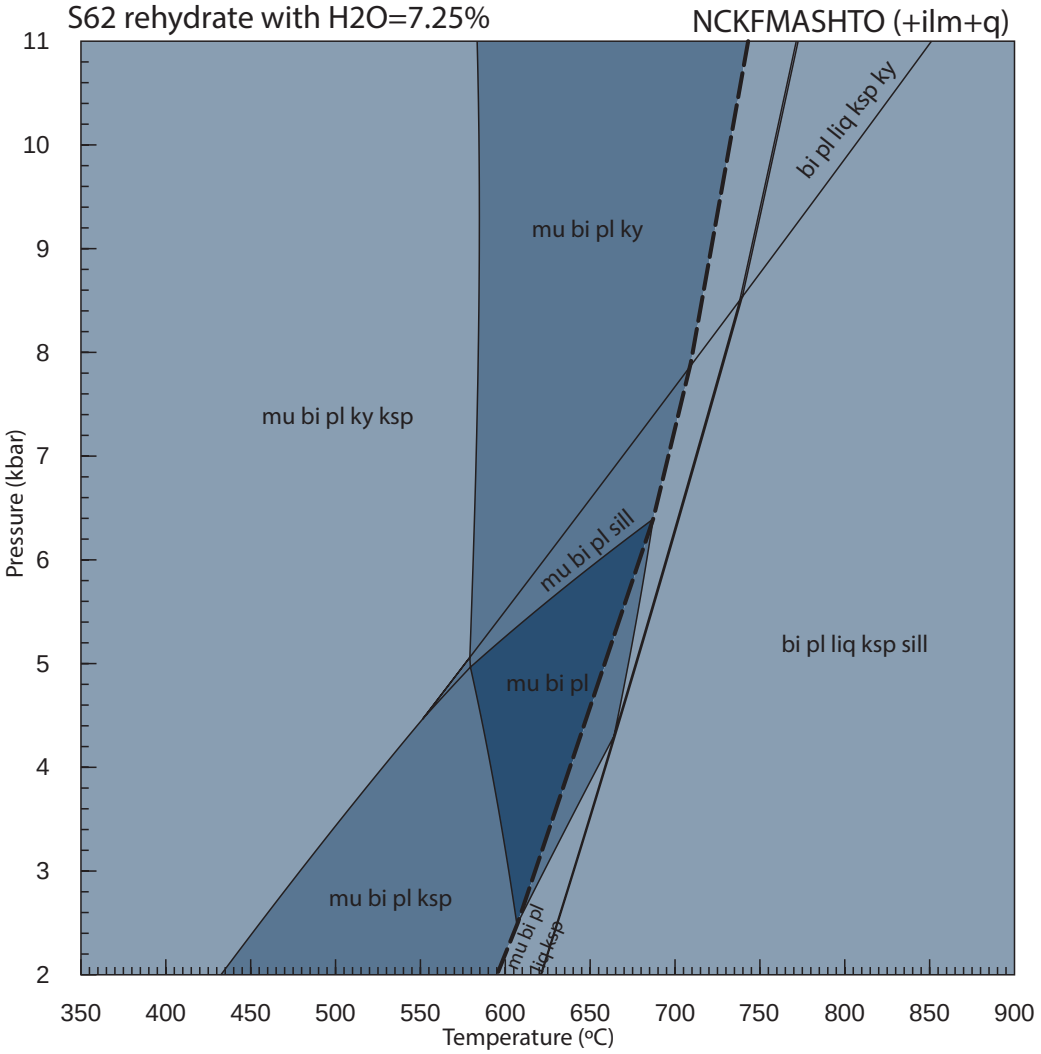

Figure 5.6: Calculated pseudosection for the composition of sample S62, rehydrated with 7.25 wt% H_2O. The solidus is indicated with a dashed line.

S64

The inferred granulite facies peak assemblage of biotite, garnet, K-feldspar, plagioclase, quartz, sillimanite, ilmenite and melt is stable on the residual pseudosection between 805 and 880 °C , and 6.2 to 11.6 kbar (Figure 5.7). The field is bounded by biotite breakdown to higher temperatures, and the solidus to lower temperatures. To higher pressures kyanite replaces sillimanite, and to lower pressures cordierite becomes stable. The inferred retrograde assemblage of muscovite, biotite, plagioclase, k-feldspar, quartz, sillimanite and ilmenite is not stable anywhere on the pseudosection for the residual composition. Muscovite has formed on the rims of sillimanite clots, suggesting it formed as a result of sillimanite breakdown, consis-

tent with rehydration (Spear, 1995). On a partially rehydrated pseudosection, calculated with 5 wt% H_2O, this retrograde assemblage is stable below 700 °C and 7.8 kbar (Figure 5.8). The field is bounded by the kyanite-sillimanite transition to higher pressures and by k-feldspar breakdown, as well as melt-formation, to higher temperatures. The pressure-temperature range constrained by this field is wide and as there is little variation in mineral composition across the sample, contours are of little use in constraining it further.

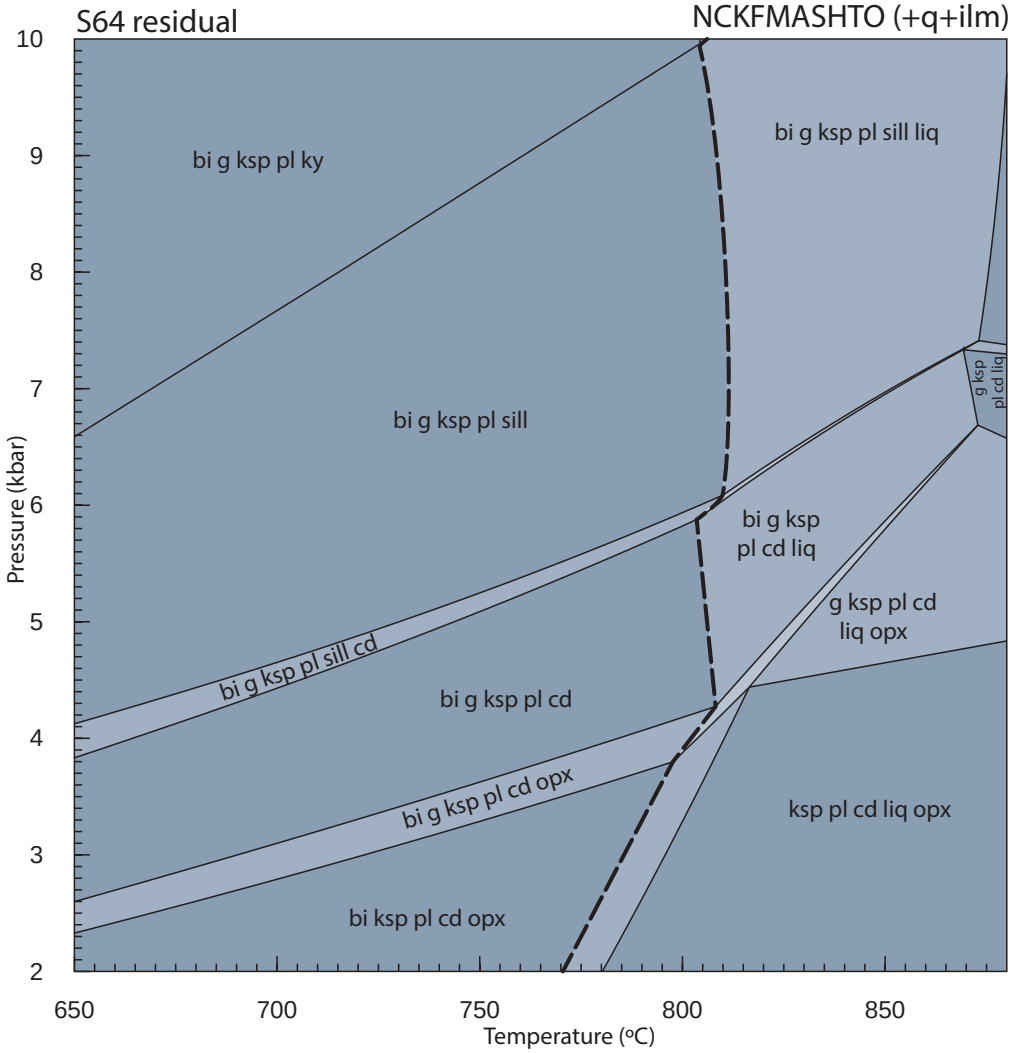

Figure 5.7: Calculated pseudosection for the residuum composition of sample S64. The solidus is indicated with a dashed line.

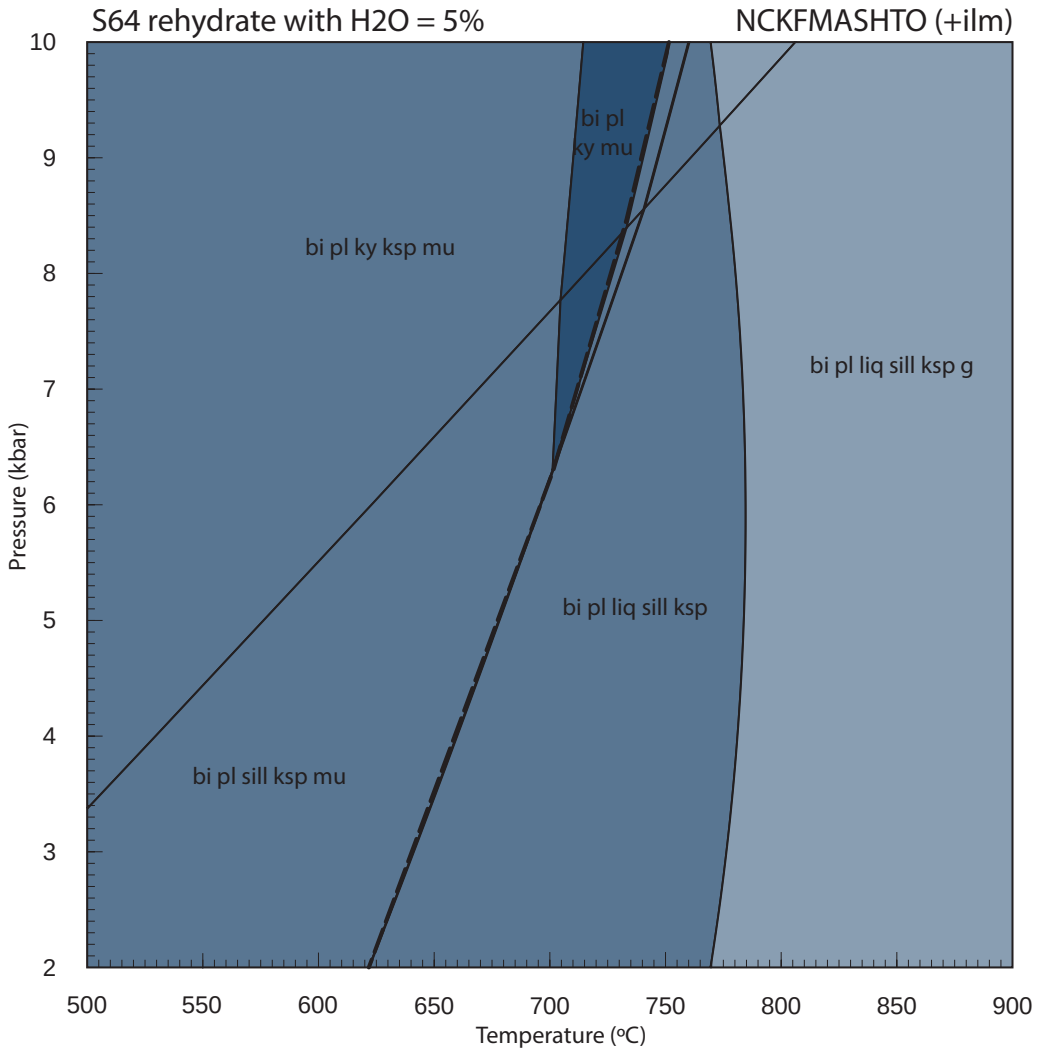

Figure 5.8: Calculated pseudosection for the composition of sample S64, rehydrated with 5 wt% H_2O. The solidus is indicated with a dashed line.

Chapter 6

Discussion

6.1 Estimation of peak and retrograde P-T conditions

6.1.1 Mafic Samples

In sample S65, Fe/Mg ratios in garnet show that garnet grains are commonly zoned, with cores showing X_{Fe}=0.62 and rims showing X_{Fe}=0.72. Contours in the peak assemblage stability field show an increase in X_{Fe} in garnet with a decrease in pressure and temperature. This indicates that the sample underwent re-equilibration following decompression from more than 14 kbar to below 9 kbar where garnet was no longer stable (Figure 5.1). The replacement of garnet by plagioclase and cummingtonite indicates further decompression to around 5 kbar, at ∼640 °C , where the retrograde assemblage developed.

Sample S67 shows zoning in both the plagioclase and garnet grains. Contouring the peak assemblage field for anorthite content in plagioclase and Fe/Mg ratio in garnet shows that plagioclase becomes more anorthitic, and garnet more Fe-rich, with a decrease in pressure and, to a lesser extent, temperature. The increase from core to rim in anorthite content in plagioclase and Fe content in garnet shows the sample experienced retrogression followed by garnet breakdown, from above ∼10 kbar and ∼800 °C to conditions at the lower-temperature end of the hb-q-ru-pl (+bi+H_2O) stability field (Figure 5.2). Plagioclase rims show X_{An}=0.9, and therefore the retrograde assemblage can be constrained to 550–665 °C and 3–6.8 kbar.

The fabric in S67, defined by the alignment of biotite, hornblende and ilmenite, anastomoses around the garnet relics, which appear unaffected by the deformation, as the plagioclase-cummingtonite-biotite symplectite displays the sub-idioblastic shape of the original garnet. The biotite within the breakdown-textures is not aligned, whereas the biotite in the rest of the

sample is strongly aligned. This indicates that garnet breakdown (and therefore retrograde metamorphism) must have occurred after the main fabric-forming deformation event.

Sample S33's stability field is confined to a narrow range of temperatures, from 520 to 700 °C , but a very wide range of pressures. It overlaps with S67 and S53 between 550 and 650 °C , and from 3 to 6.4 kbar (Figure 5.3). Contouring the field for Na in hornblende indicates a decrease in Na content with a decrease in pressure (Figure 5.3). Zoning in hornblende grains in S33 shows the cores to be more Na- and Al-rich than the rims (Figure 4.10), indicating a decompressive retrogression. Exactly how much cooling occurred during this retrogression is unconstrained, but it was likely more than ∼150 °C . S33 does not preserve evidence of a separate peak assemblage, but the zoning preserved in the hornblende shows clear evidence of decompression, with some potential cooling.

The stable assemblage in S53 is less tightly constrained than the other samples as the assemblage is stable over a very wide field. This field overlaps with the conditions constrained by S33, S65 and S67. Microprobe data shows the cores of plagioclase grains as less anorthitic than the rims (X_{An}core=0.30, X_{An}rim=0.48). As X_{An} increases across the field, with decreasing pressure and increasing temperature, the zoning could be the result of decompression with minimal temperature changes (Figure 5.4).

6.1.2 Summary of metamorphic conditions recorded by mafic samples

Both S65 and S67 show clear evidence for a peak assemblage followed by decompression and cooling to form a retrograde assemblage. If the peak assemblage fields for S65 and S67 are overlapped, they constrain a range of peak metamorphic conditions above 735 °C at more than 9 kbar (Figure 6.1).

Overlapping the retrograde assemblage fields of all four samples shows that S33, S53 and S67 all overlap and constrain a pressure and temperature field between 555 and 645 °C , and 3.2 and 6.4 kbar (Figure 6.1). The retrograde assemblage in S65 sits at slightly lower pressures and higher temperatures, and this may be because the retrograde assemblage developed in isolated pockets, out of equilibrium with the rest of the rock, and so this assemblage was modelled with the incorrect/inappropriate bulk composition.

The zoning in S65 and S67 (where plagioclase cores are more anorthitic than rims, and garnet cores are more Fe-rich than rims) indicates retrograde re-equilibration of some kind. This could show early retrogression after peak conditions, from above ∼800 °C at 10 kbar,

to ∼720 °C at 8 kbar (Figures 5.1 and 5.2). However, the zoning in these minerals may also simply represent the partial re-equilibration of the peak assemblage to the retrograde conditions at a later stage. The zoning is not used in constraining the P-T conditions, but does indicate the trajectory of retrogression at some point in the poly-metamorphic history.

6.1.3 Summary of conditions recorded by metapelitic samples

Samples S62 and S64 overlap to constrain peak temperatures and pressures to be essentially those constrained by S62. The upper P limit of the peak stability field in both samples is the kyanite-sillimanite transition. It is therefore possible that the samples experienced conditions where kyanite was stable, but that during decompression this kyanite broke down to form sillimanite. Thus the samples may have come from higher pressures than those recorded here (perhaps similar to the conditions suggested by Board *et al.* (2005)). The sillimanite in S64 is clearly replaced, at least partially, by muscovite. It is likely that the same process occurred in S62, but to a greater extent, resulting in the complete replacement of sillimanite by muscovite. Together, the peak fields of S62 and S64 constrain peak metamorphic conditions to be between 820 and 880 °C , and 6.4–11.6 kbar. The retrograde assemblages of S62 and S64 overlap between 500 and 605 °C at less than 5 kbar (Figure 6.1).

6.2 Likely P-T paths and comparisons with previous work

Overlapping the conditions constrained by the pelitic samples with those constrained by the mafic samples shows that the peak conditions overlap between 820 and 880 °C , at 9.5–11.6 kbar, while the retrograde conditions show overlap between 555 and 595 °C , at 3.2–4.8 kbar.

It may be that both the peak and retrograde conditions recorded in the Nupskåpa area occurred during the Pan-African event, such that a direct transition occurred, from ∼850 °C at 12.5 kbar, to ∼575 °C at 4 kbar (Figure 6.2). However, based on previous metamorphic studies conducted in the area (e.g. Groenewald & Hunter, 1991; Groenewald *et al.*, 1995; Grantham *et al.*, 1995; Board *et al.*, 2005), the 'peak' conditions are instead closer to the M_1 conditions of Groenewald & Hunter (1991), indicating a likely Grenvillian age for this assemblage (see Figure 6.4). The 'retrograde' conditions are recorded by minerals that formed after the fabric-forming deformational event. This event was dated by Board (2001) and found to have an age of ∼ 540 Ma, indicating that the post-tectonic 'retrograde' conditions are likely have occurred during a late stage of the M_2 metamorphic event. These M_2 conditions are

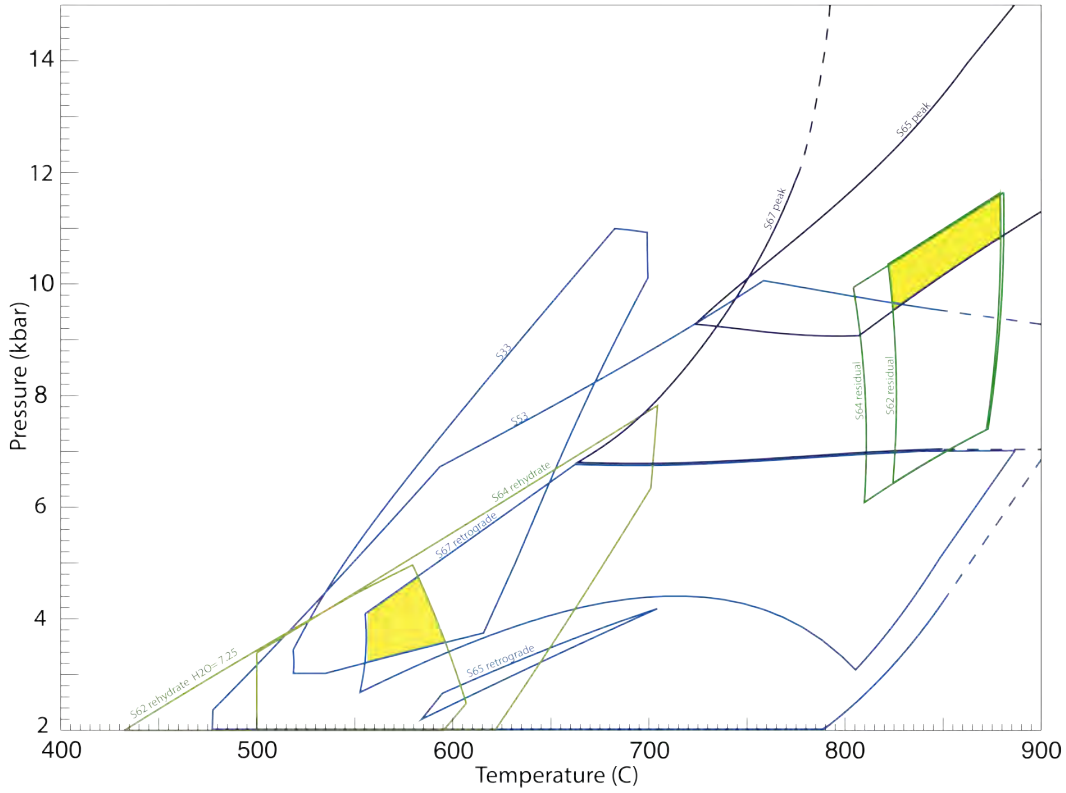

Figure 6.1: Overlapping the stable assemblage fields for all 6 samples shows that the mafic samples overlap to constrain peak conditions above 735 °C at more than 9 kbar, and retrograde conditions of 555–645 °C , and 3.2–6.4 kbar. The pelitic samples overlap to constrain peak conditions of 820–880 °C , at 6.4–11.6 kbar. The retrograde assemblages of S62 and S64 overlap between 500 and 605 °C at less than 5 kbar. Final constrained conditions are shaded in yellow, and show that peak conditions were between 820 and 880 °C at 9.5–11.6 kbar, while the retrograde conditions were between 555 and 595 °C at 3.2–4.8 kbar.

lower than the three sets of M_2 conditions identified by Board *et al.* (2005). However, they do lie along the retrograde path, between the M_{2c} stage and the point at which the rocks reached the ∼500 °C closure temperature of hornblende (at ∼486 Ma; Figure 6.4). Thus it appears plausible that the 'peak' and 'retrograde' conditions of this study are likely to have resulted from two separate metamorphic cycles, and that there is evidence of both Grenvillian and Pan-African metamorphism recorded in the Nupskåpa area (Figure 6.3). A more certain P-T-t path for the Nupskåpa area could be achieved through isotopic dating of the minerals that make up the different assemblages but that is beyond the scope of this study.

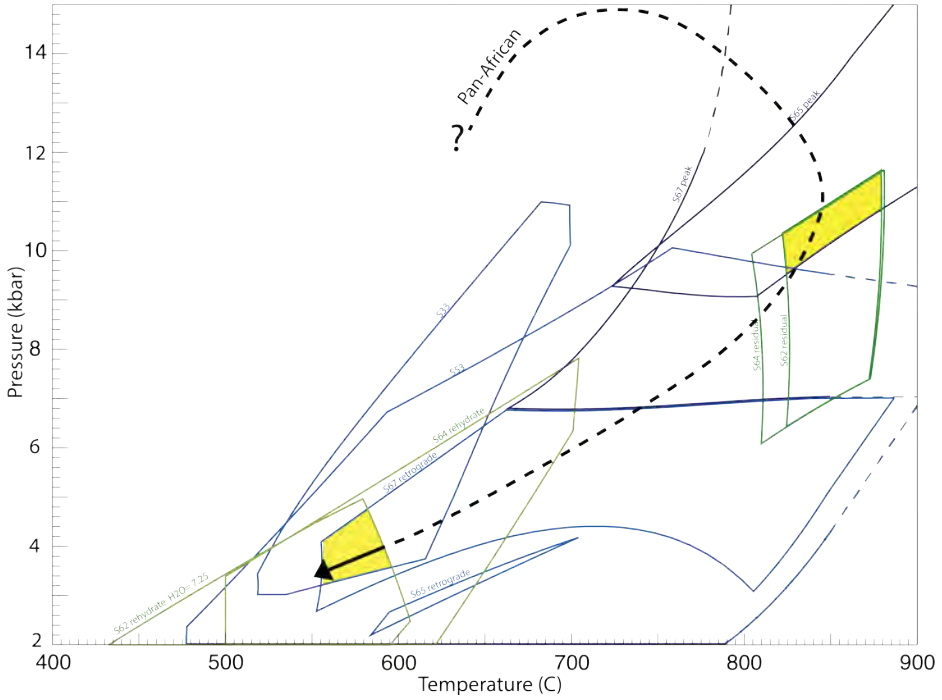

Figure 6.2: P-T path if both conditions occurred during the Pan-African orogeny.

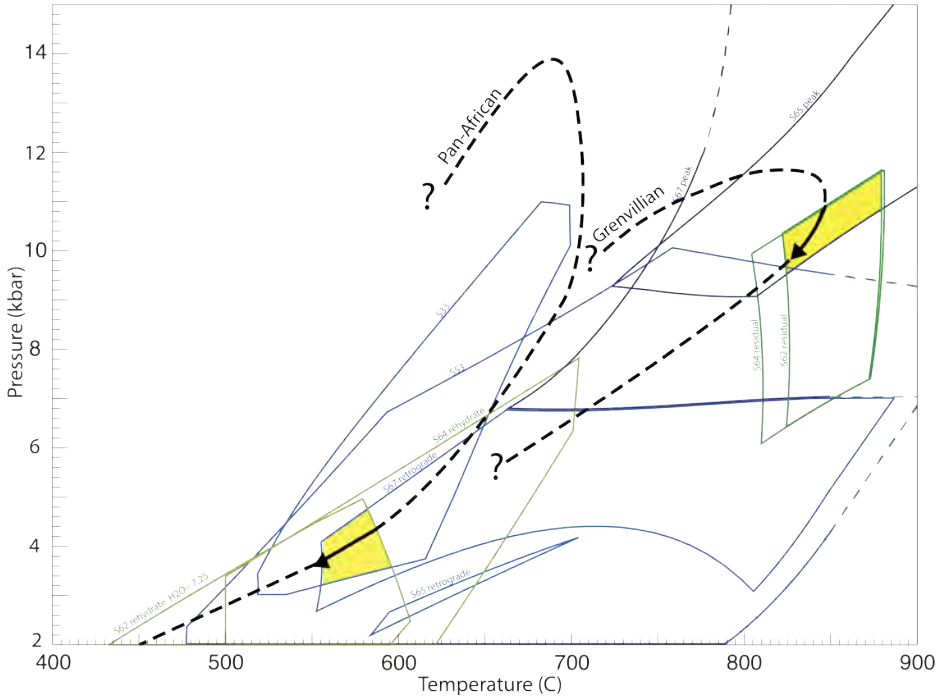

Figure 6.3: Possible P-T paths if the peak conditions occurred during the Grenvillian orogeny, and the retrograde conditions during the Pan-African orogeny.

Both Groenewald *et al.* (1995) and Board *et al.* (2005) found evidence for eclogite-facies metamorphic conditions, around 750 °C at more than 12 kbar. Groenewald *et al.* (1995) attributed these to an early M_1 event while Board *et al.* (2005) related them the M_{2a} Pan-African event (Figure 6.4). No evidence was found in the Nupskåpa area for similar high-pressure conditions. The samples collected in the Nupksåpa area record much higher temperatures than those of the M_{2a} event (Figure 6.4). The stability field of S33 is situated at the right temperatures for the M_{2a} event, and is bounded by the garnet breakdown line to higher pressures. If garnet relics were found in this sample one could infer that S33 might potentially have experienced conditions similar to the M_{2a} conditions of Board *et al.* (2005). However, none were found in either the hand sample or thin section. The high-pressure conditions identified by Board *et al.* (2005) were for an inferred assemblage, based on Na content in clinopyroxene, which suggested it was originally omphacite. The clinopyroxene in samples from the Nupskåpa area have very low sodium and aluminium content (Table 4.2), and so no high-pressure omphacite-bearing assemblage was inferred for this study.

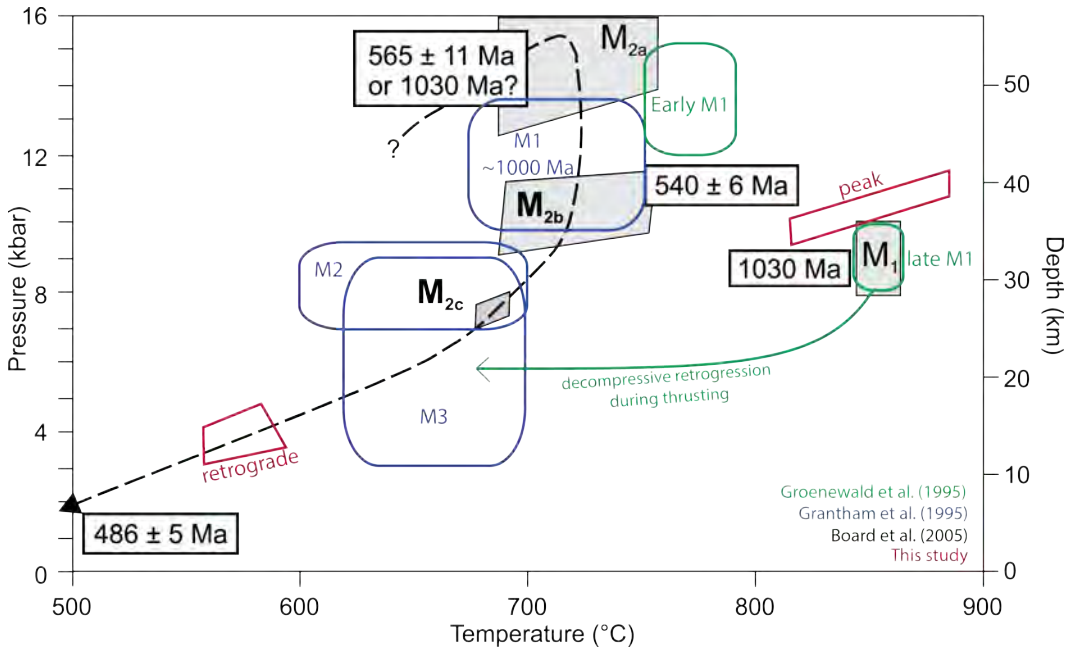

Figure 6.4: The peak and retrograde conditions recorded in the Nupskåpa area (red), compared with the P-T conditions identified by Groenewald *et al.* (1995) (green), Grantham *et al.* (1995) (blue) and Board *et al.* (2005) (black with grey shading).

Regardless of the details of the early poly-metamorphic history of the Nupskåpa area, the late-M_2 conditions are recorded in a post-tectonic assemblage, made up of minerals that do not show any preferred orientation. The retrogression associated with the formation of this assemblage required the introduction of fluid into the crust (White & Powell, 2002). The formation of the M_2 shear zones is likely to have resulted in the introduction of fluid into the host rocks, which later resulted in the formation of the retrograde assemblage. The intrusion of the composite leucogranites occurred after the formation of these shear zones(see Figure 3.8). The late-M_2 conditions are therefore likely to be the maximum physical conditions under which intrusion of the composite dyke phase could have occurred. These conditions, of $\sim$575 °C at 4 kbar, lie between the wet solidus (Figures 5.5 to 5.8) (Vigneresse, 2006) and the brittle-viscous transition (Handy *et al.*, 2001), and indicate a location in the mid-crust where temperatures are high, but more than 100 °C below the solidus, where a pervasive network of small-scale melt-bearing structures would no longer be feasible, but where temperatures are still high enough to also hinder focused migration (Weinberg, 1999; Faber, 2012). Thus, these conditions represent a likely location where one might expect the transition from pervasive to focused migration to occur.

6.3 Inferred style of melt migration

The P-T estimates indicate that suprasolidus conditions were reached by both metapelitic samples, and that melting is therefore most likely to have occurred under M_1 conditions. The host-rock paragneiss of the Nupskåpa Cliff should therefore contain evidence of melting and melt segregation. The oldest intrusive phase in the cliff has a leucogranitic composition and forms a small to mesoscale pervasive leucosome network, consisting of predominantly centimetre-scale subhorizontal structures, with smaller diffuse stromatic leucosome structures connecting to larger, discordant structures. The leucosomes have diffuse feathery boundaries, and therefore appear to have been fed by melt from within the country rock (Sawyer *et al.*, 2011; Brown, 2013). They also exhibit pinch-and-swell and boudinage structures, and are generally oriented parallel to the gneissic host rock fabric. The larger structures of the oldest leucosome, although somewhat discordant to the gneissic fabric, are connected to foliation-parallel leucosomes and connect the dilatant sites formed in the fold hinges of the foliation, and so are still occupying pre-existing zones of weakness and low-pressure (Figure 3.3; Vernon & Paterson, 2001). Thus this phase seems to represent melting and melt segregation within

the host rock during M_1 granulite facies peak metamorphism.

The temperatures experienced by the Nupskåpa area during M_2, inferred to represent the Pan-African event, are below the original peak conditions reached during the M_1 event (even if we take the conditions of Grantham *et al.* (1995); Groenewald *et al.* (1995) and Board *et al.* (2005) as peak). The rocks would have become dehydrated during the first high-grade metamorphic cycle and the solidus temperatures would have been elevated. Furthermore there is no evidence that these rocks were rehydrated following M_1 (which may have allowed melting during M_2, so melting is unlikely to have occurred again at the lower temperatures of M_2 peak metamorphism (White & Powell, 2002; Diener *et al.*, 2008). Thus, even though they reached reasonably high temperatures, the rocks exposed in the Nupskåpa area do not appear to have melted during the Pan-African M_2 event. According to McGibbon (2014), the deformation related to the Pan-African orogenic event did not form a penetrative fabric across the Nupskåpa area, but was instead partitioned into areas that were weaker due to features such as pre-existing fabrics, finer grain sizes, retrogressed minerals and the presence of melt. This resulted in the narrow and localised shear zones seen across the field area. The Nupskåpa cliff is not located in such a shear zone and so only represents M_1 fabric formation.

Cooling and exhumation following peak M_1 conditions may have involved melt fluxing through these rocks, from anatectic rocks at greater depth. The second-oldest melt phase (mapped in pink in Figure 3.3) shows sharp boundaries, some interconnectivity, and is less extensive over the outcrop than the older phase. The individual structures are generally discordant and some are at $\sim$90 °C to each other. This phase is clearly not fed by smaller leucosomes from within the host rock, and so represents melt intrusion after the period of initial *in situ* melting and melt segregation, and may be the result of melt produced at greater depths attempting to rise through these rocks. This phase is contained in relatively fine structures that form a pervasive network and so must have intruded when the rocks were close to, but likely below, the solidus. The narrow structures are not deformed in the Nupskåpa outcrop, but as this phase is not that extensive across the field area it is difficult to tell its cross-cutting relationship with the Pan-African shear zones. Thus this phase may represent either a post-peak M_1, or near-peak M_2 intrusion of melt into hot, but subsolidus, rocks.

The composite dykes form the third intrusive phase in the Nupskåpa outcrop. Through U-Pb SHRIMP dating of zircon, Board (2001) identified a late Pan-African age for these 'monzogranitic dykes'. These dykes are sub-vertical and highly discordant to the subhor-

izontal gneissic fabric in the host rocks. As they cross-cut shear zones (Figure 3.8), they must have intruded after the Pan-African thrusting event which confirms the post-tectonic age given to these dykes by Board *et al.* (2005). Older leucosome structures can be matched up across the width of individual dykes and show almost no shear displacement (maximum ∼30 cm), indicating that the dykes resulted from tensile fracture (Figure 2.4). This suggests that their intrusion occurred during extensional or strike-slip deformation, under conditions of low differential stress, probably coupled to high magma pressure. In the Nupskåpa area, the post-M_2 mineral assemblage records conditions of ∼575 °C at 4 kbar. The retrograde minerals represent late M_2 conditions, after the formation of the Pan-African shear zones (for more one the distribution of retrogression, see Sebetlela (2013)). The composite dykes are thought to have a similar age of intrusion and so these conditions are inferred to be the maximum physical conditions at which the dykes intruded. Based on an average crustal density of 2.8 g/cm^3, the metamorphic conditions of the country rock indicate a mid-crustal position, at a depth of ∼15 km, when the composite dykes intruded (Figure 6.4; Board *et al.*, 2005).

These dykes contain several phases of leucogranite with different mineralogies and textures. The different phases do not show consistent age relations, indicating the heterogeneity cannot be the result of successive melt batches pulsing through the same structures (a method suggested by Brown & Solar (1998a), Bons *et al.* (2004) and Brown (2013), amongst others). This implies that the source was extremely heterogeneous, and that the dykes were fed by compositionally different melt sources simultaneously. At the least, it implies that successive melt batches must have intruded before the previous batches had solidified or completely left the structure.

The composite dykes range between 0.5 and 2 m in width. At the base of the cliff, narrower dykes can be seen to coalesce and feed into the wider dykes (see Figures 3.3 and 3.7). This same process must have occurred several times before, below the level of this outcrop, in order for contrasting melt phases to be contained in the same structure in such a disorganised way. It must be noted that the preserved widths of the intrusive features in the Nupskåpa Cliff are not necessarily the same as the width during melt transport through them, as large melt-bearing structures can lose melt and appear very thin (Clemens & Mawer, 1992; Brown, 1994; Bons *et al.*, 2004). It is also very hard to tell just how extensive these dykes were in strike direction at the time of melt flux. While it can be estimated from generalised aspect ratios (breadth-width-height, see Vermilye & Scholz (1995)), in the 2-dimensional outcrop

of the Nupskåpa cliff we can only measure the width (measured perpendicular to fracture wall) at the time of freezing. An assumption made in this study is that relative widths are preserved, such that the smaller dykes feeding into the larger ones showed similar size relationships during melt transport. Individual dykes show a similar lack of consistent age relations between the different leucogranite phases. Furthermore, where two dykes join up to make one, there does appear to be some mixing of the magmas from different sources. Thus it is assumed that together they represent a 'snapshot' in time, and that the majority of the dykes intruded near-simultaneously, rather than as separate events spread out over time.

The composite dykes show sharp, straight boundaries indicating that they formed as a result of melt intrusion rather than melt segregation from within this outcrop. They are mostly vertical, irrespective of the anastomosing sub-horizontal host rock fabric, and formed through tensile fracture with negligible vertical displacement of the host rock, implying that their intrusion was independent of existing anisotropies and occurred under low differential stress. They show little interconnectivity, at least in the view displayed by the Nupskåpa Cliff, and are fed by smaller dykes at the base of the cliff. Therefore they do not represent a network of *in situ* melt, but rather the far-field transport of melt from a spatially removed source, anywhere from 5 to 15 km below this outcrop (Board, 2001). These features are characteristic of a focused migration style.

The composite dykes are found right across the field area, and even beyond it in the more eastern parts of H.U. Sverdrupfjella (Board, 2001). The numerous dykes are commonly not more than a few metres apart. Thus, although individually they are discrete and focused structures, together they do not represent a wholly focused melt transfer system. Furthermore, based on P-T estimates, the dykes appear to have intruded into a mid-crustal location, and therefore into a likely position where the transition from pervasive to focused migration can be expected to occur.

The numerical model produced by Bons *et al.* (2004) describes a way in which melt migration may become more focused through a gradual coarsening of the melt network. In this model melt moves from the grain boundaries where it is first formed into discrete batches that make up veins. These veins grow larger as they are fed by more melt. Eventually neighbouring veins may coalesce to make larger melt batches. As the melt volume increases, buoyancy forces become greater and melt begins to move upward along steep veins. Eventually veins are large enough to move through the crust without freezing and leave the system as dykes. In this model, mixing and mingling of magmas occurs throughout the hierarchical accumulation and

ascent system, as smaller batches gradually join up to make larger ones (Bons *et al.*, 2004). This could be seen as a hybrid version of the two end-members of mixing and mingling outlined by Collins *et al.* (2000), i.e. mixing and mingling does not take place solely in the source or in the final emplacement structure but rather throughout the process of melt migration.

Similarly, the numerical modelling of dykes in low-viscosity asthenosphere below mid-ocean ridges, performed by Ito & Martel (2002), showed that neighbouring dykes create distortions in the local stress field that can be attractive or repulsive according to vertical and horizontal spacing. Two adjacent dykes will tend to merge if they initiate within a few hundred metres of each other. This implies that smaller dykes, transporting separate melt batches parallel to each other, could gradually begin to interact and join up, combining the volume of melt and enabling the larger dyke to migrate further (Ito & Martel, 2002; Brown, 2013). This would result in a gradual 'coarsening' of the melt network, with smaller melt structures feeding into fewer, larger ones (see Figure 1.1).

The study performed by Ito & Martel (2002) did not address the potential for interaction of dykes in the continental crust. However, at the base of the Nupskåpa cliff (and higher up on the western side of the cliff) narrow dykes can be seen to coalesce and form wider ones (Figure 3.7). If we assume that the relative widths along the length of the dykes were preserved, this coalescing might be an example of the melt-focusing mechanism described by the models of Bons *et al.* (2004) and Ito & Martel (2002). The vertical length of a dyke is dependent on the aperture (width perpendicular to fracture wall) and wider dykes containing more melt will be able to propagate further (Weertman, 1971; Clemens & Mawer, 1992). Dykes containing more melt also contain more heat and so would be able to intrude cooler country rock without freezing.

This model of gradual focusing of the melt network also explains how the dykes came to be composite and contain multiple melt phases simultaneously. Mixing and mingling of magmas occurred during melt migration, rather than only in the source or final emplacement structure. As dykes carrying different melt batches (from laterally and horizontally dispersed sources) coalesced, the different melt batches were mixed together. If this is the case, the transition from pervasive to focused migration appears to be a gradual one, with smaller structures joining up to make larger ones which can propagate further due to the increased melt volume now contained within them. The composite dykes in the Nupskåpa area would then represent a 'mostly-focused' melt network. The melt was no longer moving in a pervasive

style, but was not yet completely focused either, resulting in the numerous, closely spaced composite dykes seen across the field area. Above the Nupskåpa cliff, the dykes may in turn have joined up to make even fewer, wider structures which eventually could have fed a pluton. For instance, the two composite dykes on the far western side of the cliff face are only 2 metres apart at the top of the cliff, and above this height may well have joined up to make a single wider dyke. However, there is no outcrop directly above this cliff and so no clear indication as to whether or not they did coalesce above it.

Based on the composite dyke phase seen in the Nupskåpa area, a hybrid style of melt migration can be envisaged for the mid-crust, which incorporates characteristics of both pervasive and focused melt migration. Melting occurs at depths anywhere between 20 and 70 km (Brown *et al.*, 2011; Sawyer *et al.*, 2011). Melt segregation and accumulation begins in the near-source region, eventually forming a pervasive melt network made up of small (cm-scale) structures that are highly interconnected (much like the earliest M_1 leucosome phase seen in the Nupskåpa cliff). As the melt migrates higher, the smaller structures of this network gradually join up to make larger structures. This results in smaller melt batches coalescing into larger ones, which allows the melt fractures to having a larger maximum aspect ratio, and therefore a larger maximum vertical length (Weertman, 1971; Clemens & Mawer, 1992; Vermilye & Scholz, 1995). Longer, wider structures can then transport melt further. As the melt network moves higher, it gradually becomes more focused with larger structures that are less interconnected, at some point resulting in the situation seen in the Nupskåpa cliff. Above this structural level, the 0.5–2 m wide dykes perhaps in turn joined up to form even larger structures, which may have eventually fed into a pluton. A schematic diagram of how the full melt network might look is presented in Figure 6.5.

This scenario assumes that by the time the migrating melt reaches subsolidus country rock it has coalesced into large enough volumes to be able to continue moving through colder rock without freezing. This hybrid style does not preclude the occasional stage of melt accumulation at deeper levels in the network, such as that described by Diener *et al.* (2014). It must be noted that the composite dykes may also represent a 'failed attempt' by the magma to move through the host rock. While the flow structures created by the different phases and alignment of biotite in the rocks do seem to indicate that there was significant movement of the magma within these structures, it is impossible to tell from this outcrop whether the major movement was upwards or laterally (i.e. perpendicular to the cliff surface). Some fraction of the magma volume must have remained trapped in the outcrop, otherwise they

would simply be present as fractures rather than felsic dykes.

The lack of any significant shearing of the country rocks around the composite dykes is indicative of low differential stress at the time of emplacement. The dykes appear to have resulted from tensile fracture, which requires low differential stress (Etheridge, 1983). Perhaps if differential stress had been higher, melt-lubricated shear zones may have formed instead (Brown & Solar, 1998b) which would result in a different style of melt migration in the mid-crust (Hollister & Crawford, 1986; Brown & Solar, 1998b; Handy *et al.*, 2001). Thus the lack of any major differential stress is necessary in order for this hybrid style to operate.

In the Nupskåpa area, the composite dykes can be seen to cross-cut several different rock types, apparently irrespective of any potential strength variations that might have resulted from variations in grain size, mineralogy, fluid content or pre-existing foliations (Figure 2.4; Brown & Solar, 1998a). This could indicate that the intrusion occurred when the rocks were cool enough to be isotropic with regard to strength, so that pre-existing foliations and variations in rock type were not important, or the subhorizontal fabric was poorly oriented for the buoyant, upward flow, and so was not utilized by the melt. It could also indicate that the melt pressure in the dyke structures was high enough to form tensile fractures across rocks with variable strength (it may well have been the result of a combination of all three).

The last intrusive phase seen in the Nupskåpa outcrop is a pegmatitic leucogranite phase, which has intruded in several orientations. Some pegmatitic dykes are vertical and discordant, while others are subhorizontal, and exploit the weakness of the host-rock fabric, as can be seen in Figure 3.11. The pegmatitic phase appears to have intruded under somewhat different conditions to the intrusion of the composite dyke phase, as their orientations are different. The pegmatitic phase can be seen to intrude parallel to the gneissic fabric of the host rock, as well as subvertically and discordant to the fabric. As the pegmatitic phase intruded after the composite phase, the difference in orientation between the two is likely the result of the host rocks sitting at shallower depths. With less depth and therefore less overburden, lower melt pressure would be required for horizontal flow to occur. The differences in orientation may also have resulted from a combination of changes in melt pressure, differential stress and the orientation of the pre-existing weaknesses relative to the principle stresses. The pegmatitic phase may also represent more than one intrusive event, with the more concordant features having intruded under different conditions to the vertical ones (alhough there is no clear mineralogical distinction between dykes with different orientations).

6.4 Implications for far-field melt transfer

The Nupskåpa cliff represents an example of melt migration under mid-crustal conditions. Melt transport appears to have occurred in numerous focused structures, that are spaced up to 10 m apart and together form a pervasive intrusion of the country rock. The cliff also indicates how melt accumulation can occur during transport and ascent in dyke-like structures. Accumulation occurs via a gradual or step-wise process with smaller dykes coalescing and feeding into larger dykes, which can exist parallel to each other for several tens or hundreds of metres but may eventually join up to make larger structures.

This study shows an example of melt migration very different to the example described by Diener *et al.* (2014). In the Aus granulite terrain in southern Namibia, these authors report evidence of melt redistribution and accumulation occurring in the suprasolidus near-source region. The implication of this is that melt batches entering the subsolidus crust would be relatively large (on the order of several 10s of m^3) and would already consist of several smaller melt batches with differing compositions. The transition from pervasive to focused migration is thought to occur in the near-source region, with large dykes initiating from the large batches of accumulated melt (Rubin, 1995; Diener *et al.*, 2014). Larger propagating dykes would be less likely to become trapped by obstacles and further accumulation of melt during ascent would not be required (Diener *et al.*, 2014).

The style of melt migration represented by the composite dykes in the Nupskåpa area seems instead to have involved a gradual transition from pervasive to focused migration, with intermittent accumulation occurring during transport. Smaller dyke structures coalesce into larger ones, resulting in the mixing of melt batches en route. This reduces the need for, but does not preclude, substantial accumulation in the near-source region.

The composite nature of the dykes indicates that the melt within them came from multiple source areas, or a heterogeneous source. Whether these areas are distributed laterally or vertically in space is hard to tell, but it is likely a combination of both (Figure 6.5). The lack of consistent relative age relations amongst the different phases implies that the different melt batches were contained simultaneously, not in separate pulses of different compositions. Researchers (e.g Weertman, 1971; Bons *et al.*, 2001, 2004; Brown, 2013) have suggested that dykes are kept open by successive melt pulses, but this does not appear necessary for the Nupskåpa composite dykes. They appear to have had different melt phases moving through them simultaneously, resulting in the disorganised leucosome phases now seen in the cliff. As

the dykes are thought to have intruded at temperatures significantly below the solidus, it is unlikely that the different phases resulted from separate pulses of melt, with some of each phase staying liquid long enough to mix with successive melt pulses within the dyke.

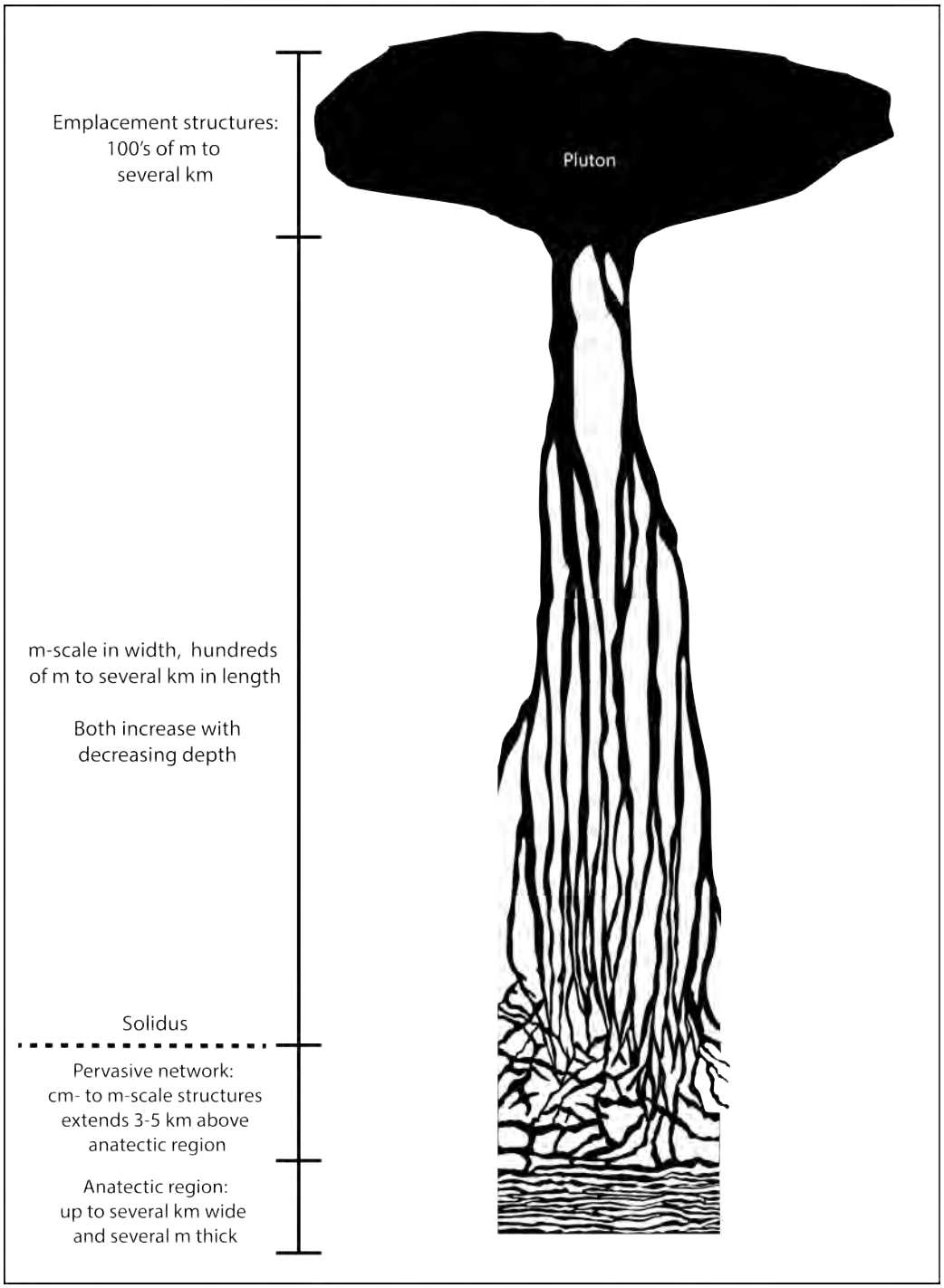

Figure 6.5: An idealised crustal-scale melt migration network, suggested by the composite dyke phase in the Nupskåpa area. Scale of melt-bearing structures indicated on left side.

6.5 Conclusions

The samples taken from the Nupskåpa area show evidence of two equilibrium mineral assemblages. The 'peak' assemblage records metamorphic conditions of 820–880 °C at 9.5–11.6 kbar. These granulite facies conditions are more than 100 °C higher than the Pan-African peak conditions. They are much closer to the Grenvillian conditions identified in other parts of H.U. Sverdrupfjella and the rest of the Maud Belt (Grantham *et al.*, 1995; Groenewald *et al.*, 1995; Board *et al.*, 2005). The area also preserves retrograde mineral assemblages, which record metamorphic conditions of 555–595 °C at 3.2–4.8 kbar. As this assemblage is preserved in these rocks it must post-date the last metamorphic event to have had temperatures greater than 595 °C , otherwise a higher grade assemblage would be recorded instead. Because the retrograde minerals show no preferred orientation, and based on dating by other researchers, the retrograde conditions are interpreted as having a post-tectonic Pan-African age (Board, 2001). These late M_2 conditions lie between the wet solidus and brittle-viscous transition and indicate a mid-crustal location, and the most likely conditions under which the composite dykes were intruded. No direct evidence was found in the Nupskåpa area for Pan-African eclogite-facies conditions, as reported by Board (2001), although early Grenvillian metamorphism may potentially have involved high-pressure granulite facies conditions.

The Nupskåpa cliff shows evidence of multiple phases of melt intrusion. The oldest is a concordant leucosome phase which is interpreted to represent initial melting and melt segregation during M_1 granulite-facies metamorphism. Younger, subvertical composite dykes which cross-cut granulite fabric and concordant leucosome appear to have contained multiple leucogranitic melt phases simultaneously. Melt migration through these structures is thought to have occurred via tensile fracturing of the host rock, under conditions of low differential stress and after the period of low-angle Pan-African thrusting had ceased to operate. It is likely that melt pressure was sufficiently high to enable tensile fractures to propagate across rocks of different grain size and composition, apparently irrespective of variations in strength between the different rock types. The final intrusive phase is a pegmatitic leucogranite which occurs in subvertical discordant structures as well as concordant structures that appear to have exploited the subhorizontal foliation of the host rock. This phase is inferred to have intruded at shallower conditions, and therefore lower pressures than the composite dyke phase

The composite dykes are inferred to represent an example of a gradual transition from pervasive to focused migration. This transition appears to have occurred in the mid-crust, at

subsolidus temperatures, after the melt phases had been transported an estimated 5–15 km from the source. This transition involves a network of smaller melt-filled fractures gradually coalescing into larger ones which can then propagate further due to the increase in melt volume (and therefore increased aperture as well as increased melt pressure). These larger fractures may in turn have joined up at levels above this outcrop to make major dykes which ultimately fed into emplacement structures at higher crustal levels. If pervasive migration becomes focused via this gradual transition, melt accumulation and mixing need not occur solely in the source or final emplacement structure, but rather occurs throughout transport of the magma.

References

Anderson, E. M., 1951. *The Dynamics of Faulting and Dyke Formation with Applications to Britain*, Oliver & Boyd.

Arndt, N., Todt, W., Chauvel, C., Tapfer, M. & Weber, K., 1991. U-Pb zircon age and Nd isotopic composition of granitoids, charnockites and supracrustal rocks from Heimefrontfjella, Antarctica. *Geologische Rundschau*, **80**, 759–777.

Bateman, R., 1984. On the mechanics of igneous diapirism, stoping, and zone-melting - comment. *American Journal of Science*, **284**(8), 979–980.

Beaumont, C., Jamieson, R., Butler, J. & Warren, C., 2009. Crustal structure: A key constraint on the mechanism of ultra-high-pressure rock exhumation. *Earth and Planetary Science Letters*, **287**, 116–129.

Bisnath, A. & Frimmel, H. E., 2005. Metamorphic evolution of the Maud Belt: PTt path for high-grade gneisses in Gjelsvikfjella, Dronning Maud Land, East Antarctica. *Journal of African Earth Sciences*, **43**, 505–524.

Bisnath, A., Frimmel, H. E., Armstrong, R. A. & Board, W. S., 2006. Tectono-thermal evolution of the Maud Belt: New SHRIMP U-Pb zircon data from Gjelsvikfjella, Dronning Maud Land, East Antarctica. *Precambrian Research*, **150**(1-2), 95–121.

Board, W. S., 2001. *Tectonothermal evolution of the Southern H.U. Sverdrupfjella, Western Dronning Maud Land, Antarctica*. PhD thesis, University of Cape Town.

Board, W. S., Frimmel, H. & Armstrong, R., 2005. Pan-African Tectonism in the Western Maud Belt: P-T-t Path for High-grade Gneisses in the H.U. Sverdrupfjella, East Antarctica. *Journal of Petrology*, **46**, 671–699.

Bons, P. D., Arnold, J., Elburg, M. A., Kaldad, J., Soesoo, A. & van Milligen, B. P., 2004. Melt extraction and accumulation from partially molten rocks. *Lithos*, **78**, 25–42.

Bons, P. D., Druguet, E., Castano, L.-M. & Elburg, M. A., 2008. Finding what is now not there anymore: Recognizing missing fluid and magma volumes. *Geology*, **36**(11), 851–854.

Bons, P., Dougherty-Page, J. & Elburg, M., 2001. Stepwise accumulation and ascent of magmas. *Journal of Metamorphic Geology*, **19**(5), 625–631.

Brown, M., 1994. The generation, segregation, ascent and emplacement of granite magma - The migmatite-to-crustally-derived-granite connection in thickened orogens. *Earth-Science Reviews*, **36**, 83–130.

Brown, M., 2004. The mechanism of melt extraction from lower continental crust of orogens. *Transactions of the Royal Society of Edinburgh: Earth Sciences*, **95**(1-2), 35–48.

Brown, M., 2010. Melting of the continental crust during orogenesis: the thermal, rheological, and compositional consequences of melt transport from lower to upper continental crust. *Canadian Journal of Earth Sciences*, **47**, 655–694.

Brown, M., 2013. Granite: From genesis to emplacement. *Geological Society of America Bulletin*, **125**(7-8), 1079–1113.

Brown, M. & Solar, G., 1998a. Granite ascent and emplacement during contractional deformation in convergent orogens. *Journal of Structural Geology*, **20**, 1365–1393.

Brown, M. & Solar, G., 1998b. Shear-zone systems and melts: feedback relations and self-organization in orogenic belts. *Journal of Structural Geology*, **20**, 221–227.

Brown, M. & Solar, G., 1999. The mechanism of ascent and emplacement of granite magma during transpression: a syntectonic granite paradigm. *Tectonophysics*, **312**, 1–33.

Brown, M., Korhonen, F. J. & Siddoway, C. S., 2011. Organizing Melt Flow through the Crust. *Elements*, **7**, 261–266.

Clemens, J. & Mawer, C., 1992. Granitic magma transport by fracture propagation. *Tectonophysics*, **204**, 339–360.

Clemens, J. & Vielzeuf, D., 1987. Constraints on melting and magma production in the crust. *Earth and Planetary Science Letters*, **86**, 287–306.

Clemens, J., Petford, N. & Mawer, C., 1997. Ascent mechanisms of granitic magmas: causes and consequences.. In: *Deformation-enhanced Fluid Transport in the Earth's Crust and Mantle*, (ed. Holness, M. B.), pp. 145–172. Chapman & Hall for the Mineralogical Society Series.

Coggon, R. & Holland, T. J. B., 2002. Mixing properties of phengitic micas and revised garnet–phengite thermobarometers. *Journal of Metamorphic Geology*, **20**, 683–696.

Collins, W. & Sawyer, E., 1996. Pervasive granitoid magma transfer through the lower-middle crust during non-coaxial compressional deformation. *Journal of metamorphic Geology*, **14**(5), 565–579.

Collins, W. J., Richards, S. R., Healy, B. E. & Ellison, P. I., 2000. Origin of heterogeneous mafic enclaves by two-stage hybridisation in magma conduits (dykes) below and in granitic magma chambers. *Earth and Environmental Science Transactions of the Royal Society of Edinburgh*, **91**, 27–45.

Connolly, J. A. D. & Podladchikov, Y. Y., 2007. Decompaction weakening and channeling instability in ductile porous media: Implications for asthenospheric melt segregation. *Journal of Geophysical Research*, **112**, B10205.

Diener, J. F. A. & Powell, R., 2012. Revised activity–composition models for clinopyroxene and amphibole. *Journal of Metamorphic Geology*, **30**, 131–142.

Diener, J. F. A., Powell, R., White, R. W. & Holland, T. J. B., 2007. A new thermodynamic model for clino- and orthoamphiboles in the system Na_2O–CaO–FeO–MgO–Al_2O_3–SiO_2–H_2O–O. *Journal of Metamorphic Geology*, **25**, 631–656.

Diener, J. F., White, R. W. & Hudson, T. J., 2014. Melt production, redistribution and accumulation in mid-crustal source rocks, with implications for crustal-scale melt transfer. *Lithos*, **200-201**, 212–225.

Diener, J., White, R. & Powell, R., 2008. Granulite facies metamorphism and subsolidus fluid-absent reworking, Strangways Range, Arunta Block, central Australia. *Journal of Metamorphic Geology*, **26**, 603622.

Etheridge, M., 1983. Differential stress magnitudes during regional deformation and metamorphism - upper bound imposed by tensile fracturing. *Geology*, **11**(4), 231–234.

Faber, C., (2012). *Processes of felsic melt migration through the mid-crust: evidence from field relations in the central zone of the damara belt, namibia*, Master's thesis, University of Cape Town.

Fitzsimons, I., 2000a. A review of tectonic events in the East Antarctic Shield and their implications for Gondwana and earlier supercontinents. *Journal of African Earth Sciences*, **31**, 3–23.

Fitzsimons, I., 2000b. Grenville-age basement provinces in East Antarctica: Evidence for three separate collisional orogens. *Geology*, **28**(10), 879–882.

Grantham, G., 1992. *Geological evolution of western H.u. Sverdrupfje/la, Dronning Maud Land, Antarctica*. PhD thesis, University of Natal, Pietermaritzburg.

Grantham, G. H., Jackson, C., Moyes, A. B., Groenewald, P. B., Harris, P. D., Ferrar, G. & Krynauw, J. R., 1995. The tectonothermal evolution of the KirwanveggenH.U. Sverdrupfjella areas, Dronning Maud Land, Antarctica. *Precambrian Research*, **75**, 209–229.

Grantham, G.H., G. P. & Hunter, D., 1988. Geology of the northern h.u. sverdrupfjella, western dronning maud land, and implications for gondwana reconstructions. *South African Journal of Antarctic Research*, **18**, 2–10.

Green, E. C. R., Holland, T. J. B. & Powell, R., 2007. An order–disorder model for omphacitic pyroxenes in the system jadeite–diopside–hedenbergite–acmite, with applications to eclogitic rocks. *American Mineralogist*, **92**, 1181–1189.

Groenewald, P. B. & Hunter, D. R., 1991. Granulites of the northern H.U. Sverdrupfjella, western Dronning Maud Land: Metamorphic history from garnetpyroxene assemblages, coronas and hydration reactions. In: *Geological Evolution of Antarctica.*, (eds Thomson, M. R. A., Crame, J. A. & Thomson, J. W.). Cambridge University Press.

Groenewald, P. B., Moyes, A. B., Grantham, G. H. & Krynauw, J. R., 1995. East Antarctic crustal evolution: Geological constraints and modelling in western Dronning Maud Land. *Precambrian Research*, **75**, 231–250.

Groenewald, P., Grantham, G. & Watkeys, M., 1991. Geological evidence for a Proterozoic to Mesozoic link between Southeastern Africa and Dronning Maud Land, Antarctica. *Journal of the Geological Society*, **148**(6), 1115–1123.

Hall, D. & Kisters, A., 2012. The stabilization of self-organised leucogranite networksImplicationsfor melt segregation and far-field melt transfer in the continental crust. *Earth and Planetary Science Letters*, **355-356**, 1–12.

Handy, M., Braun, J., Brown, M., Kukowski, N., Paterson, M., Schmid, S., Stockhert, B., Stuwe, K., Thompson, A. & Wosnitza, E., 2001. Rheology and geodynamic modelling: the next step forward. *International Journal of Earth Sciences*, **90**(1), 149–156.

Harris, C. & Grantham, G., 1993. Geology and petrogenesis of the Straumsvola nepheline syenite complex, Dronning Maud Land, Antarctica. *Geological Magazine*, **130**, 523–532.

Harris, P., Moyes, A., Fanning, C. & Armstrong, R., 1995. Zircon ion microprobe results from the Maudheim high-grade gneiss terrane, western Dronning Maud Land, Antarctica. *Extended Abstracts, Centennial Geocongress, Rand Afrikaans University, Johannesburg, South Africa*, pp. 240–243.

Harrison, T. & Fitzgerald, J., 1986. Exsolution in hornblende and its consequences for ^{40}Ar–^{39}Ar age spectra and closure temperature. *Geochimica et Cosmochimica Acta*, **50**, 247–253.

Hjelle, A., 1974. Some observations on the geology of the H.U. Sverdrupfjella, Dronning Maud Land, Antarctica. *Norsk Polarinstitutt.*, **Arbor 1972**, 7–22.

Holland, T. J. B. & Powell, R., 1998. An internally consistent thermodynamic dataset for phases of petrological interest. *Journal of Metamorphic Geology*, **16**, 309–343.

Holland, T. J. B. & Powell, R., 2003. Activity–composition relations for phases in petrological calculations: an asymmetric multicomponent formulation. *Contributions to Mineralogy and Petrology*, **145**, 492–501.

Holland, T. J. B., Baker, J. M. & Powell, R., 1998. Mixing properties and activity–composition relationships of chlorites in the system MgO–FeO–Al_2O_3–SiO_2–H_2O . *European Journal of Mineralogy*, **10**, 395–406.

Hollister, L. S. & Crawford, M. L., 1986. Melt-enhanced deformation: A major tectonic process. *Geology*, **14**, 558–561.

Ito, G. & Martel, S., 2002. Focusing of magma in the upper mantle through dike interaction. *Journal Of Geophysical Research-Solid Earth*, **107**(B10).

Jamieson, R. & Beaumont, C., 2011. Coeval thrusting and extension during lower crustal ductile flow implications for exhumation of high-grade metamorphic rocks. *Journal of metamorphic Geology*, **29**, 33–51.

Kisters, A., Ward, R., Anthonissen, C. & Vietze, M., 2009. Melt segregation and far-field melt transfer in the mid-crust. *Journal of the Geological Society*, **166**, 905–918.

Leitch, A. & Weinberg, R., 2002. Modelling granite migration by mesoscale pervasive flow. *Earth and Planetary Science Letters*, **200**(1-2), 131–146.

Lister, J. & Kerr, R., 1991. Fluid-mechanical models of crack-propagation and their application to magma transport in dykes. *Journal of Geophysical Research*, **96**(B6), 10049–10077.

Mahon, K., Harrison, T. & Drew, D., 1988. Ascent of a granitoid diapir in a temperature varying medium. *Journal of Geophysical Research*, **B93**, 1174–1188.

Marsh, B. D., 1982. On the mechanics of igneous diapirism, stoping and zone melting. *American Journal of Science*, **282**, 808–855.

McGibbon, D., 2014. *Shear Zones of the Maud Belt, Antarctica: Kinematics and Deformation Mechanisms*. PhD thesis, University of Cape Town.

McNulty, B., Tobisch, O. T., Cruden, A. R. & Gilder, S., 2000. Multistage emplacement of the Mount Givens pluton, central Sierra Nevada batholith, California. *Geological Society of America Bulletin*, **112**, 119–135.

Morfin, S., Sawyer, E. W. & Bandyayera, D., 2013. Large volumes of anatectic melt retained in granulite facies migmatites: An injection complex in northern Quebec. *Lithos*, **168**, 200–218.

Ohta, Y., (1996). 1996: Nature environment map, h.u. sverdrupfjella 1:150000, *Technical report*, Norsk Polarinstitutt Temakart Nr. 28.

Paterson, S. & Vernon, R., 1995. Bursting the bubble of ballooning plutons - a return to nested diapirs emplaced by multiple processes. *Geological Society of America Bulletin*, **107**(11), 1356–1380.

Paterson, S. R. & Fowler, T., 1993. Re-examining pluton emplacement processes. *Journal of Structural Geology*, **15**, 191–206.

Paulsson, O. & Austrheim, H., 2003. A geochronological and geochemical study of rocks from Gjelsvikfjella, Dronning Maud Land, Antarctica - implications for Mesoproterozoic correlations and assembly of Gondwana. *Precambrian Research*, **125**(1-2), 113–138.

Petford, N., 1996. Dykes or Diapirs? *Transactions of the Royal Society of Edinburgh: Earth Sciences*, **87**, 105–114.

Petford, N., Kerr, R. & Lister, J., 1993. Dike transport of granitoid magmas. *Geology*, **21**(9), 845–848.

Petford, N., Lister, J. & Kerr, R., 1994. The ascent of felsic magmas in dykes. *Lithos*, **32 (1-2)**, 161–168.

Reichardt, H. & Weinberg, R. E., 2012. The dike swarm of the Karakoram shear zone, Ladakh, NW India: Linking granite source to batholith. *Geological Society of America Bulletin*, **124**(1-2), 89–103.

Rubin, A., 1995. Propagation of magma-filled cracks. *Annual Review of Earth And Planetary Sciences*, **23**, 287–336.

Sawyer, E. W., 1994. Melt Segregation in the continental crust. *The Geological Society of America*, **22**, 1019–1022.

Sawyer, E. W., Cesare, B. & Brown, M., 2011. When the Continental Crust Melts. *Elements*, **7**, 220–234.

Schulmann, K., Lexa, O., Stipska, P., Racek, M., Tajcmanova, L., Konopasek, J., Edel, J., Peschler, A. & Lehmann, J., 2008. Vertical extrusion and horizontal channel flow of orogenic lower crust: key exhumation mechanisms in large hot orogens? *Journal of Metamorphic Geology*, **26**, 273–297.

Sebetlela, T., (2013). *Geometry and deformation mechanisms of a polydeformed retrograde shear zone of the Maud Belt, Antarctica*, Honours thesis, University of Cape Town.

Sleep, N., 1988. Tapping of melt by veins and dikes. *Journal of Geophysical Research*, **93**(B9), 10255–10272.

Spear, F. S., 1995. *Metamorphic Phase Equilibria And Presure-Temperature-Time-Paths*, Mineralogical Society of America Monograph.

Stevens, G., Clemens, J. & Droop, G. T., 1997. Melt production during granulite-facies anatexis: experimental data from 'primitive' metasedimentary protoliths. *Contributions to Mineralogy and Petrology*, **128**, 352–370.

Sweeney, J., 1975. Diapiric granite batholiths in south-central Maine. *American Journal of Science*, **275**(10), 1183–1191.

Vanderhaeghe, O., 2001. Melt Segregation, Pervasive Melt Migration and Magma Mobility in the Continental Crust: The Structural Record from Pores to Orogens. *Physics and Chemistry of the Earth*, **26**, 213–223.

Vermilye, J. M. & Scholz, C. H., 1995. Relation between vein length and aperture. *Journal of Structural Geology*, **17**, 423–434.

Vernon, R. H. & Paterson, S. R., 2001. Axial-surface leucosomes in anatectic migmatites. *Tectonophysics*, **335.**, 183–192.

Vielzeuf, D. & Schmidt, M., 2001. Melting relations in hydrous systems revisited: application to metapelites, metagreywackes and metabasalts. *Contributions to Mineralogy and Petrology*, **141**, 251–267.

Vigneresse, J. L., 2006. Granitic batholiths: from pervasive and continuous melting in the lower crust to discontinuous and spaced plutonism in the upper crust. *Transactions of the Royal Society of Edinburgh: Earth Sciences*, **97**, 311–324.

Weertman, J., 1971. Theory of water-filled crevasses in glaciers applied to vertical magma transport beneath oceanic ridges. *Journal of Geophysical Research*, **76**, 1171–1183.

Weinberg, R. & Podladchikov, Y., 1994. Diapiric ascent of magmas through power law crust and mantle. *Journal of Geophysical Research*, **99**, 9543–9559.

Weinberg, R. F., 1996. Ascent of felsic magmas: news and reviews. *Transactions of the Royal Society of Edinburgh: Earth Sciences*, **87**, 95–103.

Weinberg, R. F., 1999. Mesoscale pervasive felsic magma migration: alternatives to dyking. *Lithos*, **46**, 393–410.

Weinberg, R. F. & Regenauer-Lieb, K., 2010. Ductile fractures and magma migration from source. *Geology*, **38**(4), 363–366.

White, R. & Powell, R., 2002. Melt loss and the preservation of granulite facies mineral assemblages. *Journal of Metamorphic Geology*, **20**, 621632.

White, R., Powell, R. & Halpin, J., 2004. Spatially-focussed melt formation in aluminous metapelites from Broken Hill, Australia. *Journal of Metamorphic Geology*, **22**, 825845.

White, R. W., Powell, R. & Clarke, G. L., 2002. The interpretation of reaction textures in Fe-rich metapelitic granulites of the Musgrave Block, central Australia: constraints from mineral equilibria calculations in the system K_2O–FeO–MgO–Al_2O_3–SiO_2–H_2O–TiO_2–Fe_2O_3. *Journal of Metamorphic Geology*, **20**, 41–55.

White, R. W., Powell, R. & Holland, T. J. B., 2007. Progress relating to calculation of partial melting equilibria for metapelites. *Journal of Metamorphic Geology*, **25**, 511–527.

White, W., Powell, R., Holland, T. J. B. & Worley, B. A., 2000. The effect of TiO_2 and Fe_2O_3 on metapelitic assemblages at greenschist and amphibolite facies conditions: mineral equilibria calculations in the system K_2O–FeO–MgO–Al_2O_3–SiO_2–H_2O–TiO_2–Fe_2O_3. *Journal of Metamorphic Geology*, **18**, 497–511.

Whitney, P. R. & McLelland, J. M., 1983. Origin of Biotite-Hornblende-Garnet Coronas between Oxides and Plagioclase in Olivine Metagabbros, Adirondack Region, New York. *Contributions to Mineralogy and Petrology*, **82**, 34–41.

Appendix A

Electron microprobe tables

Table A.1: Electron microprobe results for garnet in all samples

	S01-1	**S01-2**	**S01-3**	**S01-4**	**S01-5**	**S01-6**	**S01-7**	**S01-8**	**S01-9**	**S01-10**	**S01-11**	**S01-12**	**S01-13**
SiO_2	38.85	37.31	37.41	37.69	37.40	37.57	36.67	36.55	46.29	36.77	36.88	36.75	36.52
TiO_2	0.06	0.04	0.05	0.03	0.01	0.09	0.08	0.05	0.00	0.02	0.04	0.06	0.07
Al_2O_3	18.88	21.80	22.02	22.30	21.80	22.04	21.69	21.81	5.45	21.95	22.00	21.91	21.63
Cr_2O_3	0.02	0.00	0.01	0.00	0.03	0.04	0.06	0.00	0.00	0.02	0.01	0.00	0.02
FeO	32.95	32.44	31.25	29.29	31.47	30.37	33.05	32.54	35.26	32.12	32.07	32.04	32.99
MnO	1.42	1.49	1.31	1.15	1.37	1.24	1.79	1.71	0.74	1.71	1.58	1.50	1.60
MgO	4.11	2.54	3.15	3.15	2.71	3.11	2.13	2.40	11.60	2.27	2.53	2.70	2.21
CaO	6.26	6.48	7.28	9.07	7.67	8.01	6.59	6.84	1.67	7.37	7.04	6.82	6.90
Na_2O	0.06	0.02	0.01	0.02	0.03	0.00	0.04	0.03	0.00	0.08	0.04	0.03	0.06
Total	102.61	102.13	102.50	102.70	102.49	102.47	102.10	101.93	101.01	102.32	102.19	101.81	102.00
Oxygens	24	24	24	24	24	24	24	24	24	24	24	24	24
Si	6.10	5.88	5.85	5.85	5.86	5.86	5.82	5.80	7.34	5.80	5.81	5.81	5.80
Ti	0.01	0.01	0.01	0.00	0.00	0.01	0.01	0.01	0.00	0.00	0.00	0.01	0.01
Al	3.49	4.05	4.06	4.08	4.03	4.05	4.05	4.08	1.02	4.08	4.09	4.08	4.05
Cr	0.00	0.00	0.00	0.00	0.00	0.00	0.01	0.00	0.00	0.00	0.00	0.00	0.00
Fe	4.33	4.27	4.08	3.80	4.12	3.96	4.38	4.32	4.67	4.24	4.23	4.24	4.38
Mn	0.19	0.20	0.17	0.15	0.18	0.16	0.24	0.23	0.10	0.23	0.21	0.20	0.22
Mg	0.96	0.60	0.73	0.73	0.63	0.72	0.50	0.57	2.74	0.53	0.59	0.64	0.52
Ca	1.05	1.09	1.22	1.51	1.29	1.34	1.12	1.16	0.28	1.25	1.19	1.16	1.17
Na	0.02	0.01	0.00	0.01	0.01	0.00	0.01	0.01	0.00	0.02	0.01	0.01	0.02
Total	16.15	16.10	16.12	16.12	16.13	16.11	16.15	16.16	16.15	16.16	16.14	16.14	16.17

...continued on next page

Table A.1 **Garnet** – continued from previous page

	S01-14	**S01-15**	**S01-16**	**S01-17**	**S01-18**	**S01-19**	**S10-2**	**S10-3**	**S10-4**	**S10-5**	**s52-1**	**s52-2**	**s52-3**
10pt **SiO_2**	36.61	46.29	35.72	35.76	47.14	35.96	35.45	35.82	36.07	36.05	40.35	39.94	39.69
TiO_2	0.08	0.04	0.06	0.00	0.06	0.12	0.13	0.09	0.05	0.04	0.09	0.05	0.03
Al_2O_3	21.98	4.02	21.83	21.69	1.16	21.11	21.13	21.11	20.93	21.46	21.84	21.56	21.50
Cr_2O_3	0.00	0.01	0.00	0.00	0.00	0.01	0.02	0.00	0.02	0.04	0.00	0.01	0.02
FeO	32.80	37.30	33.10	34.17	38.92	28.82	27.95	27.86	28.01	25.18	29.91	30.05	27.67
MnO	1.39	0.67	1.69	1.67	0.59	1.29	1.66	1.99	2.02	5.94	1.13	0.71	3.39
MgO	2.42	11.15	2.13	2.27	11.82	1.75	1.55	1.75	1.81	1.00	1.70	1.95	0.85
CaO	6.85	1.10	6.90	5.65	0.53	11.55	11.42	11.22	11.23	10.18	9.71	10.04	10.39
Na_2O	0.06	0.03	0.01	0.00	0.05	0.04	0.10	0.07	0.04	0.11	0.01	0.10	0.00
Total	102.19	100.60	101.44	101.22	100.28	100.65	99.41	99.91	100.17	100.00	104.73	104.41	103.54
Oxygens	24	24	24	24	24	24	24	24	24	24	24	24	24
Si	5.79	7.44	5.72	5.75	7.66	5.77	5.75	5.78	5.81	5.82	6.12	6.08	6.11
Ti	0.01	0.00	0.01	0.00	0.01	0.01	0.02	0.01	0.01	0.00	0.01	0.01	0.00
Al	4.10	0.76	4.12	4.11	0.22	3.99	4.04	4.01	3.97	4.08	3.90	3.87	3.90
Cr	0.00	0.00	0.00	0.00	0.00	0.00	0.00	0.00	0.00	0.01	0.00	0.00	0.00
Fe	4.34	5.01	4.43	4.59	5.29	3.86	3.79	3.76	3.77	3.40	3.79	3.83	3.56
Mn	0.19	0.09	0.23	0.23	0.08	0.17	0.23	0.27	0.28	0.81	0.14	0.09	0.44
Mg	0.57	2.67	0.51	0.54	2.86	0.42	0.38	0.42	0.43	0.24	0.38	0.44	0.19
Ca	1.16	0.19	1.18	0.97	0.09	1.98	1.99	1.94	1.94	1.76	1.58	1.64	1.71
Na	0.02	0.01	0.00	0.00	0.02	0.01	0.03	0.02	0.01	0.03	0.00	0.03	0.00
Total	16.16	16.18	16.21	16.20	16.23	16.23	16.23	16.21	16.21	16.15	15.93	15.99	15.93

...continued on next page

Table A.1 **Garnet** – continued from previous page

	s52-4	**s52-5**	**s52-6**	**s52-7**	**s52-9**	**s52-10**	**s64-1**	**s64-2**	**s64-3**	**s62-1**	**s62-2**	**s62-3**	**s62-4**
10pt **SiO_2**	39.83	39.99	37.47	37.38	37.02	36.27	36.77	36.92	36.48	35.41	35.15	34.50	39.33
TiO_2	0.05	0.07	0.08	0.06	0.03	0.04	0.02	0.04	0.03	0.03	0.03	0.00	0.00
Al_2O_3	21.69	21.66	21.79	21.90	21.46	21.44	21.99	22.05	21.74	22.03	21.97	21.81	21.44
Cr_2O_3	0.01	0.01	0.00	0.00	0.00	0.00	0.00	0.04	0.00	0.04	0.01	0.00	0.02
FeO	29.14	29.66	29.46	30.18	29.57	29.16	34.75	34.58	34.09	34.00	33.01	32.90	32.92
MnO	0.60	2.24	0.57	0.63	1.67	0.74	4.37	4.21	4.44	5.57	7.16	7.06	6.88
MgO	2.24	1.21	2.04	2.09	1.34	1.86	2.98	2.90	3.00	2.50	2.08	2.08	2.08
CaO	10.10	9.66	10.02	9.38	10.02	11.11	1.58	1.85	1.41	1.10	1.08	1.06	1.22
Na_2O	0.00	0.06	0.06	0.01	0.03	0.05	0.01	0.01	0.04	0.05	0.05	0.00	0.04
Total	103.66	104.56	101.50	101.63	101.14	100.67	102.47	102.59	101.23	100.73	100.54	99.41	103.93
Oxygens	24	24	24	24	24	24	24	24	24	24	24	24	24
Si	6.08	6.10	5.90	5.88	5.89	5.79	5.83	5.84	5.85	5.74	5.73	5.70	6.11
Ti	0.01	0.01	0.01	0.01	0.00	0.01	0.00	0.00	0.00	0.00	0.00	0.00	0.00
Al	3.90	3.89	4.04	4.06	4.02	4.04	4.11	4.11	4.11	4.21	4.22	4.25	3.93
Cr	0.00	0.00	0.00	0.00	0.00	0.00	0.00	0.00	0.00	0.01	0.00	0.00	0.00
Fe	3.72	3.78	3.88	3.97	3.93	3.90	4.61	4.57	4.57	4.61	4.50	4.54	4.28
Mn	0.08	0.29	0.08	0.08	0.22	0.10	0.59	0.56	0.60	0.77	0.99	0.99	0.91
Mg	0.51	0.28	0.48	0.49	0.32	0.44	0.70	0.68	0.72	0.60	0.51	0.51	0.48
Ca	1.65	1.58	1.69	1.58	1.71	1.90	0.27	0.31	0.24	0.19	0.19	0.19	0.20
Na	0.00	0.02	0.02	0.00	0.01	0.02	0.00	0.00	0.01	0.01	0.02	0.00	0.01
Total	15.96	15.95	16.08	16.08	16.10	16.19	16.11	16.10	16.10	16.15	16.16	16.18	15.93

...continued on next page

Table A.1 **Garnet** – continued from previous page

	s62-5	**s50-1**	**s50-2**	**s50-3**	**s50-4**	**s50-6**	**s50-7**	**s50-8**	**s50-9**	**s50-10**	**s55-1**	**s55-2**	**s55-3**
SiO_2	39.36	39.51	38.79	39.35	38.48	39.78	39.31	38.95	38.81	38.45	38.60	38.08	38.35
TiO_2	0.00	0.05	0.02	0.09	0.01	0.08	0.06	0.06	0.07	0.04	0.03	0.06	0.09
Al_2O_3	21.42	21.36	21.42	21.47	21.02	21.34	21.50	21.66	21.57	21.76	21.79	21.65	21.63
Cr_2O_3	0.01	0.01	0.00	0.01	0.06	0.00	0.03	0.00	0.00	0.04	0.00	0.00	0.05
FeO	32.87	29.82	30.46	29.37	29.59	29.59	30.21	29.41	30.36	29.41	30.54	29.78	30.62
MnO	6.53	0.73	2.03	0.52	2.23	0.49	1.81	0.63	1.64	0.65	0.60	2.60	0.83
MgO	2.32	2.34	1.21	2.50	1.05	2.53	1.17	2.45	1.49	2.57	2.34	1.18	1.92
CaO	1.12	9.55	9.09	9.70	9.02	9.80	9.27	9.67	9.04	9.74	9.41	9.37	9.62
Na_2O	0.05	0.00	0.04	0.05	0.10	0.01	0.03	0.06	0.01	0.04	0.02	0.02	0.04
Total	103.67	103.37	103.05	103.06	101.55	103.63	103.38	102.89	102.99	102.70	103.34	102.74	103.15
Oxygens	24	24	24	24	24	24	24	24	24	24	24	24	24
Si	6.12	6.07	6.04	6.06	6.07	6.09	6.08	6.01	6.03	5.96	5.96	5.96	5.95
Ti	0.00	0.01	0.00	0.01	0.00	0.01	0.01	0.01	0.01	0.00	0.00	0.01	0.01
Al	3.93	3.87	3.93	3.89	3.91	3.85	3.92	3.94	3.95	3.97	3.97	3.99	3.96
Cr	0.00	0.00	0.00	0.00	0.01	0.00	0.00	0.00	0.00	0.00	0.00	0.00	0.01
Fe	4.27	3.83	3.96	3.78	3.90	3.79	3.91	3.80	3.94	3.81	3.94	3.89	3.97
Mn	0.86	0.10	0.27	0.07	0.30	0.06	0.24	0.08	0.22	0.09	0.08	0.34	0.11
Mg	0.54	0.54	0.28	0.57	0.25	0.58	0.27	0.56	0.35	0.59	0.54	0.28	0.44
Ca	0.19	1.57	1.52	1.60	1.52	1.61	1.54	1.60	1.50	1.62	1.56	1.57	1.60
Na	0.01	0.00	0.01	0.02	0.03	0.00	0.01	0.02	0.00	0.01	0.01	0.01	0.01
Total	15.92	15.99	16.00	16.00	15.99	15.98	15.96	16.02	15.99	16.06	16.06	16.04	16.06

...continued on next page

Table A.1 **Garnet** – continued from previous page

	s55-4	**s55-5**	**s55-6**	**s55-7**	**s55-8**	**s55-9**	**s65-1**	**s65-2**	**s65-3**	**s65-4**	**s65-5**	**s65-6**	**s67-1**
SiO_2	38.39	37.84	37.46	37.30	37.35	37.59	38.94	38.53	38.51	38.30	38.42	38.28	37.81
TiO_2	0.02	0.05	0.03	0.07	0.07	0.05	0.00	0.01	0.03	0.06	0.00	0.00	0.06
Al_2O_3	21.80	21.89	21.72	21.85	21.26	21.69	22.67	22.78	22.82	22.77	22.68	22.55	21.86
Cr_2O_3	0.01	0.01	0.03	0.01	0.00	0.01	0.14	0.11	0.06	0.12	0.09	0.11	0.08
FeO	29.99	30.48	27.89	31.47	29.79	30.67	24.94	26.04	26.78	25.87	27.23	28.00	26.70
MnO	2.28	0.62	3.79	0.79	2.89	0.60	1.08	1.05	1.76	1.07	1.69	2.05	0.90
MgO	1.22	2.01	0.71	1.77	0.95	1.95	8.47	7.87	6.38	7.17	6.56	6.13	4.35
CaO	9.64	9.58	10.48	9.43	10.17	9.48	4.95	4.89	5.20	5.71	5.17	4.98	8.16
Na_2O	0.00	0.05	0.74	0.04	0.05	0.03	0.02	0.01	0.04	0.02	0.02	0.01	0.00
Total	103.35	102.53	102.85	102.72	102.54	102.07	101.21	101.30	101.58	101.09	101.86	102.11	99.91
Oxygens	24	24	24	24	24	24	24	24	24	24	24	24	24
Si	5.96	5.91	5.88	5.85	5.89	5.90	5.92	5.88	5.91	5.88	5.89	5.88	5.94
Ti	0.00	0.01	0.00	0.01	0.01	0.01	0.00	0.00	0.00	0.01	0.00	0.00	0.01
Al	3.99	4.03	4.02	4.04	3.95	4.01	4.06	4.10	4.12	4.12	4.10	4.08	4.05
Cr	0.00	0.00	0.00	0.00	0.00	0.00	0.02	0.01	0.01	0.01	0.01	0.01	0.01
Fe	3.90	3.98	3.66	4.13	3.93	4.03	3.17	3.33	3.43	3.32	3.49	3.60	3.51
Mn	0.30	0.08	0.50	0.10	0.39	0.08	0.14	0.14	0.23	0.14	0.22	0.27	0.12
Mg	0.28	0.47	0.17	0.41	0.22	0.46	1.92	1.79	1.46	1.64	1.50	1.40	1.02
Ca	1.60	1.60	1.76	1.58	1.72	1.59	0.81	0.80	0.85	0.94	0.85	0.82	1.37
Na	0.00	0.02	0.23	0.01	0.02	0.01	0.01	0.00	0.01	0.01	0.00	0.00	0.00
Total	16.04	16.08	16.22	16.13	16.13	16.09	16.04	16.06	16.03	16.05	16.06	16.07	16.02

...continued on next page

Table A.1 **Garnet** – continued from previous page

	s67-2	**s67-3**	**s67-4**	**s67-5**	**s67-6**	**s67-7**	**s67-8**	**s67-9**	**s67-10**	**s67-11**	**s67-12**	**s67-13**
SiO_2	37.75	37.84	37.81	37.35	37.40	37.66	37.75	37.73	37.45	37.21	37.28	37.99
TiO_2	0.01	0.07	0.04	0.03	0.04	0.03	0.03	0.04	0.06	0.04	0.01	0.09
Al_2O_3	21.65	23.29	22.32	21.74	21.72	21.93	21.91	22.11	21.69	21.73	21.71	21.95
Cr_2O_3	0.08	0.00	0.01	0.00	0.09	0.00	0.02	0.06	0.05	0.00	0.07	0.05
FeO	28.48	24.30	26.52	28.12	27.72	27.31	27.87	26.00	28.29	28.57	28.30	26.94
MnO	1.89	0.95	0.90	2.20	1.98	1.61	1.54	0.74	2.02	1.97	2.38	0.91
MgO	3.50	3.33	4.53	3.05	3.20	3.29	3.67	5.00	3.34	3.24	2.88	4.24
CaO	6.84	9.44	8.28	6.81	7.72	8.52	7.83	8.50	7.20	7.42	6.98	8.56
Na_2O	0.04	0.07	0.01	0.01	0.06	0.03	0.03	0.06	0.00	0.02	0.00	0.02
Total	100.24	99.29	100.42	99.31	99.93	100.39	100.64	100.24	100.10	100.20	99.61	100.75
Oxygens	24	24	24	24	24	24	24	24	24	24	24	24
Si	5.97	5.93	5.90	5.96	5.93	5.93	5.93	5.89	5.93	5.90	5.95	5.93
Ti	0.00	0.01	0.01	0.00	0.00	0.00	0.00	0.01	0.01	0.01	0.00	0.01
Al	4.03	4.30	4.11	4.09	4.06	4.07	4.06	4.07	4.05	4.06	4.08	4.04
Cr	0.01	0.00	0.00	0.00	0.01	0.00	0.00	0.01	0.01	0.00	0.01	0.01
Fe	3.76	3.18	3.46	3.75	3.68	3.60	3.66	3.40	3.75	3.79	3.77	3.52
Mn	0.25	0.13	0.12	0.30	0.27	0.21	0.20	0.10	0.27	0.26	0.32	0.12
Mg	0.82	0.78	1.05	0.73	0.76	0.77	0.86	1.16	0.79	0.77	0.68	0.99
Ca	1.16	1.58	1.38	1.16	1.31	1.44	1.32	1.42	1.22	1.26	1.19	1.43
Na	0.01	0.02	0.00	0.00	0.02	0.01	0.01	0.02	0.00	0.01	0.00	0.01
Total	16.02	15.93	16.04	15.99	16.04	16.04	16.04	16.07	16.03	16.06	16.01	16.04

Table A.2: Electron microprobe results for amphibole

	S01-1	**S01-2**	**S01-3**	**S01-4**	**S01-5**	**S01-6**	**S01-7**	**S01-8**	**S01-9**	**S01-10**	**S01-13**	**S01-14**	**S01-15**
SiO_2	41.06	41.07	41.19	41.31	40.28	40.59	40.63	38.90	41.95	40.51	40.69	40.67	40.95
TiO_2	1.88	1.87	1.76	1.56	1.80	2.06	2.19	1.59	1.67	1.35	1.71	1.64	1.62
Al_2O_3	12.97	12.81	13.14	12.93	14.64	13.92	13.47	11.63	12.36	14.30	12.70	12.99	13.36
Cr_2O_3	0.00	0.01	0.01	0.00	0.00	0.05	0.02	0.00	0.03	0.00	0.00	0.00	0.00
FeO	21.87	21.47	21.75	21.27	19.77	19.80	20.17	18.66	20.26	20.24	21.56	21.73	21.62
MnO	0.16	0.13	0.20	0.16	0.16	0.14	0.14	0.11	0.08	0.08	0.14	0.17	0.24
MgO	7.69	7.73	7.86	8.47	8.25	8.35	8.44	8.55	9.10	8.30	7.75	7.81	7.95
CaO	10.99	10.89	10.84	10.82	11.31	11.32	11.21	10.47	11.41	11.44	10.92	11.07	10.82
Na_2O	2.37	2.41	2.46	2.50	2.59	2.61	2.50	2.28	2.39	2.60	2.42	2.46	2.47
K_2O	0.91	0.85	0.81	0.67	0.64	0.69	0.79	0.63	0.70	0.68	0.70	0.67	0.68
Total	99.90	99.23	100.01	99.69	99.44	99.53	99.56	92.83	99.96	99.50	98.59	99.21	99.71
Oxygens	23	23	23	23	23	23	23	23	23	23	23	23	23
Si	6.20	6.23	6.20	6.22	6.05	6.10	6.11	6.26	6.27	6.09	6.21	6.18	6.18
Ti	0.21	0.21	0.20	0.18	0.20	0.23	0.25	0.19	0.19	0.15	0.20	0.19	0.18
Al	2.31	2.29	2.33	2.29	2.59	2.46	2.39	2.20	2.18	2.53	2.29	2.33	2.37
Cr	0.00	0.00	0.00	0.00	0.00	0.01	0.00	0.00	0.00	0.00	0.00	0.00	0.00
Fe	2.76	2.72	2.74	2.68	2.48	2.49	2.54	2.51	2.53	2.55	2.75	2.76	2.73
Mn	0.02	0.02	0.02	0.02	0.02	0.02	0.02	0.01	0.01	0.01	0.02	0.02	0.03
Mg	1.73	1.75	1.76	1.90	1.85	1.87	1.89	2.05	2.03	1.86	1.76	1.77	1.79
Ca	1.78	1.77	1.75	1.74	1.82	1.82	1.81	1.80	1.83	1.84	1.79	1.80	1.75
Na	0.69	0.71	0.72	0.73	0.75	0.76	0.73	0.71	0.69	0.76	0.72	0.72	0.72
K	0.17	0.16	0.16	0.13	0.12	0.13	0.15	0.13	0.13	0.13	0.14	0.13	0.13
Total	15.87	15.85	15.87	15.89	15.89	15.88	15.89	15.87	15.86	15.93	15.87	15.90	15.88

...continued on next page

Table A.2 **Amphiboles** – continued from previous page

	S01-16	**S01-17**	**S01-18**	**S01-20**	**S01-21**	**S01-22**	**S01-23**	**S01-24**	**S01-25**	**S01-26**	**S01-27**	**S01-28**	**S01-29**
SiO_2	40.85	41.55	41.18	41.66	40.86	40.59	39.92	41.20	40.28	34.76	39.77	39.57	39.66
TiO_2	1.62	1.35	0.90	1.23	1.50	1.66	1.48	1.40	1.50	3.68	1.53	1.81	1.56
Al_2O_3	13.30	12.85	13.71	12.61	12.64	13.17	14.21	12.99	12.49	15.82	12.95	12.99	12.83
Cr_2O_3	0.05	0.00	0.00	0.00	0.01	0.00	0.00	0.04	0.00	0.00	0.03	0.00	0.03
FeO	21.44	20.77	19.98	22.58	22.18	22.26	22.29	21.48	22.76	25.40	22.79	23.30	22.79
MnO	0.13	0.16	0.12	0.16	0.19	0.11	0.11	0.21	0.16	0.03	0.23	0.21	0.20
MgO	8.07	9.03	9.06	8.20	7.90	7.57	7.27	8.03	7.51	9.21	7.28	7.17	7.43
CaO	11.02	10.81	10.79	10.91	10.95	11.07	11.03	10.92	10.54	0.00	10.63	10.57	10.53
Na_2O	2.44	2.44	2.51	2.43	2.47	2.34	2.48	2.38	2.38	0.46	2.55	2.58	2.49
K_2O	0.69	0.62	0.65	0.58	0.63	0.71	0.80	0.68	0.61	8.94	0.65	0.66	0.62
Total	99.61	99.57	98.90	100.36	99.33	99.48	99.60	99.33	98.23	98.31	98.41	98.86	98.13
Oxygens	23	23	23	23	23	23	23	23	23	23	23	23	23
Si	6.17	6.24	6.20	6.26	6.21	6.16	6.06	6.23	6.21	5.55	6.13	6.09	6.13
Ti	0.18	0.15	0.10	0.14	0.17	0.19	0.17	0.16	0.17	0.44	0.18	0.21	0.18
Al	2.37	2.27	2.43	2.23	2.26	2.36	2.54	2.32	2.27	2.97	2.35	2.36	2.34
Cr	0.01	0.00	0.00	0.00	0.00	0.00	0.00	0.01	0.00	0.00	0.00	0.00	0.00
Fe	2.71	2.61	2.52	2.84	2.82	2.83	2.83	2.72	2.93	3.39	2.94	3.00	2.95
Mn	0.02	0.02	0.01	0.02	0.02	0.01	0.01	0.03	0.02	0.00	0.03	0.03	0.03
Mg	1.82	2.02	2.03	1.84	1.79	1.71	1.65	1.81	1.73	2.19	1.67	1.65	1.71
Ca	1.78	1.74	1.74	1.76	1.78	1.80	1.79	1.77	1.74	0.00	1.76	1.74	1.74
Na	0.71	0.71	0.73	0.71	0.73	0.69	0.73	0.70	0.71	0.14	0.76	0.77	0.75
K	0.13	0.12	0.12	0.11	0.12	0.14	0.16	0.13	0.12	1.82	0.13	0.13	0.12
Total	15.89	15.89	15.91	15.90	15.91	15.89	15.94	15.86	15.90	16.51	15.96	15.97	15.95

...continued on next page

Table A.2 **Amphiboles** – continued from previous page

	S10-1	**S10-2**	**S10-3**	**S10-4**	**S10-5**	**S10-9**	**S10-10**	**S10-11**	**S10-12**	**S10-13**	**S10-14**	**S10-15**	**S10-16**
SiO_2	38.66	39.27	33.49	38.72	39.16	38.76	38.75	38.44	38.61	39.33	38.69	38.89	39.12
TiO_2	1.63	1.29	2.42	1.74	1.59	1.64	1.19	1.75	1.70	1.38	1.63	1.67	1.51
Al_2O_3	13.05	13.03	17.06	13.48	12.90	12.91	13.24	13.12	12.87	13.04	13.34	13.16	13.18
Cr_2O_3	0.00	0.00	0.02	0.02	0.02	0.00	0.00	0.00	0.03	0.00	0.01	0.00	0.00
FeO	24.36	25.02	27.28	24.91	24.49	25.03	24.88	24.87	24.43	24.59	24.39	24.21	24.40
MnO	0.62	0.64	0.35	0.65	0.59	0.64	0.64	0.64	0.71	0.66	0.63	0.56	0.66
MgO	4.85	4.75	6.06	4.66	4.82	4.72	4.71	4.66	4.40	4.60	4.56	4.54	4.84
CaO	11.62	11.59	0.01	11.59	11.61	11.65	11.76	11.57	11.37	11.49	11.32	11.33	11.52
Na_2O	1.22	1.16	0.05	1.36	1.24	1.25	1.04	1.21	1.25	1.15	1.19	1.39	1.15
K_2O	1.72	1.66	9.31	1.87	1.76	1.71	1.59	1.80	1.73	1.64	1.88	1.84	1.72
Total	97.73	98.40	96.05	99.01	98.18	98.30	97.81	98.07	97.10	97.88	97.65	97.59	98.09
Oxygens	23	23	23	23	23	23	23	23	23	23	23	23	23
Si	6.10	6.16	5.54	6.05	6.15	6.10	6.12	6.07	6.14	6.19	6.11	6.14	6.14
Ti	0.19	0.15	0.30	0.20	0.19	0.19	0.14	0.21	0.20	0.16	0.19	0.20	0.18
Al	2.43	2.41	3.33	2.48	2.39	2.40	2.46	2.44	2.41	2.42	2.48	2.45	2.44
Cr	0.00	0.00	0.00	0.00	0.00	0.00	0.00	0.00	0.00	0.00	0.00	0.00	0.00
Fe	3.22	3.28	3.78	3.26	3.22	3.30	3.28	3.28	3.25	3.23	3.22	3.20	3.20
Mn	0.08	0.08	0.05	0.09	0.08	0.09	0.09	0.09	0.10	0.09	0.08	0.07	0.09
Mg	1.14	1.11	1.50	1.09	1.13	1.11	1.11	1.10	1.04	1.08	1.07	1.07	1.13
Ca	1.97	1.95	0.00	1.94	1.95	1.96	1.99	1.96	1.94	1.94	1.92	1.92	1.94
Na	0.37	0.35	0.02	0.41	0.38	0.38	0.32	0.37	0.39	0.35	0.37	0.43	0.35
K	0.35	0.33	1.97	0.37	0.35	0.34	0.32	0.36	0.35	0.33	0.38	0.37	0.34
Total	15.85	15.83	16.48	15.89	15.83	15.87	15.83	15.87	15.82	15.78	15.83	15.84	15.81

...continued on next page

Table A.2 **Amphiboles** – continued from previous page

	S10-17	**S10-18**	**S10-19**	**S10-20**	**s52-1**	**s52-2**	**s52-7**	**s52-8**	**s52-9**	**s52-10**	**s52-12**	**s52-13**	**s52-14**
SiO_2	38.85	33.91	33.27	38.90	41.30	41.17	40.44	38.96	38.69	38.71	41.57	40.81	38.16
TiO_2	1.61	3.04	3.26	1.33	1.57	1.48	1.74	1.18	0.10	0.07	1.69	1.26	0.06
Al_2O_3	12.95	16.52	15.77	12.84	13.24	13.33	13.33	13.13	22.77	22.83	13.05	13.84	22.81
Cr_2O_3	0.00	0.03	0.00	0.01	0.00	0.05	0.02	0.00	0.00	0.00	0.00	0.00	0.00
FeO	24.52	27.69	27.06	23.98	26.41	26.34	26.59	26.27	29.07	30.06	27.14	26.36	29.03
MnO	0.63	0.50	0.42	0.63	0.29	0.34	0.35	0.25	0.57	1.53	0.33	0.34	0.65
MgO	4.64	5.77	5.79	4.63	4.14	4.02	3.64	3.81	2.31	1.31	3.81	3.73	2.00
CaO	11.40	0.03	0.05	11.49	11.39	11.46	11.46	9.97	10.41	9.96	11.39	11.47	10.81
Na_2O	1.37	0.06	0.12	1.10	1.41	1.07	1.29	1.01	0.02	0.05	1.31	1.25	0.01
K_2O	1.80	9.03	9.05	1.62	1.71	1.58	1.72	1.51	0.01	0.01	1.73	1.57	0.00
Total	97.77	96.58	94.80	96.53	101.46	100.84	100.58	96.08	103.97	104.53	102.02	100.63	103.53
Oxygens	23	23	23	23	23	23	23	23	23	23	23	23	23
Si	6.13	5.58	5.59	6.20	6.27	6.28	6.21	6.25	5.66	5.67	6.29	6.24	5.62
Ti	0.19	0.38	0.41	0.16	0.18	0.17	0.20	0.14	0.01	0.01	0.19	0.14	0.01
Al	2.41	3.21	3.12	2.41	2.37	2.40	2.41	2.48	3.93	3.94	2.33	2.49	3.96
Cr	0.00	0.00	0.00	0.00	0.00	0.01	0.00	0.00	0.00	0.00	0.00	0.00	0.00
Fe	3.24	3.81	3.80	3.19	3.35	3.36	3.42	3.52	3.56	3.68	3.43	3.37	3.58
Mn	0.08	0.07	0.06	0.08	0.04	0.04	0.05	0.03	0.07	0.19	0.04	0.04	0.08
Mg	1.09	1.42	1.45	1.10	0.94	0.91	0.83	0.91	0.50	0.29	0.86	0.85	0.44
Ca	1.93	0.01	0.01	1.96	1.85	1.87	1.89	1.71	1.63	1.56	1.85	1.88	1.71
Na	0.42	0.02	0.04	0.34	0.41	0.32	0.39	0.31	0.01	0.01	0.38	0.37	0.00
K	0.36	1.90	1.94	0.33	0.33	0.31	0.34	0.31	0.00	0.00	0.33	0.31	0.00
Total	15.86	16.39	16.43	15.77	15.74	15.66	15.74	15.68	15.37	15.36	15.71	15.70	15.39

...continued on next page

Table A.2 **Amphiboles** – continued from previous page

	s52-15	**s52-16**	**s52-17**	**s52-20**	**s52-21**	**s50-1**	**s50-2**	**s50-3**	**s50-4**	**s50-7**	**s50-8**	**s50-10**	**s50-12**
SiO_2	37.91	35.33	39.05	37.99	37.72	41.52	40.47	41.65	41.76	41.19	39.37	41.08	41.38
TiO_2	0.03	0.13	1.20	1.81	1.47	1.66	0.97	1.47	1.20	1.35	0.60	1.61	1.54
Al_2O_3	22.30	18.34	13.68	13.24	13.57	13.32	15.95	13.53	13.66	13.34	16.58	13.06	13.11
Cr_2O_3	0.00	0.00	0.01	0.01	0.00	0.01	0.01	0.01	0.05	0.01	0.02	0.00	0.00
FeO	28.64	28.94	26.24	25.94	26.52	24.65	24.47	24.45	24.69	24.77	24.80	24.88	24.52
MnO	0.65	2.77	0.34	0.26	0.31	0.27	0.16	0.18	0.22	0.16	0.17	0.17	0.20
MgO	1.90	2.33	3.72	4.06	4.01	5.09	4.25	5.20	4.96	5.23	4.18	5.35	5.51
CaO	10.94	6.03	11.38	11.23	11.40	11.47	11.58	11.54	11.37	11.16	11.53	11.45	11.44
Na_2O	0.00	0.06	1.17	1.46	1.28	1.32	1.19	1.43	1.41	1.42	1.05	1.10	1.26
K_2O	0.00	0.69	1.64	1.74	1.65	1.27	1.22	1.23	1.20	1.14	1.16	1.08	1.13
Total	102.37	94.62	98.44	97.74	97.92	100.59	100.27	100.69	100.52	99.75	99.45	99.78	100.09
Oxygens	23	23	23	23	23	23	23	23	23	23	23	23	23
Si	5.65	5.79	6.14	6.04	6.00	6.29	6.13	6.29	6.32	6.29	6.03	6.27	6.29
Ti	0.00	0.02	0.14	0.22	0.18	0.19	0.11	0.17	0.14	0.15	0.07	0.18	0.18
Al	3.92	3.54	2.54	2.48	2.54	2.38	2.85	2.41	2.43	2.40	2.99	2.35	2.35
Cr	0.00	0.00	0.00	0.00	0.00	0.00	0.00	0.00	0.01	0.00	0.00	0.00	0.00
Fe	3.57	3.97	3.45	3.45	3.53	3.12	3.10	3.09	3.12	3.16	3.18	3.18	3.12
Mn	0.08	0.38	0.04	0.03	0.04	0.03	0.02	0.02	0.03	0.02	0.02	0.02	0.03
Mg	0.42	0.57	0.87	0.96	0.95	1.15	0.96	1.17	1.12	1.19	0.95	1.22	1.25
Ca	1.75	1.06	1.92	1.91	1.94	1.86	1.88	1.87	1.84	1.82	1.89	1.87	1.86
Na	0.00	0.02	0.36	0.45	0.39	0.39	0.35	0.42	0.41	0.42	0.31	0.33	0.37
K	0.00	0.14	0.33	0.35	0.33	0.25	0.24	0.24	0.23	0.22	0.23	0.21	0.22
Total	15.39	15.50	15.79	15.90	15.91	15.65	15.63	15.67	15.65	15.68	15.67	15.64	15.66

...continued on next page

Table A.2 **Amphiboles** – continued from previous page

	s50-13	**s50-14**	**s50-16**	**s50-19**	**s50-20**	**s50-21**	**s55-2**	**s55-3**	**s55-4**	**s55-5**	**s55-6**	**s55-7**	**s55-8**
SiO_2	41.14	40.75	40.60	40.89	40.51	41.50	39.80	40.34	40.20	38.74	40.02	39.65	39.24
TiO_2	1.48	1.37	1.38	1.59	1.74	1.30	1.65	1.53	1.53	1.70	1.47	1.67	1.21
Al_2O_3	13.45	13.11	13.31	13.20	13.00	12.59	13.59	13.31	13.63	13.21	13.58	13.48	13.98
Cr_2O_3	0.00	0.00	0.01	0.00	0.00	0.01	0.01	0.00	0.00	0.01	0.02	0.03	0.00
FeO	24.30	24.82	24.70	24.47	24.69	24.61	26.84	26.83	26.05	25.50	26.31	26.26	26.35
MnO	0.14	0.21	0.14	0.20	0.20	0.22	0.26	0.33	0.29	0.34	0.25	0.25	0.24
MgO	5.43	5.32	5.37	5.14	5.23	5.12	3.84	3.87	3.69	3.96	3.80	3.99	3.90
CaO	11.22	11.43	11.45	11.47	11.29	11.27	11.40	11.46	11.34	11.16	11.50	11.35	11.45
Na_2O	1.32	1.20	1.12	1.40	1.34	1.35	1.22	1.09	1.14	1.30	1.25	1.30	1.15
K_2O	1.27	1.21	1.20	1.31	1.43	1.14	1.75	1.67	1.68	1.69	1.70	1.78	1.71
Total	99.74	99.43	99.27	99.67	99.43	99.10	100.37	100.43	99.55	97.61	99.90	99.75	99.23
Oxygens	23	23	23	23	23	23	23	23	23	23	23	23	23
Si	6.27	6.26	6.24	6.26	6.23	6.37	6.14	6.21	6.22	6.14	6.19	6.15	6.12
Ti	0.17	0.16	0.16	0.18	0.20	0.15	0.19	0.18	0.18	0.20	0.17	0.19	0.14
Al	2.42	2.37	2.41	2.38	2.36	2.28	2.47	2.41	2.49	2.47	2.47	2.46	2.57
Cr	0.00	0.00	0.00	0.00	0.00	0.00	0.00	0.00	0.00	0.00	0.00	0.00	0.00
Fe	3.10	3.19	3.17	3.13	3.18	3.16	3.46	3.45	3.37	3.38	3.40	3.40	3.43
Mn	0.02	0.03	0.02	0.03	0.03	0.03	0.03	0.04	0.04	0.05	0.03	0.03	0.03
Mg	1.23	1.22	1.23	1.17	1.20	1.17	0.88	0.89	0.85	0.94	0.88	0.92	0.91
Ca	1.83	1.88	1.88	1.88	1.86	1.85	1.88	1.89	1.88	1.89	1.90	1.89	1.91
Na	0.39	0.36	0.33	0.42	0.40	0.40	0.37	0.33	0.34	0.40	0.37	0.39	0.35
K	0.25	0.24	0.23	0.26	0.28	0.22	0.34	0.33	0.33	0.34	0.34	0.35	0.34
Total	15.67	15.70	15.68	15.70	15.73	15.65	15.78	15.73	15.70	15.80	15.76	15.80	15.80

...continued on next page

Table A.2 **Amphiboles** – continued from previous page

	s55-9	**s55-11**	**s21-1**	**s21-2**	**s21-3**	**s21-4**	**s21-5**	**s21-6**	**s21-7**	**s21-8**	**s21-9**	**s21-10**	**S21-11**
SiO_2	39.93	39.22	42.38	41.35	42.59	41.12	40.75	42.19	42.70	42.15	41.00	40.49	42.35
TiO_2	1.37	1.62	0.98	1.12	0.84	1.06	1.01	0.96	0.96	0.95	1.02	1.20	0.95
Al_2O_3	13.06	13.44	12.77	13.21	12.93	13.44	13.77	13.18	12.99	12.94	13.35	13.96	13.39
Cr_2O_3	0.04	0.01	0.01	0.05	0.04	0.03	0.10	0.03	0.06	0.07	0.03	0.02	0.00
FeO	26.00	26.92	18.76	18.90	18.79	18.39	18.81	18.91	18.59	18.57	19.08	18.69	18.64
MnO	0.30	0.32	0.22	0.29	0.26	0.29	0.30	0.24	0.25	0.30	0.30	0.23	0.20
MgO	4.18	4.04	8.82	8.64	8.73	8.62	8.28	8.77	8.76	8.73	8.28	8.51	8.57
CaO	11.57	11.45	11.85	11.68	11.66	11.53	11.61	11.68	11.73	11.64	11.52	11.77	11.77
Na_2O	1.21	1.36	1.06	1.28	1.12	1.37	1.25	1.05	1.14	1.19	1.29	1.36	1.19
K_2O	1.66	1.74	0.71	0.87	0.75	0.94	0.89	0.78	0.80	0.82	0.91	1.00	0.86
Total	99.31	100.12	97.58	97.39	97.71	96.78	96.77	97.79	97.98	97.37	96.78	97.22	97.93
Oxygens	23	23	23	23	23	23	23	23	23	23	23	23	23
Si	6.21	6.09	6.41	6.30	6.43	6.29	6.25	6.37	6.42	6.39	6.29	6.19	6.38
Ti	0.16	0.19	0.11	0.13	0.10	0.12	0.12	0.11	0.11	0.11	0.12	0.14	0.11
Al	2.39	2.46	2.28	2.37	2.30	2.42	2.49	2.35	2.30	2.31	2.41	2.51	2.38
Cr	0.00	0.00	0.00	0.01	0.00	0.00	0.01	0.00	0.01	0.01	0.00	0.00	0.00
Fe	3.38	3.49	2.37	2.41	2.37	2.35	2.41	2.39	2.34	2.36	2.45	2.39	2.35
Mn	0.04	0.04	0.03	0.04	0.03	0.04	0.04	0.03	0.03	0.04	0.04	0.03	0.03
Mg	0.97	0.94	1.99	1.96	1.96	1.97	1.89	1.97	1.96	1.97	1.89	1.94	1.93
Ca	1.93	1.90	1.92	1.91	1.89	1.89	1.91	1.89	1.89	1.89	1.89	1.93	1.90
Na	0.36	0.41	0.31	0.38	0.33	0.41	0.37	0.31	0.33	0.35	0.38	0.40	0.35
K	0.33	0.34	0.14	0.17	0.14	0.18	0.17	0.15	0.15	0.16	0.18	0.19	0.17
Total	15.78	15.87	15.56	15.66	15.56	15.67	15.66	15.57	15.56	15.59	15.66	15.72	15.58

...continued on next page

Table A.2 **Amphiboles** – continued from previous page

	S21-12	**S21-13**	**S21-14**	**S21-15**	**S21-16**	**S21-17**	**S21-19**	**S21-20**	**S21-21**	**S21-22**	**S21-23**	**S21-26**	**S21-27**
SiO_2	41.79	42.44	42.91	42.61	42.77	42.18	42.56	42.08	43.27	42.47	43.01	42.95	42.33
TiO_2	1.16	0.95	1.05	1.19	1.11	1.15	1.03	1.16	0.95	1.12	0.99	1.16	1.17
Al_2O_3	13.18	13.28	12.81	12.82	12.70	13.04	13.31	13.45	13.05	13.70	13.17	12.77	13.60
Cr_2O_3	0.03	0.03	0.05	0.00	0.03	0.00	0.08	0.08	0.06	0.05	0.01	0.06	0.02
FeO	18.68	18.61	18.62	18.39	18.47	18.51	18.66	18.87	19.00	18.88	18.83	18.91	18.64
MnO	0.30	0.24	0.32	0.28	0.24	0.30	0.24	0.33	0.28	0.27	0.26	0.26	0.29
MgO	8.26	8.69	8.77	8.86	8.87	8.62	8.51	8.48	8.97	8.43	8.80	9.04	8.83
CaO	11.61	11.88	11.80	11.69	11.63	11.66	11.78	11.74	11.89	11.65	11.96	11.80	11.85
Na_2O	1.27	1.32	1.23	1.31	1.33	1.16	1.42	1.27	1.24	1.34	1.18	1.28	1.37
K_2O	0.89	0.86	0.86	0.91	0.84	0.89	0.90	0.93	0.86	0.93	0.80	0.81	0.93
Total	97.17	98.29	98.40	98.06	97.98	97.51	98.49	98.38	99.58	98.84	99.01	99.05	99.03
Oxygens	23	23	23	23	23	23	23	23	23	23	23	23	23
Si	6.36	6.38	6.43	6.41	6.44	6.39	6.38	6.33	6.42	6.35	6.41	6.41	6.32
Ti	0.13	0.11	0.12	0.13	0.13	0.13	0.12	0.13	0.11	0.13	0.11	0.13	0.13
Al	2.36	2.35	2.26	2.27	2.25	2.33	2.35	2.38	2.28	2.41	2.31	2.24	2.39
Cr	0.00	0.00	0.01	0.00	0.00	0.00	0.01	0.01	0.01	0.01	0.00	0.01	0.00
Fe	2.38	2.34	2.33	2.31	2.32	2.34	2.34	2.37	2.36	2.36	2.35	2.36	2.33
Mn	0.04	0.03	0.04	0.04	0.03	0.04	0.03	0.04	0.03	0.03	0.03	0.03	0.04
Mg	1.87	1.95	1.96	1.99	1.99	1.95	1.90	1.90	1.98	1.88	1.95	2.01	1.96
Ca	1.89	1.91	1.90	1.88	1.87	1.89	1.89	1.89	1.89	1.87	1.91	1.89	1.89
Na	0.37	0.38	0.36	0.38	0.39	0.34	0.41	0.37	0.36	0.39	0.34	0.37	0.40
K	0.17	0.16	0.16	0.17	0.16	0.17	0.17	0.18	0.16	0.18	0.15	0.15	0.18
Total	15.59	15.61	15.57	15.60	15.58	15.58	15.61	15.62	15.59	15.60	15.57	15.60	15.64

...continued on next page

Table A.2 **Amphiboles** – continued from previous page

	S33-1	**S33-2**	**S33-3**	**S33-4**	**S33-5**	**S33-6**	**S33-7**	**S33-8**	**S33-9**	**S33-10**	**S33-11**	**S33-12**	**S33-13**
SiO_2	43.24	44.26	45.40	46.02	48.95	48.06	42.44	42.33	42.54	44.56	43.65	47.20	41.83
TiO_2	1.46	1.48	1.04	1.05	0.54	0.50	1.61	1.54	1.40	1.32	1.43	0.72	1.63
Al_2O_3	11.54	10.47	9.24	9.16	6.29	7.47	12.11	12.75	12.61	10.62	11.26	7.73	13.49
Cr_2O_3	0.09	0.07	0.11	0.10	0.08	0.08	0.09	0.12	0.14	0.09	0.11	0.12	0.07
FeO	17.01	16.24	15.36	15.65	14.90	15.27	16.64	16.64	16.82	16.30	16.49	14.95	16.94
MnO	0.32	0.34	0.33	0.38	0.27	0.35	0.39	0.36	0.33	0.30	0.34	0.36	0.32
MgO	10.27	10.85	11.59	11.52	13.10	12.64	9.98	9.77	9.68	10.67	10.35	12.43	9.28
CaO	12.32	12.07	11.98	12.23	12.35	12.41	12.05	12.13	12.07	12.13	12.17	12.43	12.05
Na_2O	1.31	1.27	1.19	1.03	0.76	0.87	1.50	1.44	1.44	1.28	1.35	0.88	1.41
K_2O	1.19	1.03	0.83	0.85	0.48	0.56	1.30	1.43	1.35	1.06	1.17	0.62	1.65
Total	98.76	98.09	97.07	98.00	97.72	98.21	98.10	98.51	98.38	98.33	98.32	97.44	98.68
Oxygens	23	23	23	23	23	23	23	23	23	23	23	23	23
Si	6.45	6.60	6.79	6.82	7.20	7.06	6.37	6.33	6.37	6.63	6.52	7.00	6.26
Ti	0.16	0.17	0.12	0.12	0.06	0.06	0.18	0.17	0.16	0.15	0.16	0.08	0.18
Al	2.03	1.84	1.63	1.60	1.09	1.29	2.14	2.25	2.23	1.86	1.98	1.35	2.38
Cr	0.01	0.01	0.01	0.01	0.01	0.01	0.01	0.01	0.02	0.01	0.01	0.01	0.01
Fe	2.12	2.03	1.92	1.94	1.83	1.88	2.09	2.08	2.11	2.03	2.06	1.85	2.12
Mn	0.04	0.04	0.04	0.05	0.03	0.04	0.05	0.05	0.04	0.04	0.04	0.05	0.04
Mg	2.28	2.41	2.58	2.55	2.87	2.77	2.23	2.18	2.16	2.37	2.30	2.75	2.07
Ca	1.97	1.93	1.92	1.94	1.95	1.95	1.94	1.94	1.94	1.93	1.95	1.97	1.93
Na	0.38	0.37	0.35	0.30	0.22	0.25	0.44	0.42	0.42	0.37	0.39	0.25	0.41
K	0.23	0.20	0.16	0.16	0.09	0.10	0.25	0.27	0.26	0.20	0.22	0.12	0.32
Total	15.67	15.59	15.52	15.48	15.35	15.41	15.71	15.71	15.69	15.58	15.63	15.43	15.72

...continued on next page

Table A.2 **Amphiboles** – continued from previous page

	S33-14	**S33-15**	**S33-16**	**S33-17**	**S33-18**	**S33-19**	**S33-20**	**S33-21**	**S65-1**	**S65-2**	**S65-3**	**S65-4**	**S65-5**
SiO_2	42.03	41.98	40.25	45.40	43.98	46.40	43.28	43.95	54.37	44.35	53.77	44.87	44.78
TiO_2	1.55	1.63	6.06	1.01	1.40	1.06	1.68	1.21	0.02	0.63	0.04	1.04	0.96
Al_2O_3	13.08	13.37	11.67	9.40	10.94	8.70	11.95	11.20	1.09	14.04	1.71	14.23	14.07
Cr_2O_3	0.09	0.07	0.09	0.03	0.04	0.08	0.14	0.08	0.06	0.37	0.09	0.15	0.08
FeO	16.96	16.82	14.26	14.80	16.40	16.11	16.87	16.66	19.13	11.87	19.90	10.56	12.13
MnO	0.33	0.39	0.24	0.33	0.33	0.34	0.28	0.34	0.45	0.22	0.52	0.19	0.19
MgO	9.53	9.38	7.96	11.17	10.62	11.88	10.06	10.42	21.38	13.10	20.22	13.90	14.38
CaO	11.97	11.99	14.39	12.16	12.27	12.06	12.01	12.25	0.44	10.74	0.91	11.71	10.02
Na_2O	1.56	1.45	1.19	0.95	1.07	1.20	1.35	1.27	0.05	1.46	0.06	1.42	1.37
K_2O	1.52	1.57	1.33	0.84	1.09	0.79	1.27	1.10	0.00	0.21	0.01	0.47	0.59
Total	98.62	98.65	97.45	96.09	98.14	98.62	98.88	98.48	96.99	96.99	97.23	98.54	98.57
Oxygens	23	23	23	23	23	23	23	23	23	23	23	23	23
Si	6.29	6.28	6.10	6.84	6.56	6.84	6.43	6.55	7.84	6.47	7.78	6.43	6.43
Ti	0.17	0.18	0.69	0.11	0.16	0.12	0.19	0.14	0.00	0.07	0.00	0.11	0.10
Al	2.31	2.36	2.08	1.67	1.92	1.51	2.09	1.97	0.19	2.41	0.29	2.40	2.38
Cr	0.01	0.01	0.01	0.00	0.00	0.01	0.02	0.01	0.01	0.04	0.01	0.02	0.01
Fe	2.12	2.10	1.81	1.86	2.05	1.99	2.10	2.07	2.31	1.45	2.41	1.26	1.46
Mn	0.04	0.05	0.03	0.04	0.04	0.04	0.03	0.04	0.05	0.03	0.06	0.02	0.02
Mg	2.13	2.09	1.80	2.51	2.36	2.61	2.23	2.31	4.60	2.85	4.36	2.97	3.08
Ca	1.92	1.92	2.34	1.96	1.96	1.91	1.91	1.95	0.07	1.68	0.14	1.80	1.54
Na	0.45	0.42	0.35	0.28	0.31	0.34	0.39	0.37	0.01	0.41	0.02	0.39	0.38
K	0.29	0.30	0.26	0.16	0.21	0.15	0.24	0.21	0.00	0.04	0.00	0.08	0.11
Total	15.74	15.71	15.47	15.43	15.58	15.52	15.64	15.62	15.07	15.46	15.08	15.49	15.51

...continued on next page

Table A.2 **Amphiboles** – continued from previous page

	S65-6	**S65-7**	**S65-8**	**S67-1**	**S67-2**	**S67-3**	**S67-4**	**S67-5**	**S67-7**	**S67-8**	**S67-10**	**S67-11**	**S67-12**
SiO_2	45.77	53.73	44.22	44.20	46.03	45.44	46.09	45.69	45.27	46.04	43.43	45.44	42.28
TiO_2	0.98	0.09	0.86	1.01	0.60	0.55	0.60	0.63	0.75	0.59	1.00	0.66	1.36
Al_2O_3	13.09	1.89	14.15	12.71	11.77	12.01	10.83	11.21	12.32	11.34	13.88	11.59	14.97
Cr_2O_3	0.08	0.05	0.14	0.18	0.07	0.08	0.08	0.05	0.07	0.18	0.10	0.09	0.11
FeO	12.48	19.75	11.33	15.68	15.58	15.32	15.19	15.88	15.52	14.86	15.89	14.79	15.70
MnO	0.15	0.58	0.23	0.23	0.22	0.17	0.25	0.20	0.18	0.19	0.25	0.19	0.26
MgO	14.60	20.37	13.10	11.03	11.55	11.53	11.94	11.90	11.24	11.76	10.30	11.45	10.20
CaO	9.81	1.00	11.40	11.18	10.87	11.22	11.41	10.70	11.49	11.67	11.47	11.49	11.59
Na_2O	1.31	0.14	1.38	1.05	0.85	0.95	0.93	1.01	0.99	0.89	1.23	1.00	1.14
K_2O	0.44	0.01	0.30	0.73	0.39	0.38	0.33	0.38	0.40	0.31	0.59	0.37	0.96
Total	98.70	97.61	97.11	97.99	97.94	97.65	97.65	97.64	98.22	97.83	98.14	97.08	98.57
Oxygens	23	23	23	23	23	23	23	23	23	23	23	23	23
Si	6.55	7.74	6.44	6.52	6.74	6.68	6.78	6.73	6.63	6.75	6.41	6.72	6.24
Ti	0.11	0.01	0.09	0.11	0.07	0.06	0.07	0.07	0.08	0.06	0.11	0.07	0.15
Al	2.21	0.32	2.43	2.21	2.03	2.08	1.88	1.95	2.13	1.96	2.42	2.02	2.60
Cr	0.01	0.01	0.02	0.02	0.01	0.01	0.01	0.01	0.01	0.02	0.01	0.01	0.01
Fe	1.49	2.38	1.38	1.94	1.91	1.88	1.87	1.96	1.90	1.82	1.96	1.83	1.94
Mn	0.02	0.07	0.03	0.03	0.03	0.02	0.03	0.02	0.02	0.02	0.03	0.02	0.03
Mg	3.12	4.38	2.85	2.43	2.52	2.53	2.62	2.61	2.46	2.57	2.27	2.52	2.24
Ca	1.50	0.15	1.78	1.77	1.71	1.77	1.80	1.69	1.80	1.83	1.81	1.82	1.83
Na	0.36	0.04	0.39	0.30	0.24	0.27	0.27	0.29	0.28	0.25	0.35	0.29	0.33
K	0.08	0.00	0.06	0.14	0.07	0.07	0.06	0.07	0.07	0.06	0.11	0.07	0.18
Total	15.45	15.10	15.46	15.47	15.33	15.38	15.38	15.40	15.39	15.35	15.49	15.37	15.56

...continued on next page

Table A.2 **Amphiboles** – continued from previous page

	S67-13	**S67-14**	**S67-15**	**S67-16**	**S67-17**	**S67-18**	**S67-19**	**S67-20**	**S67-21**	**S67-22**	**S67-23**	**S67-24**	**S53-1**
SiO_2	45.85	42.72	43.91	42.22	44.14	42.48	44.40	43.20	43.93	42.17	44.61	42.69	42.80
TiO_2	0.73	1.28	0.90	1.34	0.81	1.30	0.77	1.28	0.88	1.31	0.80	1.11	1.41
Al_2O_3	11.04	14.23	13.20	14.09	12.88	14.39	12.74	13.91	13.46	14.74	12.80	14.40	13.18
Cr_2O_3	0.11	0.11	0.14	0.11	0.12	0.06	0.10	0.11	0.12	0.10	0.09	0.15	0.06
FeO	14.62	15.56	15.45	15.36	15.57	15.88	15.64	15.54	15.50	15.58	15.21	15.60	14.58
MnO	0.16	0.24	0.22	0.17	0.20	0.21	0.25	0.17	0.26	0.24	0.24	0.25	0.21
MgO	11.85	10.10	10.55	10.13	10.92	9.89	11.03	10.34	10.44	9.85	10.95	10.01	11.29
CaO	11.35	11.50	11.33	11.43	11.36	11.37	11.42	11.40	11.29	11.38	11.33	11.29	12.32
Na_2O	0.86	1.06	1.16	1.20	1.13	1.22	1.07	1.14	1.18	1.17	1.11	1.09	1.52
K_2O	0.35	0.86	0.48	0.99	0.48	0.88	0.50	0.69	0.51	0.89	0.51	0.75	1.25
Total	96.92	97.66	97.35	97.04	97.61	97.69	97.92	97.78	97.59	97.43	97.65	97.34	98.62
Oxygens	23	23	23	23	23	23	23	23	23	23	23	23	23
Si	6.77	6.35	6.51	6.32	6.53	6.32	6.55	6.40	6.50	6.29	6.58	6.36	6.32
Ti	0.08	0.14	0.10	0.15	0.09	0.15	0.09	0.14	0.10	0.15	0.09	0.12	0.16
Al	1.92	2.49	2.31	2.49	2.25	2.52	2.21	2.43	2.35	2.59	2.22	2.53	2.29
Cr	0.01	0.01	0.02	0.01	0.01	0.01	0.01	0.01	0.01	0.01	0.01	0.02	0.01
Fe	1.81	1.93	1.92	1.92	1.93	1.98	1.93	1.92	1.92	1.94	1.88	1.94	1.80
Mn	0.02	0.03	0.03	0.02	0.03	0.03	0.03	0.02	0.03	0.03	0.03	0.03	0.03
Mg	2.61	2.24	2.33	2.26	2.41	2.19	2.43	2.28	2.30	2.19	2.41	2.22	2.49
Ca	1.80	1.83	1.80	1.83	1.80	1.81	1.80	1.81	1.79	1.82	1.79	1.80	1.95
Na	0.25	0.31	0.33	0.35	0.33	0.35	0.31	0.33	0.34	0.34	0.32	0.32	0.44
K	0.07	0.16	0.09	0.19	0.09	0.17	0.09	0.13	0.10	0.17	0.10	0.14	0.24
Total	15.33	15.49	15.44	15.55	15.46	15.53	15.45	15.47	15.44	15.52	15.42	15.48	15.71

...continued on next page

Table A.2 **Amphiboles** – continued from previous page

	S53-2	**S53-3**	**S53-4**	**S53-5**	**S53-6**	**S53-7**	**S53-8**	**S53-9**	**S53-10**	**S53-11**	**S53-12**	**S53-15**	**S53-17**
SiO_2	42.67	42.49	42.92	43.91	42.90	42.10	42.86	42.45	43.20	42.27	43.51	33.46	46.87
TiO_2	1.39	1.56	1.27	1.29	1.28	1.38	1.18	1.31	1.25	1.40	1.31	0.03	0.95
Al_2O_3	12.95	13.92	12.72	12.14	12.54	13.68	12.52	13.70	13.16	13.71	11.73	10.98	8.79
Cr_2O_3	0.08	0.11	0.07	0.10	0.12	0.14	0.06	0.11	0.09	0.10	0.11	0.00	0.10
FeO	15.08	14.73	14.87	14.61	14.76	14.54	14.64	14.54	14.30	14.64	14.04	22.18	16.13
MnO	0.23	0.32	0.30	0.34	0.25	0.29	0.27	0.25	0.27	0.30	0.29	0.16	0.38
MgO	11.36	11.00	11.47	11.86	11.33	10.97	11.27	11.07	11.31	11.14	11.94	10.79	11.39
CaO	12.29	11.96	12.55	12.45	12.38	12.31	12.44	12.28	12.29	12.31	12.47	2.06	11.68
Na_2O	1.40	1.65	1.32	1.25	1.43	1.58	1.35	1.51	1.60	1.53	1.18	0.50	0.94
K_2O	1.33	1.18	1.27	1.25	1.26	1.31	1.30	1.35	1.30	1.35	1.14	0.50	0.74
Total	98.79	98.92	98.74	99.20	98.25	98.30	97.90	98.57	98.78	98.74	97.72	80.66	97.97
Oxygens	23	23	23	23	23	23	23	23	23	23	23	23	23
Si	6.31	6.26	6.34	6.44	6.37	6.25	6.38	6.28	6.36	6.25	6.46	6.20	6.93
Ti	0.15	0.17	0.14	0.14	0.14	0.15	0.13	0.15	0.14	0.16	0.15	0.00	0.11
Al	2.26	2.42	2.22	2.10	2.19	2.39	2.20	2.39	2.28	2.39	2.05	2.40	1.53
Cr	0.01	0.01	0.01	0.01	0.01	0.02	0.01	0.01	0.01	0.01	0.01	0.00	0.01
Fe	1.86	1.81	1.84	1.79	1.83	1.80	1.82	1.80	1.76	1.81	1.74	3.44	1.99
Mn	0.03	0.04	0.04	0.04	0.03	0.04	0.03	0.03	0.03	0.04	0.04	0.02	0.05
Mg	2.50	2.41	2.53	2.59	2.51	2.43	2.50	2.44	2.48	2.45	2.64	2.98	2.51
Ca	1.95	1.89	1.99	1.96	1.97	1.96	1.98	1.95	1.94	1.95	1.98	0.41	1.85
Na	0.40	0.47	0.38	0.36	0.41	0.45	0.39	0.43	0.46	0.44	0.34	0.18	0.27
K	0.25	0.22	0.24	0.23	0.24	0.25	0.25	0.25	0.24	0.25	0.22	0.12	0.14
Total	15.73	15.70	15.71	15.66	15.71	15.74	15.70	15.72	15.71	15.74	15.64	15.75	15.40

...continued on next page

Table A.2 **Amphiboles** – continued from previous page

	S53-18	**S65-10**	**S65-11**	**S65-12**	**S65-13**	**S65-14**	**S65-15**	**S65-16**	**S65-17**	**S65-18**	**S65-19**	**S65-20**	**S65-21**
SiO_2	43.04	46.43	55.30	45.07	45.23	44.69	45.57	45.64	45.42	44.28	45.84	46.63	54.68
TiO_2	1.55	1.05	0.14	1.01	1.11	1.15	0.80	1.00	0.84	0.46	0.89	0.59	0.01
Al_2O_3	12.95	12.47	1.57	14.08	13.66	13.84	13.83	13.46	13.88	14.75	14.00	12.52	2.00
Cr_2O_3	0.09	0.18	0.03	0.11	0.21	0.15	0.15	0.06	0.16	0.34	0.23	0.13	0.12
FeO	14.74	11.81	19.41	10.91	11.14	11.11	10.76	11.43	11.79	12.67	11.07	11.97	19.72
MnO	0.29	0.24	0.44	0.20	0.16	0.16	0.18	0.16	0.27	0.24	0.18	0.20	0.56
MgO	11.08	13.75	20.47	13.40	13.50	13.31	13.74	13.61	13.40	12.30	13.52	14.22	19.72
CaO	11.32	11.22	1.17	12.16	12.04	11.81	12.05	11.77	11.68	11.30	12.07	11.34	1.49
Na_2O	1.48	1.20	0.12	1.40	1.40	1.30	1.32	1.33	1.34	1.40	1.40	1.25	0.19
K_2O	1.26	0.33	0.01	0.46	0.46	0.39	0.49	0.38	0.35	0.24	0.34	0.32	0.03
Total	97.80	98.68	98.66	98.81	98.91	97.91	98.89	98.85	99.12	97.97	99.54	99.17	98.52
Oxygens	23	23	23	23	23	23	23	23	23	23	23	23	23
Si	6.39	6.65	7.85	6.45	6.48	6.46	6.51	6.53	6.49	6.43	6.50	6.65	7.80
Ti	0.17	0.11	0.01	0.11	0.12	0.12	0.09	0.11	0.09	0.05	0.09	0.06	0.00
Al	2.27	2.10	0.26	2.38	2.30	2.36	2.33	2.27	2.34	2.52	2.34	2.10	0.34
Cr	0.01	0.02	0.00	0.01	0.02	0.02	0.02	0.01	0.02	0.04	0.03	0.01	0.01
Fe	1.83	1.41	2.30	1.31	1.33	1.34	1.28	1.37	1.41	1.54	1.31	1.43	2.35
Mn	0.04	0.03	0.05	0.02	0.02	0.02	0.02	0.02	0.03	0.03	0.02	0.02	0.07
Mg	2.45	2.93	4.33	2.86	2.88	2.87	2.92	2.90	2.86	2.66	2.86	3.02	4.19
Ca	1.80	1.72	0.18	1.87	1.85	1.83	1.84	1.80	1.79	1.76	1.83	1.73	0.23
Na	0.43	0.33	0.03	0.39	0.39	0.36	0.37	0.37	0.37	0.39	0.39	0.34	0.05
K	0.24	0.06	0.00	0.08	0.08	0.07	0.09	0.07	0.06	0.04	0.06	0.06	0.00
Total	15.63	15.38	15.02	15.48	15.48	15.45	15.46	15.44	15.46	15.46	15.44	15.43	15.05

...continued on next page

Table A.2 **Amphiboles** – continued from previous page

	S65-22	**S67-25**	**S67-26**	**S67-27**	**S67-28**	**S67-29**	**S67-30**	**S67-31**	**S67-32**	**S67-33**	**S67-34**	**S67-35**	**S67-36**
SiO_2	46.21	45.42	45.63	45.38	44.73	45.43	43.19	44.99	43.14	47.14	42.98	44.64	44.58
TiO_2	0.56	0.87	0.62	0.84	0.97	0.81	1.21	0.86	1.39	0.58	1.41	0.81	0.80
Al_2O_3	13.56	12.01	11.67	12.31	12.76	12.30	14.28	12.42	14.37	9.71	14.42	12.66	12.50
Cr_2O_3	0.33	0.10	0.12	0.05	0.07	0.14	0.15	0.11	0.08	0.04	0.11	0.17	0.08
FeO	12.69	16.18	15.94	16.25	16.10	15.88	16.09	16.08	16.26	15.02	15.87	15.69	15.72
MnO	0.26	0.20	0.22	0.19	0.18	0.27	0.27	0.24	0.19	0.23	0.19	0.21	0.23
MgO	13.26	10.98	11.16	11.08	10.66	11.07	10.36	10.82	10.11	12.32	10.14	10.81	10.96
CaO	10.57	11.56	12.09	12.02	11.90	11.92	11.76	11.98	11.71	11.85	11.68	11.68	11.53
Na_2O	1.41	1.07	1.01	1.02	1.08	1.04	1.10	0.94	1.20	0.83	1.12	1.12	1.13
K_2O	0.30	0.46	0.38	0.52	0.52	0.44	0.93	0.49	0.81	0.31	0.90	0.44	0.49
Total	99.15	98.85	98.84	99.66	98.97	99.30	99.33	98.94	99.27	98.03	98.83	98.22	98.03
Oxygens	23	23	23	23	23	23	23	23	23	23	23	23	23
Si	6.60	6.64	6.67	6.59	6.54	6.61	6.33	6.58	6.32	6.90	6.32	6.57	6.57
Ti	0.06	0.10	0.07	0.09	0.11	0.09	0.13	0.09	0.15	0.06	0.16	0.09	0.09
Al	2.28	2.07	2.01	2.11	2.20	2.11	2.47	2.14	2.48	1.67	2.50	2.19	2.17
Cr	0.04	0.01	0.01	0.01	0.01	0.02	0.02	0.01	0.01	0.00	0.01	0.02	0.01
Fe	1.51	1.98	1.95	1.97	1.97	1.93	1.97	1.97	1.99	1.84	1.95	1.93	1.94
Mn	0.03	0.03	0.03	0.02	0.02	0.03	0.03	0.03	0.02	0.03	0.02	0.03	0.03
Mg	2.82	2.39	2.43	2.40	2.33	2.40	2.26	2.36	2.21	2.69	2.22	2.37	2.41
Ca	1.62	1.81	1.89	1.87	1.87	1.86	1.85	1.88	1.84	1.86	1.84	1.84	1.82
Na	0.39	0.30	0.29	0.29	0.31	0.29	0.31	0.27	0.34	0.24	0.32	0.32	0.32
K	0.05	0.09	0.07	0.10	0.10	0.08	0.17	0.09	0.15	0.06	0.17	0.08	0.09
Total	15.41	15.42	15.43	15.45	15.45	15.43	15.54	15.42	15.53	15.35	15.51	15.44	15.46

...continued on next page

Table A.2 **Amphiboles** – continued from previous page

	S33-23	**S33-24**	**S33-25**	**S33-26**	**S33-27**	**S33-29**	**S33-23**	**S33-24**	**S33-34**	**s33-1**	**s33-2**	**s33-4**	**s33-5**
SiO_2	46.45	44.16	46.31	47.53	52.57	47.64	50.14	53.10	51.43	46.44	50.42	44.88	46.69
TiO_2	1.13	1.60	1.14	0.95	0.16	0.80	0.10	0.07	0.17	1.08	0.27	1.20	0.99
Al_2O_3	9.47	11.34	9.20	8.98	3.52	7.96	2.77	2.77	3.59	9.56	5.48	10.52	8.68
Cr_2O_3	0.12	0.09	0.11	0.08	0.03	0.15	0.10	0.11	0.09	0.15	0.10	0.10	0.12
FeO	15.63	16.88	16.18	16.25	15.24	16.09	13.41	13.91	14.63	15.15	13.72	15.42	14.97
MnO	0.36	0.38	0.37	0.34	0.35	0.37	0.35	0.35	0.37	0.36	0.34	0.34	0.36
MgO	11.21	10.21	11.29	11.45	14.14	11.81	13.35	14.87	13.77	11.61	13.78	10.76	11.58
CaO	12.13	11.48	11.70	11.37	11.59	11.92	13.57	12.64	12.23	11.94	12.47	11.98	11.96
Na_2O	0.94	1.43	1.03	1.10	0.39	1.09	0.30	0.48	0.53	1.17	0.62	1.23	1.05
K_2O	0.90	1.19	0.87	0.77	0.25	0.69	0.25	0.16	0.19	0.91	0.39	1.11	0.83
Total	98.34	98.76	98.19	98.82	98.25	98.51	99.51	100.51	101.51	98.38	97.60	97.55	97.23
Oxygens	23	23	23	23	23	23	23	23	23	23	23	23	23
Si	6.85	6.55	6.85	6.96	7.62	7.01	7.59	7.66	7.56	6.83	7.36	6.69	6.94
Ti	0.13	0.18	0.13	0.10	0.02	0.09	0.01	0.01	0.02	0.12	0.03	0.14	0.11
Al	1.64	1.98	1.60	1.55	0.60	1.38	0.49	0.47	0.62	1.66	0.94	1.85	1.52
Cr	0.01	0.01	0.01	0.01	0.00	0.02	0.01	0.01	0.01	0.02	0.01	0.01	0.01
Fe	1.93	2.09	2.00	1.99	1.85	1.98	1.70	1.68	1.80	1.86	1.67	1.92	1.86
Mn	0.04	0.05	0.05	0.04	0.04	0.05	0.05	0.04	0.05	0.05	0.04	0.04	0.05
Mg	2.46	2.26	2.49	2.50	3.05	2.59	3.01	3.20	3.02	2.55	3.00	2.39	2.56
Ca	1.92	1.83	1.85	1.78	1.80	1.88	2.20	1.95	1.93	1.88	1.95	1.91	1.90
Na	0.27	0.41	0.30	0.31	0.11	0.31	0.09	0.13	0.15	0.33	0.18	0.36	0.30
K	0.17	0.23	0.16	0.14	0.05	0.13	0.05	0.03	0.04	0.17	0.07	0.21	0.16
Total	15.42	15.59	15.44	15.39	15.14	15.43	15.21	15.18	15.19	15.46	15.26	15.53	15.42

Table A.3: Electron microprobe results for pyroxenes

	S01-1	**S01-2**	**S01-3**	**S01-4**	**S01-5**	**S01-6**	**S01-7**	**S01-8**	**S01-12**	**S01-13**	**S01-14**	**S01-15**	**S01-16**
SiO_2	53.92	51.26	51.52	51.46	50.89	50.14	50.52	51.65	50.46	50.54	49.00	48.41	50.17
TiO_2	0.35	0.49	0.29	0.38	0.20	0.11	1.20	0.43	0.19	0.19	0.08	0.07	0.18
Al_2O_3	2.40	2.26	2.26	2.86	2.16	0.22	2.41	2.29	1.81	1.90	0.16	0.22	2.22
Cr_2O_3	0.01	0.01	0.01	0.01	0.00	0.00	0.00	0.00	0.00	0.00	0.02	0.00	0.00
FeO	10.89	12.15	10.61	10.33	12.02	30.75	11.83	11.32	11.30	12.43	34.48	34.05	13.38
MnO	0.18	0.25	0.16	0.21	0.23	0.45	0.20	0.23	0.15	0.25	0.57	0.56	0.25
MgO	11.99	11.47	11.64	11.59	11.89	15.66	11.42	11.27	11.56	11.12	13.66	13.51	10.54
CaO	21.35	21.64	21.73	21.14	20.77	0.80	20.59	20.80	21.49	20.92	0.35	0.41	20.48
Na_2O	1.02	0.72	0.99	1.19	0.82	0.07	1.14	1.12	1.00	0.86	0.00	0.04	1.00
Total	102.10	100.24	99.20	99.17	98.99	98.20	99.32	99.11	97.95	98.21	98.33	97.27	98.23
Oxygens	6	6	6	6	6	6	6	6	6	6	6	6	6
Si	1.98	1.94	1.96	1.95	1.95	1.99	1.93	1.96	1.95	1.95	1.98	1.98	1.95
Ti	0.01	0.01	0.01	0.01	0.01	0.00	0.03	0.01	0.01	0.01	0.00	0.00	0.01
Al	0.10	0.10	0.10	0.13	0.10	0.01	0.11	0.10	0.08	0.09	0.01	0.01	0.10
Cr	0.00	0.00	0.00	0.00	0.00	0.00	0.00	0.00	0.00	0.00	0.00	0.00	0.00
Fe	0.33	0.38	0.34	0.33	0.38	1.02	0.38	0.36	0.37	0.40	1.17	1.16	0.43
Mn	0.01	0.01	0.00	0.01	0.01	0.02	0.01	0.01	0.00	0.01	0.02	0.02	0.01
Mg	0.66	0.65	0.66	0.65	0.68	0.93	0.65	0.64	0.67	0.64	0.82	0.82	0.61
Ca	0.84	0.88	0.88	0.86	0.85	0.03	0.84	0.85	0.89	0.87	0.02	0.02	0.85
Na	0.07	0.05	0.07	0.09	0.06	0.01	0.08	0.08	0.07	0.06	0.00	0.00	0.07
Total	4.00	4.02	4.02	4.02	4.03	4.00	4.03	4.01	4.04	4.03	4.01	4.02	4.03

...continued on next page

Table A.3 **Pyroxenes** – continued from previous page

	S01-19	**S01-20**	**S01-21**	**S01-22**	**S01-23**	**S01-24**	**S01-26**	**S01-27**	**s33-3**	**s33-7**	**s33-8**	**s33-9**	**s33-12**
SiO_2	48.12	48.48	48.56	48.52	48.32	48.48	48.16	36.13	52.98	53.05	53.33	53.79	52.98
TiO_2	0.07	0.07	0.04	0.07	0.00	0.06	0.07	0.02	0.00	0.00	0.01	0.01	0.03
Al_2O_3	0.39	0.28	0.32	0.38	0.28	0.30	0.36	21.53	0.18	0.25	0.30	0.34	0.35
Cr_2O_3	0.00	0.00	0.02	0.00	0.01	0.00	0.00	0.00	0.03	0.05	0.07	0.01	0.02
FeO	35.64	35.68	35.68	35.33	35.99	35.93	35.32	30.87	8.67	9.07	9.20	9.02	9.34
MnO	0.57	0.58	0.59	0.56	0.55	0.57	0.56	1.68	0.54	0.45	0.35	0.44	0.37
MgO	12.75	12.82	12.61	12.55	12.60	12.64	13.01	2.10	12.53	13.11	12.96	12.82	12.77
CaO	0.42	0.35	0.41	1.00	0.44	0.44	0.40	6.25	24.58	24.29	24.18	24.39	23.97
Na_2O	0.04	0.05	0.03	0.02	0.05	0.02	0.04	0.03	0.16	0.22	0.17	0.19	0.25
Total	98.00	98.31	98.25	98.44	98.25	98.44	97.92	98.61	99.70	100.49	100.59	101.01	100.09
Oxygens	6	6	6	6	6	6	6	6	6	6	6	6	6
Si	1.97	1.97	1.98	1.97	1.97	1.97	1.97	1.47	2.00	1.99	1.99	2.00	1.99
Ti	0.00	0.00	0.00	0.00	0.00	0.00	0.00	0.00	0.00	0.00	0.00	0.00	0.00
Al	0.02	0.01	0.02	0.02	0.01	0.01	0.02	1.03	0.01	0.01	0.01	0.01	0.02
Cr	0.00	0.00	0.00	0.00	0.00	0.00	0.00	0.00	0.00	0.00	0.00	0.00	0.00
Fe	1.22	1.21	1.21	1.20	1.23	1.22	1.21	1.05	0.27	0.28	0.29	0.28	0.29
Mn	0.02	0.02	0.02	0.02	0.02	0.02	0.02	0.06	0.02	0.01	0.01	0.01	0.01
Mg	0.78	0.78	0.77	0.76	0.77	0.77	0.79	0.13	0.70	0.73	0.72	0.71	0.72
Ca	0.02	0.02	0.02	0.04	0.02	0.02	0.02	0.27	0.99	0.97	0.97	0.97	0.96
Na	0.00	0.00	0.00	0.00	0.00	0.00	0.00	0.00	0.01	0.02	0.01	0.01	0.02
Total	4.02	4.02	4.01	4.02	4.02	4.02	4.02	4.01	4.01	4.02	4.01	4.00	4.01

...continued on next page

Table A.3 **Pyroxenes** – continued from previous page

	s33-13	**S33-20**	**S33-21**	**S33-22**	**S33-25**	**S33-32**	**S33-35**	**S33-37**
SiO_2	52.82	53.09	52.87	52.75	52.88	53.47	52.87	52.94
TiO_2	0.00	0.03	0.02	0.00	0.03	0.00	0.03	0.03
Al_2O_3	0.32	0.19	0.28	0.15	0.33	0.24	0.35	0.26
Cr_2O_3	0.03	0.06	0.02	0.02	0.04	0.02	0.01	0.07
FeO	9.68	9.29	9.33	9.54	9.51	9.85	9.43	9.42
MnO	0.41	0.56	0.40	0.48	0.48	0.47	0.48	0.50
MgO	12.56	12.91	12.79	12.75	12.56	12.34	13.56	12.54
CaO	24.06	25.87	24.94	25.29	23.99	24.79	23.57	24.06
Na_2O	0.17	0.12	0.24	0.11	0.23	0.12	0.20	0.16
Total	100.04	102.14	100.91	101.09	100.08	101.31	100.52	100.01
Oxygens	6	6	6	6	6	6	6	6
Si	1.99	1.97	1.98	1.97	1.99	1.99	1.98	1.99
Ti	0.00	0.00	0.00	0.00	0.00	0.00	0.00	0.00
Al	0.01	0.01	0.01	0.01	0.01	0.01	0.02	0.01
Cr	0.00	0.00	0.00	0.00	0.00	0.00	0.00	0.00
Fe	0.30	0.29	0.29	0.30	0.30	0.31	0.29	0.30
Mn	0.01	0.02	0.01	0.02	0.02	0.01	0.02	0.02
Mg	0.71	0.71	0.71	0.71	0.70	0.69	0.76	0.70
Ca	0.97	1.03	1.00	1.01	0.97	0.99	0.94	0.97
Na	0.01	0.01	0.02	0.01	0.02	0.01	0.01	0.01
Total	4.01	4.03	4.03	4.03	4.01	4.01	4.02	4.01

Table A.4: Electron microprobe results for feldspars

	S01-1	**S01-2**	**S01-3**	**S01-4**	**S01-5**	**S01-6**	**S01-7**	**S01-8**	**S01-9**	**S01-10**	**S01-12**	**S01-13**	**S01-14**
SiO_2	54.04	56.60	63.56	62.61	57.78	63.03	56.91	54.52	59.61	63.20	56.56	61.33	56.19
TiO_2	0.01	0.99	0.05	0.00	0.76	0.08	0.07	0.20	0.03	0.00	0.31	0.02	0.03
Al_2O_3	29.29	27.37	23.32	24.00	26.17	23.32	27.51	28.14	25.55	23.30	27.39	23.14	27.35
FeO	0.49	1.22	0.40	0.16	0.94	0.22	0.40	1.30	0.04	0.00	0.83	0.81	0.05
MnO	0.02	0.01	0.03	0.01	0.10	0.03	0.00	0.02	0.07	0.01	0.05	0.03	0.00
MgO	0.10	0.02	0.01	0.00	0.00	0.00	0.03	0.08	0.00	0.02	0.11	0.10	0.00
CaO	10.02	8.44	3.85	4.67	7.37	3.99	8.33	8.52	6.54	4.02	7.93	4.05	8.66
Na_2O	5.39	6.33	8.67	8.40	6.96	8.81	6.56	6.02	7.55	8.56	6.64	8.28	6.23
K_2O	0.05	0.06	0.15	0.18	0.11	0.19	0.09	0.08	0.11	0.17	0.16	0.26	0.07
Total	99.42	101.05	100.04	100.03	100.20	99.67	99.89	98.87	99.50	99.29	99.98	98.02	98.59
Oxygens	8	8	8	8	8	8	8	8	8	8	8	8	8
Si	2.45	2.52	2.80	2.77	2.59	2.79	2.55	2.49	2.67	2.80	2.54	2.77	2.55
Ti	0.00	0.03	0.00	0.00	0.03	0.00	0.00	0.01	0.00	0.00	0.01	0.00	0.00
Al	1.57	1.44	1.21	1.25	1.38	1.22	1.45	1.51	1.35	1.22	1.45	1.23	1.46
Fe	0.02	0.05	0.01	0.01	0.04	0.01	0.01	0.05	0.00	0.00	0.03	0.03	0.00
Mn	0.00	0.00	0.00	0.00	0.00	0.00	0.00	0.00	0.00	0.00	0.00	0.00	0.00
Mg	0.01	0.00	0.00	0.00	0.00	0.00	0.00	0.01	0.00	0.00	0.01	0.01	0.00
Ca	0.49	0.40	0.18	0.22	0.35	0.19	0.40	0.42	0.31	0.19	0.38	0.20	0.42
Na	0.47	0.55	0.74	0.72	0.60	0.76	0.57	0.53	0.65	0.74	0.58	0.73	0.55
K	0.00	0.00	0.01	0.01	0.01	0.01	0.00	0.00	0.01	0.01	0.01	0.01	0.00
Total	5.01	5.00	4.96	4.97	5.00	4.98	5.00	5.02	4.99	4.96	5.02	4.98	4.99

...continued on next page

Table A.4 **Feldspars** – continued from previous page

	S01-15	**S01-16**	**S01-17**	**S01-18**	**S01-19**	**S01-20**	**S10-1**	**S10-2**	**S10-3**	**S10-4**	**S10-5**	**S10-6**	**S10-7**
SiO_2	57.38	55.77	55.74	55.48	59.29	59.86	59.97	60.39	59.25	100.02	63.72	63.72	63.72
TiO_2	0.02	0.00	0.12	0.01	0.16	0.24	0.01	0.00	0.00	0.05	0.04	0.01	0.03
Al_2O_3	26.81	27.71	27.38	27.98	25.29	22.99	24.63	24.93	25.45	0.00	18.93	18.87	18.75
FeO	0.10	1.28	0.52	1.82	0.46	0.75	0.03	0.05	0.11	0.02	0.00	0.01	0.05
MnO	0.03	0.05	0.05	0.03	0.03	0.00	0.01	0.05	0.02	0.06	0.01	0.00	0.01
MgO	0.02	0.05	0.01	0.08	0.00	0.01	0.02	0.01	0.00	0.00	0.02	0.02	0.00
CaO	7.61	7.57	8.20	7.40	6.18	4.26	5.56	5.61	6.46	0.01	0.00	0.00	0.00
Na_2O	7.11	6.80	6.51	6.62	7.91	8.52	8.20	7.96	7.60	0.01	0.93	0.92	0.85
K_2O	0.07	0.07	0.08	0.08	0.10	0.15	0.19	0.24	0.12	0.00	15.08	15.21	15.36
Total	99.14	99.30	98.60	99.50	99.43	96.77	98.63	99.25	99.01	100.16	98.72	98.76	98.77
Oxygens	8	8	8	8	8	8	8	8	8	8	8	8	8
Si	2.59	2.53	2.54	2.51	2.66	2.75	2.70	2.70	2.66	4.00	2.97	2.97	2.98
Ti	0.00	0.00	0.00	0.00	0.01	0.01	0.00	0.00	0.00	0.00	0.00	0.00	0.00
Al	1.42	1.48	1.47	1.49	1.34	1.24	1.31	1.31	1.35	0.00	1.04	1.04	1.03
Fe	0.00	0.05	0.02	0.07	0.02	0.03	0.00	0.00	0.00	0.00	0.00	0.00	0.00
Mn	0.00	0.00	0.00	0.00	0.00	0.00	0.00	0.00	0.00	0.00	0.00	0.00	0.00
Mg	0.00	0.00	0.00	0.01	0.00	0.00	0.00	0.00	0.00	0.00	0.00	0.00	0.00
Ca	0.37	0.37	0.40	0.36	0.30	0.21	0.27	0.27	0.31	0.00	0.00	0.00	0.00
Na	0.62	0.60	0.57	0.58	0.69	0.76	0.72	0.69	0.66	0.00	0.08	0.08	0.08
K	0.00	0.00	0.00	0.00	0.01	0.01	0.01	0.01	0.01	0.00	0.90	0.91	0.92
Total	5.01	5.03	5.01	5.03	5.01	5.01	5.01	4.99	5.00	4.00	5.00	5.00	5.00

...continued on next page

Table A.4 **Feldspars** – continued from previous page

	S10-8	**S10-9**	**S10-10**	**S10-12**	**S10-13**	**S10-14**	**S10-16**	**S10-17**	**S10-18**	**S10-19**	**S10-20**	**S10-23**	**S52-s1**
SiO_2	60.20	60.73	59.61	63.45	60.15	60.15	63.50	62.88	99.29	59.34	59.65	64.07	64.28
TiO_2	0.00	0.00	0.00	0.00	0.01	0.00	0.03	0.03	0.02	0.00	0.00	0.00	0.00
Al_2O_3	24.40	24.19	25.31	18.90	24.77	25.30	19.15	18.78	0.00	25.17	25.26	18.92	18.97
FeO	0.07	0.05	0.24	0.02	0.05	0.00	0.00	0.00	0.04	0.03	0.03	0.02	0.00
MnO	0.07	0.04	0.07	0.06	0.05	0.05	0.02	0.06	0.03	0.03	0.02	0.00	0.00
MgO	0.00	0.02	0.01	0.00	0.02	0.00	0.00	0.00	0.00	0.02	0.00	0.00	0.01
CaO	5.44	5.13	6.13	0.00	5.57	6.03	0.00	0.00	0.01	6.16	6.22	0.02	0.00
Na_2O	8.05	8.41	7.69	0.85	8.11	7.90	0.88	0.54	0.01	7.94	7.75	0.90	1.04
K_2O	0.17	0.20	0.16	15.31	0.27	0.13	15.25	15.81	0.00	0.16	0.15	15.15	15.55
Total	98.40	98.78	99.23	98.58	98.99	99.56	98.83	98.09	99.41	98.86	99.09	99.09	99.86
Oxygens	8	8	8	8	8	8	8	8	8	8	8	8	8
Si	2.71	2.73	2.67	2.97	2.70	2.68	2.96	2.97	4.00	2.67	2.68	2.98	2.97
Ti	0.00	0.00	0.00	0.00	0.00	0.00	0.00	0.00	0.00	0.00	0.00	0.00	0.00
Al	1.30	1.28	1.34	1.04	1.31	1.33	1.05	1.04	0.00	1.34	1.34	1.04	1.03
Fe	0.00	0.00	0.01	0.00	0.00	0.00	0.00	0.00	0.00	0.00	0.00	0.00	0.00
Mn	0.00	0.00	0.00	0.00	0.00	0.00	0.00	0.00	0.00	0.00	0.00	0.00	0.00
Mg	0.00	0.00	0.00	0.00	0.00	0.00	0.00	0.00	0.00	0.00	0.00	0.00	0.00
Ca	0.26	0.25	0.29	0.00	0.27	0.29	0.00	0.00	0.00	0.30	0.30	0.00	0.00
Na	0.70	0.73	0.67	0.08	0.71	0.68	0.08	0.05	0.00	0.69	0.67	0.08	0.09
K	0.01	0.01	0.01	0.91	0.02	0.01	0.91	0.95	0.00	0.01	0.01	0.90	0.92
Total	4.99	5.00	5.00	5.01	5.00	5.00	5.00	5.01	4.00	5.01	5.00	4.99	5.02

...continued on next page

Table A.4 **Feldspars** – continued from previous page

	S52-2	**S52-6**	**S52-7**	**S52-9**	**S52-12**	**S52-13**	**S52-14**	**S64-1**	**S64-3**	**S64-6**	**S64-7**	**S64-9**	**S64-11**
SiO_2	63.91	57.36	57.78	101.05	62.23	55.96	56.12	58.01	101.46	59.24	59.31	63.96	59.48
TiO_2	0.01	0.00	0.01	0.01	0.04	0.01	0.01	0.05	0.03	0.00	0.04	0.03	0.00
Al_2O_3	19.11	26.28	26.13	0.01	19.05	26.06	26.21	24.51	0.00	23.79	23.82	22.16	24.31
FeO	0.00	0.11	0.19	0.06	0.05	0.21	0.06	0.00	0.03	0.03	0.28	0.00	0.16
MnO	0.06	0.03	0.05	0.07	0.04	0.04	0.01	0.00	0.01	0.04	0.02	0.03	0.02
MgO	0.02	0.01	0.02	0.02	0.00	0.00	0.00	0.02	0.01	0.01	0.02	0.01	0.00
CaO	0.02	7.15	7.02	0.00	0.02	6.99	6.87	5.14	0.01	4.48	4.49	3.73	4.78
Na_2O	0.91	7.22	7.18	0.02	0.99	7.09	7.45	8.20	0.01	8.80	8.83	8.60	8.68
K_2O	15.59	0.15	0.17	0.01	15.25	0.17	0.16	0.33	0.01	0.23	0.12	0.05	0.10
Total	99.63	98.31	98.55	101.25	97.67	96.53	96.90	96.27	101.57	96.62	96.93	98.57	97.53
Oxygens	8	8	8	8	8	8	8	8	8	8	8	8	8
Si	2.96	2.61	2.62	4.00	2.95	2.59	2.59	2.68	4.00	2.72	2.72	2.85	2.71
Ti	0.00	0.00	0.00	0.00	0.00	0.00	0.00	0.00	0.00	0.00	0.00	0.00	0.00
Al	1.04	1.41	1.40	0.00	1.06	1.42	1.43	1.33	0.00	1.29	1.29	1.16	1.30
Fe	0.00	0.00	0.01	0.00	0.00	0.01	0.00	0.00	0.00	0.00	0.01	0.00	0.01
Mn	0.00	0.00	0.00	0.00	0.00	0.00	0.00	0.00	0.00	0.00	0.00	0.00	0.00
Mg	0.00	0.00	0.00	0.00	0.00	0.00	0.00	0.00	0.00	0.00	0.00	0.00	0.00
Ca	0.00	0.35	0.34	0.00	0.00	0.35	0.34	0.25	0.00	0.22	0.22	0.18	0.23
Na	0.08	0.64	0.63	0.00	0.09	0.64	0.67	0.73	0.00	0.78	0.78	0.74	0.77
K	0.92	0.01	0.01	0.00	0.92	0.01	0.01	0.02	0.00	0.01	0.01	0.00	0.01
Total	5.02	5.01	5.00	4.00	5.03	5.02	5.03	5.03	4.00	5.03	5.03	4.94	5.03

...continued on next page

Table A.4 **Feldspars** – continued from previous page

	S64-12	**S64-13**	**S62-2**	**S62-3**	**S62-4**	**S62-5**	**S62-6**	**S62-7**	**S62-8**	**S62-9**	**S62-10**	**S62-11**	**S62-12**
SiO_2	59.52	59.08	64.50	63.90	64.30	64.25	64.16	64.05	66.82	67.73	66.43	66.25	66.32
TiO_2	0.00	0.00	0.00	0.01	0.02	0.01	0.02	0.01	0.02	0.00	0.01	0.00	0.00
Al_2O_3	23.94	24.73	22.95	23.78	23.12	23.64	23.46	23.39	18.50	21.27	18.65	18.80	18.64
FeO	0.06	0.14	0.00	0.06	0.29	0.00	0.06	0.25	0.04	0.00	0.02	0.05	0.15
MnO	0.10	0.01	0.04	0.05	0.08	0.02	0.02	0.04	0.01	0.03	0.03	0.03	0.05
MgO	0.00	0.02	0.00	0.02	0.03	0.00	0.00	0.00	0.02	0.02	0.01	0.03	0.00
CaO	4.61	5.23	4.45	4.97	4.31	4.82	4.75	4.78	0.00	2.10	0.01	0.06	0.03
Na_2O	9.03	8.44	8.51	8.24	8.72	8.10	8.21	8.50	1.39	10.04	1.14	1.37	0.99
K_2O	0.10	0.11	0.17	0.22	0.14	0.30	0.29	0.11	14.35	0.11	15.08	14.67	15.45
Total	97.37	97.75	100.63	101.25	101.01	101.15	100.98	101.13	101.15	101.30	101.38	101.26	101.63
Oxygens	8	8	8	8	8	8	8	8	8	8	8	8	8
Si	2.72	2.69	2.82	2.79	2.81	2.80	2.80	2.80	3.02	2.93	3.01	3.00	3.00
Ti	0.00	0.00	0.00	0.00	0.00	0.00	0.00	0.00	0.00	0.00	0.00	0.00	0.00
Al	1.29	1.33	1.18	1.22	1.19	1.21	1.21	1.20	0.99	1.08	1.00	1.00	1.00
Fe	0.00	0.01	0.00	0.00	0.01	0.00	0.00	0.01	0.00	0.00	0.00	0.00	0.01
Mn	0.00	0.00	0.00	0.00	0.00	0.00	0.00	0.00	0.00	0.00	0.00	0.00	0.00
Mg	0.00	0.00	0.00	0.00	0.00	0.00	0.00	0.00	0.00	0.00	0.00	0.00	0.00
Ca	0.23	0.25	0.21	0.23	0.20	0.23	0.22	0.22	0.00	0.10	0.00	0.00	0.00
Na	0.80	0.74	0.72	0.70	0.74	0.68	0.70	0.72	0.12	0.84	0.10	0.12	0.09
K	0.01	0.01	0.01	0.01	0.01	0.02	0.02	0.01	0.83	0.01	0.87	0.85	0.89
Total	5.04	5.03	4.95	4.96	4.97	4.94	4.95	4.96	4.96	4.96	4.98	4.98	4.99

...continued on next page

Table A.4 **Feldspars** – continued from previous page

	S62-14	**S62-15**	**S62-16**	**S62-17**	**S62-18**	**S62-19**	**S50-2**	**S50-3**	**S50-4**	**S50-5**	**S50-6**	**S50-7**	**S50-8**
SiO_2	66.53	63.76	63.04	63.53	63.40	62.88	59.57	58.29	58.45	58.96	59.02	58.97	60.24
TiO_2	0.00	0.03	0.00	0.01	0.00	0.05	0.01	0.03	0.06	0.35	0.04	0.00	0.02
Al_2O_3	18.39	23.53	23.87	23.47	23.87	24.06	25.86	26.47	26.61	26.15	26.02	25.11	25.22
FeO	0.02	0.00	0.07	0.18	0.21	0.12	0.13	0.25	0.47	0.59	0.21	0.05	0.16
MnO	0.00	0.00	0.03	0.05	0.05	0.05	0.05	0.06	0.04	0.05	0.00	0.02	0.00
MgO	0.00	0.00	0.00	0.01	0.01	0.03	0.02	0.01	0.02	0.00	0.02	0.01	0.00
CaO	0.03	4.83	4.84	4.58	4.90	5.11	6.90	7.79	7.96	7.48	7.33	6.66	6.13
Na_2O	1.24	8.18	8.32	8.80	8.48	8.14	7.16	6.91	6.74	6.97	7.10	7.14	7.73
K_2O	14.88	0.21	0.17	0.11	0.12	0.10	0.09	0.08	0.09	0.07	0.11	0.10	0.08
Total	101.09	100.54	100.34	100.74	101.05	100.54	99.79	99.90	100.44	100.61	99.84	98.06	99.58
Oxygens	8	8	8	8	8	8	8	8	8	8	8	8	8
Si	3.02	2.80	2.78	2.79	2.77	2.76	2.66	2.61	2.60	2.62	2.64	2.67	2.69
Ti	0.00	0.00	0.00	0.00	0.00	0.00	0.00	0.00	0.00	0.01	0.00	0.00	0.00
Al	0.98	1.22	1.24	1.21	1.23	1.25	1.36	1.40	1.40	1.37	1.37	1.34	1.33
Fe	0.00	0.00	0.00	0.01	0.01	0.00	0.00	0.01	0.02	0.02	0.01	0.00	0.01
Mn	0.00	0.00	0.00	0.00	0.00	0.00	0.00	0.00	0.00	0.00	0.00	0.00	0.00
Mg	0.00	0.00	0.00	0.00	0.00	0.00	0.00	0.00	0.00	0.00	0.00	0.00	0.00
Ca	0.00	0.23	0.23	0.22	0.23	0.24	0.33	0.37	0.38	0.36	0.35	0.32	0.29
Na	0.11	0.70	0.71	0.75	0.72	0.69	0.62	0.60	0.58	0.60	0.61	0.63	0.67
K	0.86	0.01	0.01	0.01	0.01	0.01	0.01	0.00	0.01	0.00	0.01	0.01	0.00
Total	4.97	4.95	4.97	4.98	4.97	4.96	4.98	4.99	4.99	4.99	4.99	4.97	4.99

...continued on next page

Table A.4 **Feldspars** – continued from previous page

	S50-9	**S50-10**	**S50-11**	**S50-13**	**S55-1**	**S55-2**	**S55-3**	**S55-4**	**S55-5**	**S55-6**	**S55-7**	**S55-8**	**S21-2**
SiO_2	59.37	57.84	57.77	64.95	65.76	64.77	58.54	58.35	64.31	64.06	63.72	57.36	52.88
TiO_2	0.01	0.05	0.02	0.35	0.00	0.02	0.01	0.00	0.00	0.02	0.01	0.00	0.01
Al_2O_3	25.68	26.60	26.60	18.74	18.85	18.87	26.26	26.25	19.08	19.27	19.16	25.96	28.71
FeO	0.16	0.38	0.14	0.57	0.03	0.01	0.25	0.11	0.00	0.02	0.00	0.18	0.11
MnO	0.05	0.00	0.00	0.04	0.00	0.07	0.03	0.05	0.04	0.04	0.02	0.06	0.07
MgO	0.01	0.02	0.00	0.00	0.00	0.01	0.00	0.02	0.01	0.01	0.01	0.02	0.02
CaO	6.74	7.74	7.77	0.00	0.03	0.00	7.25	7.29	0.00	0.00	0.00	6.87	9.70
Na_2O	7.44	6.71	6.75	0.04	1.30	0.89	7.16	7.14	0.80	1.06	0.81	7.46	5.66
K_2O	0.18	0.12	0.09	16.54	15.32	15.68	0.14	0.14	15.96	15.59	15.87	0.15	0.08
Total	99.63	99.46	99.14	101.24	101.30	100.31	99.64	99.36	100.21	100.08	99.60	98.06	97.24
Oxygens	8	8	8	8	8	8	8	8	8	8	8	8	8
Si	2.66	2.60	2.60	2.97	2.99	2.98	2.62	2.62	2.97	2.96	2.96	2.61	2.45
Ti	0.00	0.00	0.00	0.01	0.00	0.00	0.00	0.00	0.00	0.00	0.00	0.00	0.00
Al	1.35	1.41	1.41	1.01	1.01	1.02	1.39	1.39	1.04	1.05	1.05	1.39	1.57
Fe	0.01	0.01	0.01	0.02	0.00	0.00	0.01	0.00	0.00	0.00	0.00	0.01	0.00
Mn	0.00	0.00	0.00	0.00	0.00	0.00	0.00	0.00	0.00	0.00	0.00	0.00	0.00
Mg	0.00	0.00	0.00	0.00	0.00	0.00	0.00	0.00	0.00	0.00	0.00	0.00	0.00
Ca	0.32	0.37	0.37	0.00	0.00	0.00	0.35	0.35	0.00	0.00	0.00	0.34	0.48
Na	0.65	0.58	0.59	0.00	0.11	0.08	0.62	0.62	0.07	0.10	0.07	0.66	0.51
K	0.01	0.01	0.01	0.97	0.89	0.92	0.01	0.01	0.94	0.92	0.94	0.01	0.00
Total	5.00	4.99	4.99	4.99	5.01	5.01	5.00	5.00	5.02	5.02	5.02	5.02	5.02

...continued on next page

Table A.4 **Feldspars** – continued from previous page

	S21-3	**S21-4**	**S21-5**	**S21-6**	**S21-8**	**S21-11**	**S21-12**	**S21-13**	**S21-14**	**S21-15**	**S21-16**	**S51-1**	**S51-2**
SiO_2	52.21	52.28	53.15	53.46	53.18	54.77	54.87	56.20	56.01	55.75	30.55	65.05	65.11
TiO_2	0.00	0.00	0.01	0.02	0.02	0.00	0.00	0.01	0.04	0.05	38.50	0.03	0.02
Al_2O_3	29.38	29.50	28.73	28.59	29.31	28.84	28.85	28.74	28.06	28.49	1.50	19.13	19.09
FeO	0.10	0.06	0.06	0.26	0.10	0.06	0.07	0.04	0.07	0.28	0.43	0.01	0.26
MnO	0.04	0.06	0.07	0.03	0.01	0.03	0.00	0.00	0.08	0.03	0.10	0.00	0.00
MgO	0.01	0.00	0.00	0.01	0.00	0.01	0.02	0.00	0.01	0.02	0.02	0.00	0.00
CaO	10.19	10.08	9.39	9.41	10.08	10.40	10.40	9.53	9.68	9.73	27.53	0.00	0.00
Na_2O	5.28	5.32	5.69	5.75	5.40	5.27	5.33	5.80	5.70	5.64	0.05	0.44	0.69
K_2O	0.09	0.03	0.06	0.04	0.07	0.04	0.07	0.06	0.06	0.04	0.00	16.81	16.21
Total	97.29	97.33	97.17	97.56	98.16	99.42	99.61	100.38	99.70	100.03	98.70	101.47	101.37
Oxygens	8	8	8	8	8	8	8	8	8	8	8	8	8
Si	2.42	2.42	2.46	2.47	2.44	2.48	2.48	2.51	2.52	2.50	1.61	2.97	2.97
Ti	0.00	0.00	0.00	0.00	0.00	0.00	0.00	0.00	0.00	0.00	1.53	0.00	0.00
Al	1.61	1.61	1.57	1.55	1.58	1.54	1.54	1.51	1.49	1.51	0.09	1.03	1.03
Fe	0.00	0.00	0.00	0.01	0.00	0.00	0.00	0.00	0.00	0.01	0.02	0.00	0.01
Mn	0.00	0.00	0.00	0.00	0.00	0.00	0.00	0.00	0.00	0.00	0.00	0.00	0.00
Mg	0.00	0.00	0.00	0.00	0.00	0.00	0.00	0.00	0.00	0.00	0.00	0.00	0.00
Ca	0.51	0.50	0.47	0.47	0.50	0.50	0.50	0.46	0.47	0.47	1.56	0.00	0.00
Na	0.47	0.48	0.51	0.51	0.48	0.46	0.47	0.50	0.50	0.49	0.01	0.04	0.06
K	0.01	0.00	0.00	0.00	0.00	0.00	0.00	0.00	0.00	0.00	0.00	0.98	0.94
Total	5.02	5.01	5.01	5.01	5.01	4.99	4.99	4.99	4.98	4.99	4.82	5.02	5.02

...continued on next page

Table A.4 **Feldspars** – continued from previous page

	S51-3	**S51-4**	**S51-5**	**S51-6**	**S51-7**	**S51-8**	**S51-9**	**S51-10**	**S51-11**	**S51-12**	**S51-13**	**S55-1**	**S33-1**
SiO_2	65.02	65.66	60.33	65.07	65.24	59.89	65.04	64.73	64.52	60.74	64.73	64.98	60.71
TiO_2	0.02	0.00	0.00	0.00	0.00	0.03	0.01	0.00	0.06	0.00	0.04	0.01	0.00
Al_2O_3	19.02	19.03	25.86	19.11	19.12	26.55	19.10	19.12	19.17	25.52	19.16	18.80	25.03
FeO	0.04	0.05	0.03	0.04	0.00	0.03	0.03	0.01	0.01	0.05	0.00	0.00	0.00
MnO	0.01	0.00	0.02	0.00	0.05	0.03	0.06	0.04	0.04	0.08	0.05	0.00	0.02
MgO	0.03	0.00	0.00	0.00	0.00	0.00	0.00	0.01	0.00	0.01	0.02	0.00	0.00
CaO	0.00	0.00	6.75	0.04	0.00	7.33	0.01	0.00	0.00	6.32	0.00	0.00	6.06
Na_2O	0.86	0.92	7.49	0.97	0.77	7.21	1.00	0.76	0.94	7.71	0.89	0.89	7.74
K_2O	16.04	16.12	0.14	15.98	15.84	0.11	15.83	16.03	15.94	0.15	15.99	16.00	0.22
Total	101.04	101.78	100.63	101.22	101.03	101.19	101.09	100.70	100.68	100.58	100.88	100.68	99.78
Oxygens	8	8	8	8	8	8	8	8	8	8	8	8	8
Si	2.97	2.98	2.67	2.97	2.98	2.64	2.97	2.97	2.96	2.68	2.97	2.98	2.70
Ti	0.00	0.00	0.00	0.00	0.00	0.00	0.00	0.00	0.00	0.00	0.00	0.00	0.00
Al	1.03	1.02	1.35	1.03	1.03	1.38	1.03	1.03	1.04	1.33	1.04	1.02	1.31
Fe	0.00	0.00	0.00	0.00	0.00	0.00	0.00	0.00	0.00	0.00	0.00	0.00	0.00
Mn	0.00	0.00	0.00	0.00	0.00	0.00	0.00	0.00	0.00	0.00	0.00	0.00	0.00
Mg	0.00	0.00	0.00	0.00	0.00	0.00	0.00	0.00	0.00	0.00	0.00	0.00	0.00
Ca	0.00	0.00	0.32	0.00	0.00	0.35	0.00	0.00	0.00	0.30	0.00	0.00	0.29
Na	0.08	0.08	0.64	0.09	0.07	0.62	0.09	0.07	0.08	0.66	0.08	0.08	0.67
K	0.94	0.93	0.01	0.93	0.92	0.01	0.92	0.94	0.93	0.01	0.93	0.94	0.01
Total	5.02	5.02	4.98	5.02	5.00	4.98	5.02	5.01	5.02	4.99	5.02	5.02	4.98

...continued on next page

Table A.4 **Feldspars** – continued from previous page

	S33-3	**S33-4**	**S33-5**	**S33-6**	**S33-7**	**S33-8**	**S33-9**	**S33-10**	**S33-11**	**S33-12**	**S33-13**	**S33-14**	**S33-15**
SiO_2	62.82	60.24	60.76	60.73	60.31	59.42	60.56	59.81	60.16	59.23	60.25	60.23	60.76
TiO_2	0.01	0.00	0.00	0.00	0.00	0.00	0.00	0.00	0.00	0.31	0.04	0.02	0.00
Al_2O_3	24.00	25.29	24.70	25.15	25.07	26.00	25.60	25.72	24.95	25.52	25.18	24.92	24.67
FeO	0.20	0.12	0.05	0.10	0.03	0.14	0.08	0.20	0.02	0.32	0.07	0.14	0.06
MnO	0.01	0.01	0.01	0.03	0.04	0.00	0.04	0.00	0.01	0.09	0.00	0.03	0.10
MgO	0.02	0.01	0.01	0.00	0.00	0.00	0.00	0.02	0.01	0.13	0.00	0.01	0.01
CaO	4.77	6.34	5.88	6.15	6.09	7.08	6.40	6.34	6.14	7.02	6.13	6.12	5.55
Na_2O	8.60	7.67	7.30	7.91	7.98	7.38	7.57	7.65	7.54	7.06	7.52	7.85	7.89
K_2O	0.09	0.11	0.26	0.12	0.15	0.11	0.19	0.15	0.19	0.14	0.15	0.15	0.33
Total	100.53	99.78	98.96	100.19	99.67	100.13	100.45	99.89	99.02	99.81	99.34	99.46	99.36
Oxygens	8	8	8	8	8	8	8	8	8	8	8	8	8
Si	2.76	2.68	2.72	2.69	2.69	2.64	2.68	2.66	2.70	2.65	2.69	2.69	2.71
Ti	0.00	0.00	0.00	0.00	0.00	0.00	0.00	0.00	0.00	0.01	0.00	0.00	0.00
Al	1.24	1.33	1.30	1.31	1.32	1.36	1.33	1.35	1.32	1.34	1.33	1.31	1.30
Fe	0.01	0.00	0.00	0.00	0.00	0.01	0.00	0.01	0.00	0.01	0.00	0.01	0.00
Mn	0.00	0.00	0.00	0.00	0.00	0.00	0.00	0.00	0.00	0.00	0.00	0.00	0.00
Mg	0.00	0.00	0.00	0.00	0.00	0.00	0.00	0.00	0.00	0.01	0.00	0.00	0.00
Ca	0.22	0.30	0.28	0.29	0.29	0.34	0.30	0.30	0.29	0.34	0.29	0.29	0.27
Na	0.73	0.66	0.63	0.68	0.69	0.64	0.65	0.66	0.66	0.61	0.65	0.68	0.68
K	0.01	0.01	0.01	0.01	0.01	0.01	0.01	0.01	0.01	0.01	0.01	0.01	0.02
Total	4.98	4.99	4.95	4.99	5.00	4.99	4.98	5.00	4.98	4.98	4.97	4.99	4.99

...continued on next page

Table A.4 **Feldspars** – continued from previous page

	S33-16	**S33-17**	**S33-18**	**S33-19**	**S33-21**	**S33-22**	**S65-1**	**S65-2**	**S65-3**	**S65-4**	**S65-5**	**S65-6**	**S65-8**
SiO_2	59.65	59.72	60.53	59.92	60.38	60.57	51.01	54.49	58.03	52.25	51.37	50.34	53.37
TiO_2	0.01	0.01	0.02	0.02	0.01	0.02	0.00	0.00	0.00	0.03	0.01	0.02	0.00
Al_2O_3	25.45	25.85	24.92	25.56	25.18	25.43	31.79	29.33	26.97	30.68	31.93	32.63	30.30
FeO	0.10	0.04	0.05	0.06	0.05	0.06	0.03	0.09	0.05	0.08	0.17	0.15	0.36
MnO	0.06	0.04	0.02	0.03	0.06	0.00	0.01	0.08	0.01	0.01	0.02	0.03	0.06
MgO	0.00	0.01	0.01	0.02	0.00	0.01	0.02	0.01	0.01	0.00	0.00	0.00	0.00
CaO	6.22	6.55	5.92	6.47	6.19	6.29	13.59	10.54	7.72	12.41	13.52	14.21	11.77
Na_2O	7.38	6.78	7.62	7.49	7.68	7.64	3.49	5.17	6.98	4.19	3.57	3.25	4.57
K_2O	0.16	0.11	0.15	0.18	0.20	0.17	0.02	0.04	0.05	0.03	0.02	0.01	0.04
Total	99.03	99.12	99.25	99.74	99.74	100.18	99.97	99.75	99.82	99.69	100.61	100.64	100.48
Oxygens	8	8	8	8	8	8	8	8	8	8	8	8	8
Si	2.68	2.67	2.70	2.67	2.69	2.69	2.32	2.46	2.60	2.37	2.32	2.28	2.40
Ti	0.00	0.00	0.00	0.00	0.00	0.00	0.00	0.00	0.00	0.00	0.00	0.00	0.00
Al	1.35	1.36	1.31	1.34	1.32	1.33	1.70	1.56	1.42	1.64	1.70	1.74	1.61
Fe	0.00	0.00	0.00	0.00	0.00	0.00	0.00	0.00	0.00	0.00	0.01	0.01	0.01
Mn	0.00	0.00	0.00	0.00	0.00	0.00	0.00	0.00	0.00	0.00	0.00	0.00	0.00
Mg	0.00	0.00	0.00	0.00	0.00	0.00	0.00	0.00	0.00	0.00	0.00	0.00	0.00
Ca	0.30	0.31	0.28	0.31	0.30	0.30	0.66	0.51	0.37	0.60	0.65	0.69	0.57
Na	0.64	0.59	0.66	0.65	0.66	0.66	0.31	0.45	0.61	0.37	0.31	0.28	0.40
K	0.01	0.01	0.01	0.01	0.01	0.01	0.00	0.00	0.00	0.00	0.00	0.00	0.00
Total	4.98	4.95	4.97	4.99	4.99	4.98	4.99	4.99	5.00	4.99	4.99	5.00	4.99

...continued on next page

Table A.4 **Feldspars** – continued from previous page

	S65-9	**S65-10**	**S67-1**	**S67-2**	**S67-3**	**S67-4**	**S67-5**	**S67-6**	**S67-8**	**S67-9**	**S67-10**	**S67-11**	**S53-1**
SiO_2	53.47	100.51	44.98	45.33	45.90	46.18	46.69	46.01	45.53	45.33	46.22	46.99	59.15
TiO_2	0.00	0.00	0.00	0.00	0.00	0.00	0.00	0.02	0.01	0.03	0.01	0.00	0.00
Al_2O_3	30.45	0.00	35.22	34.46	35.09	34.52	34.26	34.96	34.91	35.18	34.44	33.78	26.11
FeO	0.25	0.00	0.03	0.81	0.09	0.05	0.05	0.05	0.06	0.09	0.01	0.05	0.02
MnO	0.02	0.04	0.06	0.01	0.01	0.05	0.00	0.01	0.03	0.02	0.04	0.03	0.06
MgO	0.00	0.00	0.02	0.34	0.00	0.00	0.00	0.00	0.02	0.01	0.00	0.02	0.02
CaO	11.95	0.00	17.72	15.95	17.42	16.72	16.40	17.26	17.49	17.59	16.74	16.19	7.00
Na_2O	4.73	0.02	1.09	1.05	1.22	1.67	1.83	1.38	1.13	1.02	1.66	1.94	7.16
K_2O	0.03	0.01	0.01	0.17	0.00	0.03	0.00	0.00	0.01	0.02	0.01	0.03	0.07
Total	100.90	100.59	99.14	98.12	99.73	99.22	99.24	99.70	99.18	99.28	99.14	99.03	99.59
Oxygens	8	8	8	8	8	8	8	8	8	8	8	8	8
Si	2.40	4.00	2.09	2.12	2.11	2.14	2.15	2.12	2.11	2.10	2.14	2.17	2.64
Ti	0.00	0.00	0.00	0.00	0.00	0.00	0.00	0.00	0.00	0.00	0.00	0.00	0.00
Al	1.61	0.00	1.93	1.90	1.90	1.88	1.86	1.90	1.91	1.92	1.88	1.84	1.37
Fe	0.01	0.00	0.00	0.03	0.00	0.00	0.00	0.00	0.00	0.00	0.00	0.00	0.00
Mn	0.00	0.00	0.00	0.00	0.00	0.00	0.00	0.00	0.00	0.00	0.00	0.00	0.00
Mg	0.00	0.00	0.00	0.02	0.00	0.00	0.00	0.00	0.00	0.00	0.00	0.00	0.00
Ca	0.57	0.00	0.88	0.80	0.86	0.83	0.81	0.85	0.87	0.87	0.83	0.80	0.34
Na	0.41	0.00	0.10	0.10	0.11	0.15	0.16	0.12	0.10	0.09	0.15	0.17	0.62
K	0.00	0.00	0.00	0.01	0.00	0.00	0.00	0.00	0.00	0.00	0.00	0.00	0.00
Total	5.00	4.00	5.00	4.98	4.99	5.00	5.00	4.99	4.99	4.99	5.00	5.00	4.98

...continued on next page

Table A.4 **Feldspars** – continued from previous page

	S53-2	**S53-3**	**S53-4**	**S53-5**	**S53-6**	**S53-7**	**S53-8**	**S53-9**	**S53-10**	**S53-11**	**S53-12**	**S53-13**	**S53-14**
SiO_2	56.41	59.07	58.52	57.38	56.47	57.61	59.75	58.14	57.73	56.01	57.55	57.36	59.33
TiO_2	0.00	0.00	0.03	0.00	0.04	0.01	0.00	0.01	0.00	0.02	0.00	0.00	0.00
Al_2O_3	27.70	26.07	26.65	27.04	27.59	26.80	25.77	26.99	27.07	28.24	27.26	27.25	25.53
FeO	0.04	0.02	0.21	0.03	0.19	0.21	0.09	0.12	0.03	0.19	0.06	0.23	0.08
MnO	0.00	0.05	0.02	0.02	0.02	0.00	0.00	0.00	0.07	0.05	0.06	0.02	0.02
MgO	0.02	0.01	0.01	0.02	0.00	0.01	0.00	0.02	0.00	0.00	0.00	0.01	0.00
CaO	8.37	7.22	8.15	8.24	9.08	7.99	6.56	7.96	8.27	9.58	8.40	8.36	6.72
Na_2O	6.51	7.20	6.78	6.44	5.91	6.27	7.66	6.68	6.74	5.62	6.54	6.35	7.05
K_2O	0.11	0.09	0.19	0.14	0.25	0.47	0.26	0.20	0.08	0.14	0.10	0.39	0.68
Total	99.15	99.73	100.56	99.31	99.55	99.38	100.10	100.12	99.99	99.85	99.97	99.98	99.42
Oxygens	8	8	8	8	8	8	8	8	8	8	8	8	8
Si	2.55	2.64	2.60	2.58	2.54	2.59	2.66	2.59	2.58	2.52	2.58	2.57	2.66
Ti	0.00	0.00	0.00	0.00	0.00	0.00	0.00	0.00	0.00	0.00	0.00	0.00	0.00
Al	1.47	1.37	1.40	1.43	1.46	1.42	1.35	1.42	1.43	1.50	1.44	1.44	1.35
Fe	0.00	0.00	0.01	0.00	0.01	0.01	0.00	0.00	0.00	0.01	0.00	0.01	0.00
Mn	0.00	0.00	0.00	0.00	0.00	0.00	0.00	0.00	0.00	0.00	0.00	0.00	0.00
Mg	0.00	0.00	0.00	0.00	0.00	0.00	0.00	0.00	0.00	0.00	0.00	0.00	0.00
Ca	0.40	0.35	0.39	0.40	0.44	0.39	0.31	0.38	0.40	0.46	0.40	0.40	0.32
Na	0.57	0.62	0.58	0.56	0.52	0.55	0.66	0.58	0.58	0.49	0.57	0.55	0.61
K	0.01	0.01	0.01	0.01	0.01	0.03	0.01	0.01	0.00	0.01	0.01	0.02	0.04
Total	5.00	4.99	4.99	4.99	4.99	4.98	5.00	4.99	5.00	4.98	4.99	5.00	4.99

...continued on next page

Table A.4 **Feldspars** – continued from previous page

	S53-18	**S65-12**	**S65-13**	**S65-14**	**S65-15**	**S65-16**	**S65-17**	**S65-18**	**S65-19**	**S65-20**	**S65-21**	**S65-22**	**S65-23**
SiO_2	56.40	53.01	48.19	48.62	60.66	51.73	48.91	48.12	60.63	61.14	61.83	61.43	61.70
TiO_2	0.02	0.02	0.05	0.00	0.02	0.02	0.01	0.01	0.00	0.00	0.03	0.02	0.01
Al_2O_3	27.97	30.66	33.97	33.57	25.43	31.29	33.10	33.93	25.14	25.17	24.89	25.03	24.55
FeO	0.15	0.31	0.21	0.05	0.05	0.02	0.11	0.06	0.13	0.07	0.23	0.05	0.09
MnO	0.05	0.08	0.07	0.08	0.08	0.06	0.04	0.08	0.00	0.01	0.05	0.03	0.05
MgO	0.00	0.00	0.01	0.01	0.00	0.00	0.02	0.03	0.00	0.01	0.00	0.00	0.00
CaO	9.22	11.87	15.04	15.08	6.33	12.91	15.24	15.42	6.10	5.89	5.70	5.74	5.50
Na_2O	6.18	4.36	2.25	2.49	7.33	3.92	2.47	2.15	7.47	7.65	7.98	7.75	7.90
K_2O	0.05	0.01	0.01	0.00	0.03	0.03	0.00	0.01	0.04	0.04	0.02	0.02	0.03
Total	100.04	100.32	99.80	99.90	99.93	100.00	99.91	99.82	99.51	99.97	100.73	100.07	99.83
Oxygens	8	8	8	8	8	8	8	8	8	8	8	8	8
Si	2.53	2.39	2.20	2.22	2.69	2.34	2.23	2.20	2.70	2.71	2.72	2.72	2.73
Ti	0.00	0.00	0.00	0.00	0.00	0.00	0.00	0.00	0.00	0.00	0.00	0.00	0.00
Al	1.48	1.63	1.83	1.81	1.33	1.67	1.78	1.83	1.32	1.31	1.29	1.30	1.28
Fe	0.01	0.01	0.01	0.00	0.00	0.00	0.00	0.00	0.00	0.00	0.01	0.00	0.00
Mn	0.00	0.00	0.00	0.00	0.00	0.00	0.00	0.00	0.00	0.00	0.00	0.00	0.00
Mg	0.00	0.00	0.00	0.00	0.00	0.00	0.00	0.00	0.00	0.00	0.00	0.00	0.00
Ca	0.44	0.57	0.74	0.74	0.30	0.63	0.75	0.76	0.29	0.28	0.27	0.27	0.26
Na	0.54	0.38	0.20	0.22	0.63	0.34	0.22	0.19	0.65	0.66	0.68	0.66	0.68
K	0.00	0.00	0.00	0.00	0.00	0.00	0.00	0.00	0.00	0.00	0.00	0.00	0.00
Total	5.00	4.99	4.98	4.99	4.96	4.99	4.99	4.98	4.96	4.96	4.97	4.96	4.96

...continued on next page

Table A.4 **Feldspars** – continued from previous page

	S65-24	**S65-25**	**S65-26**	**S65-27**	**S67-10**	**S67-11**	**S67-12**	**S67-13**	**S67-14**	**S67-15**	**S67-16**	**S67-17**	**S67-18**
SiO_2	47.16	46.13	51.68	56.28	44.97	45.33	44.86	46.11	46.83	46.04	45.56	45.96	45.61
TiO_2	0.00	0.00	0.01	0.01	0.02	0.00	0.04	0.00	0.01	0.00	0.00	0.00	0.01
Al_2O_3	34.66	35.38	31.51	27.99	36.42	36.16	36.14	35.55	34.63	35.15	35.43	35.21	35.44
FeO	0.07	0.44	0.02	0.25	0.16	0.25	0.32	0.17	0.08	0.10	0.10	0.08	0.11
MnO	0.07	0.11	0.02	0.06	0.00	0.02	0.00	0.04	0.02	0.10	0.01	0.03	0.00
MgO	0.00	0.00	0.00	0.09	0.00	0.01	0.03	0.00	0.00	0.02	0.00	0.01	0.00
CaO	16.63	16.89	12.40	8.83	17.75	17.89	17.40	17.36	16.80	16.75	16.80	16.55	16.50
Na_2O	1.66	1.29	3.72	5.26	0.90	0.87	0.89	1.23	1.53	1.39	1.12	1.29	1.30
K_2O	0.02	0.01	0.02	0.19	0.01	0.00	0.04	0.00	0.02	0.02	0.00	0.01	0.00
Total	100.26	100.25	99.38	98.96	100.24	100.53	99.72	100.46	99.92	99.57	99.02	99.13	98.97
Oxygens	8	8	8	8	8	8	8	8	8	8	8	8	8
Si	2.15	2.11	2.35	2.54	2.06	2.07	2.07	2.11	2.15	2.12	2.11	2.12	2.11
Ti	0.00	0.00	0.00	0.00	0.00	0.00	0.00	0.00	0.00	0.00	0.00	0.00	0.00
Al	1.87	1.91	1.69	1.49	1.97	1.95	1.96	1.91	1.87	1.91	1.93	1.92	1.93
Fe	0.00	0.02	0.00	0.01	0.01	0.01	0.01	0.01	0.00	0.00	0.00	0.00	0.00
Mn	0.00	0.00	0.00	0.00	0.00	0.00	0.00	0.00	0.00	0.00	0.00	0.00	0.00
Mg	0.00	0.00	0.00	0.01	0.00	0.00	0.00	0.00	0.00	0.00	0.00	0.00	0.00
Ca	0.81	0.83	0.60	0.43	0.87	0.88	0.86	0.85	0.83	0.83	0.83	0.82	0.82
Na	0.15	0.11	0.33	0.46	0.08	0.08	0.08	0.11	0.14	0.12	0.10	0.12	0.12
K	0.00	0.00	0.00	0.01	0.00	0.00	0.00	0.00	0.00	0.00	0.00	0.00	0.00
Total	4.99	4.99	4.97	4.95	4.99	4.99	4.99	4.99	4.99	4.99	4.98	4.98	4.98

...continued on next page

Table A.4 **Feldspars** – continued from previous page

	S67-19	**S33-23**	**S33-24**	**S33-25**	**S33-26**	**S33-27**	**S33-28**	**S33-29**	**S33-30**	**S33-31**	**S33-32**	**S33-33**	**S33-34**
SiO_2	45.29	60.90	59.88	61.32	60.20	61.51	59.62	61.02	60.37	61.21	59.89	62.24	60.24
TiO_2	0.01	0.01	0.03	0.06	0.13	0.00	0.01	0.00	0.02	0.00	0.02	0.04	0.01
Al_2O_3	35.69	25.04	25.47	25.18	25.24	24.80	25.74	25.04	25.75	24.73	25.63	24.44	25.09
FeO	0.23	0.02	0.23	0.04	0.03	0.03	0.11	0.07	0.22	0.07	0.11	0.10	0.08
MnO	0.03	0.05	0.00	0.01	0.03	0.05	0.02	0.04	0.04	0.05	0.04	0.01	0.03
MgO	0.00	0.01	0.04	0.02	0.00	0.02	0.03	0.00	0.06	0.03	0.00	0.00	0.00
CaO	17.22	6.03	6.60	6.23	6.30	5.44	6.17	6.00	6.57	5.87	6.85	5.27	6.57
Na_2O	1.05	7.49	7.22	7.39	7.71	7.79	7.43	7.50	7.21	7.43	7.04	7.87	7.33
K_2O	0.04	0.21	0.14	0.34	0.12	0.41	0.08	0.24	0.13	0.41	0.12	0.19	0.10
Total	99.55	99.76	99.61	100.59	99.76	100.06	99.22	99.90	100.37	99.80	99.70	100.17	99.46
Oxygens	8	8	8	8	8	8	8	8	8	8	8	8	8
Si	2.09	2.71	2.67	2.70	2.68	2.72	2.67	2.71	2.67	2.72	2.67	2.75	2.69
Ti	0.00	0.00	0.00	0.00	0.00	0.00	0.00	0.00	0.00	0.00	0.00	0.00	0.00
Al	1.94	1.31	1.34	1.31	1.33	1.29	1.36	1.31	1.34	1.30	1.35	1.27	1.32
Fe	0.01	0.00	0.01	0.00	0.00	0.00	0.00	0.00	0.01	0.00	0.00	0.00	0.00
Mn	0.00	0.00	0.00	0.00	0.00	0.00	0.00	0.00	0.00	0.00	0.00	0.00	0.00
Mg	0.00	0.00	0.00	0.00	0.00	0.00	0.00	0.00	0.00	0.00	0.00	0.00	0.00
Ca	0.85	0.29	0.32	0.29	0.30	0.26	0.30	0.29	0.31	0.28	0.33	0.25	0.31
Na	0.09	0.65	0.62	0.63	0.67	0.67	0.64	0.65	0.62	0.64	0.61	0.67	0.63
K	0.00	0.01	0.01	0.02	0.01	0.02	0.00	0.01	0.01	0.02	0.01	0.01	0.01
Total	4.99	4.97	4.97	4.96	4.99	4.97	4.98	4.97	4.97	4.96	4.96	4.96	4.97

Table A.5: Electron microprobe results for biotite

	S01-6	**S01-7**	**S01-8**	**S01-9**	**S01-10**	**S01-12**	**S01-13**	**S01-14**	**S01-15**	**S01-16**	**S01-17**	**S10-1**	**S10-2**
SiO_2	34.78	34.87	34.70	34.13	34.56	34.43	33.78	34.65	34.09	33.85	34.91	33.91	34.14
TiO_2	3.53	3.46	3.88	3.66	3.94	3.61	3.57	3.66	3.45	3.66	3.38	2.89	3.34
Al_2O_3	15.27	15.26	15.85	15.70	15.28	15.47	15.06	15.66	15.77	15.65	15.60	16.73	16.77
Cr_2O_3	0.02	0.02	0.00	0.01	0.03	0.00	0.03	0.00	0.01	0.02	0.00	0.01	0.00
FeO	22.63	23.19	23.28	23.56	24.25	23.76	22.73	24.43	24.12	23.42	23.28	26.79	26.71
MnO	0.11	0.04	0.07	0.07	0.01	0.15	0.06	0.07	0.07	0.04	0.07	0.41	0.39
MgO	9.92	9.98	9.36	8.78	8.60	9.46	8.97	9.13	9.48	9.33	9.59	5.97	5.72
CaO	0.07	0.04	0.09	0.09	0.05	0.02	0.07	0.16	0.02	0.08	0.06	0.01	0.08
Na_2O	0.54	0.46	0.53	0.47	0.24	0.47	0.55	0.47	0.41	0.48	0.50	0.07	0.20
K_2O	8.80	8.70	8.77	8.71	9.03	8.84	8.59	8.72	8.82	8.51	8.64	9.42	9.00
Total	95.67	96.02	96.53	95.17	95.99	96.21	93.40	96.95	96.24	95.05	96.04	96.20	96.35
Oxygens	11	11	11	11	11	11	11	11	11	11	11	11	11
Si	2.70	2.70	2.67	2.67	2.69	2.67	2.69	2.67	2.65	2.65	2.70	2.67	2.68
Ti	0.21	0.20	0.22	0.22	0.23	0.21	0.21	0.21	0.20	0.22	0.20	0.17	0.20
Al	1.40	1.39	1.44	1.45	1.40	1.41	1.41	1.42	1.44	1.44	1.42	1.55	1.55
Cr	0.00	0.00	0.00	0.00	0.00	0.00	0.00	0.00	0.00	0.00	0.00	0.00	0.00
Fe	1.47	1.50	1.50	1.54	1.58	1.54	1.51	1.57	1.57	1.53	1.50	1.77	1.75
Mn	0.01	0.00	0.00	0.00	0.00	0.01	0.00	0.00	0.00	0.00	0.00	0.03	0.03
Mg	1.15	1.15	1.07	1.02	1.00	1.09	1.07	1.05	1.10	1.09	1.10	0.70	0.67
Ca	0.01	0.00	0.01	0.01	0.00	0.00	0.01	0.01	0.00	0.01	0.00	0.00	0.01
Na	0.08	0.07	0.08	0.07	0.04	0.07	0.08	0.07	0.06	0.07	0.08	0.01	0.03
K	0.87	0.86	0.86	0.87	0.90	0.87	0.87	0.86	0.87	0.85	0.85	0.95	0.90
Total	7.88	7.87	7.86	7.86	7.84	7.89	7.87	7.87	7.90	7.87	7.86	7.86	7.81

...continued on next page

Table A.5 **Biotite** – continued from previous page

	S10-3	**S10-4**	**S10-5**	**S10-6**	**S10-7**	**S10-8**	**S10-10**	**S20-1**	**S20-2**	**S20-3**	**s21-1**	**s21-2**	**s21-3**
SiO_2	33.92	33.67	33.72	33.99	33.42	33.67	33.75	36.40	35.07	35.66	36.09	36.04	36.46
TiO_2	3.16	3.07	3.40	2.96	2.99	3.07	2.69	3.43	3.45	3.07	2.99	3.08	3.03
Al_2O_3	16.45	16.69	16.41	16.61	16.51	16.36	16.73	20.39	19.03	19.81	16.66	16.83	16.80
Cr_2O_3	0.03	0.00	0.02	0.00	0.00	0.00	0.00	0.01	0.07	0.03	0.06	0.04	0.07
FeO	26.93	26.84	26.86	25.56	25.94	26.21	26.65	20.33	20.90	20.95	20.45	20.84	20.70
MnO	0.50	0.45	0.45	0.44	0.39	0.44	0.38	0.04	0.02	0.08	0.15	0.13	0.11
MgO	5.99	5.96	6.01	5.87	5.92	5.83	5.77	8.24	8.61	9.77	10.70	10.66	10.92
CaO	0.02	0.04	0.02	0.10	0.05	0.01	0.07	0.05	0.01	0.01	0.02	0.06	0.01
Na_2O	0.14	0.08	0.28	0.24	0.32	0.14	0.08	0.29	0.16	0.17	0.24	0.28	0.26
K_2O	9.26	8.87	9.11	9.04	9.06	9.24	8.82	8.81	9.27	8.85	9.28	9.04	9.06
Total	96.40	95.67	96.29	94.81	94.60	94.97	94.94	97.98	96.59	98.41	96.64	96.99	97.41
Oxygens	11	11	11	11	11	11	11	11	11	11	11	11	11
Si	2.67	2.67	2.66	2.70	2.67	2.69	2.69	2.68	2.65	2.63	2.73	2.71	2.73
Ti	0.19	0.18	0.20	0.18	0.18	0.18	0.16	0.19	0.20	0.17	0.17	0.17	0.17
Al	1.53	1.56	1.52	1.56	1.56	1.54	1.57	1.77	1.70	1.72	1.48	1.49	1.48
Cr	0.00	0.00	0.00	0.00	0.00	0.00	0.00	0.00	0.00	0.00	0.00	0.00	0.00
Fe	1.77	1.78	1.77	1.70	1.74	1.75	1.77	1.25	1.32	1.29	1.29	1.31	1.30
Mn	0.03	0.03	0.03	0.03	0.03	0.03	0.03	0.00	0.00	0.01	0.01	0.01	0.01
Mg	0.70	0.70	0.71	0.70	0.71	0.69	0.69	0.91	0.97	1.08	1.21	1.20	1.22
Ca	0.00	0.00	0.00	0.01	0.00	0.00	0.01	0.00	0.00	0.00	0.00	0.00	0.00
Na	0.02	0.01	0.04	0.04	0.05	0.02	0.01	0.04	0.02	0.02	0.04	0.04	0.04
K	0.93	0.90	0.92	0.92	0.92	0.94	0.90	0.83	0.89	0.83	0.89	0.87	0.86
Total	7.85	7.83	7.86	7.82	7.86	7.84	7.82	7.68	7.76	7.76	7.82	7.82	7.81

...continued on next page

Table A.5 **Biotite** – continued from previous page

	s21-4	**s21-5**	**s21-6**	**s21-7**	**s33-1**	**s33-2**	**s33-3**	**s33-4**	**s33-5**	**s33-6**	**s33-7**	**s33-8**	**S50-3**
SiO_2	36.50	36.20	35.70	36.64	36.65	37.03	36.49	36.98	36.66	36.88	36.74	36.20	35.24
TiO_2	2.22	3.19	2.80	2.99	3.14	2.67	3.33	3.29	3.35	2.74	3.14	2.89	4.04
Al_2O_3	16.96	16.95	16.95	17.07	16.11	16.46	16.18	16.24	16.29	16.73	16.23	16.15	16.17
Cr_2O_3	0.06	0.00	0.01	0.05	0.13	0.16	0.08	0.10	0.11	0.14	0.11	0.11	0.04
FeO	20.07	20.86	20.39	21.34	19.75	19.49	19.44	19.65	19.93	19.29	19.52	19.75	27.96
MnO	0.16	0.17	0.09	0.11	0.24	0.19	0.22	0.23	0.25	0.25	0.20	0.22	0.12
MgO	11.31	10.32	10.72	10.52	11.72	12.05	11.38	11.49	11.41	11.34	11.46	11.13	6.21
CaO	0.08	0.03	0.05	0.00	0.00	0.05	0.05	0.00	0.00	0.04	0.05	0.15	0.00
Na_2O	0.28	0.19	0.16	0.14	0.14	0.13	0.22	0.20	0.11	0.20	0.22	0.35	0.07
K_2O	9.11	9.26	9.16	9.39	9.69	9.54	9.33	9.53	9.66	9.71	9.52	9.38	8.97
Total	96.76	97.17	96.03	98.25	97.57	97.77	96.72	97.71	97.77	97.31	97.20	96.32	98.82
Oxygens	11	11	11	11	11	11	11	11	11	11	11	11	11
Si	2.74	2.72	2.71	2.73	2.74	2.75	2.74	2.75	2.74	2.75	2.75	2.74	2.70
Ti	0.13	0.18	0.16	0.17	0.18	0.15	0.19	0.18	0.19	0.15	0.18	0.16	0.23
Al	1.50	1.50	1.52	1.50	1.42	1.44	1.43	1.42	1.43	1.47	1.43	1.44	1.46
Cr	0.00	0.00	0.00	0.00	0.01	0.01	0.00	0.01	0.01	0.01	0.01	0.01	0.00
Fe	1.26	1.31	1.30	1.33	1.23	1.21	1.22	1.22	1.24	1.20	1.22	1.25	1.79
Mn	0.01	0.01	0.01	0.01	0.02	0.01	0.01	0.01	0.02	0.02	0.01	0.01	0.01
Mg	1.27	1.16	1.21	1.17	1.31	1.33	1.28	1.28	1.27	1.26	1.28	1.26	0.71
Ca	0.01	0.00	0.00	0.00	0.00	0.00	0.00	0.00	0.00	0.00	0.00	0.01	0.00
Na	0.04	0.03	0.02	0.02	0.02	0.02	0.03	0.03	0.02	0.03	0.03	0.05	0.01
K	0.87	0.89	0.89	0.89	0.92	0.90	0.89	0.90	0.92	0.93	0.91	0.91	0.88
Total	7.84	7.80	7.82	7.81	7.84	7.84	7.81	7.81	7.83	7.83	7.82	7.85	7.78

...continued on next page

Table A.5 **Biotite** – continued from previous page

	S50-6	**S50-7**	**s51-1**	**s51-2**	**s51-3**	**s51-4**	**s51-5**	**s51-6**	**s51-7**	**s51-8**	**s51-9**	**s51-10**	**s51-11**
SiO_2	34.47	34.70	35.52	35.41	35.44	35.54	35.44	36.08	35.92	35.53	35.37	32.18	35.45
TiO_2	3.75	3.47	4.65	4.02	3.78	4.51	4.29	4.67	4.11	4.33	4.08	3.76	4.67
Al_2O_3	16.71	16.70	17.23	17.25	16.80	16.48	16.71	17.33	16.57	17.21	16.61	15.83	17.25
Cr_2O_3	0.05	0.05	0.02	0.01	0.00	0.01	0.01	0.00	0.02	0.00	0.04	0.05	0.02
FeO	27.62	27.21	26.40	26.70	27.25	27.46	27.51	26.08	27.74	27.10	27.80	26.73	27.38
MnO	0.12	0.14	0.12	0.22	0.27	0.32	0.22	0.14	0.22	0.25	0.24	0.29	0.23
MgO	6.46	7.10	5.92	6.57	6.44	6.11	6.26	6.52	6.41	6.01	6.32	5.76	5.89
CaO	0.03	0.01	0.00	0.01	0.00	0.01	0.03	0.00	0.00	0.07	0.00	0.07	0.00
Na_2O	0.10	0.08	0.09	0.11	0.06	0.07	0.10	0.07	0.03	0.10	0.06	0.08	0.13
K_2O	8.91	9.03	9.66	9.72	9.59	9.56	9.54	9.70	9.58	9.66	9.49	8.57	9.68
Total	98.22	98.50	99.62	100.01	99.63	100.07	100.11	100.59	100.60	100.26	100.01	93.32	100.71
Oxygens	11	11	11	11	11	11	11	11	11	11	11	11	11
Si	2.65	2.66	2.68	2.67	2.69	2.69	2.68	2.69	2.70	2.67	2.68	2.62	2.66
Ti	0.22	0.20	0.26	0.23	0.22	0.26	0.24	0.26	0.23	0.25	0.23	0.23	0.26
Al	1.52	1.51	1.53	1.53	1.50	1.47	1.49	1.52	1.47	1.53	1.48	1.52	1.53
Cr	0.00	0.00	0.00	0.00	0.00	0.00	0.00	0.00	0.00	0.00	0.00	0.00	0.00
Fe	1.78	1.74	1.67	1.68	1.73	1.74	1.74	1.62	1.74	1.71	1.76	1.82	1.72
Mn	0.01	0.01	0.01	0.01	0.02	0.02	0.01	0.01	0.01	0.02	0.02	0.02	0.01
Mg	0.74	0.81	0.67	0.74	0.73	0.69	0.70	0.72	0.72	0.67	0.71	0.70	0.66
Ca	0.00	0.00	0.00	0.00	0.00	0.00	0.00	0.00	0.00	0.01	0.00	0.01	0.00
Na	0.02	0.01	0.01	0.02	0.01	0.01	0.01	0.01	0.00	0.01	0.01	0.01	0.02
K	0.88	0.88	0.93	0.93	0.93	0.92	0.92	0.92	0.92	0.93	0.92	0.89	0.93
Total	7.81	7.83	7.76	7.81	7.81	7.79	7.80	7.76	7.80	7.79	7.81	7.83	7.79

...continued on next page

Table A.5 **Biotite** – continued from previous page

	s51-13	**s51-15**	**S52-1**	**S52-2**	**S52-3**	**S52-4**	**S52-5**	**S52-6**	**s53-1**	**s53-2**	**s53-3**	**s53-4**	**s53-5**
SiO_2	35.88	35.80	33.37	32.85	32.49	32.58	32.84	32.36	37.71	36.99	37.21	37.98	37.50
TiO_2	3.95	4.01	4.05	4.31	4.00	4.33	4.23	3.74	3.10	3.06	3.03	3.13	3.06
Al_2O_3	17.27	17.16	16.67	16.95	17.21	16.85	17.07	16.99	16.38	16.48	17.01	16.61	16.66
Cr_2O_3	0.00	0.03	0.00	0.00	0.00	0.00	0.02	0.02	0.10	0.08	0.10	0.06	0.09
FeO	26.41	26.42	29.97	29.12	29.05	28.99	29.28	28.52	17.38	17.12	16.72	17.38	17.58
MnO	0.21	0.21	0.26	0.25	0.20	0.26	0.17	0.25	0.17	0.16	0.19	0.13	0.13
MgO	6.65	6.64	4.41	4.40	4.67	4.87	4.87	4.96	14.25	13.99	13.97	14.27	14.18
CaO	0.00	0.04	0.05	0.04	0.00	0.02	0.07	0.11	0.12	0.03	0.09	0.00	0.03
Na_2O	0.08	0.24	0.10	0.10	0.14	0.12	0.10	0.16	0.47	0.42	0.36	0.42	0.42
K_2O	9.66	9.38	9.17	9.08	9.26	9.32	9.08	8.92	8.88	9.21	9.10	9.47	9.25
Total	100.11	99.93	98.06	97.10	97.03	97.34	97.73	96.03	98.56	97.54	97.78	99.45	98.90
Oxygens	11	11	11	11	11	11	11	11	11	11	11	11	11
Si	2.69	2.69	2.62	2.60	2.57	2.57	2.58	2.58	2.74	2.72	2.72	2.74	2.72
Ti	0.22	0.23	0.24	0.26	0.24	0.26	0.25	0.22	0.17	0.17	0.17	0.17	0.17
Al	1.53	1.52	1.54	1.58	1.61	1.57	1.58	1.60	1.40	1.43	1.47	1.41	1.43
Cr	0.00	0.00	0.00	0.00	0.00	0.00	0.00	0.00	0.01	0.00	0.01	0.00	0.01
Fe	1.66	1.66	1.97	1.92	1.92	1.91	1.92	1.90	1.06	1.05	1.02	1.05	1.07
Mn	0.01	0.01	0.02	0.02	0.01	0.02	0.01	0.02	0.01	0.01	0.01	0.01	0.01
Mg	0.74	0.74	0.52	0.52	0.55	0.57	0.57	0.59	1.54	1.54	1.52	1.53	1.54
Ca	0.00	0.00	0.00	0.00	0.00	0.00	0.01	0.01	0.01	0.00	0.01	0.00	0.00
Na	0.01	0.03	0.02	0.02	0.02	0.02	0.02	0.02	0.07	0.06	0.05	0.06	0.06
K	0.92	0.90	0.92	0.92	0.94	0.94	0.91	0.91	0.82	0.86	0.85	0.87	0.86
Total	7.79	7.79	7.84	7.82	7.86	7.86	7.84	7.86	7.83	7.85	7.83	7.85	7.85

...continued on next page

Table A.5 **Biotite** – continued from previous page

	s53-6	**s53-7**	**s53-8**	**S55-1**	**S55-2**	**S55-3**	**S55-4**	**S55-5**	**S55-6**	**S55-7**	**S55-8**	**S55-9**	**s55-10**
SiO_2	37.08	37.24	36.88	35.09	35.00	34.92	34.03	34.37	34.50	34.16	34.50	34.76	34.91
TiO_2	2.94	3.05	2.28	4.56	4.48	4.06	4.18	4.24	4.30	3.86	4.38	4.45	4.34
Al_2O_3	16.66	16.73	17.02	17.97	18.36	16.63	16.48	16.66	16.79	17.39	17.23	16.45	16.77
Cr_2O_3	0.06	0.05	0.09	0.00	0.01	0.00	0.02	0.00	0.00	0.00	0.01	0.00	0.00
FeO	17.29	17.67	17.85	27.50	27.37	29.54	29.44	29.64	29.53	28.96	28.81	29.54	29.06
MnO	0.20	0.13	0.20	0.05	0.00	0.25	0.22	0.20	0.19	0.25	0.20	0.20	0.19
MgO	13.82	13.83	14.17	4.85	4.60	4.76	4.59	4.67	4.65	4.78	4.81	4.89	4.72
CaO	0.10	0.07	0.06	0.00	0.00	0.00	0.02	0.00	0.01	0.01	0.01	0.00	0.00
Na_2O	0.50	0.37	0.30	0.07	0.06	0.12	0.13	0.10	0.11	0.07	0.10	0.08	0.09
K_2O	9.14	9.04	9.19	9.64	9.76	9.19	9.05	9.28	9.31	9.37	9.29	9.29	9.46
Total	97.80	98.19	98.04	99.72	99.64	99.47	98.16	99.16	99.38	98.84	99.34	99.67	99.55
Oxygens	11	11	11	11	11	11	11	11	11	11	11	11	11
Si	2.72	2.72	2.71	2.66	2.65	2.68	2.65	2.65	2.65	2.64	2.64	2.67	2.67
Ti	0.16	0.17	0.13	0.26	0.26	0.23	0.25	0.25	0.25	0.22	0.25	0.26	0.25
Al	1.44	1.44	1.47	1.60	1.64	1.50	1.51	1.52	1.52	1.58	1.56	1.49	1.51
Cr	0.00	0.00	0.01	0.00	0.00	0.00	0.00	0.00	0.00	0.00	0.00	0.00	0.00
Fe	1.06	1.08	1.10	1.74	1.73	1.90	1.92	1.91	1.90	1.87	1.85	1.89	1.86
Mn	0.01	0.01	0.01	0.00	0.00	0.02	0.01	0.01	0.01	0.02	0.01	0.01	0.01
Mg	1.51	1.51	1.55	0.55	0.52	0.54	0.53	0.54	0.53	0.55	0.55	0.56	0.54
Ca	0.01	0.01	0.00	0.00	0.00	0.00	0.00	0.00	0.00	0.00	0.00	0.00	0.00
Na	0.07	0.05	0.04	0.01	0.01	0.02	0.02	0.02	0.02	0.01	0.02	0.01	0.01
K	0.86	0.84	0.86	0.93	0.94	0.90	0.90	0.91	0.91	0.92	0.91	0.91	0.92
Total	7.86	7.83	7.88	7.75	7.75	7.79	7.80	7.81	7.80	7.81	7.79	7.80	7.79

...continued on next page

Table A.5 **Biotite** – continued from previous page

	S62-1	**S62-4**	**S62-6**	**S62-7**	**S62-8**	**S62-9**	**S62-10**	**S62-11**	**S64-1**	**S64-10**	**S64-11**	**S64-14**	**S64-16**
SiO_2	31.70	31.26	31.54	31.33	35.94	34.61	35.23	35.40	31.88	31.85	32.39	32.69	33.00
TiO_2	2.22	2.95	2.95	2.72	2.98	3.89	2.70	2.83	2.91	3.26	2.80	2.73	2.53
Al_2O_3	21.35	21.06	21.14	21.27	20.25	20.01	20.40	20.23	20.46	19.77	20.76	20.51	20.49
Cr_2O_3	0.03	0.06	0.01	0.07	0.01	0.06	0.08	0.02	0.00	0.00	0.03	0.03	0.05
FeO	21.90	21.14	21.47	22.35	21.66	19.93	20.46	21.89	21.33	21.46	21.71	21.16	21.26
MnO	0.20	0.21	0.21	0.20	0.28	0.24	0.18	0.24	0.21	0.19	0.24	0.19	0.23
MgO	8.14	8.15	8.14	7.83	8.03	7.96	8.16	8.10	8.51	8.72	8.25	8.54	8.69
CaO	0.00	0.01	0.00	0.00	0.00	0.51	0.00	0.01	0.00	0.02	0.01	0.01	0.00
Na_2O	0.11	0.20	0.15	0.11	0.11	0.34	0.11	0.19	0.27	0.17	0.18	0.20	0.23
K_2O	9.49	9.33	9.48	9.65	9.62	8.88	9.46	9.50	9.38	9.26	9.30	9.35	9.42
Total	95.14	94.37	95.09	95.52	98.89	96.43	96.78	98.41	94.96	94.70	95.67	95.42	95.90
Oxygens	11	11	11	11	11	11	11	11	11	11	11	11	11
Si	2.47	2.45	2.45	2.44	2.66	2.61	2.65	2.64	2.48	2.49	2.50	2.52	2.53
Ti	0.13	0.17	0.17	0.16	0.17	0.22	0.15	0.16	0.17	0.19	0.16	0.16	0.15
Al	1.96	1.94	1.94	1.95	1.76	1.78	1.81	1.78	1.88	1.82	1.89	1.87	1.85
Cr	0.00	0.00	0.00	0.00	0.00	0.00	0.00	0.00	0.00	0.00	0.00	0.00	0.00
Fe	1.43	1.38	1.40	1.46	1.34	1.26	1.29	1.36	1.39	1.40	1.40	1.37	1.37
Mn	0.01	0.01	0.01	0.01	0.02	0.02	0.01	0.02	0.01	0.01	0.02	0.01	0.02
Mg	0.94	0.95	0.94	0.91	0.89	0.90	0.92	0.90	0.99	1.02	0.95	0.98	0.99
Ca	0.00	0.00	0.00	0.00	0.00	0.04	0.00	0.00	0.00	0.00	0.00	0.00	0.00
Na	0.02	0.03	0.02	0.02	0.02	0.05	0.02	0.03	0.04	0.03	0.03	0.03	0.03
K	0.94	0.93	0.94	0.96	0.91	0.85	0.91	0.90	0.93	0.92	0.92	0.92	0.92
Total	7.90	7.88	7.89	7.91	7.76	7.73	7.75	7.78	7.89	7.88	7.86	7.86	7.87

...continued on next page

Table A.5 **Biotite** – continued from previous page

	S64-17	**S64-18**	**S64-21**	**S64-24**	**S64-25**	**S64-27**	**S64-29**	**S64-35**	**S64-36**	**S65-1**	**S65-2**	**S65-5**	**S65-6**
SiO_2	33.32	33.52	33.24	32.64	33.11	32.00	35.59	35.60	35.22	37.99	37.81	37.95	37.67
TiO_2	2.83	3.04	2.40	2.74	2.32	2.95	2.34	2.75	2.38	1.61	1.64	1.11	0.80
Al_2O_3	19.96	20.32	20.25	20.86	21.18	23.24	22.43	19.25	22.96	17.65	17.42	17.82	16.17
Cr_2O_3	0.05	0.00	0.04	0.00	0.01	0.00	0.03	0.04	0.04	0.19	0.30	0.70	0.12
FeO	21.22	21.84	21.45	21.67	21.54	19.94	20.85	22.82	20.86	14.76	15.32	13.48	15.97
MnO	0.26	0.27	0.18	0.21	0.18	0.23	0.20	0.20	0.23	0.11	0.11	0.09	0.13
MgO	8.66	8.54	8.86	8.49	8.30	7.68	7.38	8.26	7.32	16.25	15.27	16.28	13.28
CaO	0.04	0.03	0.04	0.00	0.00	0.02	0.00	0.03	0.00	0.07	0.07	0.17	0.16
Na_2O	0.26	0.22	0.23	0.18	0.12	0.14	0.10	0.18	0.12	0.23	0.17	0.20	0.27
K_2O	9.32	9.39	9.31	9.43	9.59	9.64	10.34	9.50	9.21	8.74	8.91	8.25	8.17
Total	95.92	97.17	95.99	96.22	96.35	95.84	99.26	98.62	98.34	97.59	97.02	96.06	92.73
Oxygens	11	11	11	11	11	11	11	11	11	11	11	11	11
Si	2.56	2.54	2.55	2.50	2.53	2.44	2.62	2.66	2.60	2.74	2.76	2.76	2.87
Ti	0.16	0.17	0.14	0.16	0.13	0.17	0.13	0.15	0.13	0.09	0.09	0.06	0.05
Al	1.80	1.82	1.83	1.89	1.91	2.09	1.94	1.69	1.99	1.50	1.50	1.53	1.45
Cr	0.00	0.00	0.00	0.00	0.00	0.00	0.00	0.00	0.00	0.01	0.02	0.04	0.01
Fe	1.36	1.39	1.38	1.39	1.38	1.27	1.28	1.43	1.29	0.89	0.93	0.82	1.02
Mn	0.02	0.02	0.01	0.01	0.01	0.02	0.01	0.01	0.01	0.01	0.01	0.01	0.01
Mg	0.99	0.97	1.01	0.97	0.95	0.87	0.81	0.92	0.80	1.75	1.66	1.77	1.51
Ca	0.00	0.00	0.00	0.00	0.00	0.00	0.00	0.00	0.00	0.01	0.01	0.01	0.01
Na	0.04	0.03	0.03	0.03	0.02	0.02	0.01	0.03	0.02	0.03	0.02	0.03	0.04
K	0.91	0.91	0.91	0.92	0.93	0.94	0.97	0.91	0.87	0.80	0.83	0.77	0.80
Total	7.85	7.85	7.87	7.87	7.86	7.82	7.78	7.80	7.71	7.83	7.82	7.79	7.77

...continued on next page

Table A.5 **Biotite** – continued from previous page

	S65-8	**S65-9**	**S65-11**	**S65-12**	**S65-13**	**S65-14**	**S65-15**	**S65-17**	**s67-1**	**s67-2**	**s67-3**	**s67-4**	**s67-6**
SiO_2	37.57	38.05	37.55	38.10	38.33	37.69	37.97	37.47	37.15	37.72	37.54	37.37	37.10
TiO_2	1.83	1.66	1.75	1.79	1.74	1.59	1.67	1.29	2.34	2.29	2.41	2.45	2.13
Al_2O_3	17.46	17.38	17.58	17.46	17.90	17.40	17.35	17.62	16.64	17.35	17.35	17.44	17.14
Cr_2O_3	0.19	0.16	0.13	0.11	0.19	0.14	0.20	0.33	0.13	0.13	0.09	0.09	0.08
FeO	16.52	16.94	15.81	16.13	16.57	16.08	16.59	16.96	16.95	17.00	17.22	17.14	17.03
MnO	0.14	0.09	0.08	0.15	0.09	0.07	0.15	0.13	0.09	0.11	0.07	0.10	0.09
MgO	14.77	15.02	14.72	15.20	15.54	15.09	14.95	14.92	13.41	13.72	13.57	13.58	13.65
CaO	0.00	0.01	0.01	0.00	0.00	0.06	0.02	0.02	0.11	0.09	0.01	0.03	0.07
Na_2O	0.21	0.23	0.36	0.25	0.26	0.22	0.18	0.20	0.32	0.31	0.19	0.19	0.20
K_2O	8.44	8.45	8.72	8.73	8.96	8.09	8.71	8.32	8.40	8.50	8.73	8.65	8.58
Total	97.12	98.00	96.72	97.92	99.57	96.43	97.79	97.26	95.53	97.23	97.17	97.04	96.07
Oxygens	11	11	11	11	11	11	11	11	11	11	11	11	11
Si	2.75	2.76	2.75	2.76	2.73	2.76	2.76	2.74	2.77	2.76	2.75	2.74	2.75
Ti	0.10	0.09	0.10	0.10	0.09	0.09	0.09	0.07	0.13	0.13	0.13	0.14	0.12
Al	1.50	1.48	1.52	1.49	1.50	1.50	1.49	1.52	1.46	1.50	1.50	1.51	1.50
Cr	0.01	0.01	0.01	0.01	0.01	0.01	0.01	0.02	0.01	0.01	0.01	0.01	0.00
Fe	1.01	1.03	0.97	0.98	0.99	0.99	1.01	1.04	1.06	1.04	1.06	1.05	1.06
Mn	0.01	0.01	0.00	0.01	0.01	0.00	0.01	0.01	0.01	0.01	0.00	0.01	0.01
Mg	1.61	1.62	1.61	1.64	1.65	1.65	1.62	1.63	1.49	1.50	1.48	1.49	1.51
Ca	0.00	0.00	0.00	0.00	0.00	0.00	0.00	0.00	0.01	0.01	0.00	0.00	0.01
Na	0.03	0.03	0.05	0.04	0.04	0.03	0.03	0.03	0.05	0.04	0.03	0.03	0.03
K	0.79	0.78	0.81	0.81	0.82	0.76	0.81	0.78	0.80	0.79	0.82	0.81	0.81
Total	7.80	7.81	7.82	7.82	7.84	7.79	7.82	7.82	7.78	7.78	7.78	7.78	7.80

...continued on next page

Table A.5 **Biotite** – continued from previous page

	s67-7	**s67-8**	**s67-9**	**s67-11**	**S67-16**	**S67-18**	**S67-19**	**S67-20**	**S67-21**
SiO_2	37.68	37.10	36.69	36.70	36.69	36.79	37.17	37.01	37.57
TiO_2	2.16	2.16	1.96	2.49	2.01	1.83	2.08	2.03	1.95
Al_2O_3	17.04	17.32	17.07	17.33	16.51	16.83	17.21	16.68	17.16
Cr_2O_3	0.10	0.08	0.11	0.22	0.07	0.13	0.08	0.08	0.17
FeO	16.86	17.57	17.96	16.94	19.41	19.39	19.28	18.73	18.47
MnO	0.11	0.12	0.13	0.11	0.14	0.11	0.07	0.11	0.13
MgO	13.79	13.33	13.41	13.28	13.32	12.74	13.54	13.20	13.33
CaO	0.07	0.07	0.24	0.08	0.07	0.03	0.10	0.04	0.00
Na_2O	0.26	0.14	0.18	0.27	0.21	0.17	0.23	0.30	0.23
K_2O	8.57	8.52	8.71	8.42	8.21	8.94	8.29	8.86	9.03
Total	96.64	96.42	96.46	95.84	96.63	96.95	98.04	97.05	98.05
Oxygens	11	11	11	11	11	11	11	11	11
Si	2.77	2.75	2.73	2.73	2.74	2.75	2.73	2.75	2.75
Ti	0.12	0.12	0.11	0.14	0.11	0.10	0.11	0.11	0.11
Al	1.48	1.51	1.50	1.52	1.45	1.48	1.49	1.46	1.48
Cr	0.01	0.00	0.01	0.01	0.00	0.01	0.00	0.00	0.01
Fe	1.04	1.09	1.12	1.05	1.21	1.21	1.18	1.16	1.13
Mn	0.01	0.01	0.01	0.01	0.01	0.01	0.00	0.01	0.01
Mg	1.51	1.47	1.49	1.47	1.48	1.42	1.48	1.46	1.46
Ca	0.01	0.01	0.02	0.01	0.01	0.00	0.01	0.00	0.00
Na	0.04	0.02	0.03	0.04	0.03	0.02	0.03	0.04	0.03
K	0.80	0.81	0.83	0.80	0.78	0.85	0.78	0.84	0.84
Total	7.78	7.79	7.83	7.78	7.83	7.85	7.82	7.85	7.83

Table A.6: Electron microprobe results for Muscovite

	S62-2	**S62-12**	**S62-13**	**S64-2**	**S64-3**	**S64-4**	**S64-5**	**S64-8**	**S64-9**	**S64-12**	**S64-13**	**S64-15**	**S64-19**
SiO_2	41.46	46.57	46.18	41.89	42.45	42.47	42.61	42.97	42.67	44.24	44.37	42.69	43.53
TiO_2	0.86	0.85	0.61	0.69	0.81	1.01	0.69	0.03	0.12	0.07	0.09	0.43	0.07
Al_2O_3	38.09	37.52	37.52	38.80	38.54	38.24	38.41	39.53	39.78	37.99	38.41	43.66	38.03
Cr_2O_3	0.07	0.09	0.02	0.04	0.00	0.03	0.00	0.04	0.00	0.00	0.01	0.01	0.03
FeO	1.10	1.15	1.08	0.84	0.88	0.84	1.05	0.66	0.67	0.81	0.84	0.64	1.18
MnO	0.03	0.03	0.06	0.05	0.03	0.05	0.01	0.01	0.03	0.06	0.01	0.00	0.07
MgO	0.57	0.49	0.49	0.38	0.37	0.42	0.56	0.32	0.29	0.51	0.52	0.35	0.66
CaO	0.01	0.00	0.00	0.00	0.00	0.00	0.00	0.00	0.01	0.00	0.00	0.00	0.00
Na_2O	0.45	0.62	0.57	0.72	0.66	0.72	0.60	0.78	0.84	0.65	0.61	0.66	0.66
K_2O	10.36	10.51	10.39	10.13	10.22	10.01	10.32	10.12	9.82	10.14	10.28	8.63	10.23
Total	93.01	97.82	96.92	93.53	93.96	93.80	94.25	94.46	94.23	94.47	95.13	97.06	94.48
Oxygens	11	11	11	11	11	11	11	11	11	11	11	11	11
Si	2.84	3.02	3.01	2.85	2.87	2.87	2.87	2.88	2.86	2.96	2.95	2.76	2.93
Ti	0.04	0.04	0.03	0.04	0.04	0.05	0.04	0.00	0.01	0.00	0.00	0.02	0.00
Al	3.08	2.86	2.89	3.11	3.07	3.05	3.05	3.12	3.15	3.00	3.01	3.32	3.01
Cr	0.00	0.00	0.00	0.00	0.00	0.00	0.00	0.00	0.00	0.00	0.00	0.00	0.00
Fe	0.06	0.06	0.06	0.05	0.05	0.05	0.06	0.04	0.04	0.05	0.05	0.03	0.07
Mn	0.00	0.00	0.00	0.00	0.00	0.00	0.00	0.00	0.00	0.00	0.00	0.00	0.00
Mg	0.06	0.05	0.05	0.04	0.04	0.04	0.06	0.03	0.03	0.05	0.05	0.03	0.07
Ca	0.00	0.00	0.00	0.00	0.00	0.00	0.00	0.00	0.00	0.00	0.00	0.00	0.00
Na	0.06	0.08	0.07	0.09	0.09	0.09	0.08	0.10	0.11	0.08	0.08	0.08	0.09
K	0.91	0.87	0.87	0.88	0.88	0.86	0.89	0.86	0.84	0.87	0.87	0.71	0.88
Total	7.06	6.98	6.98	7.05	7.04	7.03	7.05	7.04	7.03	7.01	7.01	6.96	7.04

...continued on next page

Table A.6 **Muscovite** – continued from previous page

	S64-20	**S64-22**	**S64-31**	**S64-32**	**S64-33**	**S65-7**	**S65-16**	**S65-18**
SiO_2	43.38	44.14	46.28	45.89	45.86	36.86	36.37	37.45
TiO_2	0.16	0.00	0.21	0.38	0.78	0.76	1.62	1.31
Al_2O_3	37.37	38.72	37.92	37.31	36.42	17.87	17.43	17.48
Cr_2O_3	0.00	0.02	0.08	0.00	0.05	0.31	0.43	0.31
FeO	1.37	0.90	0.75	0.83	1.09	18.16	17.54	16.75
MnO	0.06	0.03	0.00	0.05	0.07	0.12	0.09	0.11
MgO	0.68	0.46	0.22	0.30	0.49	14.10	14.61	14.93
CaO	0.01	0.02	0.00	0.00	0.00	0.18	0.18	0.15
Na_2O	0.61	0.71	0.48	0.46	0.44	0.20	0.25	0.17
K_2O	9.91	10.19	10.56	10.66	10.35	7.55	7.58	7.36
Total	93.56	95.20	96.50	95.89	95.56	96.11	96.10	96.02
Oxygens	11	11	11	11	11	11	11	11
Si	2.94	2.94	3.03	3.03	3.04	2.73	2.70	2.76
Ti	0.01	0.00	0.01	0.02	0.04	0.04	0.09	0.07
Al	2.99	3.03	2.92	2.90	2.84	1.56	1.52	1.52
Cr	0.00	0.00	0.00	0.00	0.00	0.02	0.03	0.02
Fe	0.08	0.05	0.04	0.05	0.06	1.13	1.09	1.03
Mn	0.00	0.00	0.00	0.00	0.00	0.01	0.01	0.01
Mg	0.07	0.05	0.02	0.03	0.05	1.56	1.62	1.64
Ca	0.00	0.00	0.00	0.00	0.00	0.01	0.01	0.01
Na	0.08	0.09	0.06	0.06	0.06	0.03	0.04	0.02
K	0.86	0.86	0.88	0.90	0.87	0.71	0.72	0.69
Total	7.03	7.03	6.97	6.98	6.97	7.81	7.81	7.76

Table A.7: Electron microprobe results for Sillimanite

	S20-1	S20-2	S64-26	S64-23	S64-6	S64-7	S64-28	S64-30
SiO_2	37.21	37.51	33.80	34.95	33.64	33.66	37.31	38.15
TiO_2	0.01	0.00	0.05	0.00	0.00	0.04	0.03	0.05
Al_2O_3	63.86	63.86	67.48	66.88	67.02	66.41	64.28	59.75
Cr_2O_3	0.03	0.03	0.05	0.04	0.05	0.04	0.07	0.04
FeO	0.17	0.19	0.32	0.13	0.18	0.16	0.27	1.33
MnO	0.07	0.03	0.03	0.00	0.03	0.06	0.06	0.06
MgO	0.03	0.02	0.01	0.01	0.02	0.01	0.00	0.11
CaO	0.02	0.01	0.01	0.00	0.01	0.02	0.06	0.03
Na_2O	0.00	0.02	0.01	0.00	0.01	0.04	0.09	0.06
K_2O	0.02	0.03	0.00	0.01	0.03	0.05	0.04	1.44
Total	101.41	101.70	101.75	102.02	100.98	100.47	102.21	101.03
Oxygens	11	11	11	11	11	11	11	11
Si	2.18	2.19	1.98	2.04	1.99	2.00	2.17	2.28
Ti	0.00	0.00	0.00	0.00	0.00	0.00	0.00	0.00
Al	4.41	4.40	4.67	4.60	4.67	4.65	4.41	4.20
Cr	0.00	0.00	0.00	0.00	0.00	0.00	0.00	0.00
Fe	0.01	0.01	0.02	0.01	0.01	0.01	0.01	0.07
Mn	0.00	0.00	0.00	0.00	0.00	0.00	0.00	0.00
Mg	0.00	0.00	0.00	0.00	0.00	0.00	0.00	0.01
Ca	0.00	0.00	0.00	0.00	0.00	0.00	0.00	0.00
Na	0.00	0.00	0.00	0.00	0.00	0.00	0.01	0.01
K	0.00	0.00	0.00	0.00	0.00	0.00	0.00	0.11
Total	6.61	6.61	6.68	6.66	6.68	6.68	6.62	6.68